Department of Electrical and Electronic Engineering

An Extended Induction Motor Model for Investigation of Faulted Machines and Fault Tolerant Variable Speed Drives

by

Omar Fadhel Jasim

B.Sc. (Hons), M.Sc.

Thesis submitted to the University of Nottingham for the degree of Doctor of Philosophy

October 2009

To

My respected parents,

My beloved Wife, Shaima,

and

My flowers, Amenah and Mohammed

To

Those helped me to be what I am and to do what I can

ABSTRACT

High performance variable speed induction motor drives have been commercially available for industrial applications for many years. More recently they have been proposed for applications such as hybrid automotive drives, and some pump applications on more electric aircraft. These applications will require the drive to operate in the presence of faults i.e. they must be "Fault Tolerant" and be capable of "Fault Ride Through". The aim of this project was therefore to investigate fault ride through control strategies for induction motor drives, particularly with respect to open circuit winding or power converter faults. Three objectives were identified and addressed to meet this aim.

a) A new simulation model for an induction motor was created which reflects both saturation and space harmonics effects within the drive under both symmetric (healthy) and asymmetric (faulted) conditions. The model has a relatively low computational requirement to allow it to be used in conjunction with the simulation of high performance control algorithms and power electronic equipment. For operation in both healthy and faulty conditions, comparisons show that the simulated saturation and space harmonic effects match those obtained from an experiment system. Therefore this model is a very useful tool for the development and optimisation of new control strategies for fault tolerant drive systems.

b) A novel on-line fault detection and diagnosis algorithm based on the measurement of the third harmonic component in the motor line currents has been proposed. The location of the open circuit fault is detected based on detecting a magnitude reduction for the third harmonic component of the current flowing to the motor terminals, and can be implemented in real time to give a fast response with little additional computational overhead.

c) A new open circuit fault tolerant control strategy has been designed for a delta connected induction machine suddenly affected by an open circuit winding fault. The fault ride through is achieved without any modification to either the

power converter or the motor circuit. A novel feedforward compensation algorithm is introduced which considerably reduces the current and the torque ripple in the faulted drive motor. Two methods for controlling the neutral point voltage are also presented so that the available voltage capacity of the inverter is maximised in both normal and fault mode. For high speed operation, two different methods for field weakening control are presented, so that the available voltage capacity is maximized in both normal and fault mode.

This thesis describes the theoretical derivation of the new models and algorithms, and presents experimental results from a 4kW laboratory prototype to validate the proposals. The full fault tolerant system is experimentally demonstrated on a delta connected machine which suffers an open circuit winding fault. The improved motor performance under fault conditions is clearly seen.

LIST OF PUBLICATIONS

The following publications were originated from this thesis:

[1] **O. Jasim**, C. Gerada, M. Sumner, and J. Arellano-Padilla "Investigation of induction machine phase open circuit faults using a simplified equivalent circuit model," *in Proc. 18th International Conference on Electrical Machines (ICEM '08),* Sept. 2008, pp. 1 – 6.

[2] **O. Jasim**, C. Gerada, M. Sumner, and J. Arellano-Padilla "A simplified model for induction machines with faults to aid the development of fault tolerant drives," *in Proc. 13th Power Electronics and Motion Control Conference (EPE-PEMC '08),* Sept. 2008, pp.1173-1180.

[3] **O. Jasim**, C. Gerada, M. Sumner, and J. Arellano-Padilla "Operation of an induction motor with an open circuit fault by controlling the zero sequence voltage," *in Proc. IEEE International Electric Machines and Drives Conference (IEMDC '09),* May 2009, pp. 1426 – 1433.

[4] S. Khwan-On, L. de Lillo, L. Empringham, P. Wheeler, C. Gerada, N. Othman, **O. Jasim**, and J. Clare "Fault tolerant power converter topologies for PMSM drives in aerospace applications," *in Proc. 13th International European Power Electronics and Applications Conference (EPE '09)*, Sept. 2009.

[5] **O. Jasim**, C. Gerada, M. Sumner, and J. Arellano-Padilla "Development of fault tolerant induction motor control strategies using an enhanced equivalent circuit model," *submitted to IEEE Transaction Industrial Electronic.*

[6] **O. Jasim**, C. Gerada, M. Sumner and J. Arellano-Padilla "Fault ride through control for delta connected induction motor with an open winding fault by controlling the zero sequence voltage," *accepted to be presented in the 5th International Conference on Power Electronics, Machines and Drives (PEMD 2010),* April 2010.

ACKNOWLEDGEMENTS

I would like to express my deep appreciation and gratitude to my supervisors Dr. Mark Sumner and Dr. Chris Gerada for their continuous support, encouragement, and valuable advice throughout the progress of this work.

Thanks are also due to International Office and Department of Electrical and Electronic Engineering, University of Nottingham for providing the financial support to cover my tuition fees for this research course.

I also wish to thank all my colleagues and friends in the Power Electronics, Control and Machine Group at University of Nottingham for the support and valuable discussions. Among them I would like to give a special thanks to Dr. Jesus Arellano-Padilla and Dr. Milijana Odavic for their help, and useful discussion.

I would also like to thank all of my friends for their friendship and support over the last four years. Among them, I wish to especially thank Dr. Sanaa Al-Ameen for his constant support, and encouragement. Appreciation is extended to those others who have made my research more interesting and enjoyable, are too many to mention, but particularly Dr. Kostas Kampisios and Dr. Kostas Papastergiou.

I would further like to thank Prof. Dr. Waladin Sa'id, University of Technology, Iraq for his constant support, help and encouragement. He was one of the first people that advised me to study in the University of Nottingham. I reserve my gratitude to him.

Finally, I owe the greatest debt of gratitude to my family. I would like to thank my parents and my sisters for a lifetime of support, encouragement, and education. I am also thankful to my parent-in-laws for their love, encouragement and financial support. Last, but certainly not least, I would like to thank my wife Shaima for her endless love and support.

LIST OF CONTENTS

LIST OF SYMBOLS AND ACRONYMS

Symbol	Definition
Ψ_{abcs}	The stator flux linkages
Ψ_{abcr}	The rotor flux linkages
$\psi_{\alpha s}, \psi_{\beta s}$	α and β axis stator fluxes
θ_r	Rotor electrical angular displacement
θ_e	Angular displacement of the reference frame
V_{abcs}	Stator terminal voltages
V_{abcr}	Rotor terminal voltages
$V_{abcr5,7}$	Rotor terminal voltages for the 5th and 7th harmonic components
$V_{abcr3+,3-}$	Rotor terminal voltages for the positive and negative components of the 3rd harmonic
i_{abcs}	Phase current in the stator winding
i_{abcr}	Current in the rotor winding
$i_{abcr5,7}$	Rotor currents for the 5th and 7th harmonic components
$i_{abcr3+,3-}$	Rotor currents for the positive and negative components of the 3rd harmonic
r_{abcs}	Per phase stator resistances
r_{abcr}	Per phase rotor resistances
$r_{abcr5,7}$	Per phase rotor resistances for the 5th and 7th harmonic components
$r_{abcr3+,3-}$	Per phase rotor resistances for the positive and negative components of the 3rd harmonic
L_s	Stator Inductance
L_r	Rotor Inductance
L_m	Magnetising inductance
L_{ms}	Stator magnetizing inductance
L_{ls}	Stator leakage inductance
L_{lr}	Rotor leakage inductance
w_r	Rotor electrical angular velocity
w_e	Angular velocity of the reference frame

Symbol	Definition
w_{base}	Base speed when the inverter reached the maximum voltage output ($V_{\max}$)
w_{slip}	Slip frequency
J	Moment of inertia
P	Number of poles
PP	Number of pole pairs
B_m	Viscous fraction coefficient
T_L	Load torque applied
T_e	Electromagnetic torque
W_m	Magnetic coenergy
h	Order of the space harmonic component
f_{rh}	Rotor current harmonic frequency
f_e	Supply frequency
f_r	Mechanical frequency of the rotor rotation
H	Magnetic field intensity
B	Magnetic flux
K_2, K_4, K_6	Amplitudes of the permanence variation introduced by the saturation effect.
$\rho_2,\ \rho_4,\ \rho_6$	Phase displacements of the permanence variation introduced by the saturation effect.
i_{sd}, i_{sq}	d and q axis stator currents
i_{sd}^*, i_{sq}^*	d and q axis stator reference currents
$i_{\alpha s}, i_{\beta s}$	α and β axis stator currents
i_o	Zero sequence current component
i_n	Neutral current
I_{abc}	Line currents
I_d	Rated d-axis current
$\left\|I_{abc\_3h}\right\|$	Magnitude of the third harmonic components of the line currents
$i_{asf}, i_{bsf},\ i_{csf}$	Phase current during the fault.

Symbol	Definition
V_{sd}, V_{sq}	*d* and *q* axis stator voltages
V_{ao}, V_{bo}, V_{co}	Inverter output voltages referred to the mid-point of the DC-link.
V_{an}, V_{bn}, V_{cn}	Inverter output voltages referred to the neutral point of the machine.
$V_{ab}^{*}, V_{bc}^{*}, V_{ca}^{*}$	Line voltage demands (reference voltages)
σ	Motor leakage factor
τ_r	Rotor time constant
ANFIS	Adaptive Neuro-Fuzzy Inference System
DMRM	Dynamic Mesh Reluctance Modelling
EMF	Electro Magnetic Force
FEM	Finite Element Method
FFT	Fast Fourier Transformation
MCSA	Motor Current Signature Analysis
MMF	Magneto Motive Force
NN	Neural Network
PWM-VSI	Pulse Width Modulation-Voltage Source Inverter
WFA	Winding Function Approach

LIST OF TABLES

LIST OF FIGURES

CHAPTER 1

INTRODUCTION

1.1 OVERVIEW

1.1.1 Faults in Motor Drives

The three-phase induction machine is one of the most popular rotating electrical machines used in industrial driven equipment due to its ruggedness and versatility. With the development of power electronic inverters and their digital control platforms, the three phase induction machine has become the most widely used electric machine for variable speed drive applications. However, their application has expanded beyond industrial drives and they are now used in aerospace, automotive, medical, and military applications. Some of these drives used in critical process control and cannot be interrupted under the penalty of stopping the whole process. The reliability of an adjustable speed induction machine drive is extremely important, especially if it is used for remote or safety critical applications. For this reason, induction motor drives with a high degree of fault tolerance are required for many applications, where it is very important to ensure that the continuous operation of the drive system is maintained.

The major faults of induction machines can generally be summarised as the following [1]:

1) Stator faults resulting in the opening or shorting of one or more turns of a stator phase winding.
2) Abnormal connection of the stator windings.
3) Broken rotor bar or cracked rotor end-rings.

4) Static and/or dynamic air-gap irregularities.
5) Bent shaft (similar to dynamic eccentricity) which can result in rubbing between the rotor and stator, causing serious damage to stator core and windings.
6) Bearing and gearbox failures.

From the above listed types of faults: 1) the stator faults; 2) the broken rotor bar and end ring faults of induction machines; 3) bearing; and 4) the eccentricity-related faults are the most common failures, and thus require special attention. Several studies have shown that 30-40% of induction motor failures are due to stator winding insulation breakdown [2]. The organic materials used for insulation in electric machines are subjected to deterioration, due to a combination of thermal overloading and cycling, transient voltage stresses on the insulating material, mechanical stresses, and environmental stresses. Among the possible causes, thermal stresses are the main reason for the degradation of the stator winding insulations. Generally, thermal stresses on the stator winding insulation are classified into three types: aging, overloading, and cycling. Even the best insulation will fail quickly if operated above its temperature limit. As a rule of thumb, for every $10^{o}C$ increase in temperature, the age of insulation life reduced by 50% [3]. Regardless of the causes, stator winding-related failures can be divided into the following five groups: turn-to-turn, coil-to-coil, line-to-line, line-to-ground, and single or multi-phase windings open-circuit faults as presented in Fig. 1.1.

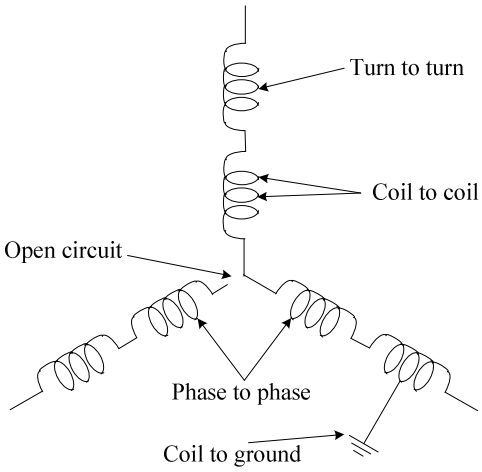

Fig. 1.1 Star connected stator showing possible failure modes [3].

It is generally believed that a large portion of stator winding-related failures are initiated by insulation failures in several turns of a stator coil within one phase which is called stator turn fault [4]. A stator turn fault in a symmetrical three-phase AC machine causes a large circulating current to flow and subsequently generates excessive heat in the shorted turns within a short time, in which the heat is proportional to the square of the circulating current. For a short period of time this fault will develop to be an open circuit winding fault and it can generally result in complete motor failure. The open circuit fault can be caused by other reasons such as mechanical failure of a machine terminal connector, an internal winding rupture, or by an electrical failure in one of the inverter phase legs [5]. Therefore, an open circuit fault can be considered to be one of the most common faults in induction motor drives [6]. However, the worst consequence of an open circuit fault in a safety-critical application would be a serious accident involving loss of human life resulting from an abrupt shutdown of the drive's operation. This work focuses on electrical faults in induction machines fed from power electronic drives using a Pulse Width Modulation-Voltage Source Inverter (PWM-VSI), and specially focuses on the open circuit fault. The main idea is to increase the stator open circuit fault tolerance of an induction motor drive in particularly for safety-critical applications.

1.1.2 Fault Tolerant Operation of Motor Drives

It is important to emphasize that fault tolerant systems need to incorporate an appropriate control architecture that includes a monitoring system which employs a fault detection strategy, and a controller which can organise reconfiguration for fault handling and subsequent post-fault operation. The definition of fault tolerance is the ability of a controlled system to maintain control objectives, despite the occurrence of a fault [7]. A degradation of control performance may be accepted but the ultimate aim is to avoid the interruption of the process. Based on the idea of keeping the electrical motor drive operating after a fault has occurred, two potential solutions have been suggested to overcome the problem and prevent overall system malfunction [8], namely:

1) Redundancy.
2) Fault diagnosis and fault-tolerant operating strategies by taking remedial actions.

Redundancy is commonly applied in improving the fault tolerance of electric motor drives. The concept of redundancy is well understood: if part of a system fails, there is an extra or spare that is able to operate in place of the failed unit such that the operation of the system is uninterrupted [8]. Although this approach is the surest way to increase the fault tolerance of an electric motor drive, it greatly increases the cost and complexity of the system. Moreover, redundancy may not be practical for an application that has a severe restriction on the installation space, such as in the case of traction drives in electric or hybrid-electric vehicles [4].

The alternative choice to the redundancy approach is fault diagnosis and fault tolerant strategies. With the appropriate machine monitoring and fault detection schemes early warning signs can be obtained to reduce maintenance, improve safety, and improve reliability for many engineering systems. The purpose of diagnosis is to detect and locate a certain failure from its point of inception so as to prevent major damage to the system and allow adequate timely actions to protect the system. Fault tolerant strategies are based on the concept that a faulty system can maintain its uninterrupted operation with the assistance of a modified topology or control algorithm. Several researchers have proposed fault-tolerant operating strategies to overcome this problem. This has been achieved by using new inverter architectures based on hardware redundancy to add reconfigurability to the system. The proposed solutions include the use of electrical motors with a redundant number of phases [6, 9-12], modifying the standard converter topologies by adding extra bidirectional switches to bypass the faulty power semiconductors, short-circuited or open circuited windings [13-15]. Other approaches include the availability of the motor stator winding neutral connection [14, 16], the use of inverters with a redundant number of controlled power switches [15, 17-19], the use direct AC–AC matrix converters instead the traditional AC–DC–AC drives [20-23], or the use of control adaptation without extra hardware [24, 25]. In addition, the reference signals to generate the post-fault switching patterns have to be modified to properly excite the motor for the resulting topology.

1.1.3 Fault Detection in Motor Drive Systems

In order to activate the fault tolerant control strategy, an accurate fault detection and diagnosis method needs to be utilised to ensure stable and reliable operation for safety critical applications. An accurate fault diagnosis system exhibits high fault detection rates and low false alarm rates, while maximising the correct classification of detected faults. If the detection capability of a fault diagnosis system is poor, then it is likely to miss developing faults which may lead to critical machine failures and breakdown of entire systems. While, if the fault detection system is too sensitive then it is likely to generate high rates of false alarms and may lead to a wrong decision being made. Different approaches for motor incipient fault detection and diagnosis have been successfully proposed by others. The common technique for online detection of motor faults is known as Motor Current Signature Analysis (MCSA) [26, 27]. It has been shown that there is a relationship between the mechanical vibration of a machine and the magnitude of the stator current component at the corresponding harmonics [1]. The objective of this technique is to detect certain components in the stator-current spectrum that are only a function of a specific fault. The spectrum is obtained using a Fast Fourier Transformation (FFT) that is performed on the signal under analysis.

For different motor faults, the fault frequencies that occur in the motor current spectra are unique. However, it has been shown mathematically and experimentally by [28] that the spectral components due shorted turns are not a reliable indicator of stator winding faults. A non-invasive technique for diagnosing machine and VSI failures in variable speed AC drives, based on the identification of unique signature patterns corresponding to the motor supply current Park's vector, was also proposed in [29, 30]. In [31, 32] the multiple reference frames theory was proposed to diagnose stator faults in three-phase induction motors directly connected to the grid. This method exploits the fact that each component present in the motor supply currents can be expressed in a reference frame in such a way that it will appear as constant within that reference frame. Almost all the proposed methods attempt to detect a change of the unbalance in the motor using indicators such as measurement of the negative sequence current [33, 34], negative-sequence impedance [35], zero sequence component [36], external signal injection [37] and change in positive-sequence current due to a stator fault [38]. References [33] and [34] describe more refined versions of the negative-

sequence-current-based schemes. In order to prevent a false alarm, causes such as voltage unbalance, saturation, eccentricity, and instrument asymmetry have also been factored in the negative-sequence-current measurement. For example, [34] enhances the work with a formula to account for them. An extensive survey of methods for detection of stator-related faults in induction machines can be found in [2].

It is important to emphasize that the use of different diagnostic techniques to diagnose different types of faults, as it appears that no technique is able to cope easily with all types of faults. In addition, some of the diagnostic techniques proposed so far rely on a detailed knowledge about the motor, usually difficult to obtain when the motors are already installed and in operation.

1.2 MODELLING MOTOR DRIVE SYSTEMS

The design of new high performance vector control algorithms often uses simulation models for initial development. These simulations ideally use a good machine model that takes the machine's non-linearities into account. Researchers working on condition monitoring and fault tolerant control of induction machines often need an accurate model to predict performance and to extract fault signatures [39]. This includes a representation of flux, current and torque harmonics in both healthy and fault conditions. Therefore, there is a real need to derive an accurate model, which can take into account the effect of saturation and field harmonics both in time and space, whilst still being embedded in a simulation, which includes real time control and a representation of power converters.

Simplified models based on the machine equivalent circuit are computationally fast and allow integration with real time control strategies, but are not accurate because they neglect the machine geometry and nonlinear magnetization effects. At the other extreme, the finite element model (FEM) provides detailed information about most machine nonlinear effects [40-47], but its solution is time consuming especially if a control algorithm needs to be incorporated [39]. A method providing a compromise between the speed of the conventional methods and the flexibility of finite-element analysis is the Dynamic Mesh Reluctance Modelling (DMRM) technique [48-52]. The

analysis is not as accurate as the FEM but its computational time is significantly faster, enabling the use of DMRM models to evaluate control applications.

Different nonlinear numerical models have been developed to simulate space harmonics and other nonlinear harmonic effects, which are based on the geometry of the squirrel cage induction motor [39, 53-61]. This modelling technique used coupled magnetic circuits approach combined with the Winding Function Approach (WFA). Such a model based on the geometry and winding distribution, having no restrictions regarding its symmetry, is more suitable for motor analysis and simulation under asymmetric and fault conditions. By comparing the various techniques, the DMRM and the WFA showed a good modelling accuracy and computational time faster than the FEM (2 hours vs 12 hours [62]). However, it is still comparatively slow when fast response current and torque control is required.

One of the aims of this work is to focus on deriving an induction machine model, which gives a good compromise between modelling accuracy and simulation time, and can be used to develop fault tolerant induction motor drives. This is achieved by developing and enhancing an equivalent circuit based model of the induction machine to include the space harmonics and machine saturation effects, such that the performance of motor drive system under healthy and faulty conditions can be simulated. The proposed model is able to provide a useful response (in terms of flux, current and torque harmonics) for the simulation of symmetrical and asymmetrical conditions, with only a short simulation time.

1.3 PROBLEM STATEMENT

An open circuit fault in an induction motor drive for a safety critical application should be detected quickly, on-line. The drive should be maintained in normal operation in order to prevent a potentially serious accident involving loss of human life or interrupting critical industrial processes. The scope of this work is to increase the stator open winding fault tolerance of induction machine drives, particularly in safety critical applications. This objective is to be achieved in three stages.

a) The development of a more realistic simulation model for an induction motor which reflects saturation and space harmonics effects whilst at the same time having a relatively low computational requirement to allow it to be used in conjunction with the simulation of high performance control algorithm and power electronic equipment.
b) To use the new model to develop a new fault detection algorithm.
c) To use the new model to develop new control algorithms for fault ride through.

To provide an accurate description of the behaviour of an open circuit fault in an induction machine drive and a reliable test bench for evaluating any method for fault detection or fault tolerant operating strategy, a model of an induction machine with open winding faults is derived and integrated with a PWM-VSI model. In the derivation of the machine model, an equivalent circuit based approach is adapted for a faster simulation speed. For more realistic simulations, this model is extended to include space harmonics and machine saturation effects and provides a useful tool for simulation of symmetrical and asymmetrical conditions that require a short simulation time, even for the case where a high performance controller is included in the simulation. The improvement is obtained by including a variation of the machine inductance with rotor position and flux position. The space harmonic effect is incorporated on the machine's mutual inductance as a function of rotor position and the saturation effect is incorporated as a flux position-dependant component in the stator mutual inductance. It is expected that by including the space harmonics and saturation effects, the model will help to identify some of the current harmonic components appearing under fault conditions. Thus, one of the main aims of the proposed model is to provide a tool for fault analysis in drives. As the model is a compromise between speed and accuracy, the model should give illustrative information about the harmonics present under various operating conditions.

The on-line open circuit fault detection method for a delta connected induction machine drive begins with a thorough evaluation of the state of the art open circuit winding fault detection methods for PWM-VSI driven applications. A novel on-line fault detection and diagnosis algorithm based on the measurement of the third harmonic component in the motor line currents has been proposed. The basis of the proposed method is that when an open circuit occurs for a delta connected machine,

the machine is transformed into a two phase star connected machine with access to the neutral point. As a result of the affected winding configuration, the triplen harmonics (third harmonic component) appear in the line currents since the system is not symmetrical. This will be reflected on the distribution of the harmonics over the three line currents, especially for the case of the third harmonic component. Therefore, the location of the open circuit winding fault is based on detecting a magnitude reduction for the third harmonic component of the current flowing to the motor's mid point connection. The use of the third harmonic component in the line current for open winding fault detection gives distinct benefits over conventional current fault detection methods. It is quite simple and easy to implement online and embedded into the processing platform of the drive as a subroutine without extra cost (i.e. no extra hardware is required), as the current sensor is already available in any PWM-VSI drive.

A new open circuit fault tolerant operating strategy specifically designed for a delta connected induction machine suddenly affected by an open circuit winding fault is proposed in this work. The description of open circuit fault tolerant operating strategy begins with a thorough evaluation of the state of the art. Most of the work addressed open circuit faults for star connected machines and most of the previous strategies have unsatisfactory performance characteristics with respect to cost, efficiency, or availability. The fault ride through is achieved without any modification to either the power converter or the motor circuit and more importantly, it does not result in the complete loss of availability of a drive in the presence of a stator open circuit fault. In fact, the proposed approach is also applicable to a fault tolerant drive containing an extra inverter leg connected to the neutral point of a star-connected machine. A novel feedforward compensation algorithm is introduced for the zero sequence component of the *dqo* reference voltages which considerably reduces the current and the torque ripple in the faulted drive motor. Two methods for controlling the neutral point voltage are also presented so that the available voltage capacity of the inverter is maximised in both normal and fault mode. For high speed operation, a field-weakening controller must be adopted by controlling the flux level to prevent inverter saturation. The main idea as speed increases is try to keep the stator voltage applied to the machine constant by reducing the magnetic flux. Two different methods for field weakening control are presented; an open loop field weakening controller using a conventional method and a

new closed loop field weakening controller that relies on the inverter voltage references and the maximum output voltage of the inverter so that the available voltage capacity is maximized in both the normal and the fault mode. Another important contribution of the proposed strategy is that the same principle can be applied to both induction machines or permanent magnet synchronous machines.

1.4 THESIS LAYOUT

This thesis is organized as follows:

Chapter 2 provides a summary of common modelling techniques which were developed by other researchers. The chapter also describes model based and signal based fault detection and diagnosis algorithms particularly for applications for electric motors. Furthermore, a review of fault tolerant control techniques is presented for different faults in electrical machine drives.

Chapter 3 presents the development of a new simulation model for an induction motor drive with an open circuit fault. The model includes space harmonics and machine saturation effects, and allows the investigation and simulation of servo drive systems under healthy and faulty operation conditions.

Chapter 4 shows the simulation and experimental results verifying the proposed model of induction machine drive under healthy and faulty operation conditions.

Chapter 5 presents a novel online scheme for phase open circuit fault detection designed specifically for a delta connected machine.

Chapter 6 presents an open circuit fault tolerant operating strategy for induction machine drives which is specifically designed for the delta connected machine suddenly affected with open circuit winding faults.

Chapter 7 illustrates the simulation and experimental results verifying the usefulness of the proposed open circuit fault detection and fault-tolerant operating strategy.

Chapter 8 summarizes the conclusions of the work and recommendations for future work.

CHAPTER 2

SUMMARY OF PREVIOUS WORK ON MODELLING, FAULT DETECTION AND FAULT TOLERANT TECHNIQUES

2.1 INTRODUCTION

This chapter describes how important and difficult it is to build an accurate model for induction machines taking into account machine non-linearities. It provides a summary of common modelling techniques which have been developed by other researchers. The theories and applications of model and signal based fault detection and diagnosis is presented, particularly for applications with electric motors. In addition, a review of fault tolerant operating techniques for different faults in electrical machine drives is presented. The last part of the chapter explores the behaviour of the three phase induction machine with a missing phase.

2.2 MODELLING AN INDUCTION MOTOR

Developing high performance control strategies for post-fault operation of induction motor drive systems requires an accurate machine model that accounts for the machine's non-linearities. However there is a trade off between accuracy and simulation time, and often simplified equivalent circuit models of induction machines are used. These simplified models lack the ability to correctly represent operation in faulted conditions where winding space harmonic and saturation effects are more pronounced due to the unbalanced nature of the machine. Hence an accurate model helps to predict the performance of the faulty machine, and to extract fault signatures [39]. Accordingly, there is a real need to develop accurate models that can take into account saturation effects and field harmonics both in time and space, whilst still being

embedded in a simulation which can be also used to develop advanced control strategies.

To be able to develop a more accurate model the machine working behaviour needs to be understood, as well as the explanation behind the existence of the current harmonics. Guldemir in [63, 64] stated that the prediction of the frequency and the amplitude of the speed-dependent harmonics in the line current are complicated even before considering the whole line current spectrum. In particular, the steady-state airgap flux-density distribution (as a function of time and space if required) is used directly to determine the induced harmonic EMFs and currents in the windings. The stator current spectrum of an induction machine in general contains a range of harmonics of different magnitudes and frequencies arising from different sources. The reasons for these harmonics are the spatial distribution of the airgap MMF and the variation in the airgap permeance. A non-constant airgap permeance results from four different factors: the stator and rotor slots, magnetic saturation, and eccentricity of the rotor and/or stator. A general expression describing the total airgap permeance wave is quite complex. The discussion of how these factors affect the permeance of the airgap is discussed in detail by Guldemir [63]. In order to understand the process of how the flux density distribution is calculated in the airgap, Fig 2.1 illustrates the computation of airgap field by MMF and permeance wave. The flux density distribution is calculated as the product of the airgap MMF and the permeance of the airgap. The variation of the airgap permeance is modelled as four blocks on the left hand side of this figure to reflect the four factors that mention above. These four blocks are multiplied together to form the non-constant airgap permeance. While the two sources of the airgap MMF have been modelled by the summation of the stator and rotor MMF as illustrated by two blocks on the right hand side. Each of the many permeance harmonics will interact with each of the many MMF harmonics to produce a series of rotating flux density harmonics which will have various speeds, pole number and direction depending on their source. The interaction between the resultant MMF and effective airgap permeance to produce the airgap field in induction machines has traditionally been expressed in terms of Fourier series expansions. The three phase currents in the induction motor set up an MMF varying with time, alternating around the circumference. In addition to the fundamental pole pair PP, space harmonics of nPP pole pairs are produced. The permeance of the airgap is altered and affected by

different phenomena such as slotting, saturation and eccentricity, hence it will not be consistent. The stator fundamental wave and the winding flux density harmonics are produced by the interaction of the MMF waves with the constant term of the permeance. The number of pole pairs of these harmonics is equal to the number of pole pairs of the MMF waves. Also, all the MMF waves interact with each permeance wave, inducing additional flux density waves of frequency and pole number equal to the sum or difference of the corresponding orders of the stator MMF and permeance waves. When the rotor is rotating, the combination of all the flux density waves passing through the airgap acts on its bars, inducing voltages in the bars. The induced voltages circulate currents through the rotor bars and end rings, producing rotor MMF waves. As a result, the new MMF waves interact with the permeance waves of the airgap to produce a new set of flux density waves rotating in the airgap. The component of these flux density waves, which is of the same order as the stator flux density wave inducing the current and which rotates at the same speed and in the same direction, reacts directly with that stator flux density wave. The other rotor fields, which have different pole numbers from the inducing stator flux density wave, develop voltages in the stator windings with frequencies different from that of the supply frequency if the rotor is moving.

There is a trade off between accuracy of the model and simulation time and therefore researchers who develop novel control schemes tend to use simplified equivalent circuit models of induction and permanent magnet machines. Therefore, it can be inferred that an accurate machine model that accounts for the machine's non-linearities is not easy and takes a long time to simulate. Modelling the machine's irregularities and non-linearities together with the control system simultaneously is essential in achieving the best possible drive performance. Control designers often struggle to achieve optimal performance from these machines due to their electromagnetic complexity and the difficulty in representing them with simplified equivalent circuits. Electromagnetic torque ripple and cogging torques, which are often associated with these drives, are difficult to suppress if a detailed machine model is not available at the research and development stage.

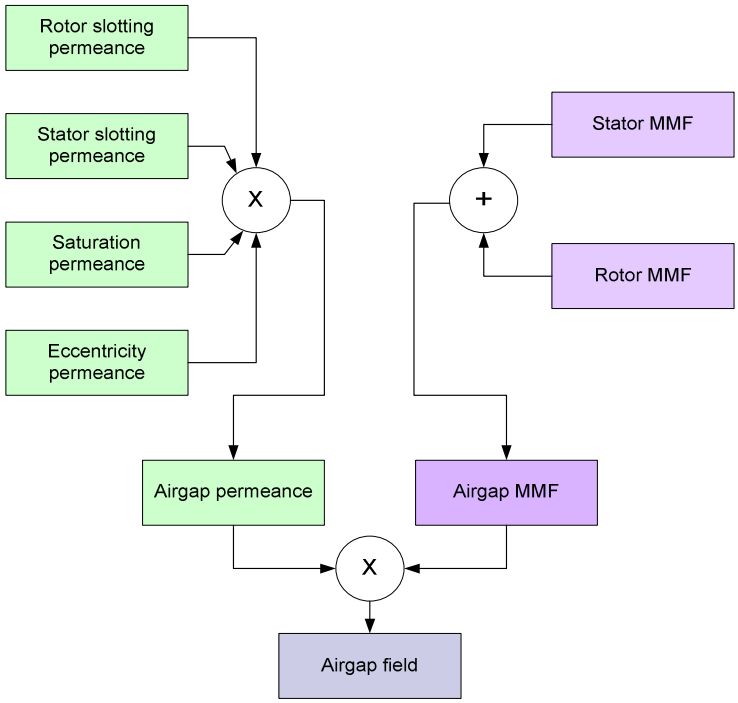

Fig. 2.1 Computation of airgap field by MMF and permeance wave technique [63].

2.3 MACHINE MODELLING METHODS

Various methods of modelling induction machines have been reported from fully detailed 3D-FE models to simpler ones based on a lumped equivalent circuit, the level of detail depending on the application at hand. This work focuses on deriving an induction machine model that provides a good compromise between modelling accuracy and simulation time for use with fault tolerant induction motor drives. Note that simplified models based on the machine equivalent circuit are computationally fast allowing the integration with high performance control strategies; however they are not accurate because they neglect the machine geometry and nonlinear magnetization effects [65]. This section describes different machine modelling methods for induction machines.

2.3.1 Modelling Based on Equivalent Circuit

Belhaj in [66, 67] proposed a circuit type frequential model of the induction machine based on the superposition principle used for electrical network simulation. Some of the models studied in the literature used integer orders based on resistance and inductance circuits in parallel or in a ladder configuration [68]. Others use non integer orders based on the integration of fractional order impedance in the rotor circuit [69]. The proposed model allowed the reproduction of the main low frequency components of the line current when the machine is supplied by non-sinusoidal voltages. The superposition principle was applied in this model considering that the field is the sum of the harmonic fields. Under these conditions, the machine was modelled by a linear circuit with localized constants for each harmonic component. The stator current was calculated by adding the obtained harmonic currents. This model was made from two parts, one used to describe the fundamental behaviour of the induction machine and another represents the harmonic contributions. One-phase classical model of the induction machine was proposed for the fundamental, and a large conductor model with an R-L ladder circuit was proposed for the harmonics [66, 67]. The principle assumes that the fundamental and harmonics phenomena are independent. The fundamental model parameters were identified with the help of open loop and lock rotor tests and the parameters of the harmonic model were identified using a genetic algorithm. It was reported that the accuracy of the harmonic model could be improved by taking into account the space harmonic and by using an adapted magnetic level during the identification test.

A different method proposes an equivalent internal circuit of the three-phase squirrel-cage induction machine for advanced signal processing including fault diagnosis [70, 71] and fault tolerant operation [72]. The internal circuit oriented model has taken into account the distributed nature of the induction machine windings and rotor bars. Stator and rotor equivalent circuits were represented on a conductor-by-conductor basis. In order to obtain a circuit-oriented model for the induction machine, individual stator coils, rotor meshes, and the magnetic field of their links must be considered. This model also takes into account the geometrical specifications of the magnetic and electric circuits of the induction machine for both stator and rotor sides. The stator model was obtained from the representation of each coil turn. Electrical parameters

such as inductances, mutual inductances, or leakage inductances are obtained by applying elementary laws to magnetic circuits. The results of the proposed model showed that the space harmonic components were matched by the analytical calculation, but there were large differences in the magnitude of some harmonics especially under fault conditions. This was due to the fact that the magnetic model is very simple; this could be improved by taking into account saturation effects which were not used in this model.

Some models take the space harmonics into account using an equivalent circuit for each harmonic component [73, 74]. Then, the superposition principle is applied considering that the field is the sum of the harmonic fields. Under these conditions, the machine is modelled by a linear circuit with localized constants for each harmonic component. The work presented in this thesis is a continuation to the model developed by Alger [73].

Saturation in induction machines is often dealt with by modifications to the equivalent circuit of the machines [75-79]. This improves matters, it is quite simplistic and neglects other non-linearities. An alternative approach proposed in [80] introduces the harmonic components of the magnetizing flux due to the nonlinear nature of saturation by modifying the air-gap length as a function of the air-gap flux position and amplitude. As a consequence of saturation, a third harmonic flux component is created within the magnetizing flux, and third harmonic currents are induced in the rotor circuits creating a ripple in the total torque and producing rotor losses. Reference [81] uses a modified equivalent circuit including the third spatial saturation harmonic for steady-state performance calculations. Hence, it is necessary to introduce into the circuit parameters of the induction motor a third harmonic magnetizing inductance relating the main component of the flux with its third harmonic component.

Nandi in [82] presents a model that incorporate the saturation in the induction machine based on phase quantities. The saturation effect is included as a sinusoidally varying second harmonic permeance component. The modelling utilises the Modified Winding Function Approach (MWFA) that has been described in [59] to accommodate a non-uniform air gap. This model is utilised to identify some new current harmonic components that appeared under fault conditions. Bispo [83] developed an approach to

model saturated induction motors in phase quantities and introduces the concept of "magnetic harmonic functions" to incorporate saturation effects. The magnetic harmonic functions were obtained via experimental procedures by measurements of terminal voltages and currents only. It considers the fundamental and third harmonic of the air-gap flux density distribution and develops equations for both star and delta connected machines. An experimentally tuned nonlinear model was described in [84], which presents a per-phase model incorporating the saturation effects in the magnetizing inductance to study a delta-connected machine. The work presented in this thesis is a continuation to the model developed by [84].

2.3.2 Modelling Based on Winding Function Approach (WFA)

The analysis of machines as a magnetic field problem requires an extensive calculation time. The geometry of electric machines normally leads to complicated boundary conditions even for simplified models. For this reason, it is more convenient and the problem will be much more simplified if a coupled magnetic circuits approach combined with the WFA is used [59]. Different nonlinear numerical models have been developed to simulate space harmonics and other nonlinear harmonic effects, which are based on the geometry of the squirrel cage induction motor [39, 53-61]. Such a model based on the geometry and winding distribution, having no restrictions regarding its symmetry, is more suitable for the motor analysis and simulation under asymmetric and fault conditions. These models are based on multiple coupled circuits and include geometry and the winding layout. A few restrictive assumptions are made when utilizing this technique [53, 54]; for example all the inductances used are derived by means of the WFA [39, 55-61] and [53, 54] are integrated using decomposition into their Fourier series. These models have been extended to monitor mechanical and electrical faults such as inter-turn short circuits in the stator windings [39, 55, 56, 58], open circuits in the stator winding [39, 55], broken rotor bars [53-55, 57, 58, 61] and air-gap eccentricity [59, 60]. Whilst the winding function technique benefits from a fast computational time, magnetic non-linearity is difficult to include in the model.

2.3.3 Modelling Based on Finite Element Method (FEM)

Other numerical approaches to model machines which are not based on the conventional topologies but rather on the machine geometry and the resulting unbalanced windings themselves is the FEM approach. It provides detailed information about the machine nonlinear effects (based on its geometry and material properties). This modelling approach is capable of obtaining an accurate and complete description of an electrical machine [40-47]. The magnetic circuit is modelled by a mesh of small elements. The field values are then assumed to be a simple function of position within these elements, enabling interpolation of results. The time required to calculate the field distribution may be very long, depending on the number of elements considered. A compromise must be reached between using finer meshes to achieve higher accuracy and the processing resources needed to achieve reasonable simulation times. The finite element method is very flexible, especially for new designs incorporating new shapes. However long time simulation requirements reduce the attractiveness of FEM especially for a case when a control algorithm needs to be incorporated [39]. Furthermore, FEM requires detailed machine specifications that are usually unavailable to application engineers.

Other work [85-88] includes an FE-based phase-variable model which combines the accuracy of the full FE machine model with reduced computation time. In these schemes the rotor-position-inductance variation is obtained by using a finite-element full cycle analysis which is stored in look-up tables and then used during the model simulation [85, 86]. In this way, the effect of space harmonics can be included. References [85, 86] report the use of the phase variable model scheme which includes accurate modelling of the machine saturation and rotor slotting effect as well as the cogging torque, all with reduced computation time.

2.3.4 Modelling Based on Dynamic Mesh Reluctance Method (DMRM)

A method providing a simulation speed compromise between conventional methods and flexibility of finite-element analysis is the DMRM technique [48-52]. The dynamic mesh reluctance method is in many ways similar to the FEM however with

some important differences. First of all, the number of elements used is much less than for the finite element method. This reduces accuracy but allows rapid computations. Accuracy may be improved by concentrating elements in critical and saturated parts of the machine. Another important difference is that flux in the reluctance mesh model can flow only in defined directions, whereas in FEM there is no restriction on the direction of flux through any element. The direction of flux in each element of the reluctance model must be decided before the method is applied, in contrast to finite-element analysis, where it is a result. In this case the analysis is not as accurate as the FEM scheme; however the computational time is significantly reduced, enabling the use of DMRM models to evaluate control applications. It has been successfully used to demonstrate the effect of the rotor skewing, iron saturation and fault condition for open and short winding in induction machines [50, 51]. Reference [48] used the DMRM technique to investigate rotor bar faults in induction machines and [52] introduced interbar currents and axial flux flow to the DMRM of induction machines.

2.3.5 Conclusion for Modelling of Induction Machines

By comparing several techniques, the DMRM and the WFA approaches showed a good modelling accuracy and computational time faster than the FEM (computation time of 2 hours vs 12 hours [62]). However, these approaches still are comparatively slow for those cases when fast response current and torque control is required. Therefore, in this work, an equivalent circuit based model for an induction machine, which includes space harmonics and machine saturation effects, is derived in terms of phase variables. The model is able to provide accurate results for the simulation of symmetrical and asymmetrical conditions, with reduced computation time. This is important for research into high performance motor drive systems operating in healthy and faulty conditions.

2.4 FAULTS AND FAULT DETECTION

With the development of power electronic inverters and their digital control platforms, the three phase induction machine has become the most used electric machine for variable speed drive applications. The reliability of an adjustable speed induction machine drive is extremely important, especially if it is used for remote or safety critical applications. Therefore, it is very important to ensure the continuous operation of the drive system under faulty conditions. To ensure stable and reliable operation of safety critical applications, fault detection, isolation and prediction techniques have become important as a better and lower cost solution [89].

Monitoring and failure detection improves the reliability and availability of an existing system. Since various failures degrade relatively slowly, there is potential for fault detection at an early stage. This avoids the sudden, total system failure which can have serious consequences for production downtime, or safety. It is particularly important first to identify the possible fault types and in which part of the variable speed drive the fault occurs, in order to judge their impact with respect to the normal control algorithm. Various faults which may occur in variable speed drives are in the machine or power converter. As a result, the failure modes can be classified into two main categories, namely electrical and mechanical faults. Electrical faults which may occur in the machine are stator winding open circuit, stator winding short circuit, broken rotor bar and broken end ring, etc. [3, 90]. On the other hand, the most common electrical faults which may occur in the power inverter are single switch short circuit, phase leg short circuit, single switch open circuit and single phase open circuit [14]. The mechanical faults can be classified into rotor eccentricity, bearing faults, shaft misalignment, etc. Mechanical faults associated with induction machines are the most commonly analysed types of fault in the literature, including work on bearing damage [91, 92], rotor eccentricity [1, 60, 91, 92] and shaft misalignment [93].

Several studies have shown that 30% - 40% of induction motor failures are due to stator winding breakdown [33]. This work focuses on electrical faults in induction machines fed from power electronic drives using (PWM-VSI), and specially focuses on open circuit fault. This type of fault can be caused by mechanical failure of a machine terminal connector, an internal winding rupture, or by an electrical failure in

one of the inverter phase legs [5]. The other major stator fault class for induction machines consists of short-circuit faults. These been addressed in a separate investigation [35, 37, 38, 94].

2.4.1 Fault Diagnosis Approaches

There are different types of fault detection and diagnosis algorithms in variable speed drives in terms of their theoretical grounds, advantages and drawbacks. However, the main objective of the fault detection and diagnosis block is to obtain a signal sensitive to faults, but robust against model uncertainty, noise and unknown disturbances. In general, the development of a fault detection and diagnosis system involves a time consuming process to identify the symptoms to be monitored, provide the correct signals for recognition of suitable fault symptoms, and then provide the correct computational methods to process the signals. In fact, in the literature, there is still no global fault detection and diagnosis algorithm that can overcome the parametric and model uncertainty, measurement noise, load torque effects and intrinsically electrical machine mechanical unbalance in variable speed drive applications [90]. For this reason, researchers have suggested different detection and diagnosis schemes with parameter settings that are developed specifically to the system under investigation. Fault detection and diagnosis methods can be classified into three approaches as described in [90].

2.4.1.1 Model Based Approach

Model based fault detection methods are based on the use of analytical redundancy, i.e. explicit mathematical models of the monitored system. The basic idea is to compare measurements with computationally obtained values of the corresponding variables, from which signals can be constructed as fault symptoms. Then these signals are sent to an evaluator to perform the diagnosis task. Complete or reduced mathematical models of the electrical machine are used to synthesise observers for residual generation in order to isolate faults [95-97]. However, the model-based

approaches are highly sensitive to model uncertainty. Hence, in order to compensate the model uncertainty or disturbances, adaptive observers have also been investigated for the induction motor [98]. The best fault detection and diagnosis algorithm depends strongly on the problem at hand, that is, electrical machine characteristics, type of measurements, hardware and capabilities, monitoring schemes (online or offline diagnosis), and motor operating conditions (constant or variable speed, constant or time-varying load torque). However, the signal-based approach is still the most used diagnosis tool in industrial applications [99]. A more comprehensive discussion of these approaches applied to induction motors can be referred to the following survey papers [2, 7, 30, 91].

2.4.1.2 Knowledge Based Approach

Knowledge based approaches utilize an insight of the process structure under various fault conditions. One form of a knowledge based system is an expert system [100]. The knowledge base is a form of database containing facts (descriptors of properties and characteristic) and information (rules). The expert system captures the knowledge of a human expert in a narrow specified domain in a machine implementable form to formulate these rules. It utilizes this knowledge to provide decision support at a level comparable to the human expert in order to recognise fault symptoms. On the other hand, the knowledge based approaches can be in different form as algorithms use input–output data in normal and fault conditions to train universal approximators (neural networks, fuzzy systems, neurofuzzy systems) in order to recognise these patterns, or to reproduce the input–output dynamical behaviour of the electrical machine [101-104]. Specifically, neural networks (NNs) have been applied to estimate the friction coefficient in an induction machine, in order to detect slowly developing (incipient) faults [101]. In [102], a NN is effectively utilised to detect an induction machine stator winding turn-fault. It illustrated the feasibility of the proposed on-line training algorithms for implementation in a commercial product. Nevertheless, the accuracy in the fault detection and isolation process depends mostly on the amount of training input–output data available. Alternatively, Adaptive Neuro-Fuzzy Inference System (ANFIS) in combination with decision trees can be used to detect different

type of faults of induction machine by using vibration and current signals [104]. It is reported that this technique has potential for fault diagnosis of induction motors.

2.4.1.3 Signal Based Approach

Signal based methods such as vibration analysis, motor current signature, instantaneous partial and total power, wavelet analysis and electrical torque harmonic analysis, do not incorporate any model and rely on features associated with the fault present in the measurement variables to determine, identify and quantify the fault types [1, 7, 91, 92, 99]. Signal based approach requires high quality sensors (acquisition system) in order for this approach to be used for detection. Fault detection associated with signal based methods consists of two stages: pattern recognition and decision making to identify different faults. The analysis of the stator currents using the Park's vector radius has been suggested to detect characteristic frequencies to identify machine and power converter faults [29, 30]. It was illustrated in [1, 91] that for mechanical and electrical faults, the frequency content of these measurements is correlated with frequency components for each specific fault condition. In this case the frequency components can be quantified by using the electrical measurements of the electrical machine, in order to diagnose a fault condition.

2.4.2 Condition Monitoring Techniques

The condition monitoring of electrical and mechanical devices has been explored in the literature. Several methods have developed over time but the most well-known techniques are thermal monitoring, vibration monitoring, and electrical monitoring.

2.4.2.1 Thermal Monitoring

The thermal monitoring of electrical machines is accomplished either by measuring the local or bulk temperatures of the motor, or by parameter estimation. The former

method requires the installation of thermocouples which is rarely happens in small machines. Thermal monitoring can in general be used as an indirect method to detect some stator faults (turn-to-turn faults) and mechanical faults (bearing faults). In [105] thermal monitoring by parameter estimation for small Permanent Magnet Synchronous Machine (PMSM) is utilised to detect faults. Firstly, a thermal model of the electrical machine is developed from the machine electrical quantities (the currents and voltages) and the thermal model is then used to estimate the temperature of the motor and identify faults. One of the drawbacks of thermal monitoring in a turn-to-turn fault is that the temperature rises in the region of the fault, but this might be too slow to detect the incipient fault before it progresses into a more severe phase-to-phase, phase open circuit or phase-to-neutral fault. In the case of detecting bearing faults, the increased bearing wear increases the friction and the temperature in that region of the machine. This is a slow process that can be detected by thermal monitoring.

2.4.2.2 Vibration Monitoring

Vibration monitoring is based on the concept that mechanical vibrations at various frequencies are related to identifiable sources in the machine and can be used to provide an indication of the condition of the machine. Vibration based diagnostics is used to detect different type of faults such as gear faults, rotor eccentricities, bearing faults, and unbalanced rotors. Almost all the rotor and bearing faults cause mechanical vibrations at specific frequencies [1]. The vibration energy of the machine is measured in one of three different measurements such as displacement probes, velocity transducers, or accelerometers units. Vibration-based diagnostics can be considered one of the best methods for fault diagnosis, but needs expensive measurements (i.e. accelerometers) and associated wiring. This limits its use in several applications, especially in small machines where cost plays a major factor in deciding the condition monitoring method.

2.4.2.3 *Electrical Monitoring*

Electrical monitoring is one of the most popular monitoring methods that have been used for the condition monitoring method. Monitoring the stator voltage, the stator current, sensing the air-gap flux, measuring shaft voltages and currents all fall under the category of electrical monitoring. These methods are used to detect various kinds of machine and inverter faults. The common technique for online detection of motor faults is known as MCSA [26, 27]. It has been shown that there is a relationship between the mechanical vibration of a machine and the magnitude of the stator current component at the corresponding harmonics [1]. The magnitude of the corresponding stator current harmonic components are increased when the mechanical vibrations increases. This is because the mechanical vibration modulates the air gap at that particular frequency. These frequency components then show up in the stator inductance, and finally in the stator current. For this reason, the MCSA can be used to detect stator, rotor, and bearing faults. The objective of this technique is to detect certain components in the stator-current spectrum that are only a function of a specific fault. The spectrum is obtained using a FFT that is performed on the signal under analysis. The fault frequencies that occur in the motor current spectra are unique for different motor faults. However, it has been shown mathematically and experimentally by [28] that the spectral components due to shorted turns are not a reliable indicator of stator winding fault.

A method for the online detection of the switching devices in a voltage-fed PWM inverter induction-motor drive was reported in [106]. The method is based on the time-domain response analysis of the induction-motor current space vector that the inverter supplies, followed by the application of a suitable pattern recognition algorithm. In [107] another online fault detection method is used to detect and localize the intermittent misfiring of the switching devices in a voltage-fed PWM inverter induction-motor drive. This method required the measurement of the phase currents only to calculate the ratio of DC to fundamental motor current as a diagnostic variable. A different kind of technique for fault detection of open switch damage in voltage-fed PMW asynchronous machine drive systems was proposed in [108]. The detection of the fault condition requires the measurement of voltages and currents and is based on analytical models of both the VSI and the asynchronous machine. In [89], a diagnostic

method was presented based on the analysis of the current-vector trajectory, as well as an approach based on the current instantaneous frequency in the faulty operating mode. A non-invasive technique for diagnosing machine and VSI failures in variable speed AC drives, based on the identification of unique signature patterns corresponding to the motor supply current Park's vector, was also proposed in [29, 30].

The effect of loosing one phase in a star connected machine could be detected easily by observing the winding currents since the current will be zero for the faulty winding as being discussed in [19]. In [31, 32] the multiple reference frames theory was proposed to diagnose stator faults in three-phase induction motors directly connected to the grid. This method exploits the fact that each component present in the motor supply currents can be expressed in a reference frame in such a way that it will appear as constant in that reference frame.

Other techniques are available to detect stator faults such as advance signal processing techniques [92], measurement of the negative sequence current [33, 34], negative-sequence impedance [35], zero sequence component [36], external signal injection [37] and change in positive-sequence current due to stator fault [38] remain some of the other methods to detect stator faults. References [33] and [34] describe more refined versions of the negative-sequence-current-based schemes. In order to prevent a false alarm, causes such as voltage unbalance, saturation, eccentricity, and instrument asymmetry have also been factored in the negative-sequence-current measurement. In fact, [34] has even come up with a formula to account for them. An extensive survey of methods for detection of stator-related faults in induction machines can be found in [2].

In [28] it was illustrated that the negative sequence current interacts with the fundamental slip frequency current in the rotor conductors to produce torque pulsating at twice the supply frequency. As a result a ripple appeared in the speed response. This ripple caused flux-density components at three times the supply frequency with respect to stator which is induced a third harmonic in the line current. Other work presented in [38] reports the detection of third harmonic component in the line current as a signature for stator fault. It was further pointed out in [82] that the fundamental

frequency reverse-rotating field (caused by the fundamental frequency–voltage unbalance and constructional asymmetry of the machine) interacts with the fundamental of the saturation-induced specific permeance function to produce the large third harmonic current due to the presence of a matching pole pair associated with the third harmonic flux-density component. The fault detection and diagnosis algorithm proposed in this work to detect the open stator winding fault is based on the existence of the third harmonic component in the line currents.

According to all the fault detection and diagnosis method which were mentioned above, the best fault detection technique that has able to detect all the stator or rotor faults is yet to be determined. Each method is found to detect a specific fault or some faults but not to be a general method.

2.5 FAULT TOLERANCE

The definition of fault tolerance is the ability of a controlled system to maintain control objectives, despite the occurrence of a fault [7]. A degradation of control performance may be accepted but the ultimate aim is to avoid the process stoppage. For this purpose, the controller design has to be prepared for such conditions and the control hardware requires some redundancy in its structure to overcome the problem when the fault occurs. It should also, ideally control the motor with minimum additional torque ripple and minimum additional losses.

Based on the idea of keeping the induction-motor drive operating after open fault detection in the machine winding or failures in the power converter, several authors have proposed fault-tolerant operating strategies to overcome this problem. This has been achieved by using a new inverter architecture based on hardware redundancy to add reconfigurability to the system. The proposed solutions were the use of induction motors with a redundant number of phases, modifying the standard converter topologies by adding extra bidirectional switches to bypass the faulty power semiconductors or short and open circuited windings, the availability of the motor stator winding neutral connection, or the use of inverters with a redundant number of controlled power switches. In addition, the references to generate the post-fault

switching patterns have to be modified to properly excite the motor with the resulting topology.

Open circuit fault tolerant techniques for 3-phase induction motor drives generally require a neutral motor connection to enable separate current control of the remaining healthy phases once a fault occurs. Reference [14, 16] proposed the use of triacs to connect the star point of the machine to the DC link midpoint of the inverter as shown in Fig. 2.2(a). After the fault is detected, the control system isolates the faulty leg through fast active fuses and connects the stator windings neutral point to the DC link middle point. A degree of control can be achieved here, but there is a significant limit to the maximum available motor line voltage [14], which restricts considerably the operating range of the machine. The strategy consists in reformulating the current references so that the rotating MMF generated by the armature currents do not change, and to minimize the electromagnetic torque ripple component, even if one phase is open circuited after a fault occurrence. In addition, this approach also provides a path for the 3rd harmonic current and can therefore lead to additional losses and torque pulsations. Another approach is proposed and discussed in [13-15], in which a pair of back-to-back-connected SCRs is used to switch off the faulty motor phase current as shown in Fig. 2.2(c). After the fault, a phase remains permanently connected to the midpoint of the DC voltage or, when insufficient voltage is available, the neutral is connected back to the midpoint, that has to be derived by using series-connected capacitors. The technique, in principle quite simple, becomes complicated by the need for preventing the capacitor midpoint voltage from drifting from the correct point. Also, the DC link filter capacitor needs to be overdesigned (by a factor of 5 to 10) in order to absorb the large fundamental frequency neutral current [25].

In order to overcome this problem and the low frequency pulsating torque without the use of the neutral-point connection, an alternative approach was proposed in [24, 25]. It is based on the injection of odd harmonic voltages at appropriate phase angles. None of these techniques requires an extra number of controlled power switches, only control-software adaptation. In [17-19] another solution is proposed to prevent using the mid-point of the DC link capacitors. It is a different topology based on the connection of the motor's star point to a fourth inverter leg as shown in Fig. 2.2(b). Furthermore, in [15] a further topology is proposed based on using fourth leg as in Fig.

2.2(b) but the three machine terminals were connected to the fourth inverter leg through a bidirectional switches as shown in Fig. 2.2(d). This topology is employed to by pass the faulty power switches in the converter only. By using an adequate control strategy for the additional leg in Fig. 2.2(b), the drive can deliver the same speed and torque ranges as those before the fault, at least on a reduced operating duty. Such a control strategy is presented in [19] where a "double controller" scheme employs one controller for the positive sequence and another for the negative sequence. In [17, 18, 109] a similar method was presented and was applied to a PMSM. A feedforward compensation was used to eliminate the unwanted current and torque components. A comparison study of these emerging topologies in terms of cost, features, and limitation is presented in [14].

An approach used recently employs direct AC–AC matrix converters instead the traditional AC–DC–AC drives for fault tolerant machine control as reported in [20-23]. It has been mentioned that the matrix converters have shown many advantages compared with traditional drives [21, 22]. For example, no DC-link capacitor is used, sinusoidal input and output currents (unity power factor) are obtained, and the resulting converter size is reduced. However, expensive solutions for overvoltage protection and complex control algorithms are required [90]. In [20, 21], a fault-tolerant topology to tolerate open and short phase failures for matrix converter drives has been proposed, where a new matrix converter structure and switching scheme have been suggested to generate three - phase balanced sinusoidal output currents, even after short circuit phase failures in the matrix converter drive. The open-phase faults considered in [20, 21] include, opened-switch faults in the converter and open circuit winding fault in the machine. In [21], the neutral connection approach was utilised as a fault-tolerant solution by connecting the motor neutral to the neutral point of three-phase supply utility as shown in Fig. 2.2(e). However, the neutral point of the supply voltage sources is not necessarily available in some power systems. Therefore, references [20, 23] address a fault-tolerant solution based on four-leg configuration to implement fault-tolerant matrix converter drives with no neutral point available from the supply utility. Similarly, in [23] only an open phase fault in the machine winding is considered and the four-leg matrix converter topology with the fault-tolerant capabilities for open phase failures is shown in Fig. 2.2(f). Reference [22] presents detailed fault conditions of the matrix converter induction motor drive system and a

novel protection strategy is proposed for the converter shutdown. The key to the proposed protection strategy was to provide a controlled free-wheeling path for the motor currents when a fault happens. It is demonstrated that the fault modes can be classified into two types: faults leading to an over-voltage, and faults leading to an over-current. In order to detect an abnormal operation, three over-current thresholds are used. Control switches are provided for a proper freewheeling path of the motor currents, so it is possible to eliminate the stored electric energy as quickly as possible.

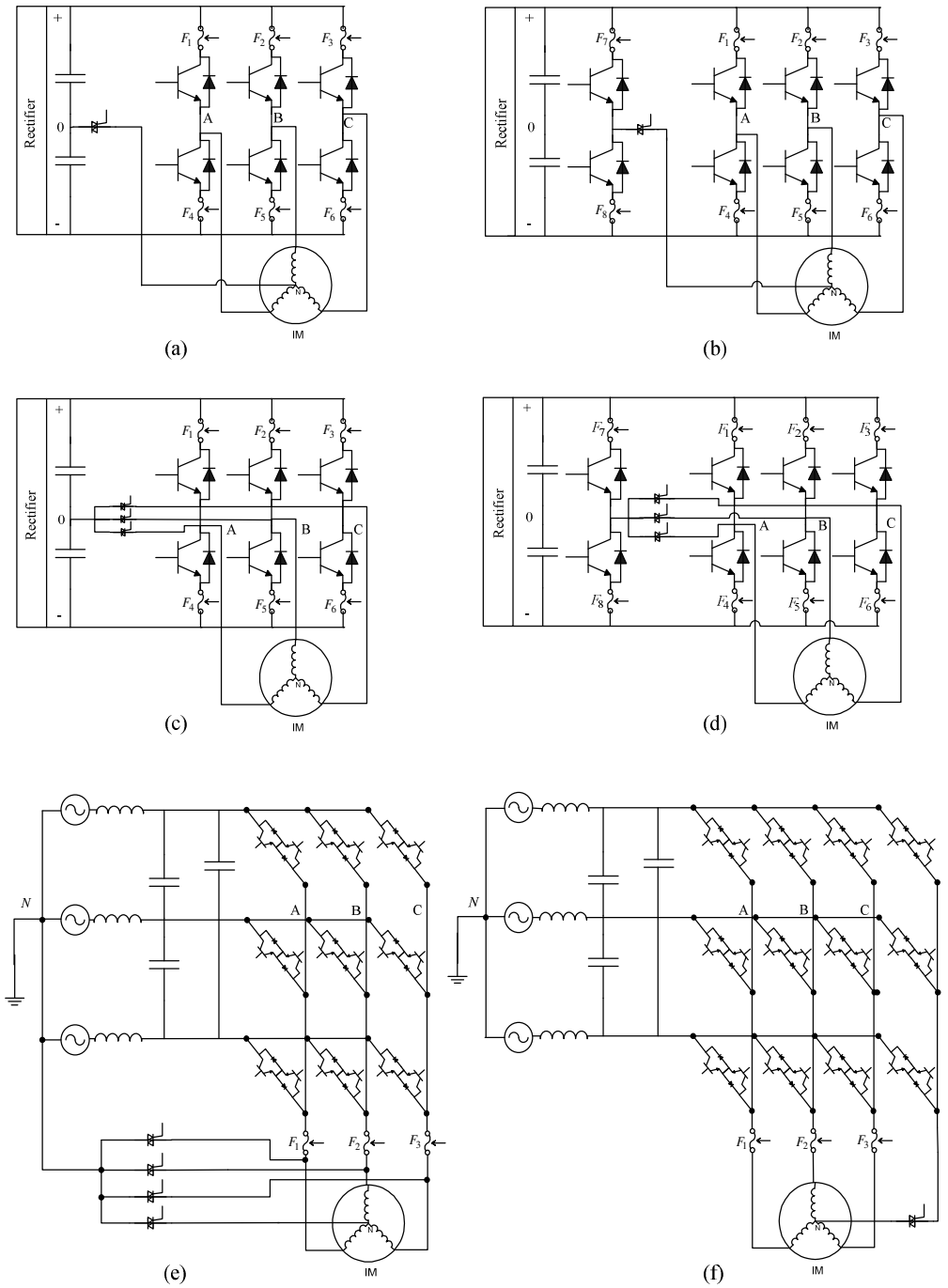

Fig. 2.2 Fault tolerant motor drive configurations

Most of the control strategies that been mentioned above to drive three-phase induction machines under fault conditions need a hardware redundancy. Other approaches have been explored in the literature which consider multiphase machine design for fault tolerant operation [6, 9-12]. Multiphase machines are advantageous over conventional three-phase machines for fault-tolerant operation. This is because in multiphase machines, when faults occur in one or more of the phases, the machines can still continue to operate using the remaining healthy phases [9] without needing to access i.e. the neutral point. Furthermore, fault-tolerant operation in multiphase machines does not require any additional hardware [6, 9-12], as it can be achieved just by using a modified control strategy. However, the choice of the number of phases is mainly a balance between the higher fault tolerance capabilities (a higher phase machine is able to give) and the lower reliability of the drive in terms of increased device count. Apart from improving fault tolerance, a multiphase machine has other advantages such as lower torque ripple, greater power density, lower stator current per phase without increasing the voltage per phase, and lower stator copper losses [6, 12]. These advantages make the multiphase machines suitable candidates for applications where high reliability is demanded. In [6, 9-12], the multiphase machines are considered to develop a fault-tolerant control strategy under open circuit fault condition (loss of one or more legs of the inverter or motor phase). The fault-tolerant operations of the multiphase PM machines and the multiphase induction machines, both with only sinusoidal stator winding distributions, are discussed in [11] and [9], respectively. In these cases, the stator phase currents are calculated to keep the rotating MMF undisturbed during faults. Reference [10] presents the application of using a third harmonic injection method to reduce the output torque ripple of a five-phase PM machine under various open circuit faults. While reference [6] designs an optimal control technique based on the instantaneous power balance and the ohmic loss minimization theory for multiphase PM machine under open circuit fault.

2.5.1 Operation of Three Phase Induction Machine with a Missing Phase

One of the most common types of faults in servo drive systems is a phase open circuit fault. It may happen either by failure of an IGBT in one of the inverter legs or by losing one of the phases in the motor due to an open circuit in the winding. For a star

connected 3-phase machine without a neutral connection or a delta connected machine, a phase open circuit at the machine terminals or in the converter would result in high pulsating torques as the machine would become a single phase machine having only one controllable current. Note that to maintain a constant rotating magnetic field in the air-gap, at least two independent stator winding currents are needed [16]. Whether this can be achieved depends on the connection of the stator winding. A topology for a three phase machine has been proposed to solve this problem [16]. In this case a neutral line connected between the motor neutral and the DC mid point is required in the presence of an open circuit fault so that the current in the remaining two phases can be individually controlled. In other words, a zero sequence component is required in a three phase machine to provide an undisturbed rotational MMF after one phase becomes open circuit. In this case, a new current control strategy can be implemented so that the torque can be maintained at its original value (i.e. the one before the fault occurred) or changed to any desired value while eliminating the negative sequence pulsating component which is usually associated with open circuit faults.

The authors in [16] proposed the use of a triac arrangement to connect the star point of the machine to the DC link midpoint of the inverter as shown in Fig. 2.2(a). In this case a degree of control can be achieved; however there is a considerable drop from the maximum available motor line voltage that will restrict significantly the operating range of the machine [14]. This approach also provides a path for the 3rd harmonic current and can therefore lead to additional losses and torque pulsations. In order to overcome this problem, [17-19] used a different topology based on the connection of the motor's star point to a fourth inverter leg as shown in Fig. 2.2(b). By using an adequate control strategy for the additional leg, the drive may deliver the same speed and torque ranges as those before the fault, or at least a reduced operating duty, with pre-fault quality.

In order to maintain a constant flux trajectory and to ensure a disturbance free operation for induction machine with a missing phase, the phase currents of the unfaulted phases (i.e. i_{csf} and i_{asf} in Fig. 2.3) need to be increased in magnitude by a factor of $\sqrt{3}$ and phase shifted 30^o away from the axis of the faulted phase as shown in Appendix F [14]. Fig. 2.3 shows a phasor diagram for the case of an open circuit fault on phase *b*.

Similarly, the phasor relationship before and after phases *a* and *c* are open circuited is shown in Fig. 2.4. The increment in magnitude of the current is given in the form of a non-torque producing zero sequence current to achieve a circular flux trajectory as was the case for the healthy machine.

One way to achieve this fault tolerant strategy uses direct control of the phase currents. The current commands in the *d-q* axis that have been found after implementing the standard indirect field orientation are transformed to three phase current command in the *abc* axis. The commanded currents are then compared to the motor stator currents which are measured from the induction machine. Three independent hysteresis controllers are then used to generate the switching pattern for each phase. The diagnosis technique determines which phase is open circuit and then the drive applies the proper phase shift to the remaining healthy phases. This project develops a fault tolerant control strategy similar in principle to that described here. Fault tolerant control topologies for induction machine will be discussed further in Chapter 6.

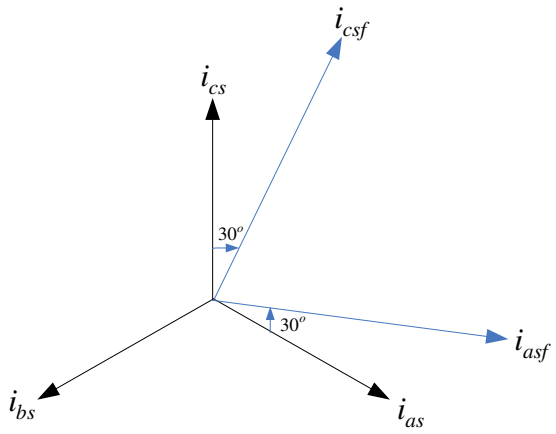

Fig. 2.3 Phasor relationships before and after phase *b* is open circuited.

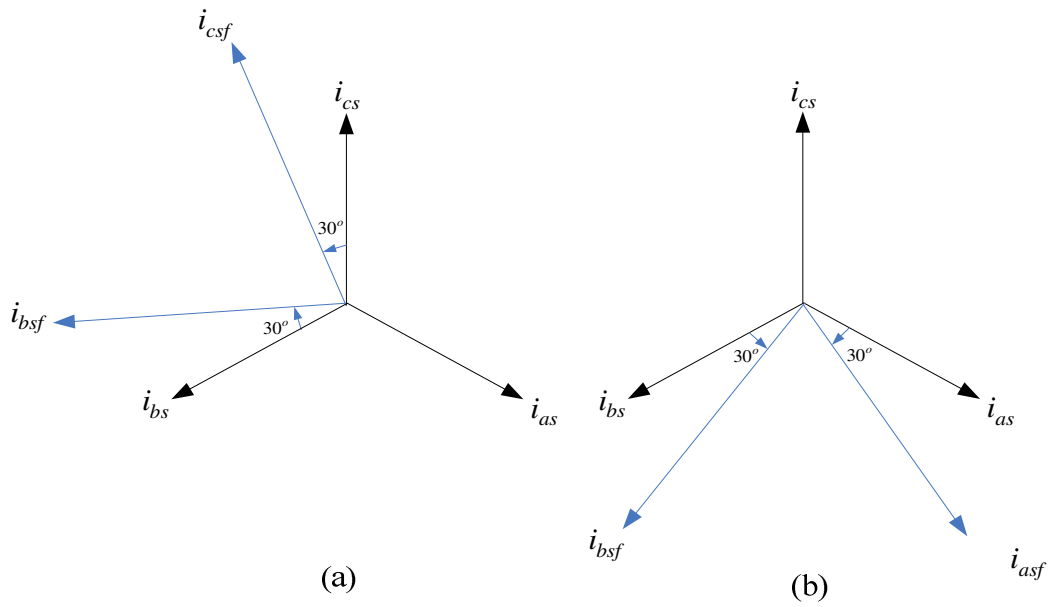

Fig. 2.4 Phasor relationships required for a unaffected operation when (a) phase *a* is open circuited and (b) phase *c* is open circuited

2.6 CONCLUSION

This chapter provides a summary of common modelling techniques which were used by other researchers to model different types of electrical machines in particular the induction machine. By comparing several techniques, the DMRM and the WFA approaches showed a good modelling accuracy and computational time faster than the FEM; however, these approaches still are comparatively slow for those cases when fast response current and torque control is required. The simplified models based on the machine equivalent circuit are computationally fast allowing the integration with high performance control strategies; however they are not accurate because they neglect the machine geometry and nonlinear magnetization effects. Therefore, in this work, an equivalent circuit based model for an induction machine, which includes space harmonics and machine saturation effects, is derived in terms of phase variables. This model is expected to provide accurate results for the simulation of symmetrical and asymmetrical conditions, with reduced computation time.

In addition, the theories and applications of model and signal based fault detection and diagnosis is presented in particularly on applications for electric motors. The most

common used condition monitoring techniques available to detect different types of faults has also been presented. Furthermore, a review of fault tolerant operation techniques through out different faults recognition in electrical machine drives is reviewed.

CHAPTER 3

MODELLING OF AN INDUCTION MACHINE WITH AN OPEN CIRCUIT FAULT

3.1 INTRODUCTION

This chapter investigates the development of a new equivalent circuit based model for an induction machine. This model includes space harmonics and machine saturation effects and allows the investigation and simulation of servo drives systems under healthy and faulty conditions. This model also provides a useful tool for simulation of symmetrical and asymmetrical conditions that require short simulation time, even for the case where a high performance controller is included in the simulation.

The improvement is obtained by including a variation of the machine inductance with rotor position and flux position. The space harmonic effect is incorporated on the machine's mutual inductance as a function of rotor position. This has been achieved by extending the equivalent circuit of the induction machine to include the effect of the two principle space harmonics; i.e. 5^{th} and 7^{th}.

In the proposed model, the saturation effect is incorporated as a flux position-dependant component in the stator mutual inductance. The inductance profile consists of three harmonic components where the magnitude and phase displacement of each component can be adjusted as required. The saturation model has been tuned to match the measured phase currents of the experimental system to allow a comparison. It is expected that by including the saturation effects, the model will help to identify some of the current harmonic components appearing under fault conditions. Thus, one of the main aims of the proposed model is to provide a tool for fault analysis in drives. As the

model is a compromise between speed and accuracy, the model should give illustrative information about the harmonics present under various operating conditions. The magnitude and phase of these harmonics will be in error, although these will be acceptable for the applications described.

This chapter has been structured as follows: Section 3.2 specifies the mathematical relationships between terminal voltages, currents, and the winding configuration that define the model differential equations. Section 3.3 presents the state space model, where the three phase stator windings are designed to produce a sinusoidally distributed MMF in the space along the air gap periphery. Section 3.4 discusses the modification of the equivalent circuit based model to include the two principal space harmonics (5^{th} and 7^{th}) of a balanced three-phase motor in terms of phase variables. The mechanism to represent the saturation effects in the state space model is presented in Section 3.5. Modification of the equivalent circuit and modelling of an open circuit fault and the consequence of losing one phase is contained in Section 3.6. The implementation of a drive integrated simulation model is discussed in section 3.7. Finally, conclusions are contained in Section 3.8.

3.2 IMPLEMENTATION OF NUMERICAL MODEL (DIFFERENTIAL EQUATIONS)

This section will define the electrical differential equations specifying the relationship between the terminal voltages, the winding currents, the winding resistance, the winding configuration and the magnetic model of the electrical machine. The stator winding configuration will be analysed in section 3.2.1 whereas the rotor winding configuration will be discussed in section 3.2.2.

3.2.1 Stator Windings

The stator phase winding of an electrical machine can be connected in a number of different configurations. The machine's terminal equations for various different configurations will be defined in this section.

3.2.1.1 Separate Phase Excitation

This configuration is the most straightforward connection, where each of the phases is analysed separately. An m-phase machine shown in Fig. 3.1, where for each phase, the voltage equation can be written as [50]:

$$V_n = R_n.i_n + L_{en}.\frac{di_n}{dt} + \frac{d\Psi_n}{dt} \tag{3.1}$$

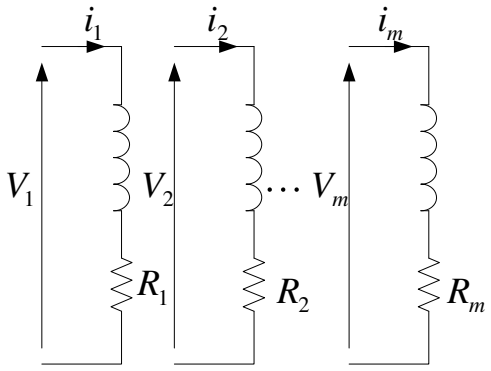

Fig. 3.1 An m-phase separately exited machine

where $V_n, R_n, i_n,$ and Ψ_n are the stator voltage of phase *n*, the stator resistance of phase *n*, the phase current of phase *n*, and the total modelled flux linking phase *n*, respectively. L_{en} represents the end winding leakage inductance, which is considered a constant. The flux linking phase *n* is calculated as:

$$\Psi_n = \sum_{k=1}^{m} L_{nsks}.i_{ks} + \sum_{k=1}^{q} L_{nskr}.i_{kr} \tag{3.2}$$

where the lowercase subscripts *s*, *r* denote the stator and rotor phase variables respectively, while *q* represents the number of the rotor phase circuits and L_{sr} is the stator-rotor mutual inductance. The number of differential equations defining the system is same as the number of phases.

3.2.1.2 Delta Connection

For the 3-phase delta connected machine which is shown in Fig. 3.2, the voltages across each phase winding are represented as:

$$V_1 = R_a.i_a + L_{ea}.\frac{di_a}{dt} + \frac{d\Psi_a}{dt}$$
$$V_2 = R_b.i_b + L_{eb}.\frac{di_b}{dt} + \frac{d\Psi_b}{dt} \quad (3.3)$$
$$V_3 = R_c.i_c + L_{ec}.\frac{di_c}{dt} + \frac{d\Psi_c}{dt}$$

The line currents will be the difference between the phase currents as in (3.4) and once again, the number of differential equations is the same as the number of phases.

$$i_1 = i_a - i_c$$
$$i_2 = i_b - i_a \quad (3.4)$$
$$i_3 = i_c - i_b$$

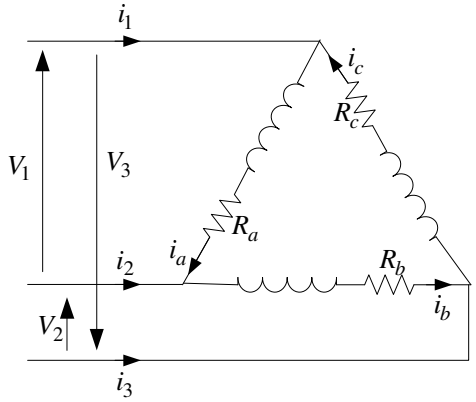

Fig. 3.2 A three-phase delta connected machine

3.2.1.3 Star Connection without Neutral

An m-phase star winding machine connected to an m-phase voltage source is shown in Fig. 3.3. When there is no neutral connection, the terminal differential equations are of this form:

$$
\begin{aligned}
V_1 &= V_{ga} - V_{gb} = R_a.i_a - R_b.i_b + L_{ea}.\frac{di_a}{dt} - L_{eb}.\frac{di_b}{dt} + \frac{d\Psi_a}{dt} - \frac{d\Psi_b}{dt} \\
V_2 &= V_{gb} - V_{gc} = R_b.i_b - R_c.i_c + L_{eb}.\frac{di_b}{dt} - L_{ec}.\frac{di_c}{dt} + \frac{d\Psi_b}{dt} - \frac{d\Psi_c}{dt} \\
&\vdots \\
V_{(m-1)} &= V_{g(m-1)} - V_{gm} = R_{(m-1)}.i_{(m-1)} - R_m.i_m + L_{e(m-1)}.\frac{di_{(m-1)}}{dt} - L_{em}.\frac{di_m}{dt} + \frac{d\Psi_{(m-1)}}{dt} - \frac{d\Psi_m}{dt}
\end{aligned}
\tag{3.5}
$$

In this case the line currents will be equal to the phase currents and the sum of all the phase currents is equal to zero $\sum_{k=1}^{m} i_k = 0$. The total number of independent voltage differential equations in the system is (*m-1*).

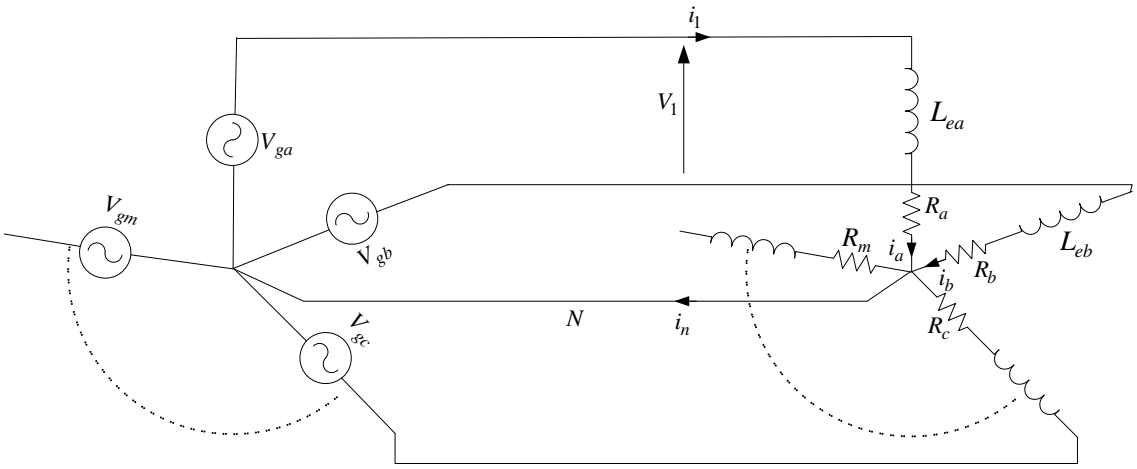

Fig. 3.3 An m-phase star connected machine

3.2.1.4 Star Connection with Neutral Point

Consider a star point connection between the machine and the voltage source supply as shown in Fig. 3.3, where any resistance in the neutral connection is neglected. The voltage across each phase can be defined as:

$$
\begin{aligned}
V_{ga} &= R_a.i_a + L_{ea}.\frac{di_a}{dt} + \frac{d\Psi_a}{dt} \\
V_{gb} &= R_b.i_b + L_{eb}.\frac{di_b}{dt} + \frac{d\Psi_b}{dt} \\
&\vdots \\
V_{gm} &= R_m.i_m + L_{em}.\frac{di_m}{dt} + \frac{d\Psi_m}{dt}
\end{aligned}
\tag{3.6}
$$

In this case the line currents will be equal to the phase currents while the neutral point will carry the sum of all the phase currents (3.7). Again, the number of equations defining the system is equal to the number of phases.

$$i_n = \sum_{k=1}^{m} i_k \tag{3.7}$$

3.2.2 Rotor Differential Equations

In general there are several types of rotor for electrical machines that may have either a distributed winding structure similar to those of the stator windings, a single-phase concentric winding as in the case of synchronous machines, a squirrel cage as is common with induction motors, a combination like in synchronous machines with an auxiliary squirrel cage, or none at all as with permanent magnet machines and switched reluctance machines. For wound rotor machines, the electrical differential equations will be similar to those of the stator windings. In general, it can be said that in an induction machine having *n* rotor bars, the cage can be viewed as *n* identical and equally spaced rotor loops, then the n-equations for the rotor can be written as:

$$\begin{aligned} V_1 &= R_{1r}.i_{1r} + \frac{d\Psi_{1r}}{dt} \\ V_2 &= R_{2r}.i_{2r} + \frac{d\Psi_{2r}}{dt} \\ &\vdots \\ V_n &= R_{nr}.i_{nr} + \frac{d\Psi_{nr}}{dt} \end{aligned} \tag{3.8}$$

Where R_{nr} is the n^{th} rotor bar resistance, i_{nr} is the current in the n^{th} rotor bar, and Ψ_{nr} is the flux linkage of the n^{th} rotor bar. In the case of a cage rotor $V_1,.....,V_n = 0$. The number of differential equations defining the system is equal to the number of bars. The circuits can be later connected in any fashion whatsoever to form the rotor bar/end ring configuration.

3.3 THE INDUCTION MACHINE MODEL

In an induction motor, the three phase stator windings are designed to produce a sinusoidally distributed MMF in the space along the air gap periphery. Assuming a uniform air gap and neglecting the effects of slot harmonics, the iron non-linearity and skin effect, the distribution of the magnetic flux will also be sinusoidal. Fig. 3.4 shows a representation for the induction machine.

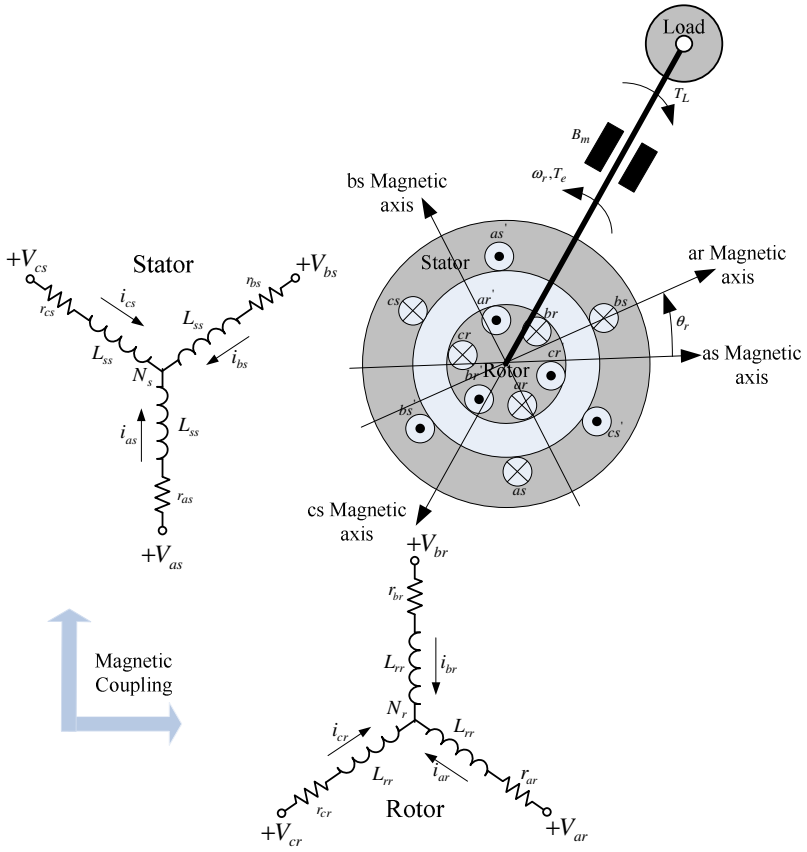

Fig. 3.4 Three phase symmetrical induction motor [65].

3.3.1 Stator and Rotor Voltage Equations

This section, describes the mathematical model of the induction machine in the *abc* frame (i.e. phase quantities) [65]. The motor phase voltages and currents will be referred to as the winding variables. From the equivalent circuit, a general form of the equations in the *abc* frame can be written in matrix form as follows:

$$\begin{bmatrix} V_{abcs} \\ V_{abcr} \end{bmatrix} = \begin{bmatrix} R_s & 0 \\ 0 & R_r \end{bmatrix} \cdot \begin{bmatrix} i_{abcs} \\ i_{abcr} \end{bmatrix} + \frac{d}{dt} \begin{bmatrix} \Psi_{abcs} \\ \Psi_{abcr} \end{bmatrix} = \begin{bmatrix} R_s & 0 \\ 0 & R_r \end{bmatrix} \cdot \begin{bmatrix} i_{abcs} \\ i_{abcr} \end{bmatrix} + \frac{d}{dt} \left(\begin{bmatrix} L_s & L'_{sr} \\ L'^{T}_{sr} & L'_r \end{bmatrix} \cdot \begin{bmatrix} i_{abcs} \\ i_{abcr} \end{bmatrix} \right) \tag{3.9}$$

the subscript *s* and *r* denotes stator and rotor variables. V_{abcs}, V_{abcr}, i_{abcs} and i_{abcr} are the stator and rotor terminal voltages, and the stator and rotor phase currents respectively. The resistance matrices R_s and R_r as well as the inductance matrices L_s, L_r and L_{sr} from (3.9) can be written as follows:

$$R_s = \begin{bmatrix} r_{as} & 0 & 0 \\ 0 & r_{bs} & 0 \\ 0 & 0 & r_{cs} \end{bmatrix}, R_r = \begin{bmatrix} r_{ar} & 0 & 0 \\ 0 & r_{br} & 0 \\ 0 & 0 & r_{cr} \end{bmatrix} \tag{3.10}$$

$$L_s = \begin{bmatrix} L_{ls} + L_{ms} & L_{abs} & L_{acs} \\ L_{bas} & L_{ls} + L_{ms} & L_{bcs} \\ L_{cas} & L_{cbs} & L_{ls} + L_{ms} \end{bmatrix} \tag{3.11}$$

$$L'_r = \begin{bmatrix} L_{lr} + L_{ms} & L_{abr} & L_{acr} \\ L_{bar} & L_{lr} + L_{ms} & L_{bcr} \\ L_{car} & L_{cbr} & L_{lr} + L_{ms} \end{bmatrix} \tag{3.12}$$

$$L'_{sr} = L_{ms} \begin{bmatrix} \cos\theta_r & \cos\left(\theta_r + \frac{2}{3}\pi\right) & \cos\left(\theta_r - \frac{2}{3}\pi\right) \\ \cos\left(\theta_r - \frac{2}{3}\pi\right) & \cos\theta_r & \cos\left(\theta_r + \frac{2}{3}\pi\right) \\ \cos\left(\theta_r + \frac{2}{3}\pi\right) & \cos\left(\theta_r - \frac{2}{3}\pi\right) & \cos\theta_r \end{bmatrix} \tag{3.13}$$

where r_{abcs} and r_{abcr} represent the per phase stator and rotor resistances respectively, L_{ls} and L_{lr} are the stator and rotor leakage inductance, L_{ms} is the magnetizing inductance, L_{abs}, …, L_{cbs} represents the mutual inductances between the stator phases, and L_{abr}, …, L_{cbr} represents the mutual inductances between the rotor phases. The rotor electrical angle is denoted by θ_r. Substituting (3.10 – 3.13) in (3.9) yields:

$$\begin{bmatrix} V_{abcs} \\ V_{abcr} \end{bmatrix} = \begin{bmatrix} R_s & 0 \\ 0 & R_r \end{bmatrix} \cdot \begin{bmatrix} i_{abcs} \\ i_{abcr} \end{bmatrix} + \begin{bmatrix} L_s & L'_{sr} \\ L'^{T}_{sr} & L'_r \end{bmatrix} \frac{d}{dt} \begin{bmatrix} i_{abcs} \\ i_{abcr} \end{bmatrix} + \begin{bmatrix} 0 & \frac{dL'_{sr}}{dt} \\ \frac{dL'^{T}_{sr}}{dt} & 0 \end{bmatrix} \cdot \begin{bmatrix} i_{abcs} \\ i_{abcr} \end{bmatrix} \tag{3.14}$$

The dynamic behaviour of the induction motor can be expressed as a function of stator currents and rotor currents in a state space form:

$$\frac{d}{dt}\begin{bmatrix} i_{abcs} \\ i_{abcr} \end{bmatrix} = -\begin{bmatrix} L_s & L'_{sr} \\ L'^{T}_{sr} & L'_r \end{bmatrix}^{-1} \cdot \begin{bmatrix} R_s & 0 \\ 0 & R_r \end{bmatrix} \cdot \begin{bmatrix} i_{abcs} \\ i_{abcr} \end{bmatrix} - \begin{bmatrix} L_s & L'_{sr} \\ L'^{T}_{sr} & L'_r \end{bmatrix}^{-1} \cdot \begin{bmatrix} \frac{dL_s}{dt} & \frac{dL'_{sr}}{dt} \\ \frac{dL'^{T}_{sr}}{dt} & \frac{dL'_r}{dt} \end{bmatrix} \cdot \begin{bmatrix} i_{abcs} \\ i_{abcr} \end{bmatrix} + \begin{bmatrix} L_s & L'_{sr} \\ L'^{T}_{sr} & L'_r \end{bmatrix}^{-1} \cdot \begin{bmatrix} V_{abcs} \\ V_{abcr} \end{bmatrix} \tag{3.15}$$

3.3.2 Calculation of Electromagnetic Torque

The electromagnetic torque for a P-pole three phase induction motor is found from the magnetic coenergy W_m such that: [65]

$$T_e = \frac{P}{2}.\frac{\partial W_m}{\partial \theta_r} = \frac{P}{2}.\begin{bmatrix} i_{abcs} & i_{abcr} \end{bmatrix} \frac{\partial \begin{bmatrix} L_s & L'_{sr} \\ L'^{T}_{sr} & L'_r \end{bmatrix}}{\partial \theta_r} \cdot \begin{bmatrix} i_{abcs} \\ i_{abcr} \end{bmatrix} \tag{3.16}$$

L_s and L'_r contain only constant elements, so that the electromagnetic equation (3.16) can be simplified to:

$$T_e = \frac{P}{2}.i^{T}_{abcs} \frac{\partial L'_{sr}}{\partial \theta_r} i_{abcr} \tag{3.17}$$

$$= -\frac{P}{2} L_{ms} \begin{bmatrix} i_{as} & i_{bs} & i_{cs} \end{bmatrix} \begin{bmatrix} \sin\theta_r & \sin\left(\theta_r + \frac{2}{3}\pi\right) & \sin\left(\theta_r - \frac{2}{3}\pi\right) \\ \sin\left(\theta_r - \frac{2}{3}\pi\right) & \sin\theta_r & \sin\left(\theta_r + \frac{2}{3}\pi\right) \\ \sin\left(\theta_r + \frac{2}{3}\pi\right) & \sin\left(\theta_r - \frac{2}{3}\pi\right) & \sin\theta_r \end{bmatrix} \cdot \begin{bmatrix} i_{ar} \\ i_{br} \\ i_{cr} \end{bmatrix}$$

$$= -\frac{P}{2} L_{ms} \begin{Bmatrix} [i_{as}(i_{ar} - 0.5i_{br} - 0.5i_{cr}) + i_{bs}(i_{br} - 0.5i_{ar} - 0.5i_{cr}) + i_{cs}(i_{cr} - 0.5i_{br} - 0.5i_{ar})]\sin(\theta_r) + \\ \frac{\sqrt{3}}{2}[i_{as}(i_{br} - i_{cr}) + i_{bs}(i_{cr} - i_{ar}) + i_{cs}(i_{ar} - i_{br})]\cos(\theta_r) \end{Bmatrix} \tag{3.18}$$

In addition, the mechanical equations of the machine must be considered [65]:

$$\frac{dw_r}{dt} = \frac{P}{2J} T_e - \frac{B_m}{J} w_r - \frac{P}{2J} T_L \tag{3.19}$$

$$\frac{d\theta_r}{dt} = w_r \tag{3.20}$$

where T_L is the load torque and T_e is the electromagnetic torque produced by the machine. w_r, θ_r are the electrical speed and position. The viscous friction is B_m and J is the moment of inertia.

3.4 SPACE HARMONICS

The layout of the winding in an electrical machine affects the MMF distribution and the performance of the machine. The coils of a winding are usually distributed over a few slots, and such a winding is known as a distributed winding. This can make better use of the stator or rotor structure and decrease harmonics. An ideal sinusoidal distribution of MMF is possible only if the machine has an infinitely large number of slots and the turns of a winding are sinusoidally distributed in the slots. This is not a practical solution. In a real machine with a finite number of stator slots as the current flows through the winding, the MMF produced is not sinusoidally distributed in the air gap and it has a stair like waveform as shown in Fig. 3.5. The harmonics in the flux density waveform of an induction machine are a result of the combination of the spatial distribution of the air gap MMF harmonics, (due to the discrete placement of the winding in slots) and the non uniform permanence seen by these fields [110]. The existence of space harmonics is known to have a significant detrimental effect on the steady state and transient characteristics of the machine [58].

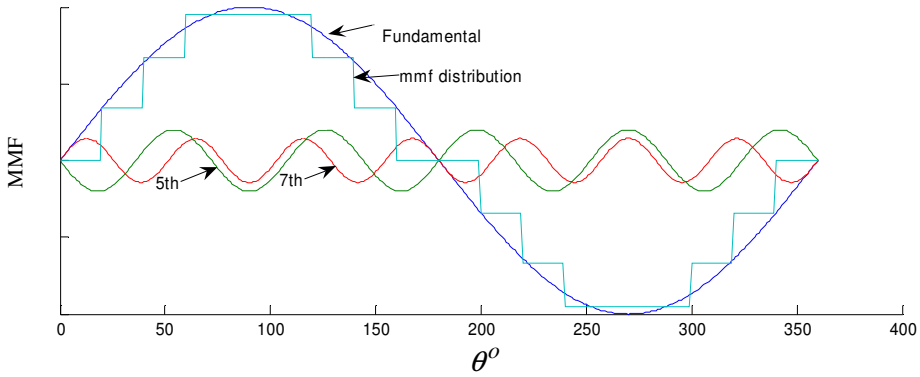

Fig. 3.5 MMF distribution in the air gap.

For a balanced machine the MMF distribution contains the fundamental and a family of space harmonics of order $h = 6k \pm 1$, where k is a positive integer. In a three phase machine, when sinusoidally varying currents flow through the windings, the resultant space harmonic fluxes will rotate at $(1/h)$ times the speed of the fundamental wave. The space harmonic fluxes rotate in the same direction as the fundamental wave if $h = 6k + 1$ and in the opposite direction if $h = 6k - 1$ [110].

3.4.1 Inclusion of Space Harmonic

Every individual coil produces a flux wave which may be decomposed into a series of harmonic components, with 2,4,6, etc. poles. Each of these harmonic flux waves may be considered as acting independently of all the others, so far as currents, voltages, and fluxes are concerned [73]. Some models take the field harmonics into account using an equivalent circuit for each harmonic component [73, 111]. The superposition principle is applied considering that the total field is the sum of the harmonic fields. Under these conditions, the machine can be modelled by a linear circuit with localised constants for each harmonic component [73].

Heller [111] indicate that any induction motor may be represented by a series of mechanically connected induction motors which have different numbers of poles, whose stator windings are connected in series. This means that a space harmonic flux of order (h) is equivalent to the flux created in a machine with ($h * P$) poles. Therefore, more than one rotor circuit should be considered, one for each harmonic, and each with a different numbers of poles. This type of approach can be used to model the space harmonic by adding to the equivalent circuit.

The standard equivalent circuit of the induction motor, Fig. 3.6(a) is modified in order to include space harmonics. For example, the circuit is expanded to include the two principal space harmonics (5^{th} and 7^{th}) of a balance three-phase motor by having two more virtual rotor circuits as shown in Fig. 3.6(b) [111]. The 3^{rd} harmonic circuit was not considered for healthy conditions as it cancels out for a three-phase machine.

In this equivalent circuit, there are three independent rotor circuits which do not interact with each other, one for each harmonic. Each harmonic rotor circuit has its rotor parameters referred to the stator. The current that passes in the stator is the same for all three harmonics, while the rotor circuits will have different currents depending on the number of poles of that harmonic circuit.

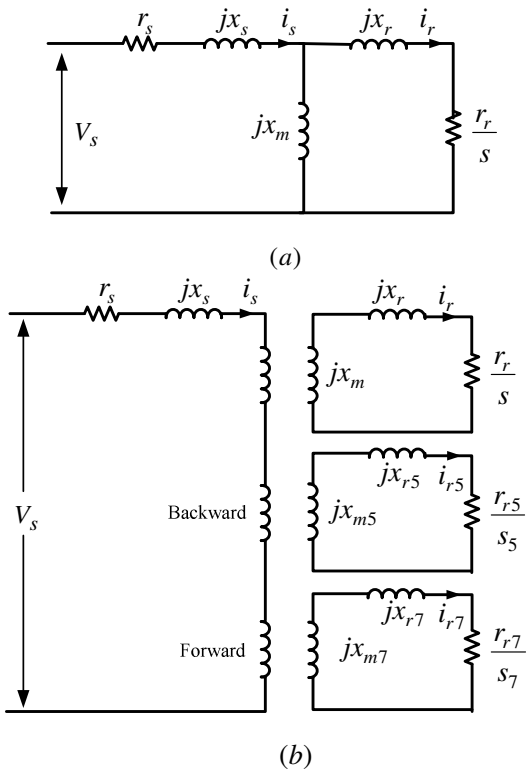

Fig. 3.6 a) Standard equivalent circuit of an induction motor b) Modified equivalent circuit to model the 5th and 7th space harmonics.

For Fig. 3.6 r_s is the stator resistance, and x_s is the leakage reactance of the stator winding representing the flux linking of the stator winding. x_m is the magnetizing reactance corresponding to the fundamental air gap flux wave of the winding, and the secondary reactance x_r is the reactance of the actual rotor winding for currents with fundamental sine wave distribution. x_{m5} and x_{m7} are the magnetizing reactance corresponding to the air gap flux waves of a particular harmonic. Each virtual rotor is represented with an equivalent resistive and leakage component. r_{r5} and r_{r7} are the corresponding rotor resistance of the 5th and 7th harmonic respectively. The secondary reactances x_{r5} and x_{r7} are the reactance of the actual rotor winding for currents of the same number of harmonic poles. The existence of the space harmonics will impress harmonic components on the rotor currents. The frequencies of these components are calculated as:

$$f_{rh} = \left(\frac{-m.f_e}{h} + f_r \right).h \tag{3.21}$$

where f_{rh} is the rotor current harmonic frequency, f_e is the supply frequency, f_r is the mechanical frequency of the rotor rotation, h is the order of the harmonic component, and m is a constant. (m = 1) for the positive sequence components and (m = -1) for negative sequence components.

For simplicity, the interaction between the stator and rotor harmonic circuits was considered unidirectional. The main aim of this modelling work was to derive a representation of the additional torque harmonics caused by space harmonics. The calculation of the addition time harmonics caused by the reverse interaction would considerably increase computing time without adding any significant information. In fact, these effects are naturally included when tuning the saturation ('time') harmonics as will be discussed later in this chapter.

It should be noted that this is only a simple approximation such that major geometrical effects can be represented in a simple model. The higher order space harmonics and space harmonics induced by the rotor have been neglected i.e. a large number of rotor bars is assumed.

3.4.2 Space Harmonic Effects Incorporated on the Stator-Rotor Mutual Inductance

A new model for the induction motor a-b-c frame (phase quantities) to model the space harmonic effect is proposed. The classical model will be extended such as to include the additional rotor circuits to take into account the MMF space harmonics. The space harmonics are included by incorporating additional rotor circuits and providing a suitable mutual inductance between the stator and these circuits which will be a function of rotor position. In particular, the analysis of the stator and rotor magnetically coupled system, which can be represented using Fig. 3.7, leads (3.9) to be modified to the following equation:

$$\begin{bmatrix} V_{abcs} \\ V_{abcr} \\ V_{abcr5} \\ V_{abcr7} \end{bmatrix} = \begin{bmatrix} R_s & 0 & 0 & 0 \\ 0 & R_r & 0 & 0 \\ 0 & 0 & R_{r5} & 0 \\ 0 & 0 & 0 & R_{r7} \end{bmatrix} \cdot \begin{bmatrix} i_{abcs} \\ i_{abcr} \\ i_{abcr5} \\ i_{abcr7} \end{bmatrix} + \frac{d}{dt} \left(\begin{bmatrix} L_s & L'_{sr} & 0 & 0 \\ L'^{T}_{sr} & L'_r & 0 & 0 \\ L'^{T}_{sr5} & 0 & L'_{r5} & 0 \\ L'^{T}_{sr7} & 0 & 0 & L'_{r7} \end{bmatrix} \cdot \begin{bmatrix} i_{abcs} \\ i_{abcr} \\ i_{abcr5} \\ i_{abcr7} \end{bmatrix} \right) \tag{3.22}$$

where $V_{abcr5,7,}$ $i_{abcr5,7}$ are the rotor terminal voltages and currents for the 5th and 7th harmonic components. L_{srh} is the modified mutual inductance between the stator and a particular harmonic rotor winding (i.e. L_{sr5} and L_{sr7}) which varies as a function of the rotor position, where h is the harmonic order. The L_{srh} and L_{rh} matrices from (3.12 - 3.13) can be written as follows:

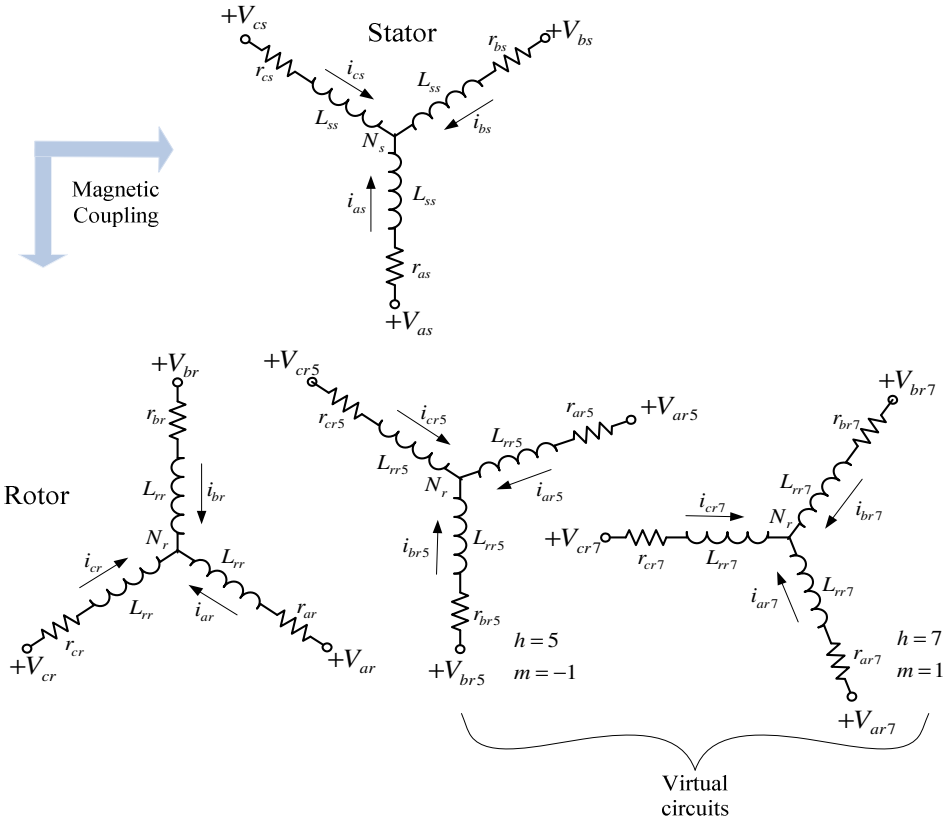

Fig. 3.7 Three phase symmetrical induction motor including three rotor circuits to model the space harmonics.

$$L_{srh} = L_{msh} \begin{bmatrix} \cos\theta_{rh} & \cos\left(\theta_{rh} + \frac{2}{3}\pi\right) & \cos\left(\theta_{rh} - \frac{2}{3}\pi\right) \\ \cos\left(\theta_{rh} - \frac{2}{3}\pi\right) & \cos\theta_{rh} & \cos\left(\theta_{rh} + \frac{2}{3}\pi\right) \\ \cos\left(\theta_{rh} + \frac{2}{3}\pi\right) & \cos\left(\theta_{rh} - \frac{2}{3}\pi\right) & \cos\theta_{rh} \end{bmatrix} \tag{3.23}$$

$$L'_{rh} = \begin{bmatrix} L'_{lr} + L_{msh} & -\frac{1}{2}L_{msh} & -\frac{1}{2}L_{msh} \\ -\frac{1}{2}L_{msh} & L'_{lr} + L_{msh} & -\frac{1}{2}L_{msh} \\ -\frac{1}{2}L_{msh} & -\frac{1}{2}L_{msh} & L'_{lr} + L_{msh} \end{bmatrix} \tag{3.24}$$

where $L_{msh} = \frac{L_{ms}}{C}$, C is a constant which is equal to h^2 [139] and θ_{rh} is the rotor position used for the calculation of the mutual inductance. $\theta_{rh} = 7\theta_r$ for the 7th harmonic (forward) and $\theta_{rh} = -5\theta_r$ for the 5th harmonic (backward).

It can be seen that the electromagnetic torque developed in the induction motor (3.16) will be modified to:

$$T_e = \frac{P}{2}.\frac{\partial W_c\left(i_{abcs}, i_{abcr}, i_{abcr5}, i_{abcr7}, \theta_r\right)}{\partial \theta_r} \tag{3.25}$$

$$T_e = \frac{P}{2}.\left(\frac{1}{2}.\left(\begin{bmatrix} i_{abcs} & i_{abcr} & i_{abcr5} & i_{abcr7} \end{bmatrix} \frac{\partial \begin{bmatrix} L_s & L'_{sr} & 0 & 0 \\ L'^{T}_{sr} & L'_r & 0 & 0 \\ L'^{T}_{sr5} & 0 & L'_{r5} & 0 \\ L'^{T}_{sr7} & 0 & 0 & L'_{r7} \end{bmatrix}}{\partial \theta_r} . \begin{bmatrix} i_{abcs} \\ i_{abcr} \\ i_{abcr5} \\ i_{abcr7} \end{bmatrix}\right)\right) \tag{3.26}$$

The electromagnetic torque T_e equation simplifies to:

$$T_e = \frac{P}{2}\left[i^T_{abcs} \frac{\partial L'_{sr}(\theta_r)}{\partial \theta_r} i_{abcr} + \frac{1}{2} i^T_{abcs} \frac{\partial L'_{sr5}(\theta_r)}{\partial \theta_r} i_{abcr5} + \frac{1}{2} i^T_{abcs} \frac{\partial L'_{sr7}(\theta_r)}{\partial \theta_r} i_{abcr7} \right] \tag{3.27}$$

The final induction motor model is therefore a simple extension to the well known approximate equivalent circuit used by simulation packages such as Matlab/Simulink [112] to model of the full motor drive system, including a vector control algorithm and a mechanical load model. The inverter in this case has been modelled by ideal controlled voltage sources, but could easily be extended to incorporate real device models if required. It can easily be programmed into most simulation environments and has a fast solution time.

3.5 SATURATION MACHINE MODEL

Magnetic saturation occurs in most electromagnetic devices, and cannot be avoided. Induction machines are no exception; hence a more accurate study of their characteristics should consider the magnetic saturation effects. Magnetic saturation results from the nonlinear characteristics of the ferromagnetic material used to construct the stator and rotor. The relationship between magnetic field intensity (H) and the magnetic flux (B) is shown in Fig. 3.8 for a typical steel used in induction motor construction. The ratio of the magnetic flux density to the magnetic field intensity at any point on the curve is called the permeability. For proper utilization of the magnetic material [82], the operating region the machine has to extend above the knee point of the $B - H$ curve. This causes saturation and a reduction of the magnetic permeability of the iron paths. Two different saturation effects will occur depending on the place where the saturation occurs: tooth head saturation in the main flux path, and core saturation. Saturation occurs at the peak of the flux wave and causes a periodic distortion of the flux wave form. This results in a harmonic component in flux at odd multiples of the supply frequency, rotating at the same speed as that of the rotating magnetic field. The third harmonic component is the most predominant one [80]. While tooth saturation results in a flat-topped flux density waveform, core saturation results in a peaked-topped flux density wave form, indicating that the saturation-related flux components are in phase opposition for tooth and core saturation. As a result, a highly saturated machine that exhibits both core and tooth saturation may not have significant saturation harmonics [82]. Fig. 3.9 shows the cross sectional view of a saturated machine showing the variation of the iron permeability in the stator and rotor parts. This leads to synchronous, asynchronous, and parasitic torques and increased losses [113]. Large saturation harmonics produce significant asynchronous torque pulsations by interacting with non saturation induced harmonics of the same order (such as space harmonics). These saturation harmonics will also reduce the fundamental toque. However, no torque, synchronous or asynchronous is produced by the interaction of the rotor and stator saturation harmonics [82].

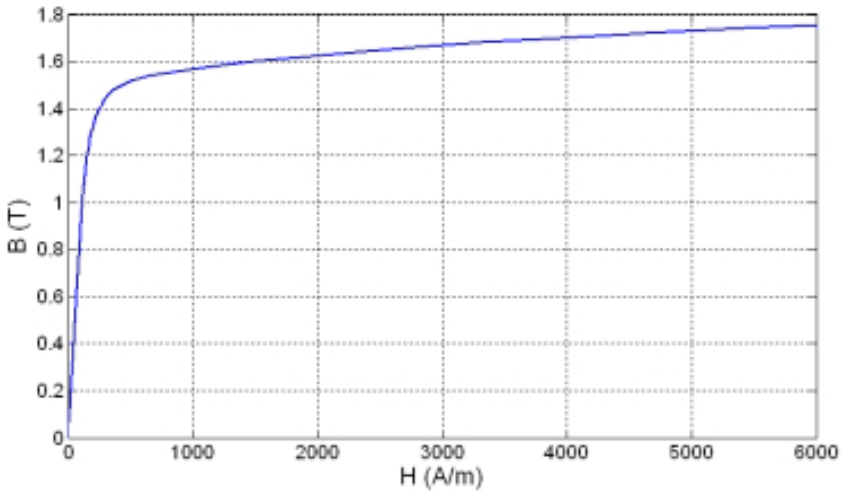

Fig. 3.8 *B-H* curve for ferromagnetic material (Newcor 800) [50]

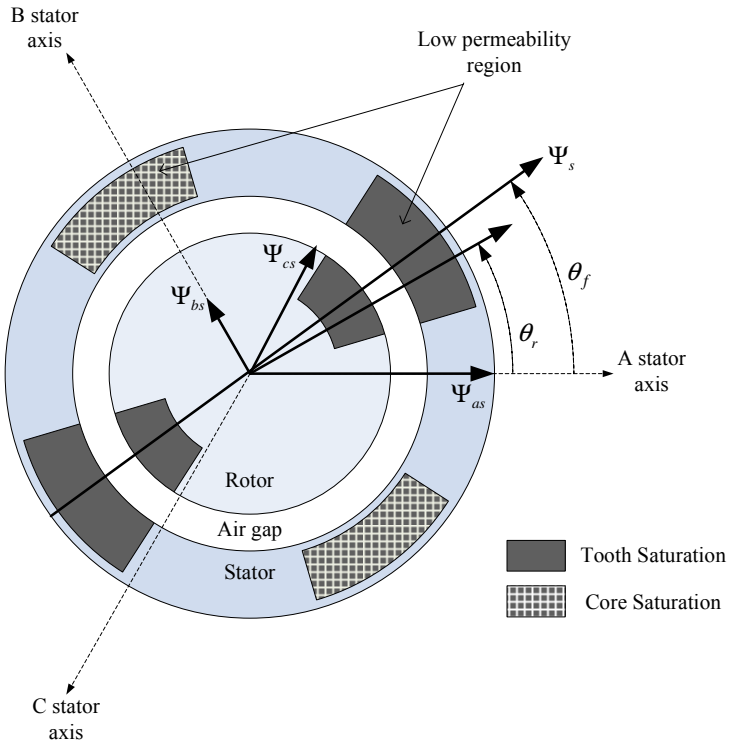

Fig. 3.9 Cross sectional view of a saturated machine showing the variation of the iron permeability in the stator and rotor parts. Saturation of tooth iron along the direction of the resultant stator flux Ψ_s is also shown. Modified diagram based on [80, 84].

The induction machine model derived here is an extension of the simple equivalent circuit model, modified to approximate the main flux saturation effects. Since the magnetic saturation is nonlinear, the dependence between the flux and current vectors is actually a complex nonlinear function. However, the flux-current relationship can be

approximated using a non-constant inductance matrix *L*, in which individual components are dependent on the motor flux and currents. For the proposed model, the saturation effects are incorporated into the stator mutual inductances as will be described in the next section.

3.5.1 Incorporating Saturation in the Stator Mutual Inductance

The conventional constant parameters of the AC machine model of (3.9) have been modified to represent saturation effects. Previous studies [80, 84] show that saturation of the stator and rotor teeth are important as a much higher flux density exists in these locations. Since the flux density vector is rotating, the saturation regions will rotate too, modifying the tooth permeability in a cyclic manner resulting in a variation of the stator winding inductances. The saturation effect is incorporated as a flux position dependant component in the stator mutual inductances. For simplicity it has therefore been assumed that only the stator mutual inductances will be modulated by the cyclic movement of saturation. For this work the variation has been approximated as the sum of the first three harmonic components. This is a significant simplification; it allows the development of a model which provides some indication of the effect of saturation whilst keeping the model complexity (and solution time) relatively low. The authors in [84] proposed a variation described with a simple mathematical equation. Although they present good results, there is only one tuning parameter available to adjust the magnitude of the saturation harmonics. For the simulation of a faulted drive the fine tuning of the saturation harmonic components is desirable. To achieve this, the profiles obtained from an FEM analysis [87, 88, 114] can be used to create a mathematical expression to incorporate the saturation effects on the stator mutual inductance.

In the conventional constant AC machine model, the expression for the stator mutual inductances as shown in (3.11) is:

$$L_{abs} = L_{bas} = L_{bcs} = L_{cbs} = L_{acs} = L_{cas} = -\frac{L_{ms}}{2} \tag{3.28}$$

The model has been modified to include the saturation effects as follows:

$$L_{abs} = L_{bas} = -\frac{L_{ms}}{2}\left[1 + K_2 \sin\left(PP.\theta_f + \rho_2\right) + K_4 \sin\left(2.PP.\theta_f + \rho_4\right) + K_6 \sin\left(3.PP.\theta_f + \rho_6\right)\right]$$

$$L_{bcs} = L_{cbs} = -\frac{L_{ms}}{2}\left[1 + K_2 \sin\left(PP.\theta_f + \rho_2 - 2.\frac{2\pi}{3}\right) + K_4 \sin\left(2.PP.\theta_f + \rho_4 - 4.\frac{2\pi}{3}\right) + K_6 \sin\left(3.PP.\theta_f + \rho_6 - 6.\frac{2\pi}{3}\right)\right] \quad (3.29)$$

$$L_{acs} = L_{cas} = -\frac{L_{ms}}{2}\left[1 + K_2 \sin\left(PP.\theta_f + \rho_2 - 2.\frac{4\pi}{3}\right) + K_4 \sin\left(2.PP.\theta_f + \rho_4 - 4.\frac{4\pi}{3}\right) + K_6 \sin\left(3.PP.\theta_f + \rho_6 - 6.\frac{4\pi}{3}\right)\right]$$

where L_{ms} is the stator magnetizing inductance, the parameters K_2, K_4 and K_6, are amplitudes and ρ_2, ρ_4, and ρ_6 are phase displacements of the permanence variation introduced by the saturation effect. The mutual inductance profiles L_{acs}=L_{cas} and L_{bcs}=L_{cbs} are shifted by 120° and 240° respectively. PP is the number of fundamental pole pairs, while θ_f represents the angular position of the stator flux vector measured from the phase "*a*" axis as shown in Fig. 3.9. This is calculated from the vector of the flux linkage of the stator *abc* phases Ψ_{as}, Ψ_{bs}, and Ψ_{cs} which are scalars. Writing

$$\alpha = e^{j(2\pi/3)} \quad (3.30)$$

The space phasor of the flux linkage vector can be expressed as

$$\Psi_s = \left[\Psi_{as} + \alpha.\Psi_{bs} + \alpha^2.\Psi_{cs}\right] \quad (3.31)$$

Then θ_f can be computed as:

$$\theta_f = \tan^{-1}\left(\frac{\mathrm{Im}\left(\Psi_s\right)}{\mathrm{Re}\left(\Psi_s\right)}\right) = \tan^{-1}\left(\frac{\left(\frac{\sqrt{3}}{2}\Psi_{bs} - \frac{\sqrt{3}}{2}\Psi_{cs}\right)}{\left(\Psi_{as} - \frac{1}{2}\Psi_{bs} - \frac{1}{2}\Psi_{cs}\right)}\right) \quad (3.32)$$

where $\mathrm{Re}\left(\Psi_s\right)$, $\mathrm{Im}\left(\Psi_s\right)$ are the real and imaginary parts of Ψ_s, respectively.

The profile (3.29) has been included in the model proposed here. For a four-pole machine, the inductance profile consists of components at 2, 4, and $6\theta_f$ as shown in Fig. 3.10. The parameters of the stator mutual inductance profiles are adjusted according to measurements made from an experimental system (the spectrum of the

winding current) [115]. By adjusting parameters K_2, K_4, and K_6 and ρ_2, ρ_4, ρ_6 all the saturation harmonic components in the winding current can be matched to experimental measurement. The magnitude of this inductance component as well as its phase displacement will vary with load, and can be analysed using FEM analysis [114]. The proposed profiles of the machine inductances are considered to be load dependent i.e. by changing the parameters K_2, K_4, and K_6 of (3.29) as a function of the load level. Therefore, for more accurate results the model can be adjusted automatically to give a good correlation with the experimental results as will be explained in Chapter 4.

As will be mentioned in the next chapter, this "calibration" of saturation parameters can also include contributions from other time harmonic sources such as the non-linearity of the power converters.

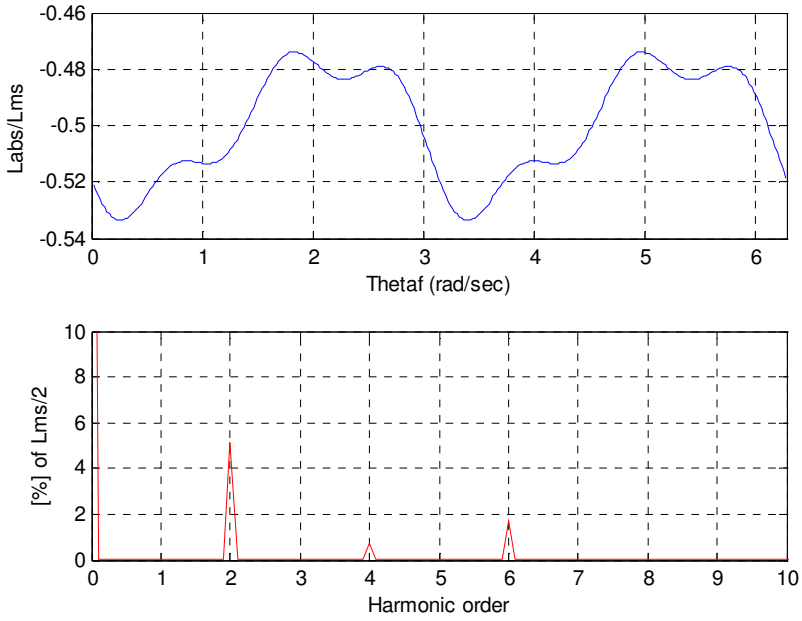

Fig. 3.10 Stator mutual inductance as a function of the stator flux angle (top) and the frequency spectrum of the inductance profile (bottom) for operation at 200 rad/sec and 50% of the nominal load.

3.6 MODELLING OF AN OPEN CIRCUIT FAULT

The state space model based the equivalent circuit described earlier, will be developed to account for an open circuit fault. This model will simulate the faulty machine together with the controlled supply, taking into consideration the effect on machine

fluxes, currents and torques with the inclusion of saturation effects as well as the space harmonic effects found in the machine.

3.6.1 Open Circuit Faults

Under faulty conditions, the equivalent circuit model of the induction machine is modified compared with that of the healthy machine shown in Fig. 3.6(b). An open circuit fault in the stator phases is simply modelled by increasing the resistance towards infinity during the simulation. It seems reasonable to suppose that the number of differential equations describing the induction machine should remain the same.

3.6.2 The Modification of the Equivalent Circuit for the Fault Condition

An open circuit in the stator winding will effect the distribution of the stator MMF in the air gap. However, to evaluate the consequence of an abnormal operating condition in the stator (losing one phase), on stator currents, the method using air-gap MMF calculation may also be used [70]. In this sense, the electrical fault must be interpreted in terms of its influence on the total MMF distribution, taking into account the localization of the corresponding phenomena.

In the modification of the equivalent circuit of the induction machine carried out in section 3.5.1, the only additional harmonics considered were the 5^{th} and 7^{th} MMF harmonics. This is valid for three phase balanced operation, where the most dominant third harmonic MMF cancels out. However, in the post fault two phase operation, MMF harmonics, and in particular the third MMF harmonic, do not cancel. The 3^{rd} harmonic MMF component will be present in the air gap and is no longer a zero sequence component. Consequently, there will be two extra waves rotating at three times the speed of the fundamental wave, of which one wave rotates in the same direction (positive sequence component) and the other in the opposite direction (negative sequence component). Therefore, the 3^{rd}, 5^{th}, and 7^{th} MMF harmonics are now considered as the most dominate harmonics.

The equivalent circuit of the induction motor Fig. 3.6(b) is modified to take into account the existence of the 3rd harmonic MMF for unbalanced conditions, by adding two more virtual rotor circuits as shown in Fig. 3.11. These were added in the same fashion as the 5th and 7th harmonic components. The equation model (3.22) is extended to include the two additional rotor circuits taking into account the positive and negative sequence third harmonic components of the MMF space harmonics as in (3.33):

$$\begin{bmatrix} V_{abcs} \\ V_{abcr} \\ V_{abcr5} \\ V_{abcr7} \\ V_{abcr3+} \\ V_{abcr3-} \end{bmatrix} = \begin{bmatrix} R_s & 0 & 0 & 0 & 0 & 0 \\ 0 & R_r & 0 & 0 & 0 & 0 \\ 0 & 0 & R_{r5} & 0 & 0 & 0 \\ 0 & 0 & 0 & R_{r7} & 0 & 0 \\ 0 & 0 & 0 & 0 & R_{r3+} & 0 \\ 0 & 0 & 0 & 0 & 0 & R_{r3-} \end{bmatrix} \cdot \begin{bmatrix} i_{abcs} \\ i_{abcr} \\ i_{abcr5} \\ i_{abcr7} \\ i_{abcr3+} \\ i_{abcr3-} \end{bmatrix} + \frac{d}{dt}\left(\begin{bmatrix} L_s & L_{sr} & 0 & 0 & 0 & 0 \\ L_{sr}^T & L_r & 0 & 0 & 0 & 0 \\ L_{sr5}^T & 0 & L_{r5} & 0 & 0 & 0 \\ L_{sr7}^T & 0 & 0 & L_{r7} & 0 & 0 \\ L_{sr3+}^T & 0 & 0 & 0 & L_{r3+} & 0 \\ L_{sr3-}^T & 0 & 0 & 0 & 0 & L_{r3-} \end{bmatrix} \cdot \begin{bmatrix} i_{abcs} \\ i_{abcr} \\ i_{abcr5} \\ i_{abcr7} \\ i_{abcr3+} \\ i_{abcr3-} \end{bmatrix} \right) \tag{3.33}$$

where $V_{abcr3+,3-}$ and $i_{abcr3+,3-}$ are the rotor terminal voltages and currents for the positive and negative components of the 3rd harmonic. $L_{sr3+,3-}$ are the modified mutual inductances between the stator and the 3rd positive and negative harmonic rotor winding which varies as a function of the rotor position. The $L_{sr3+,3-}$ and $L_{r3+,3-}$ matrices from (3.12 - 3.13) can be written as follows:

$$L_{sr3+,3-} = L_{ms3} \begin{bmatrix} \cos\theta_{r3+,3-} & \cos\left(\theta_{r3+,3-} + \frac{2}{3}\pi\right) & \cos\left(\theta_{r3+,3-} - \frac{2}{3}\pi\right) \\ \cos\left(\theta_{r3+,3-} - \frac{2}{3}\pi\right) & \cos\theta_{rh} & \cos\left(\theta_{r3+,3-} + \frac{2}{3}\pi\right) \\ \cos\left(\theta_{r3+,3-} + \frac{2}{3}\pi\right) & \cos\left(\theta_{r3+,3-} - \frac{2}{3}\pi\right) & \cos\theta_{r3+,3-} \end{bmatrix} \tag{3.34}$$

$$L_{r3+,3-} = \begin{bmatrix} L_{lr}^{'} + L_{ms3} & -\frac{1}{2}L_{ms3} & -\frac{1}{2}L_{ms3} \\ -\frac{1}{2}L_{ms3} & L_{lr}^{'} + L_{ms3} & -\frac{1}{2}L_{ms3} \\ -\frac{1}{2}L_{ms3} & -\frac{1}{2}L_{ms3} & L_{lr}^{'} + L_{ms3} \end{bmatrix} \tag{3.35}$$

where $L_{ms3} = \frac{L_{ms}}{C}$, C is a constant which is equal to 3^2 and $\theta_{r3+,3-}$ is the rotor position used for the calculation of the mutual inductance. $\theta_{r3+,3-} = 3\theta_r$ for the 3rd positive harmonic (forward) and $\theta_{r3+,3-} = -3\theta_r$ for the 3rd negative harmonic (backward). Also, the electromagnetic torque equation (3.27) is modified to include its effect as in (3.36):

$$T_e = \frac{P}{2}\left[i_{abcs}^T \frac{\partial L_{sr}(\theta_r)}{\partial \theta_r} i_{abcr} + \frac{1}{2} i_{abcs}^T \frac{\partial L_{sr5}(\theta_r)}{\partial \theta_r} i_{abcr5} + \frac{1}{2} i_{abcs}^T \frac{\partial L_{sr7}(\theta_r)}{\partial \theta_r} i_{abcr7} + \frac{1}{2} i_{abcs}^T \frac{\partial L_{sr3+}(\theta_r)}{\partial \theta_r} i_{abcr3+} + \frac{1}{2} i_{abcs}^T \frac{\partial L_{sr3-}(\theta_r)}{\partial \theta_r} i_{abcr3-} \right] \quad (3.36)$$

The new frequency components for the stator and rotor currents of the open circuit faults can then be evaluated as a function of the modification of the stator or rotor structures.

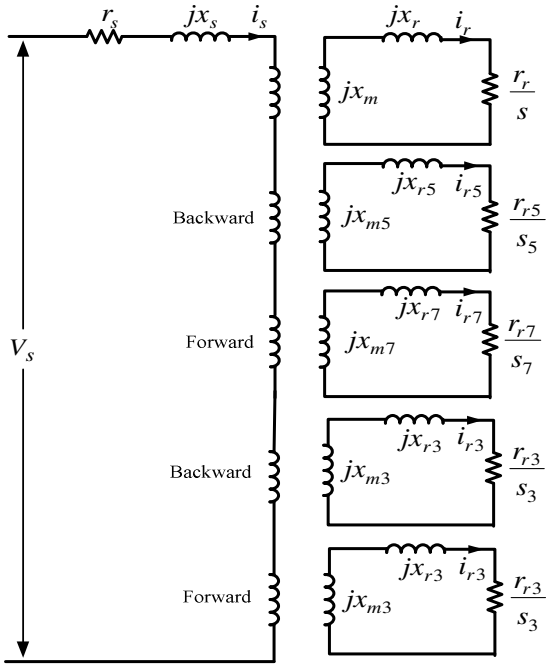

Fig. 3.11 Modified equivalent circuit for faulty operation condition to model the 3rd , 5th and 7th space harmonics.

3.7 IMPLEMENTATION OF THE DRIVE-INTEGRATED SIMULATION MODEL

Having derived the mathematical representations of an induction machine with an open stator fault, this section discusses the implementation of the drive-integrated simulation model. The drive-integrated simulation model is composed of a number of blocks and is implemented in Matlab/Simulink™. The block diagram of the developed model is presented in Fig. 3.12. The subscript * denotes the reference value of a variable, the subscript *o* represents the quantity of a stator variable referred to the midpoint of the dc-link, and the subscript *s* represents the quantity of a stator variable referred to the floating neutral point of the machine as shown in Fig. 3.4. The Induction Machine Phase-Variable Model block in Fig. 3.12 contains the induction machine model with the space harmonics and saturation effects. The implemented equations are (3.10 – 3.13), (3.19 – 3.20), (3.23 – 3.24), (3.29 – 3.32), and (3.33 – 3.36). The vector control algorithm described in Appendix A was integrated within the simulation as a standard IRFO control strategy as illustrated in Fig. 3.12. The variables used for vector control are also defined in Appendix A. The fundamental concept behind this strategy is to impose a slip frequency as calculated by (A.14), with an accurate knowledge of the rotor time constant (τ_r). This will force the drive to be "field oriented" i.e. the rotor flux is aligned to the *d*-axis of the controller and torque is proportional to i_{sq} .

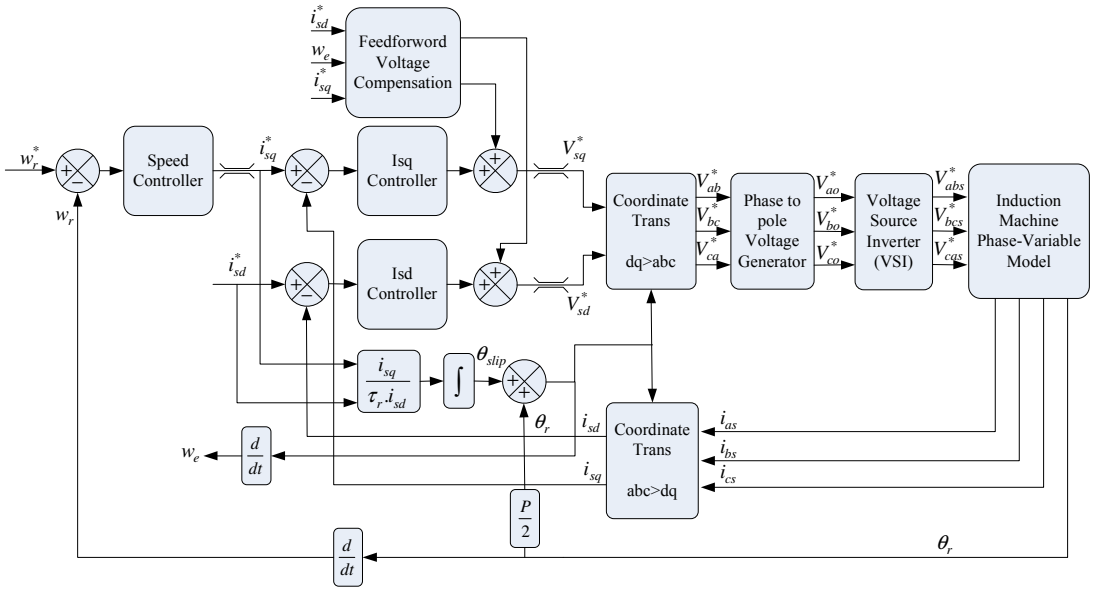

Fig. 3.12 Block diagram of the developed simulation model using the indirect rotor flux orientation scheme.

3.7.1 Speed and Current Controllers

The control system integrated within the state space induction machine is a cascade structure based upon proportional and integral (PI) controllers as shown in Fig. 3.12. The speed controller is implemented with an anti-windup proportional-integral (PI controller) and updates the torque reference at every speed control period. The *d* and *q* axis currents are regulated through synchronous anti-windup PI controllers with feed-forward decoupling compensation terms [116]. Consequently, the *d* and *q* axis voltage references are generated from the current controllers which are then transformed into the 3-phase stator reference frame. The controller designs are derived in Appendix D. They are based on the linear and time invariant induction machine equivalent circuit model of Fig. 3.6(a).

3.7.2 Stator Line-Neutral Voltage Generator

This section provides the ability to simulate either a star or delta connected machine. In any electric motor drive, there is no physical connection between the machine's neutral point and the inverter neutral point, for which the mid-point of the DC-link is generally used. In a state space induction machine drive model, the machine stator voltages are represented referred to the machine's neutral point. For a star connection machine, the two neutral points are assumed to have the same potential. However, this assumption is only valid under perfectly balanced conditions [117]. The references for the inverter pole voltages are generated from the 3-phase reference voltages and the PWM scheme. Therefore, the difference between the phase to star neutral voltage and the reference pole voltage (inverter output voltage referred to the mid-point of the dc-link) is equal to zero ($V_{an} = V_{ao}$, ..etc). In this case, the output of the vector control system will provide the phase voltage demands, which are equal to the inverter pole voltages. Thus, the phase to the pole voltage generator block in Fig. 3.12 will have a unity gain.

In the balanced condition for a delta connected machine, the output of the vector control system provides the line voltage demands. As a result, the phase to pole voltage generator block in Fig. 3.12 determines the inverter pole voltages, i.e. V_{ao}, V_{bo}, and V_{co}.

These are $\sqrt{3}$ smaller than the line voltages and lag them by 30^o. Therefore, the inverter pole voltages are expressed in terms of the 3-phase line reference voltages by:

$$V_{ao} = (V_{ab}^* - V_{ca}^*)/3$$

$$V_{bo} = (V_{bc}^* - V_{ab}^*)/3 \tag{3.37}$$

$$V_{co} = (V_{ca}^* - V_{bc}^*)/3$$

For a star connected machine, the phase to pole voltage generator block uses the following equations:

$$V_{an}^* = V_{ao}$$

$$V_{bn}^* = V_{bo} \tag{3.38}$$

$$V_{cn}^* = V_{co}$$

The final block labelled VSI in Fig. 3.12, converts the phase-inverter mid point voltages to the line voltages applied to the motor model itself. For both star and delta connected machines, these are calculated as:

$$V_{abs}^* = V_{ao} - V_{bo}$$

$$V_{bcs}^* = V_{bo} - V_{co} \tag{3.39}$$

$$V_{cas}^* = V_{co} - V_{ao}$$

3.8 CONCLUSION

A phase variable-based model of an induction machine which allows the implementation of stator open circuit fault has been developed. This model can be integrated with a PWM voltage source inverter and a high performance controller. This model is applicable to single open phase winding faults and for more realistic results, space harmonic and saturation effects have been included in the derived model.

The space harmonic effect is incorporated on the mutual inductance between stator and rotor windings as a function of rotor position. This has been achieved by extending the equivalent circuit of the induction motor to include the effect of the two principal (5^{th} and 7^{th}) space harmonics for the healthy condition, and the 3^{rd} , 5^{th} and 7^{th} space harmonics for the faulty condition.

The saturation effect is incorporated as a flux position dependant component in the stator mutual inductance. The inductance profile consists of three harmonic components and the magnitude and phase displacement of each component can be adjusted. The saturation model will be tuned to make the model currents for a particular operating condition match the measured phase currents of the equivalent experimental system.

Owing to these distinct features, the model allows the evaluation of the operation of induction motors in the presence of space harmonics and saturation effects, as well as being able to test the robustness of different field oriented controlled drives under unbalanced conditions. In addition, the proposed model can give a better evaluation of torque pulsations since it can include both time and space harmonics.

The developed model can be used as a powerful tool for investigating the characteristics of a stator open circuit fault in induction machine drives. However, this is not the only contribution of this model. It can save time and money by pointing out even a minor deficiency in any tested method for stator open circuit fault diagnosis or fault-tolerant operating strategy since the model provides a reliable test bench for evaluating the method before its application to a real drive system. The developed model will be validated through simulations and experiments, which are detailed in the next chapter.

VERIFICATION OF THE NEW INDUCTION MACHINE MODEL

4.1 INTRODUCTION

A simulation model for an induction machine drive containing an open circuit fault in the stator winding was derived in Chapter 3. In order to validate that model, experimental tests have been carried out on a 4 kW induction motor using different working conditions. The experimental setup and implementation of the open circuit fault are detailed in Appendix E. The electromagnetic torque and the phase currents during starting transients, together with the rotor currents (obtained from the dynamic model) are presented to study the effects of saturation and space harmonic components to compare them with the simulated results under steady state operation.

In this chapter Section 4.2 presents the operation condition of the healthy induction machine, while Section 4.3 presents the operation condition of the faulty induction machine when an open circuit fault occurs. Section 4.4 presents conclusions.

4.2 OPERATION FOR THE HEALTHY INDUCTION MACHINE

A four-pole, 4kW delta connected machine is modelled. The basic model is extended to incorporate the major effects of space harmonics by incorporating additional rotor circuits that provide a suitable mutual inductance between the stator and rotor circuits as a function of rotor position. All the experimental tests and simulation results were obtained with the machine operating under Indirect Rotor Field Orientated control

(IRFO). The machine's electrical parameters were obtained via conventional no-load and locked rotor tests and are listed in Appendix C.

For comparison purposes the healthy machine was first modelled using a conventional state space model (3.9). The same machine was simulated using the proposed model which includes stator space harmonic effects i.e. (3.22) as described in Chapter 3, to compare simulation and experimental results as in Section 4.2.2. Finally, the same machine was simulated again using the proposed model with the stator space harmonic and saturation effects (3.29) and compared with experimental results as illustrated in section 4.2.3. In these results the model contains inductances determined by the user profile which are load dependant. The simulation results were carried out with the machine operating at 200 rad/sec, rated flux, and at different load conditions.

To calculate the electromagnetic torque in the experimental system, the estimation of stator flux linkage is required and can be obtained as follows:

$$\overline{\psi}_s = \int \left(\overline{V_s} - r_s . \bar{i}_s \right) dt \tag{4.1}$$

where all variables are phase quantities and having their usual meaning (this is not quite as practical as it may be seem). It was found that the required direct integration is very sensitive to DC offset errors due to small drifts present in measurements for voltages and currents in the experimental system. A high pass filter (HPF) is used to remove these effects. However, the use of the HPF degrades the performance of this scheme. For example, the stator voltage is very small and significantly distorted by the non-linearities of the inverter (such as the dead-time and the voltage drop across the power devices) when operating at low speeds. However, when the speed increases, the stator voltage increases and inverter error reduces significantly. After the stator flux has been estimated, the electromagnetic torque can be calculated by using:

$$T_e = \frac{2}{3}\frac{P}{2}\left(\psi_{\alpha s} i_{\beta s} - \psi_{\beta s} i_{\alpha s} \right) \tag{4.2}$$

where P is the number of poles, and the torque is calculated using quantities transformed to the $\alpha\beta$ reference frame.

4.2.1 The Simulation and Experimental Comparison for the Conventional State Space Model

Simulations using the "conventional" state space model (3.9) to show the performance of the delta connected motor were obtained under the conditions defined in Table 4.1. The response for the speed and developed torque during the starting transient are presented in Figs. 4.1(a) and (b) respectively when a step reference input (w_{ref} = 200 rad/sec) is applied at t = 1sec at no load. The equivalent *d* and *q* components of the motor currents together with the phase currents are presented in Figs. 4.1(c) and (d) respectively. The rotor currents are illustrated in Fig. 4.1(e). The graph of Fig. 4.1(b) shows two traces of torque with time. The green trace is the estimated torque from the vector control torque equation (A.13) using i_{sd}^* and i_{sq}^*, while the blue trace is the actual electromagnetic torque produced by the machine based on the principle described in section 3.4.2. once the machine reaches the reference speed (w_{ref}) and steady state is reached (which happens around t = 2 sec) an external load of 26Nm (95% rated torque) is applied at t = 4 sec. Transients for this condition can be observed in Fig. 4.2. Note that the steady state operation is disturbed, however the speed of the machine settles back to the reference speed (w_{ref}) after a short transient as shown in Fig. 4.2(a). Transients of the developed torque, the equivalent *d* and *q* components of the motor currents, and the phase currents are presented in Fig. 4.2(b), (c) and (d), respectively. The three rotor currents which are induced in the rotor circuit have an increased frequency (slip frequency 1.935Hz) after the load is applied as presented in Fig. 4.2(e). Note that the presented results do not show any distortion in the current and speed as are found in real drives depending on factors such as slots harmonics, saturation effect, space harmonics, etc. The presented results here are pure sinusoidal and show only the fundamental components.

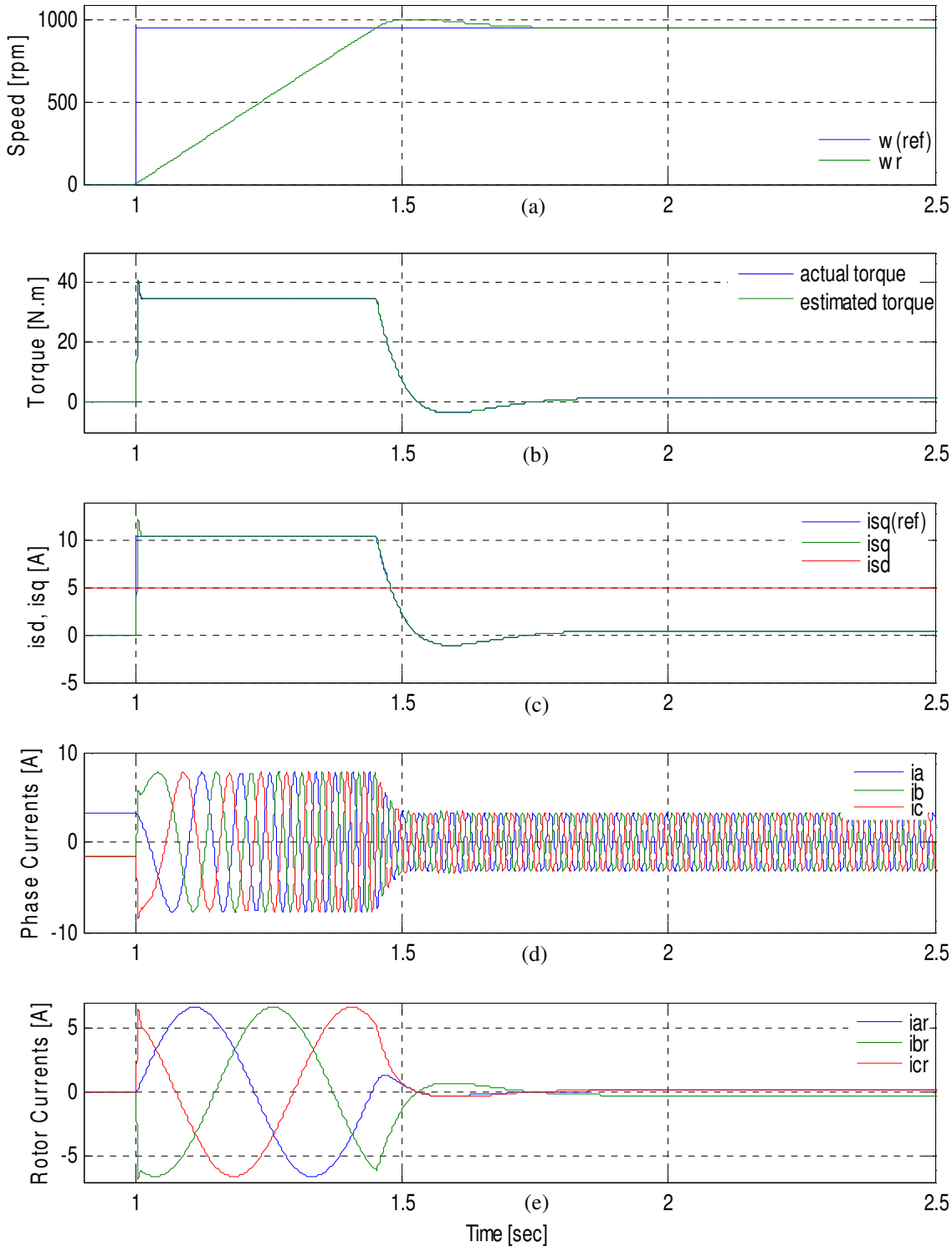

Fig. 4.1 Performance of an induction motor drive using the conventional induction machine model when a step speed command is applied at no load. a) Speed, b) Electromagnetic torque, c) i_{sd} & i_{sq} currents, d) Phase currents and e) Rotor currents.

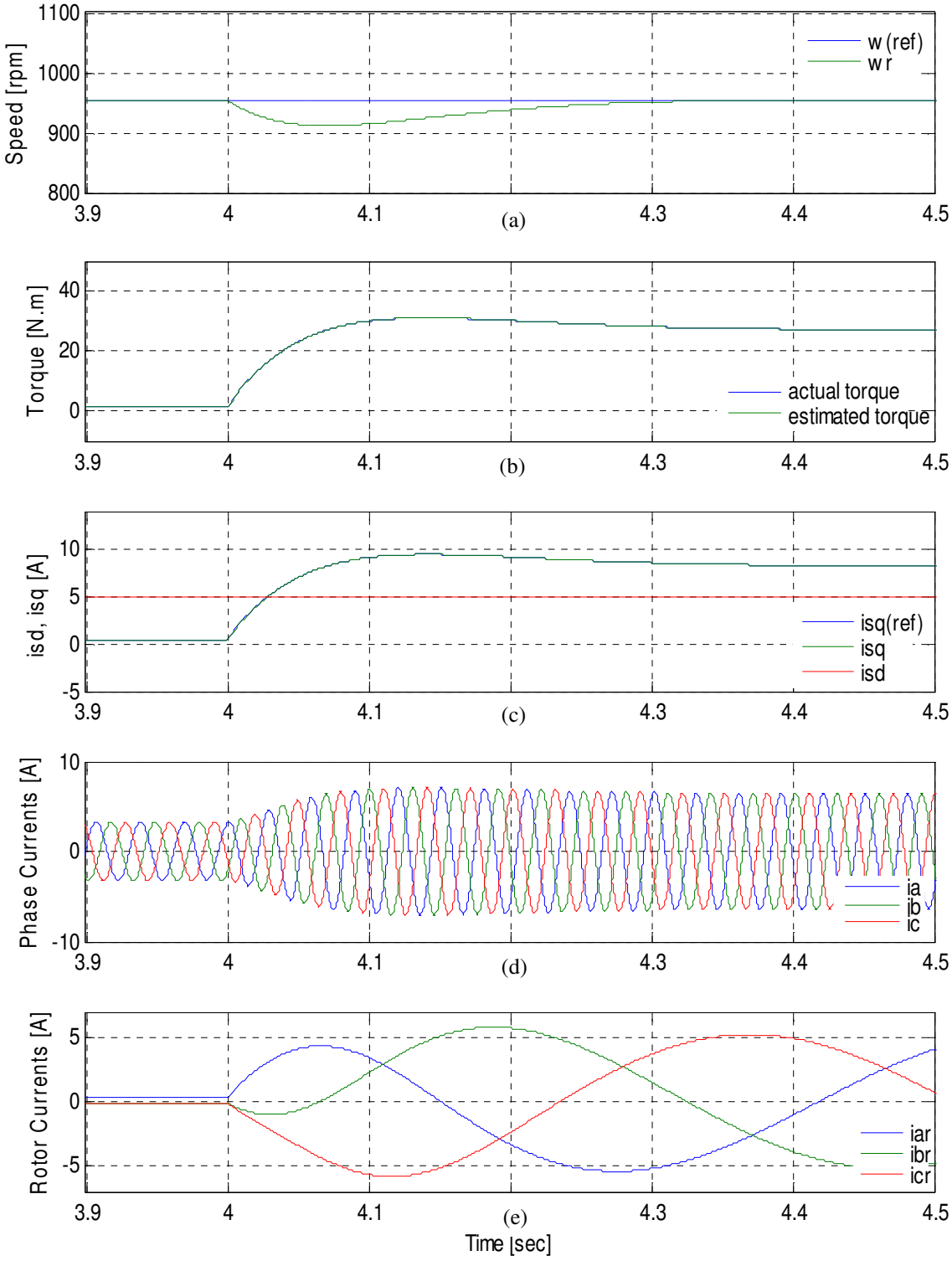

Fig. 4.2 Performance of an induction motor drive when an external load disturbance is applied at t = 4 sec. a) Speed, b) Electromagnetic torque, c) i_{sd} & i_{sq} currents, d) Phase currents and e) Rotor currents.

Table 4.1 Simulation and Experimental Conditions showing the behaviour of the induction motor drive system

Item	Unit	Value
Reference Speed	[Rad/sec]	200
Load Torque	[N.m]	0/26
Rated Field Current i_{sd}	[A]	4.9
Rated Torque Current i_{sq}	[A]	9
Limit of Torque Current i_{sq}	[A]	10.5

To compare the performance of the conventional model against the experimental system, the same test has been performed on the experimental rig under the same conditions defined in Table 4.1. The rotation speed, developed torque, the equivalent *dq* current components and the phase currents are presented in Fig. 4.3(a), (b), (c) and (d). The graph of Fig. 4.3(b) shows two traces of torque with time. The green trace is the estimated torque from the vector control torque equation (A.13) using i_{sd_ref} and i_{sq_ref} , while the blue trace is the estimated torque produced by the machine as in equation (4.2). Note that the estimated torque has distortion in the transient period of the machine when the speed reference is changed. This is a direct consequence of using the HPF, but after the dynamic response of the HPF reaches steady state, the estimated torque is matches with the torque reference as shown in the green trace. Therefore, this torque estimator can only give a measure of steady state torque.

After the machine reaches the reference speed (w_{ref}) and when steady state is reached, a load disturbance is applied at t = 4.85sec, which is equivalent to 95% of rated torque (26Nm) as illustrated in Fig. 4.4. It can be seen that the results presented (speed and currents) contain a significant background noise. The source of this distortion is due to the non-linearties effects in the machine drive, such as the slots harmonics, saturation effect, space harmonics in the machine itself, and non-ideal inverter operation (i.e. due to the dead-time effects) [66]. In general, the performance of the drive can be seen to be very similar to the simulation results, where the dynamic response of the IRFO drive is similar to that shown in Figs. 4.1 and 4.2.

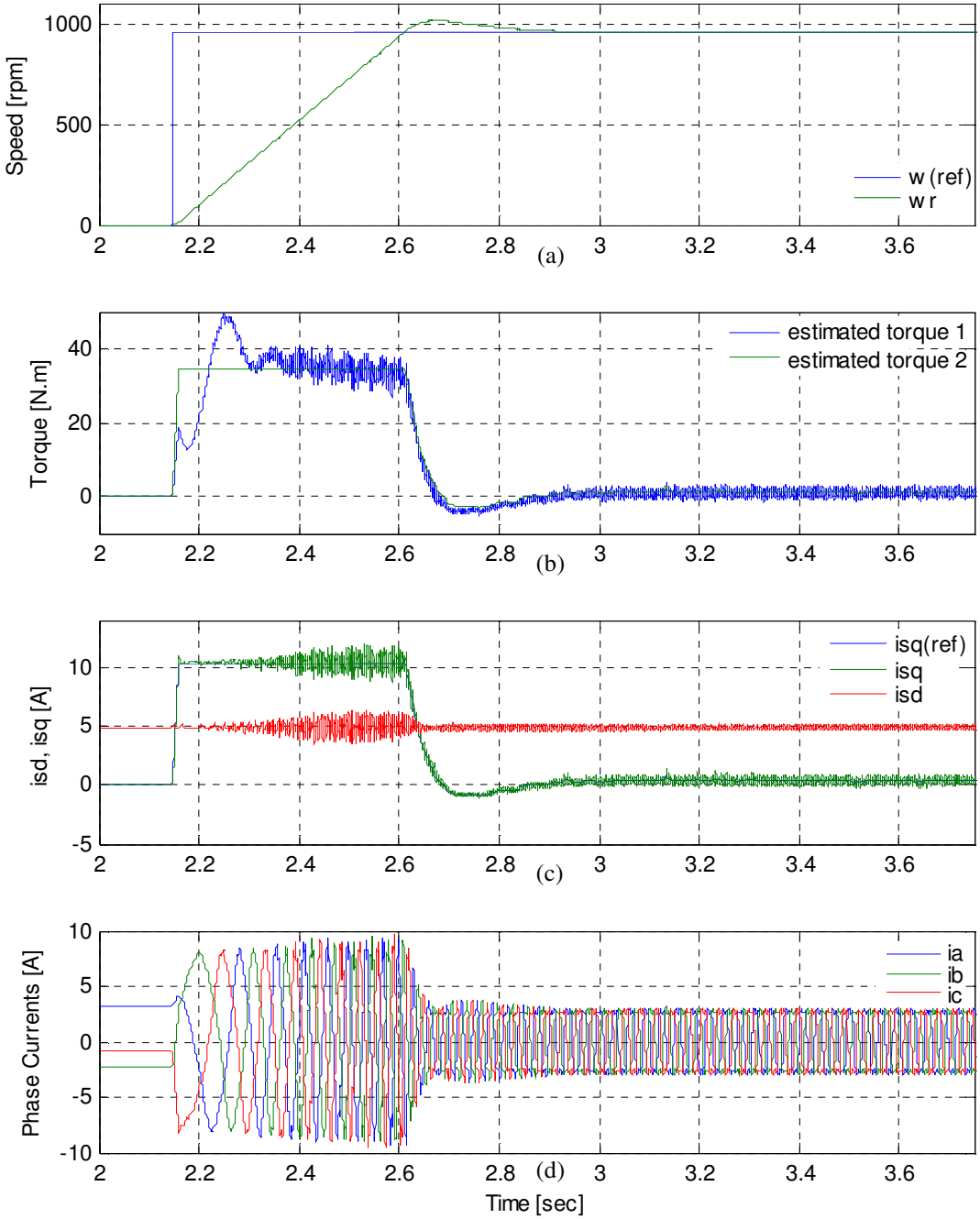

Fig. 4.3 Experimental results for induction machine drive when a step speed command is applied at no load. a) Speed, b) Electromagnetic torque, c) i_{sd} & i_{sq} currents and d) Phase currents.

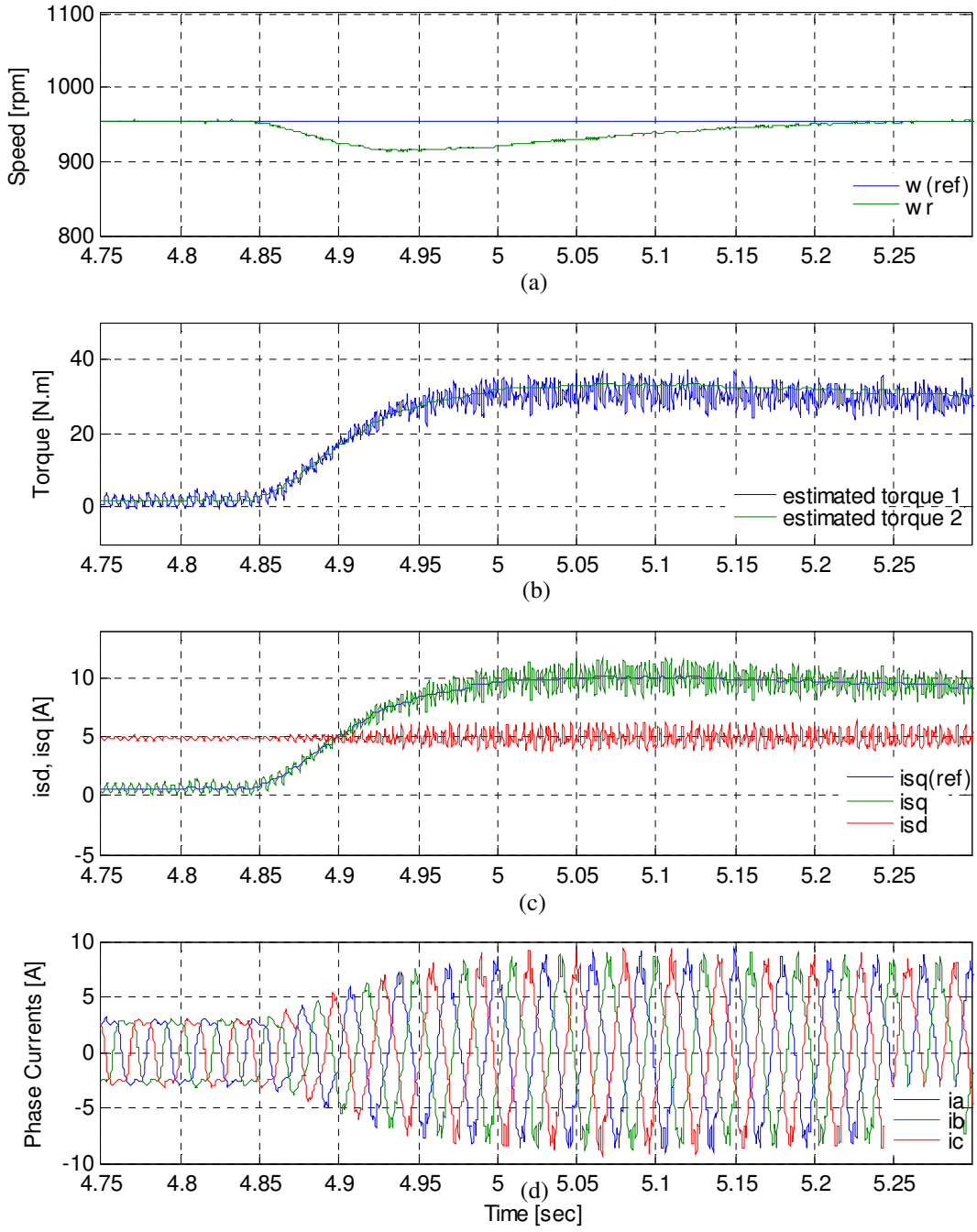

Fig. 4.4 Experimental results for induction machine drive when an external load disturbance is applied at t = 4.85 sec. a) Speed, b) Electromagnetic torque, c) i_{sd} & i_{sq} currents and d) Phase currents.

The origin of the distortion or harmonics observed in the phase current has several sources. Note that these harmonics are induced in the phase current due to the interaction of magnetic fields that rotate in the air-gap, which are produced by both the stator and rotor fields. The air-gap magnetic field generates harmonic fluxes that move relative to stator and therefore induce corresponding current harmonics in the stator winding. Some of these fields generated due to the non linear power converter effects are often called time harmonics. Other fields generated due to the machine design (non sinusoidal distribution of winding, slots, etc) are called space harmonics. Finally, there are other harmonics related to other fields generated due to the magnetic saturation. The phase current spectrum may have a combination of these three sources of harmonics. Figs. 4.5 and 4.6 show a comparison between experimental and simulation results (using the conventional model) for the phase currents of the machine running at no load. The frequency spectrum of the currents is presented. Experimental waveforms (Fig. 4.5) show that the phase current contains the 3^{rd}, 5^{th} and 7^{th} harmonics.

The 3^{rd} harmonic component is mainly caused by iron saturation, while 5^{th} and 7^{th} harmonic components are not only due the saturation but are the imposed superposition of time and space harmonics. It is clear that the presence of these harmonics is not observed in the simulation results of Fig.4.6. Since the conventional model does not include iron saturation and space harmonic effects. Despite these harmonics, both figures confirm that experimental and simulation phase current have the same peak fundamental component 3.28A.

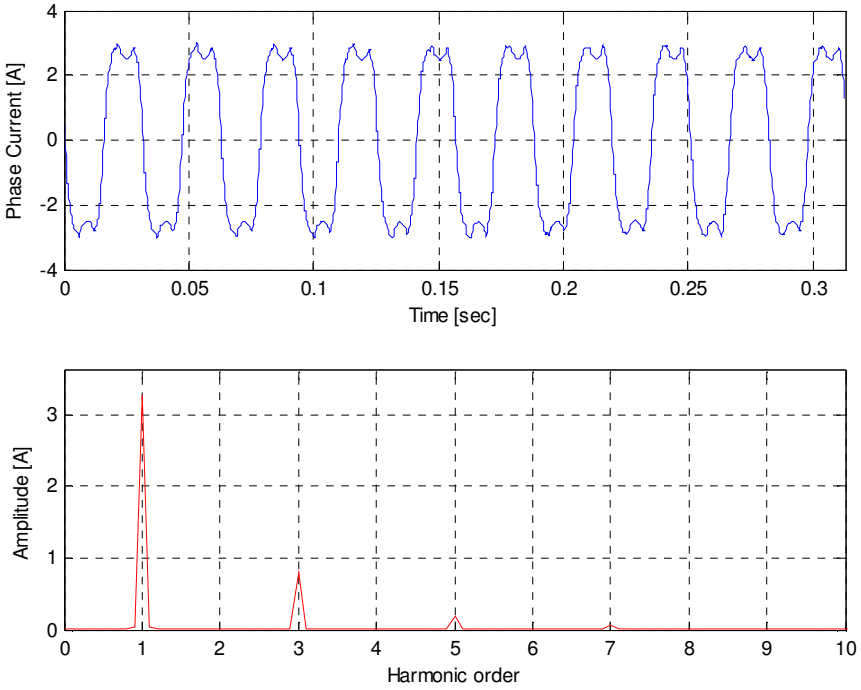

Fig. 4.5 Experimental result – no load phase current

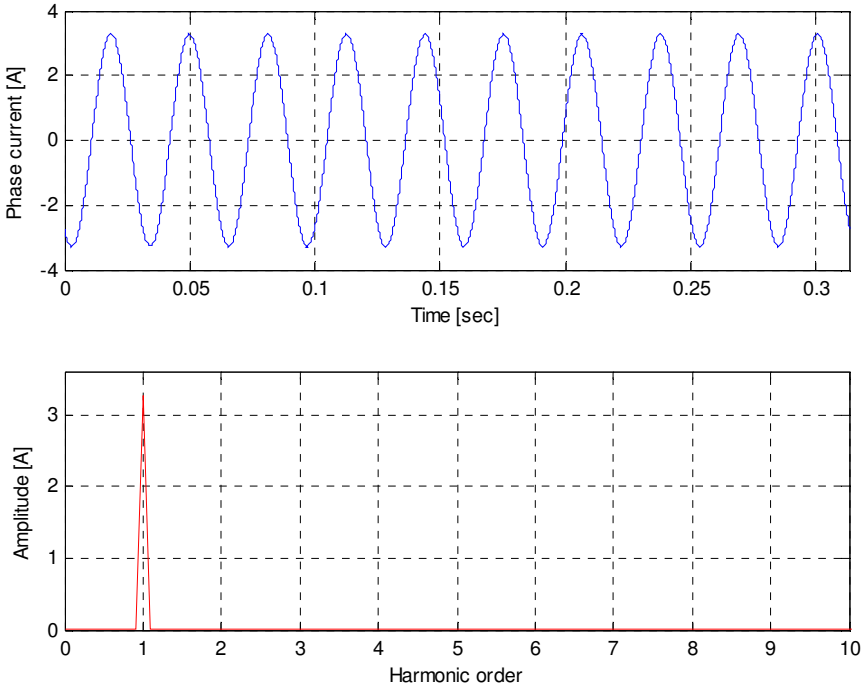

Fig. 4.6 Simulation result – no load phase current

4.2.2 Simulation and Experimental Results with the Space Harmonics Effect

The proposed model for the induction machine that contains the stator space harmonic effects as shown in equation (3.22) has been simulated in this section. The same harmonic effect is included by incorporating additional rotor circuits that provide a suitable mutual inductance between the stator and rotor circuits as a function of rotor position. The simulations to show the effects of these harmonics in the rotation speed and currents were performed under the conditions defined in Table 4.1. When a step reference (w_{ref} = 200 rad/sec) input was applied at t = 1sec at no load. The responses of the speed and developed torque during the starting transient are presented in Figs. 4.7(a) and (b), respectively. The equivalent *d* and *q* components of the motor currents together with the phase currents and the rotor currents are presented in Figs. 4.7(c), (d), and (e) respectively. The graph of Fig. 4.7(b) shows the green trace of the estimated torque from the vector control torque equation (A.13), while the blue trace is the actual electromagnetic torque produced by the machine calculated using (3.27).

After the machine reaches set speed, a load of 26Nm (slip s = 0.058) is applied to the machine at t = 2.5 sec. The speed of the machine returns to the reference speed (w_{ref}) after a short transient as shown in Fig. 4.8(a). Transients for the developed torque, equivalent *d-q* components of the motor currents, and the phase currents are presented in Fig. 4.8(b), (c), and (d), respectively. The three rotor currents which are induced in the rotor circuit after the load have slip frequency of 1.98Hz and are presented in Fig. 4.8(e). It can be easily seen that the simulation results of the proposed model with the space harmonic effects (Figs. 4.7 and Fig. 4.8) are quite different with respect to the simulation results of the conventional model presented in Figs. 4.1 and 4.2. Note that there are new frequencies induced in the rotor currents which are due to the effect of the space harmonics of the stator MMF as can be observed in Fig. 4.9. From Fig. 4.9, two additional components due to the injection of space harmonics can be seen. The induced harmonic components in the rotor currents are similar to those which were identified theoretically by (3.21). The observed frequencies 1.98, 189, and 193Hz are theoretically obtained with f_e = 33.81Hz and f_r = 31.83Hz, and these correspond to the frequencies of the simulated rotor current spectrum.

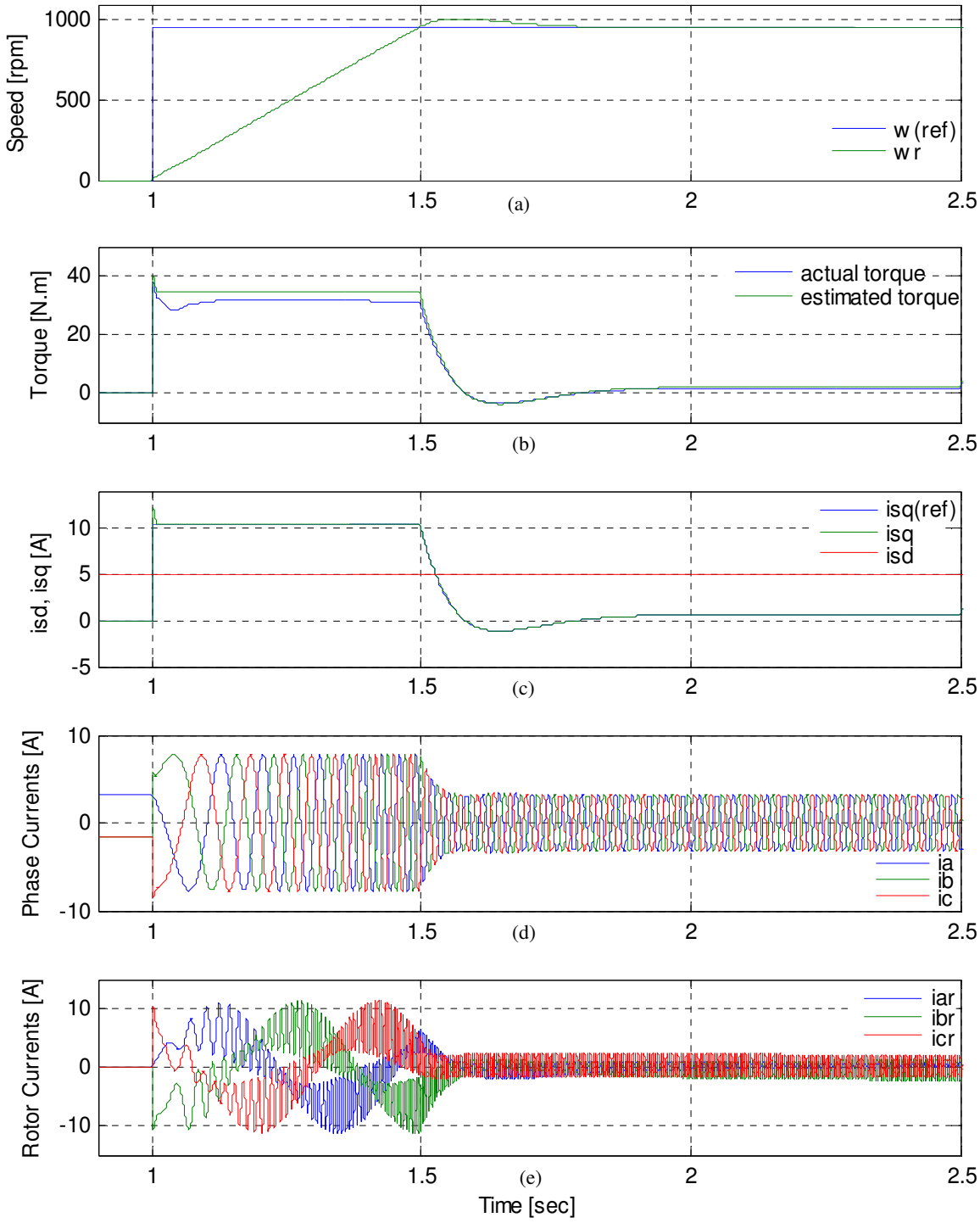

Fig. 4.7 Performance of an induction motor drive using the proposed scheme model containing the space harmonic effect when a step speed command is applied. a) Speed, b) Electromagnetic torque, c) i_{sd} & i_{sq} currents, d) Phase currents and e) Rotor currents

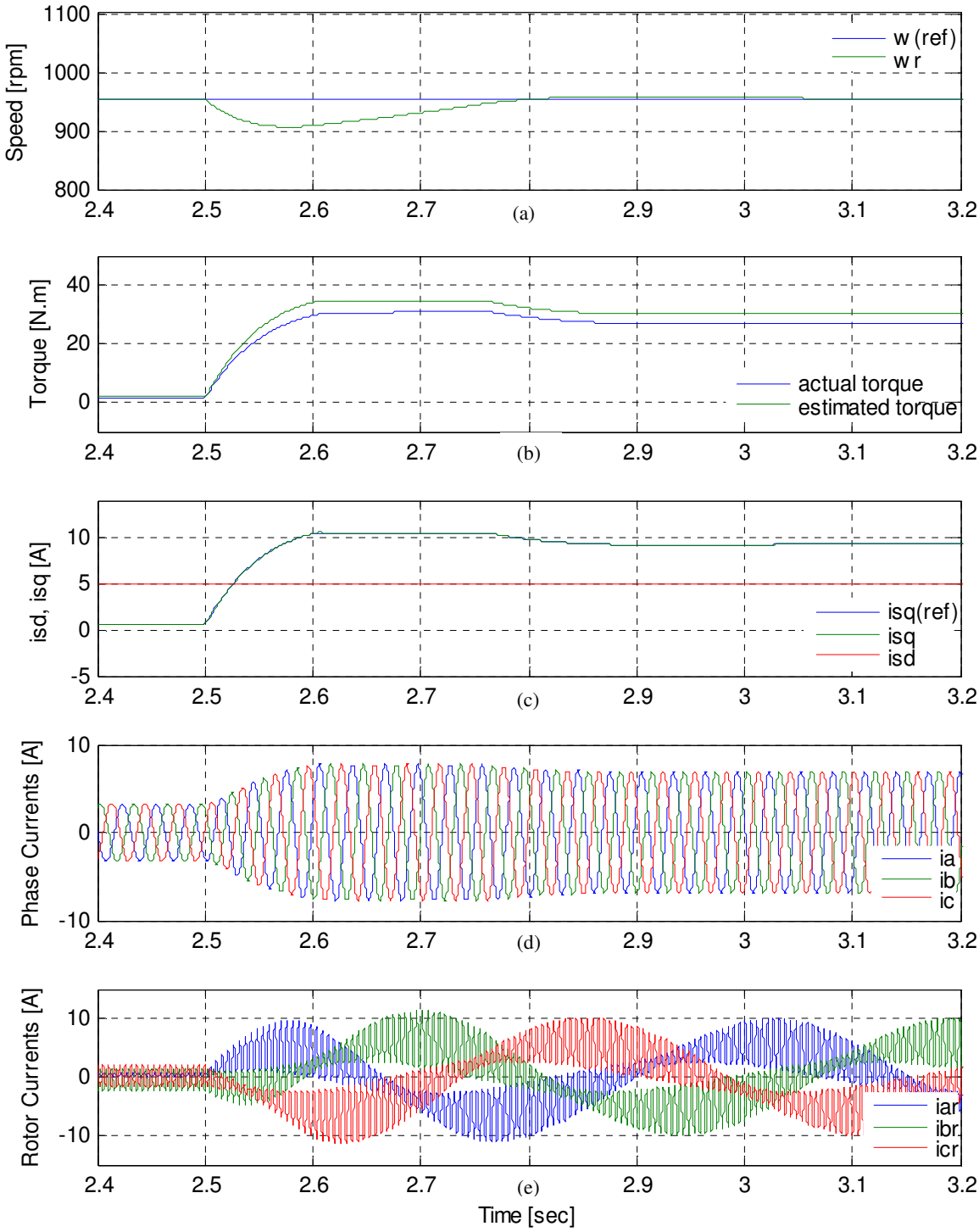

Fig. 4.8 Performance of the proposed model containing space harmonic effects when an external load disturbance is applied at t = 2.5 sec. a) Speed, b) Electromagnetic torque, c) i_{sd} & i_{sq} currents, d) Phase currents and e) Rotor currents.

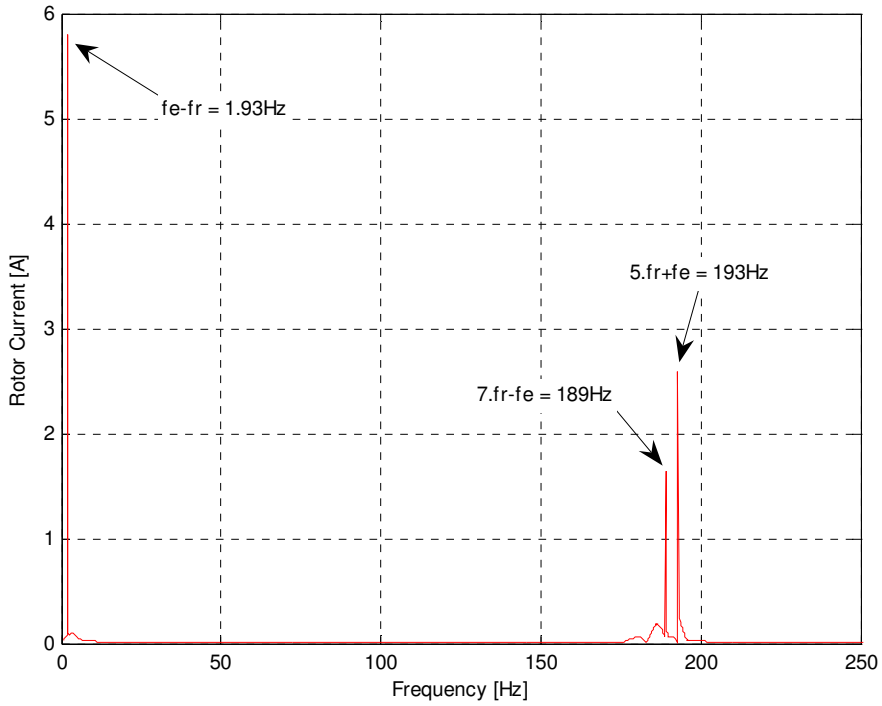

Fig. 4.9 Frequency spectrum for the rotor current using the proposed model.

Note from Figs. 4.7(b) and 4.8(b) that the actual electromagnetic torque produced by the machine is smaller than the estimated torque from vector control. The difference observed is due to the fact that the vector control derivation uses a highly idealized motor model that does not include any space harmonic content. The existence of the space harmonic will affect the torque production, and this causes the deviation from the predicted torque performance. To discuss this in further detail, Fig. 4.10 shows five torque traces which are: the estimated torque from the vector control, the net electromagnetic torque as calculated by (3.27), the electromagnetic torque generated due to the fundamental field (3.18), the electromagnetic torque generated due to the field of the 5^{th} space harmonic; and the electromagnetic torque generated due to the field of the 7^{th} space harmonic. When three phase currents start circulating through the winding, the MMF start to vary with time, alternating around the circumference. In addition to the fundamental pole pair *PP*, space harmonics of *nPP* pole pair are produced. The MMF waves interact with the fundamental permeance wave (it's assumed a smooth air gap) and produce a stator fundamental field and winding flux density harmonics. The number of pole pairs of these harmonics is equal to the number of pole pairs of the MMF waves. The fundamental field of the machine which has *PP* pole pairs and rotates at *w/PP* rad/sec will interact with the rotor to produce the

fundamental torque which is shown in Fig. 4.10. The other harmonic fields due to the 5^{th} and 7^{th} harmonics (which have pair $5PP$ and $7PP$ poles pairs and rotate at $w/5PP$ and $w/7PP$ rad/sec) will interact with the rotor to produce the 5^{th} and 7^{th} harmonic torques as observed in Fig. 4.10. The harmonic fields rotate either at a lower speed than the fundamental field, or in the opposite direction to the rotor producing a drag on the rotor through their interaction with the rotor fields [118]. Nevertheless, all the stator space harmonic fields of any order induce a current at the supply frequency [63]. Therefore, the 5^{th} and 7^{th} harmonics generate a negative torque as shown in Fig. 4.10. It can be inferred that there is no torque pulsation because there are no two fields having the same number of poles and rotating at different speed as was discussed in Section 4.2.1.

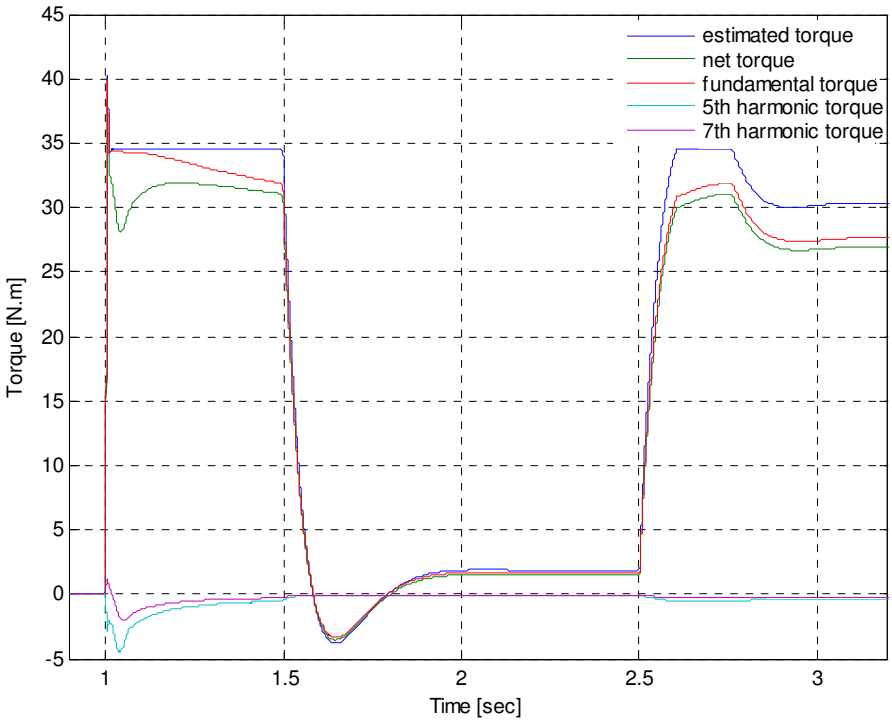

Fig. 4.10 Electromagnetic torque components using proposed scheme.

For the purpose of better understanding the influence of the time harmonics and space harmonics on the electromagnetic torque production, four experimental tests have been carried out. In the first case, the induction machine is supplied by pure sinusoidal voltages using a controlled voltage source [119]. The operation conditions of this test are phase voltage: 331V at 39.87Hz (250 rad/sec), with rated flux and no load. Experimental results of the spectrum for the line current and line to line voltage during steady state are presented in Figs. 4.11(a) and (b), respectively, where the harmonic magnitudes of the stator line current and voltage are expressed as a percentage of its fundamental component. The aim of this test was to eliminate the effect of the time harmonic components which are produced by the inverter supply. In order to make a comparison with a system using an inverter, other tests were carried out under the same operating conditions by using the inverter supply. Fig. 4.12 shows experimental results for the line current and line-line voltage for the case of speed demand of 250 rad/sec, rated flux and no load (this is a similar operating condition to that using variable power supply presented in Fig. 4.11). By comparing these results in Fig. 4.12(a) and Fig. 4.11(a), it can be seen that in both cases the line current contains 5^{th} and 7^{th} components which are due to the combination of the three sources as discussed earlier, i.e. the time harmonics, space harmonics, and magnetic saturation harmonics. The magnitudes of the 5^{th} and 7^{th} components of Fig. 4.12(a) are 7.5% and 2.37% of the fundamental component, while they are 3.61% and 0.21% of the fundamental component as in Fig. 4.11(a). The reason of this is because the time harmonics created by non linear power converter effects have been eliminated by using a pure sinusoidal power supply as can be seen in Figs. 4.11(b) and 4.12(b). From this test, it can be concluded that the line current harmonics appearing in Fig. 4.11(a) are only due to space and saturation harmonics, whereas those in Fig. 4.12(a) also include inverter related time harmonics.

As an alternative test, the machine behaviour is also investigated at 50% of the rated flux. The aim of this test was to reduce the amplitude of the line current (time) harmonics in the experimental rig by reducing the saturation effect. Figs. 4.13(a) and (b) show the result of the line current and the line-line voltage when the machine is supplied by a pure sinusoidal voltage at 165V (which corresponds approximately to 50% of the rated flux in case of vector control). The frequency is 39.87Hz (250 rad/sec), and no load. Figs. 4.14(a) and (b) show experimental results for the line current and line-line voltage when the machine is supplied by the inverter at 40% of the

rated flux, 250 rad/sec at no load. This test was carried out to maintain the machine operating under the same condition as in the case using a sinusoidal power supply. It is obvious that by reducing the flux amplitude, there is an important reduction in the amplitude in all the saturation components in the line current. The amplitudes of the 5^{th} and 7^{th} harmonic components presented in Fig. 4.14(a) are 4.3% and 2.4% respectively of the fundamental component, while they are 0.4% and 0.4% respectively of the fundamental component for the case considered in Fig. 4.13(a). The result presented in Figs. 4.15(a) and (b) show experimental results for the electromagnetic torque developed by the machine when it was supplied by the inverter under the same conditions as the previous figure. By comparing the results presented in Fig. 4.14 with Fig. 4.12, and Fig. 4.13 with Fig. 4.11; the following conclusions can be drawn:

1) The line current harmonic components are smaller when the machine is supplied by the inverter using 40% of the full rated flux (i.e. the 5^{th} harmonic component is 4.3% respect to the case of using full flux (7.5%), i.e. a reduction for this component of about 57% is obtained. Note that the amplitude of 5^{th} harmonic component is much smaller when the machine was supplied by sinusoidal voltage (0.4%) compared to the inverter supply (4.3%), i.e. a reduction of about 91% is obtained.
2) It can be observed the 6^{th} harmonic component of the electromagnetic torque is smaller when the machine is operated at 40% of the rated flux (0.82%) compared to the case of full flux (6.85%), i.e. a reduction of about 88% is observed.
3) It has been experimentally observed that a reduction in the flux magnitude reduces the saturation effects in the machine which is observed as a reduction in the amplitude of the time harmonics in the line current and the torque harmonics.

According to this a modified model of machine should include the saturation effects to provide a reliable representation for some of the physical and non-linear effects within an induction motor drive; this will be discussed in the next section.

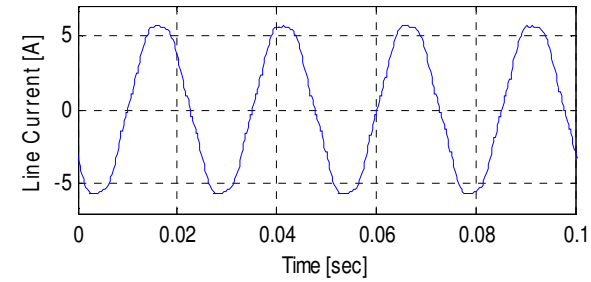

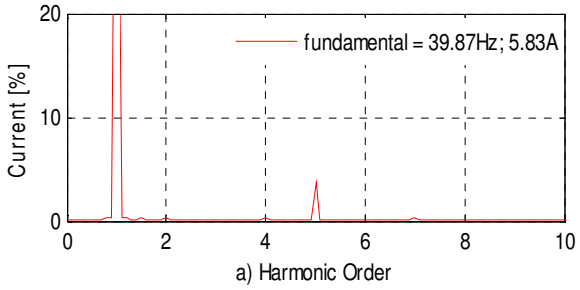

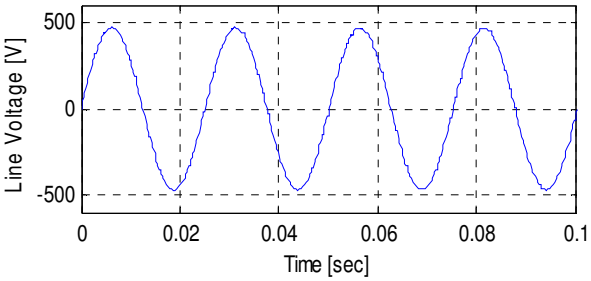

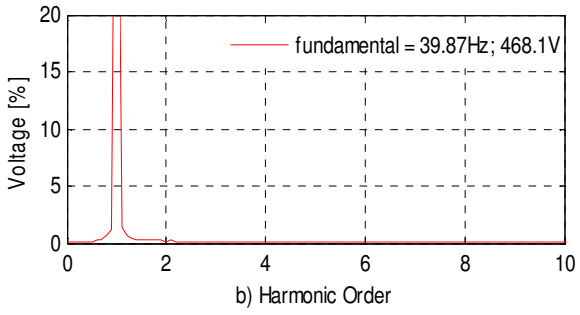

Fig. 4.11 Experimental Results using a sinusoidal power supply set at 250 rad/sec, 331Vrms (rated flux) and no load for: a) line current, b) line – line voltage.

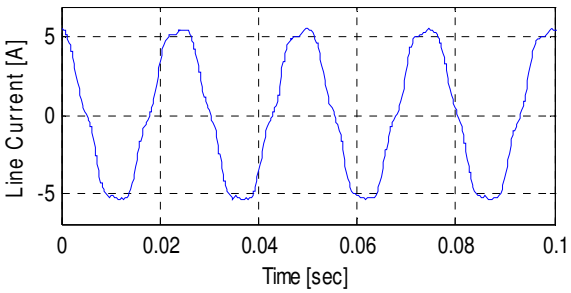

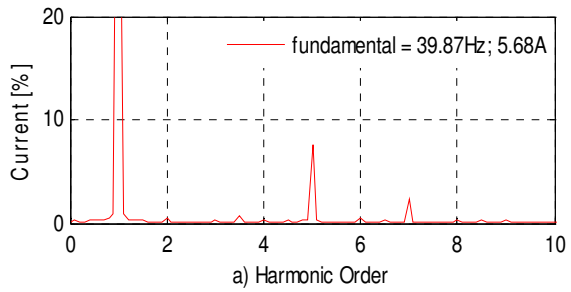

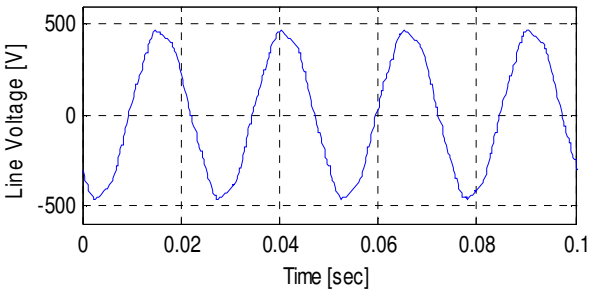

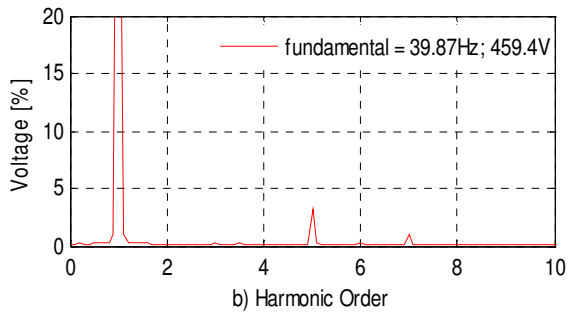

Fig. 4.12 Experimental Results using an inverter operating under IRFO control at 250 rad/sec, rated flux and no load for: a) line current, b) line – line voltage.

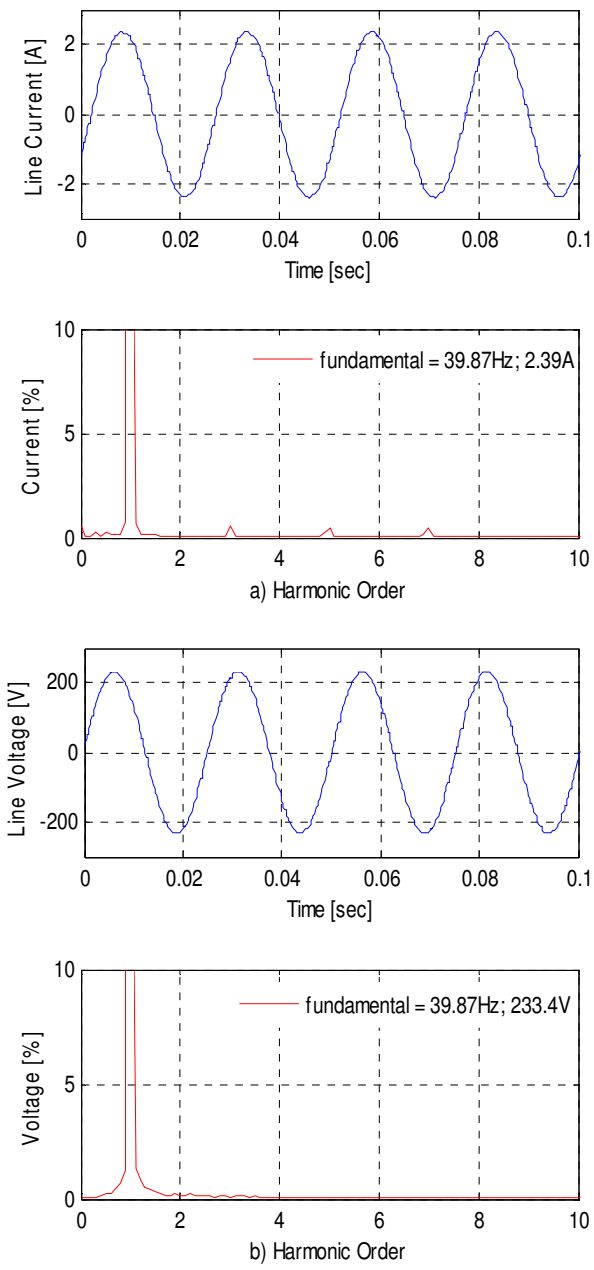

Fig. 4.13 Experimental results using a sinusoidal power supply set at 250 rad/sec, 165Vrms (50% rated flux) at no load. a) line current, b) line – line voltage.

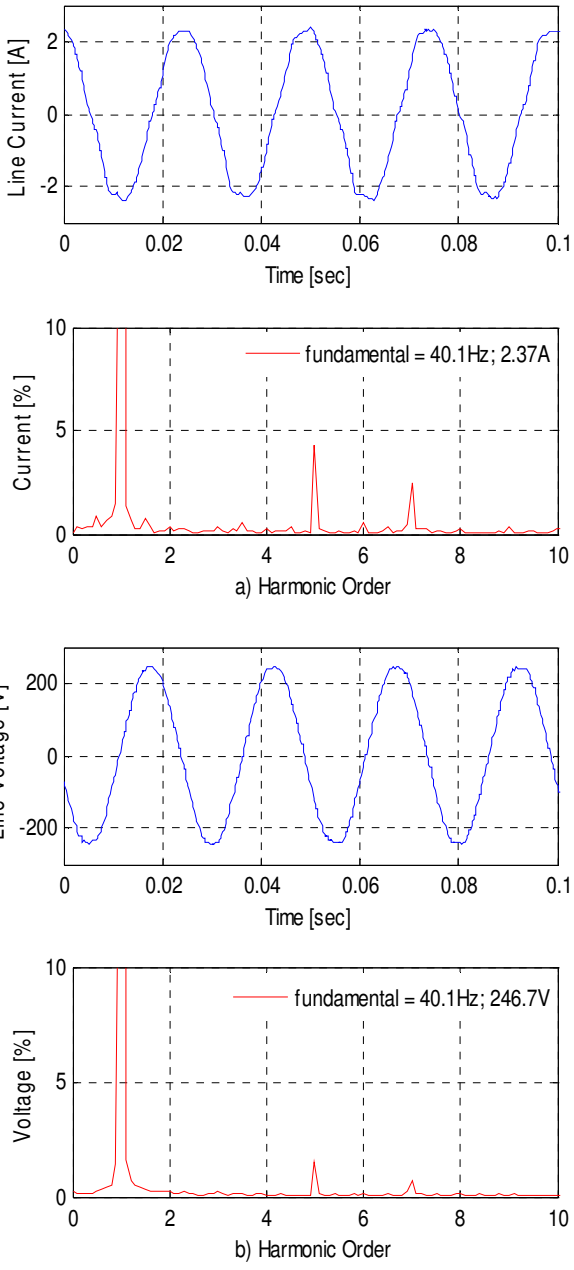

Fig. 4.14 Experimental results using an inverter operating under IRFO control at 250 rad/sec, 40% rated flux at no load for: a) line current, b) line – line voltage.

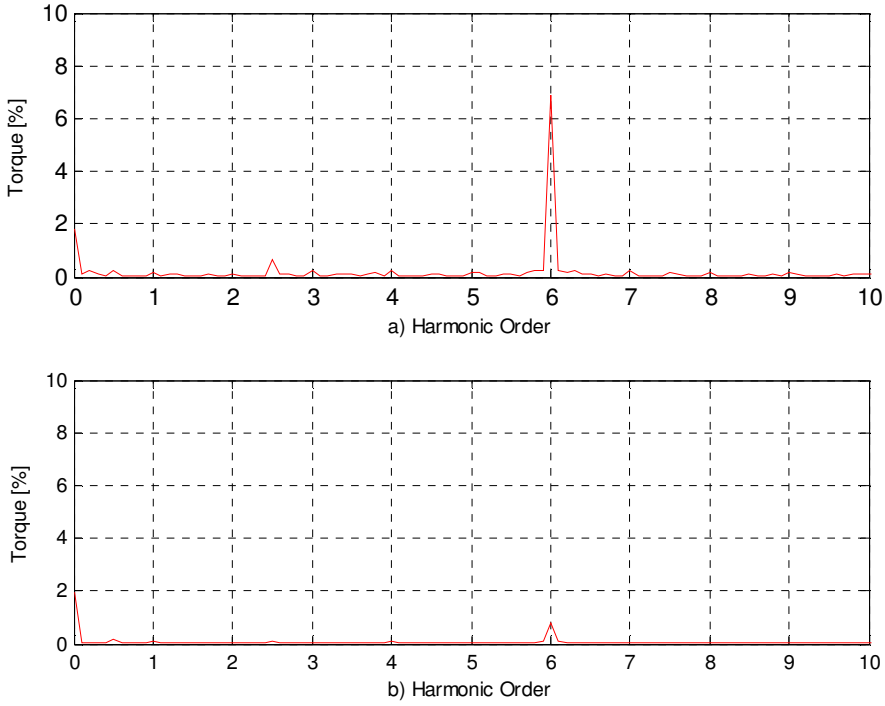

Fig. 4.15 Experimental results – frequency spectrum of the electromagnetic torque for IRFO control at 250 rad/sec, no load for: a) full rated flux b) 40% of the rated flux.

4.2.3 Simulation and Experimental Results considering Space Harmonics and Saturation Effects

In order to verify the results obtained from the proposed model which contains space harmonics and saturation effects, experimental tests have been carried out at different speeds and load conditions. The saturation effects are incorporated into the stator mutual inductances using equation (3.29) as described in Chapter 3. The phase current of the induction motor under different load conditions was captured and analysed. The proposed profiles of the machine inductances are considered to be load dependent i.e. the parameters K_2, K_4, and K_6 change as a function of the load level. For more accurate results the model will be adjusted automatically to give a good correlation with the experimental results. It should be noted that the parameters of the saturation model are tuned when the machine is working at rated flux. In this case, the stator magnetizing inductance L_{ms} will be a fixed value where it depends mainly on the stator flux [120]. The tuning of the parameters of the saturation model are described in the following section.

4.2.3.1 Model Parameter Tuning

To tune the saturation characteristic of the model, the parameters of the stator mutual inductance profiles are adjusted according to measurements made from an experimental system (the spectrum of the winding current signal) for different load condition. It is worth highlighting that the harmonics of the phase currents are the combination of different harmonic sources such as the saturation effects and the non-linearity of the power converter. Therefore, by adjusting parameters K_2, K_4, and K_6 and ρ_2, ρ_4, ρ_6 all the time harmonic components in the winding current (which are due to the saturation effects and non-linearity of the power converter) can be matched to the experimental measurements. The parameters can be adjusted as follows.

1) From no-load tests at rated flux, the phase currents of the induction motor is captured and analysed.
2) The frequency spectrum of each test is obtained by using Fourier analysis of a phase current i.e. (i_a). The 3rd, 5th, and 7th harmonic level components are determined. Note that for the healthy condition the 5th and 7th harmonics are the most important components which will be exist in the motor line current. However, accuracy for 3rd harmonic component will be required during operation with a fault. Initial values for the motor model parameters K_2, K_4, K_6, ρ_2, ρ_4, and ρ_6 are as follows: $K_2 = 0.2$, $K_4 = 0$, $K_6 = 0$, $\rho_2 = 2\pi/3$, $\rho_4 = 2\pi/3$, and $\rho_6 = 2\pi/3$.
3) The simulation of motor model is started assuming no-load operating conditions at rated flux. The value of the parameter K_2 is decreased until the 3rd harmonic level of a stator winding current (i_a) becomes equal to the one measured in the equivalent experiment.
4) After the K_2 has been fixed, the simulation is repeated using same conditions. The value of K_4 is increased until the 5th harmonic level of the stator winding current (i_a) becomes equal to the one measured in the experiment. This step will be repeated in the same way to tune the K_6 until the 7th harmonic level of the stator current becomes equal to the measured one.
5) A final adjustment may be required to get more enhanced results especially if there is overlapping between K_2 and K_4 or K_4 and K_6.

6) Steps 1 to 5 will be repeated to find the parameter K_2, K_4, and K_6 for half load and full load conditions with a rated flux.

Tests under different loads were conducted to verify the model results. As explained above, the parameters K_2, K_4, and K_6 and the phase displacement ρ_2, ρ_4, and ρ_6 have been tuned for several values of load to give a good correlation with the experimental results for the delta connected machine. If a star connected machine is used, the saturation parameters would have to be re-calibrated. Fig. 4.16 illustrates the variation of the parameters K_2, K_4, and K_6 with no-load, half load and full load operation at 200 rad/sec at rated flux. It can be noted that the parameters change as a function of the load level. Therefore, these relationships of the saturation model parameters are incorporated into the induction machine model as a function of the load level. To achieve this, three look up tables are added to the induction machine model to adjust the parameter values of the saturation model. The input for these look up tables will be the electromagnetic torque as calculated from (3.27) and the output will be the three parameter values K_2, K_4, and K_6. It is worth highlighting that a low pass filter has been used with low cut-off frequency to remove the torque ripples which are normally associated with electromagnetic torque when the saturation effect exists. In this case, the DC level value of the electromagnetic torque will be passed to the look up tables and all the ripple will be eliminated. As a result, stable outputs from the look up tables will be passes to the saturation model.

Fig. 4.17 illustrates the stator mutual inductance variation $L_{ab}(\theta_f)$ with stator flux angle for one phase of the unloaded symmetric machine. Fig. 4.17(b) details the harmonic content of the stator mutual inductance spatial variation. The stator mutual inductance harmonics are only due to magnetic saturation in the symmetric machine.

The stator mutual inductances were calculated again using different loading conditions. Figs. 4.18(a) and 4.19(a) show how the stator mutual inductance $L_{ab}(\theta_f)$ changes with stator flux position for half and full load respectively. The calculations were made with the machine operating at rated flux current i_{sd} = 4.9, and different torque currents i_{sq}. Figs. 4.18(b) and 4.19(b) show the harmonic magnitudes of the stator mutual inductance spatial variation. As the load is increased on this motor, and the magnetic loading enters into a deeper saturation, the 2nd and 4th harmonics decrease while the 6th harmonic increases. It is important to report that the phase displacement ρ_2, ρ_4, and ρ_6

were left with a fixed value ($2\pi/3$) for simplicity, while they may actually vary with load [87, 88, 114].

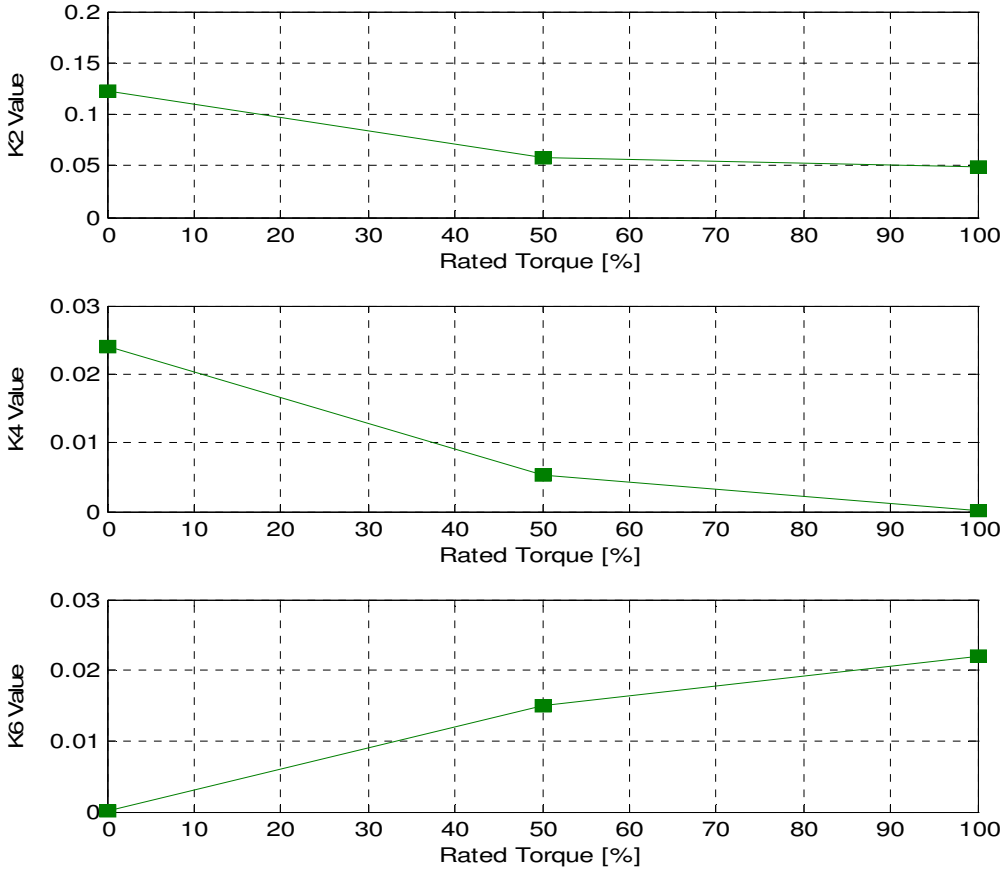

Fig. 4.16 The variation of the saturation model parameters as a function of the load level for 200 rad/sec and rated flux.

It is important to note that the saturation effect had assumed that only the stator mutual inductances will be modulated by the cyclic movement of saturation. This is a significant simplification; it allows the development of a model that provides some indication of the effect of saturation whilst keeping the model complexity (and solution time) relatively low. The magnetic circuit topologies and motor winding layouts were not considered in the model that has been used. In addition, non-linear frequency dependent variations neglected here include skin effect and eddy currents – to add these would over-complicate the model for the purpose intended. Therefore, the model does not necessarily represent the true behaviour of the real machine, and only a rough

estimate for the harmonic components (amplitude) are required, as the main objective of the model is to locate rather than quantify these harmonics.

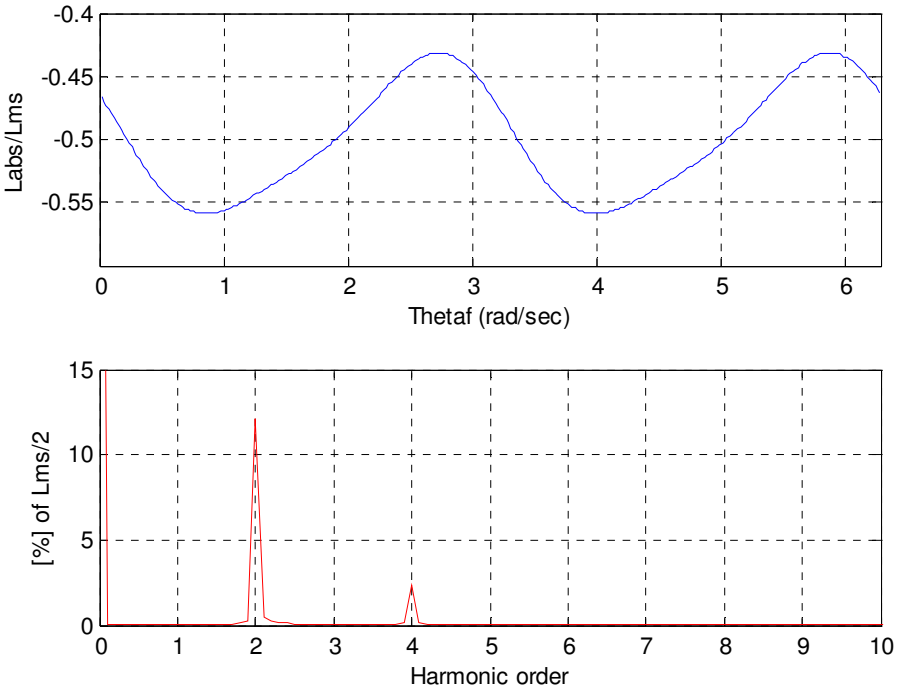

Fig. 4.17 Stator mutual inductance as a function of the stator flux angle (top) and the frequency spectrum of the inductance profile (bottom) for 200 rad/sec and no load.

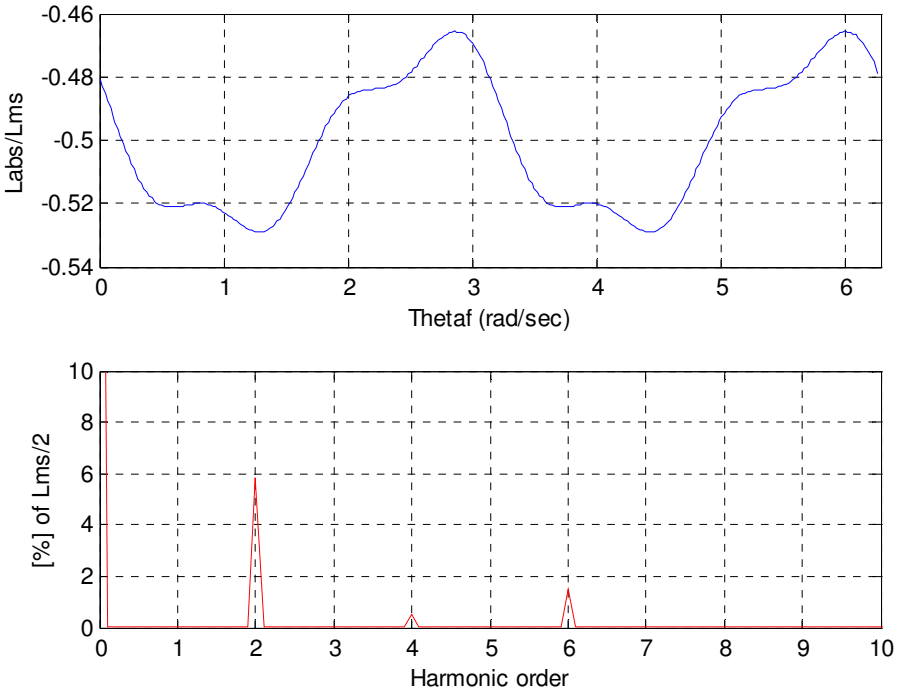

Fig. 4.18 Stator mutual inductance as a function of the stator flux angle (top) and the frequency spectrum of the inductance profile (bottom) for 200 rad/sec and 50% of the nominal load.

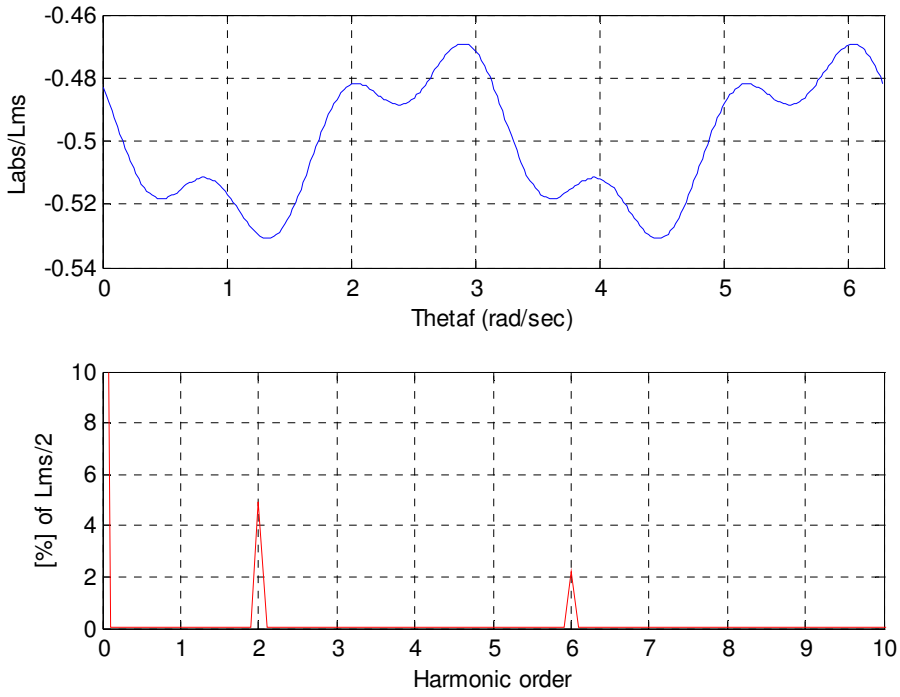

Fig. 4.19 Stator mutual inductance as a function of the stator flux angle (top) and the frequency spectrum of the inductance profile (bottom) for 200 rad/sec and 100% of the nominal load.

4.2.3.2 Simulation and Experimental Results

The saturation effect is incorporated in the induction motor model and adjusted according to the spectrum of the winding current as explained before. The frequency spectra of the simulated phase current and electromagnetic torque from the vector controlled drive were then compared to those obtained from the experimental setup for several different operating conditions to validate the result of the simulation model. The harmonic magnitudes of the stator current are expressed as a percentage of its fundamental component, while the torque was expressed as a percentage of the rated torque (27 N.m.). The comparison of the simulation model and experimental results for the healthy drive operating at rated flux, 200 rad/sec and no load is presented in Figs. 4.20 and 4.21. Note that the phase currents are not pure sinusoids but have harmonic ripple. The source of this distortion is a combination of time, space, and saturation harmonics. Figs. 4.22 and 4.23 show the spectrum of the phase current and

electromagnetic torque waveforms for the same operating conditions. All the stator space harmonic fields of any order induce a current at the supply frequency as discussed in the previous section, while the saturation harmonic fields induce currents at 3^{rd} , 5^{th} , 7^{th} , … multiplies of the supply frequency. Table 4.2 compares the results from Figs. 4.22 and 4.23 at full rated flux. All the magnitudes of the phase current harmonic components derived from the new simulation model match closely the experimental measurements. Figs. 4.22(b) and 4.23(b) show the electromagnetic torque spectra. In the simulation, the magnitude of the 6^{th} component is slightly smaller than the experimental value. The author believes that this is due to the assumption used in the model, that only the mutual inductance terms are affected by saturation.

In reality there are many other nonlinear effects that tend to interact with each other (they are the subject of future work). In general, current harmonics are all time harmonics and the developed torque is a consequence of the interaction of the fields that induced these time harmonics with the other fields which are the results of the space harmonics. A ripple is created in the electromagnetic torque when the MMF distribution and flux distribution are not synchronous, and only if they have the same number of poles. For example, if the 5^{th} and 7^{th} harmonics of the current do occur due to saturation, these interact with the 5^{th} and 7^{th} harmonics of the winding MMF distribution respectively to create together a 6^{th} harmonic component in the electromagnetic torque as shown in Fig. 4.23(b). The simulation amplitudes presented in Table 4.2 are in good agreement with the experimentally measured spectra.

Similarly Figs. 4.24 with 4.25 and 4.26 with 4.27 show the comparison of the simulation model and experimental results for the healthy drive operating at rated flux, 200 rad/sec under half and full load condition respectively. Table 4.2 summarises the most significant components of the spectrum. There is a slight mismatch in the amplitude of the simulated saturation components (5^{th}) compared to that of the experimental one. These differences can be attributed to the assumption used in the model that only the mutual inductance terms are affected by saturation. The results at full rated flux which appear in Table 4.2 show that the magnitude of the simulation results match the experimental results to the accuracy required for this project.

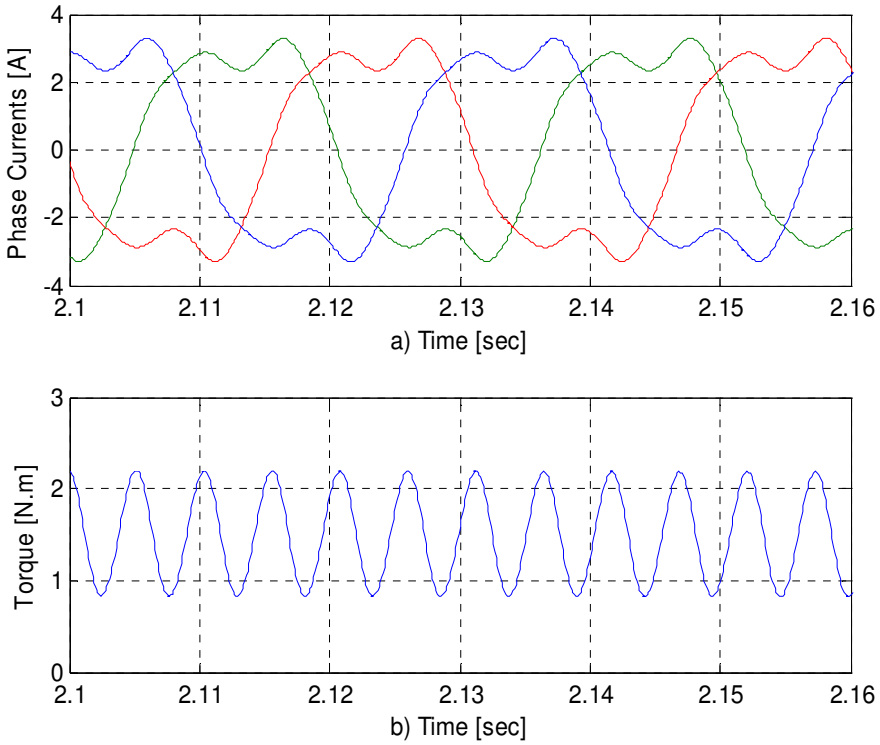

Fig. 4.20 Simulation results for the healthy drive operating at rated flux, 200 rad/sec under no load a) steady state phase currents b) electromagnetic torque.

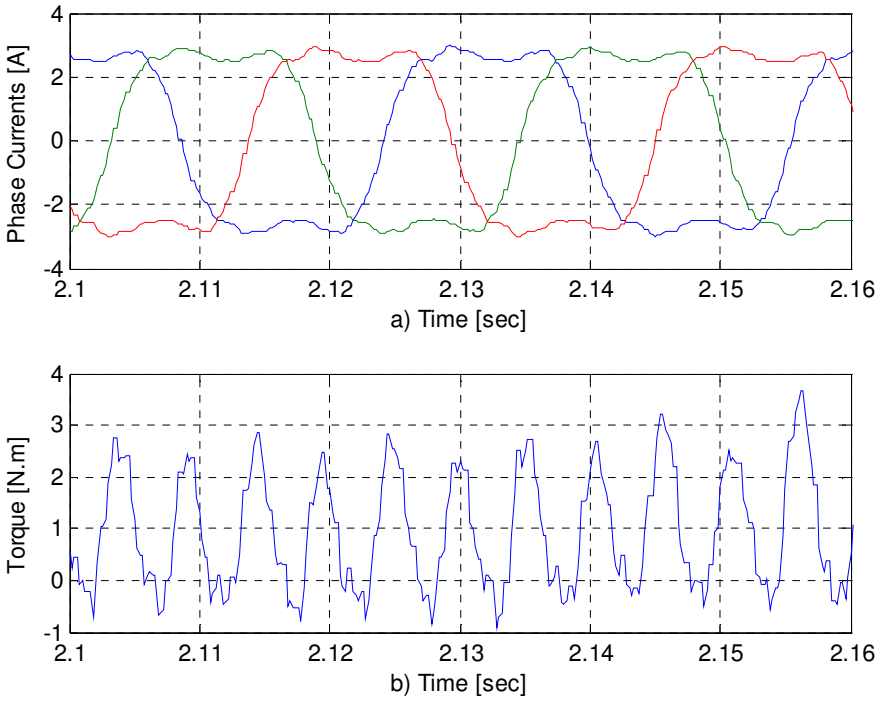

Fig. 4.21 Experimental results for the healthy drive operating at rated flux, 200 rad/sec under no load a) steady state phase currents b) electromagnetic torque.

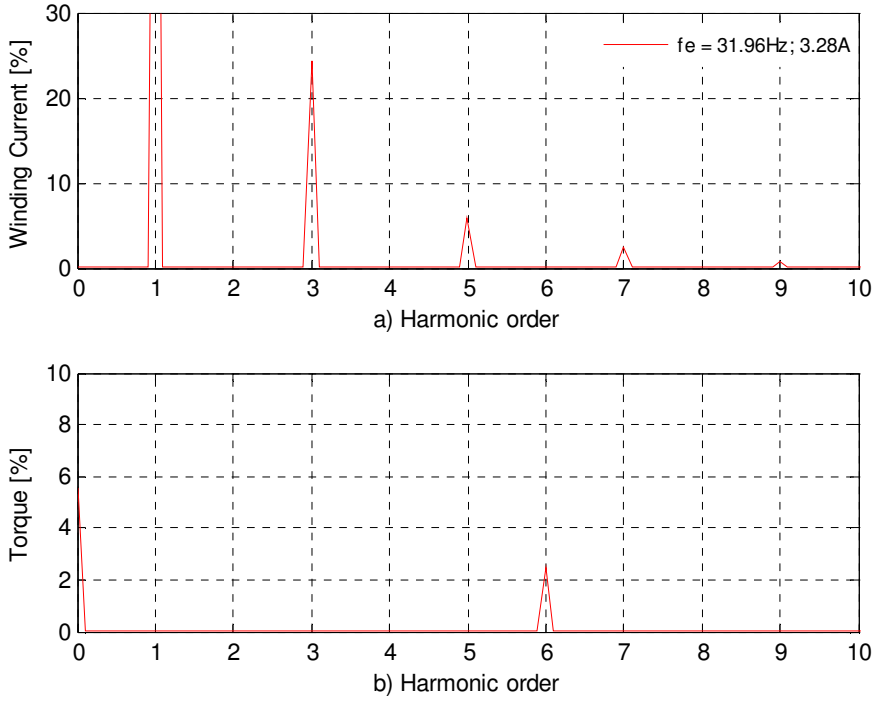

Fig. 4.22 Simulation results - Frequency spectrum of the a) winding current b) electromagnetic torque at 200 rad/sec and no load.

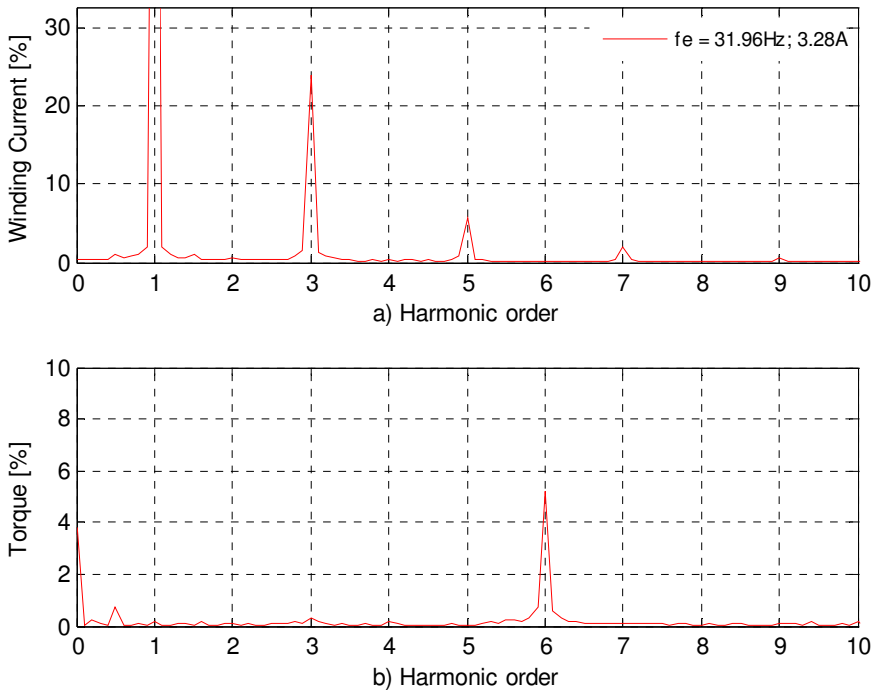

Fig. 4.23 Experimental results – Frequency spectrum of the a) winding current b) electromagnetic torque at 200 rad/sec and no load.

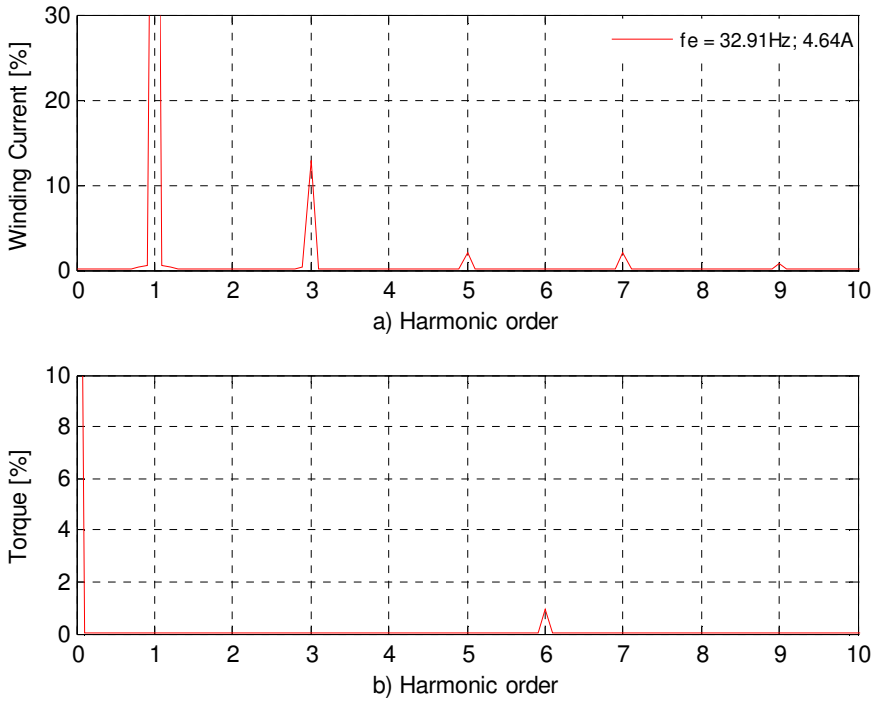

Fig. 4.24 Simulation results – Frequency spectrum of the a) winding current b) electromagnetic torque at 200 rad/sec and half load.

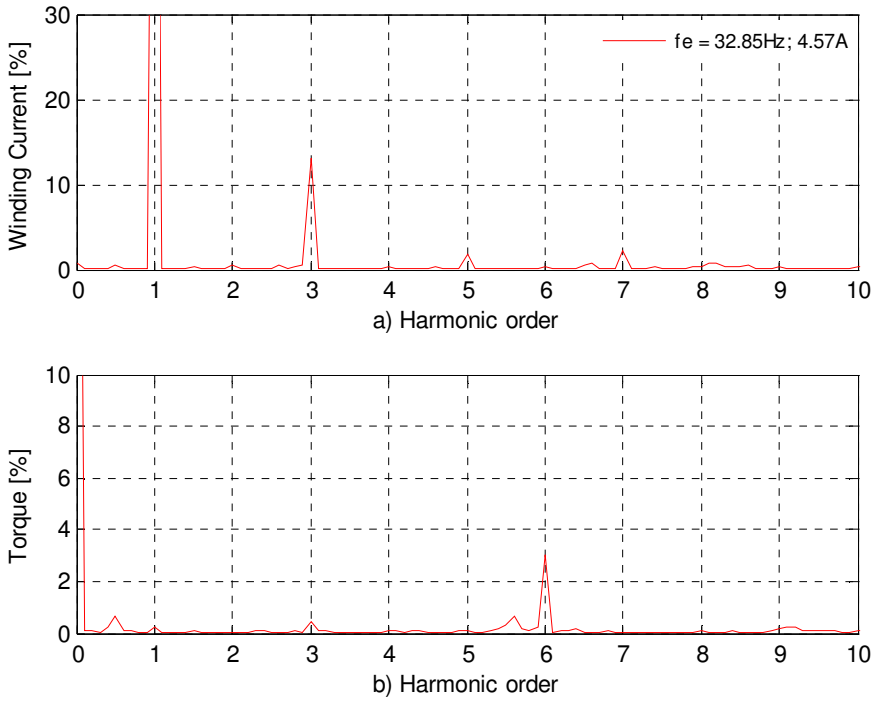

Fig. 4.25 Experimental results – Frequency spectrum of the a) winding current b) electromagnetic torque at 200 rad/sec and half load.

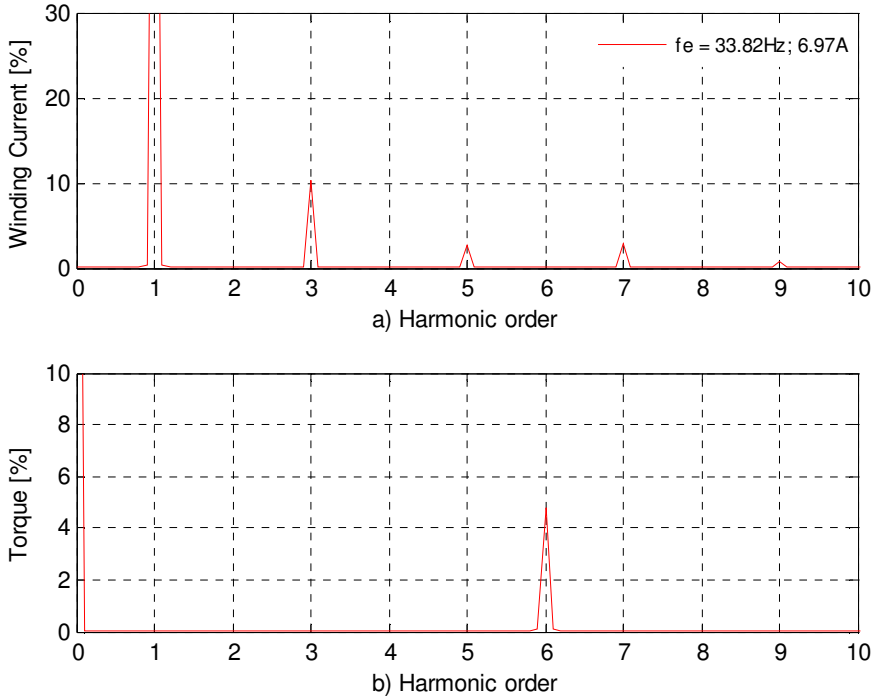

Fig. 4.26 Simulation results – Frequency spectrum of the a) winding current b) electromagnetic torque at 200 rad/sec and full load.

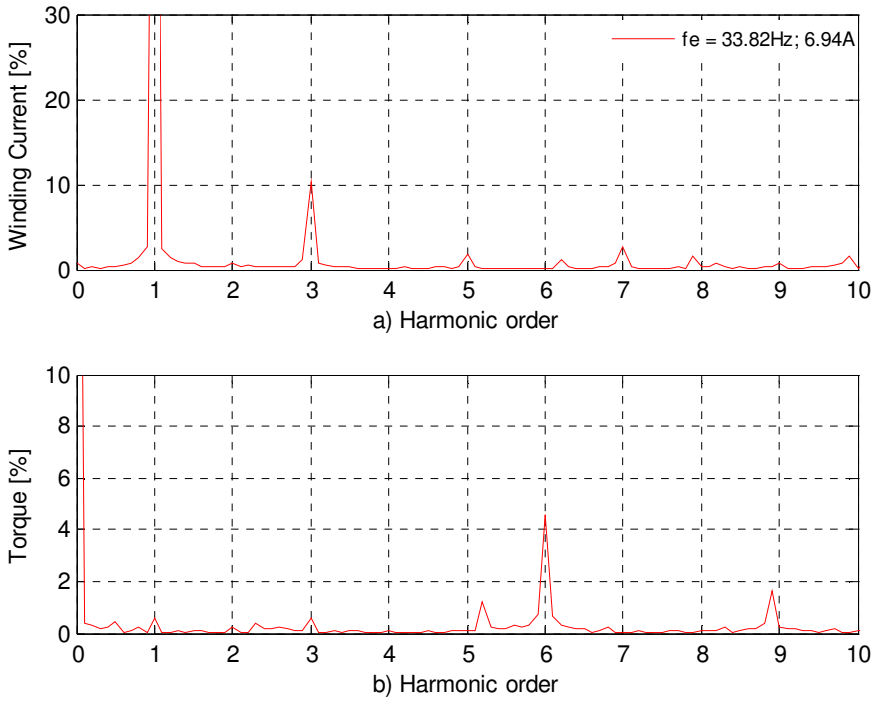

Fig. 4.27 Experimental results – Frequency spectrum of the a) winding current b) electromagnetic torque at 200 rad/sec and full load.

Table 4.2 Harmonic spectrum of the winding current and electromagnetic torque for 100% rated flux, 200 rad/sec and different load conditions.

			Experimental		Simulation	
		Harmonic order	Mag.	%	Mag.	%
No Load	Winding Current [A]	1st	3.28	100	3.28	100
		3rd	0.8	24.39	0.8	24.39
		5th	0.2	6.1	0.195	5.95
		7th	0.06	1.58	0.081	2.47
	Electromagnetic torque [N.m]	DC	1.03	4.81	1.49	5.52
		6th	1.42	5.26	0.676	2.5
Half Load	Winding Current [A]	1st	4.57	100	4.65	100
		3rd	0.6	13.13	0.6	12.9
		5th	0.09	1.97	0.095	2.04
		7th	0.1	2.19	0.095	2.04
	Electromagnetic torque [N.m]	DC	15.24	56.4	14.2	54.4
		6th	0.82	3.04	0.248	0.92
Full Load	Winding Current [A]	1st	6.94	100	6.97	100
		3rd	0.72	10.37	0.72	10.33
		5th	0.14	2.02	0.18	2.58
		7th	0.2	2.88	0.2	2.87
	Electromagnetic torque [N.m]	DC	28.2	104.4	27	100
		6th	1.287	4.76	1.295	4.79

4.3 OPERATION FOR THE INDUCTION MOTOR WITH AN OPEN CIECUIT FAULT

The three phase induction machine drive using IRFO vector control was simulated using the proposed model with an open winding fault. For the delta-connected machine, a phase open circuit turns it into a two-phase machine that has a connection to the motor mid point as shown in Fig.4.28. Operation will continue with a missing phase while there is a path for the zero sequence current. Simulation results for the case of a stator open circuit fault are given for the same machine under the same experimental conditions. A phase breakdown fault has been modelled by inserting a higher resistance into the faulted phase during the test as explained in Section 3.6.1.

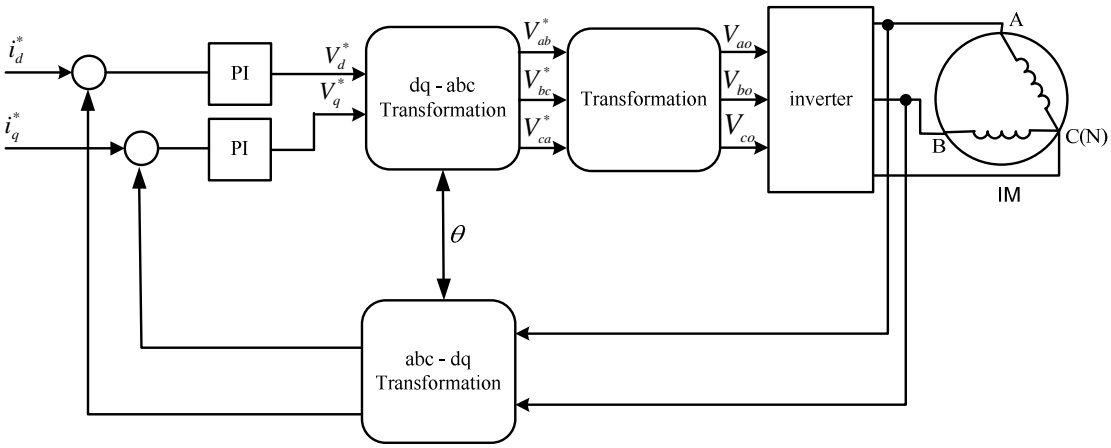

Fig. 4.28 Three phase IRFO vector control for a delta connected machine with open circuit winding fault.

The simulations to show the behaviour of an induction machine drive with a stator open circuit fault are performed under the conditions 200 rad/sec, full rated flux, and no load. Fig. 4.29 starts with the healthy machine. At time = 2 sec the open circuit fault occurs in phase *a*. The transient responses of the speed and developed torque produced before and after the fault are presented in Figs. 4.29(a) and (b), respectively. The phase currents, *d* and *q* current components, the current controller output V_d and V_q voltages are presented in Figs. 4.29(c to f), respectively. For comparison, Fig. 4.30 shows the experimental results for the same operating conditions as Fig. 4.29.

For the healthy operation condition, it can be seen that the phase currents have a flat top due to the presence of the third harmonic component of flux density. The transient of current is well predicted by the model. The control performance of the drive is still satisfactory even after an open circuit fault has occurred. The experimental results also shows some higher order oscillations, indicating the existence of higher order harmonics in the flux (i.e. slot harmonics). These are not present in the simulation result, as the model only accounts for the 3rd, 5th and 7th harmonics of flux distribution. Figs. 4.29(e),(f) and 4.30(e),(f) show the behaviour of the *d*-*q* voltages, and a slight reduction in amplitude of the simulation results compared to the experimental results. This occurs due to non linear power converter effects which was not included in the simulation model. Once again, the theoretical and experimental results are in very good correlation.

In the presence of a stator asymmetry (by losing one phase), there is an unbalance in the amplitudes of the three motor supply currents as shown in Figs. 4.29(c) and 4.30(c). This is due to the existence of a negative sequence component in these currents [94]. It can be seen that the two remaining motor currents have two different magnitudes (i_b = 5.19A and i_c = 6.14A for simulated results, and i_b = 5.3A and i_c = 6.12A for experimental results). Once again, this is well predicted by the model.

For the results presented in Figs. 4.29(b) and 4.30(b), the torque reference under the stator open circuit fault condition is slightly increased when compared to that for healthy operation. This is explained by the fact that the torque component generated from the negative sequence current component, acts against the developed torque. Thus, it can be inferred that the difference in the torque reference between a faulty and healthy conditions will exist because the negative sequence current component exists. The increased torque reference leads to increased amplitude of the *q*-axis current reference, while the flux controller maintains the same amplitude of the *d*-axis current reference as shown in the green and red traces of Figs. 4.29(d) and 4.30(d), respectively. Consequently, the simulated and experimental results in Figs. 4.29(e)-(f) and 4.30(e)-(f) show that an open circuit fault results in increasing the amplitudes of the *d*-and *q*-axis voltage references when compared to those for the healthy condition.

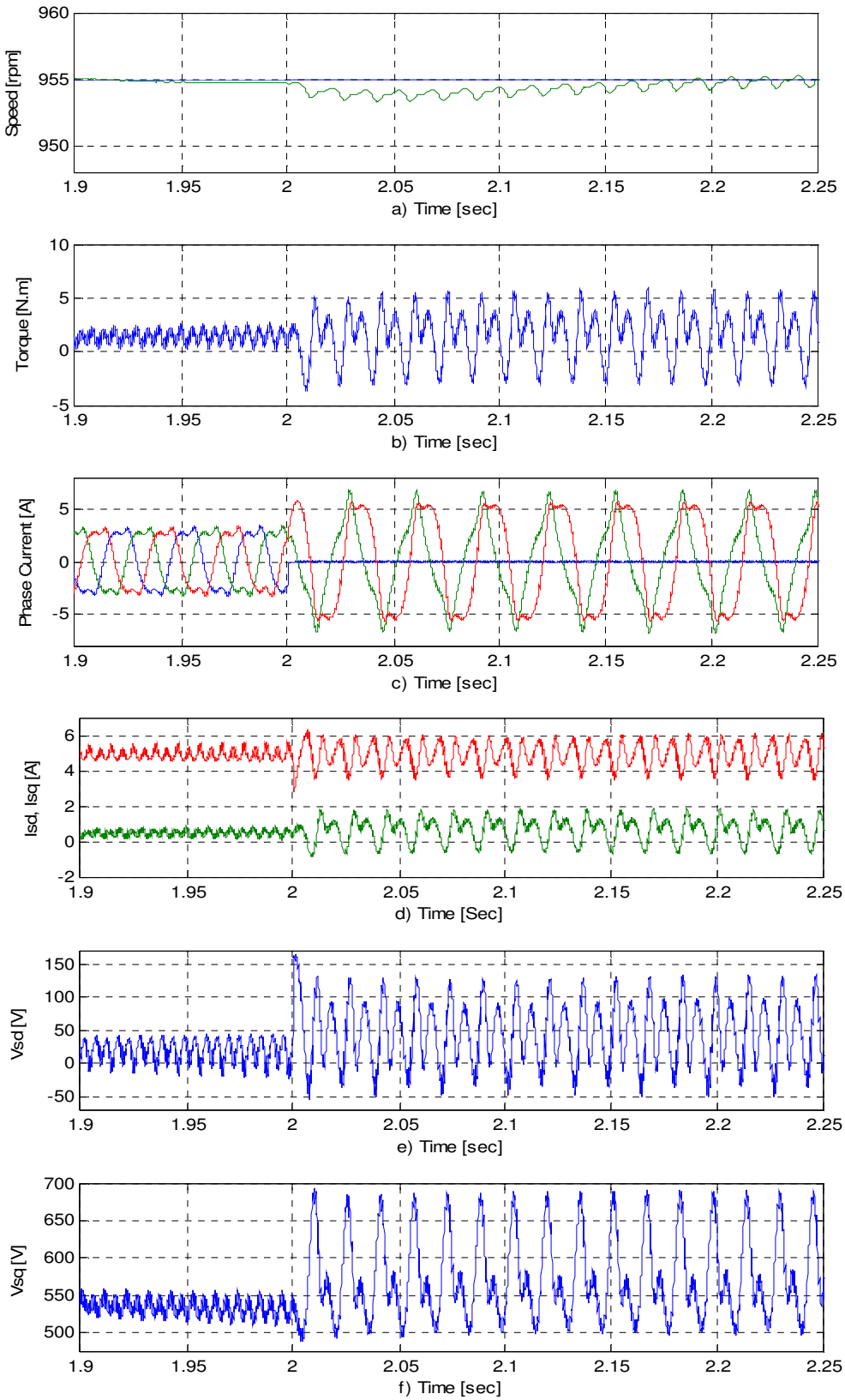

Fig. 4.29 Simulation results of induction motor using IRFO vector control at 200 rad/sec rotating speed, full rated flux, and no load before and after an open circuit fault in phase *a*, a) speed b) torque c) phase currents d) *d-q* current components e) V_d voltage and f) V_q voltage.

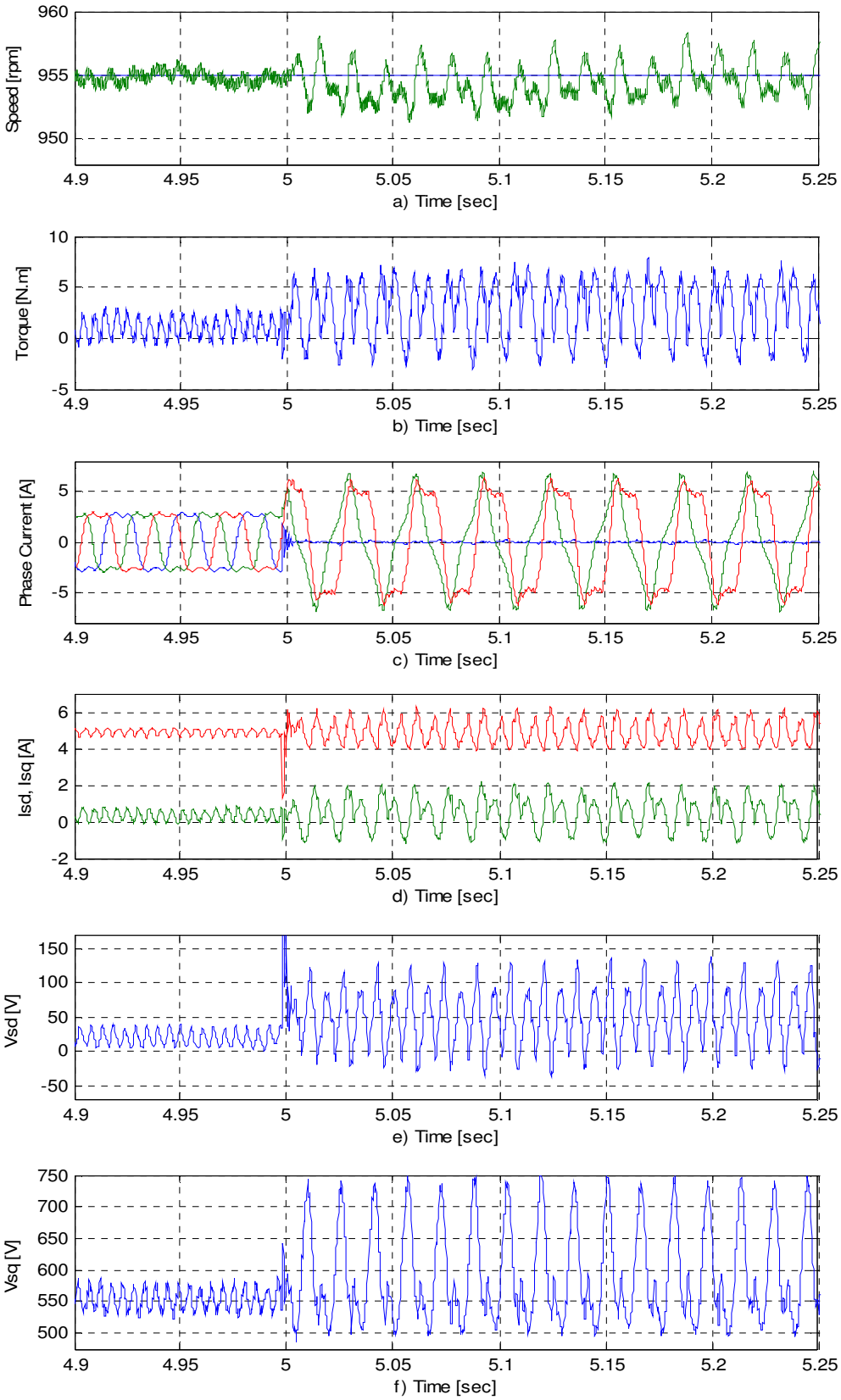

Fig. 4.30 Experimental results of induction motor using IRFO control at 200 rad/sec rotating speed, full rated flux, and no load before and after an open circuit fault in phase *a*, a) speed b) torque c) phase currents d) *d-q* current components e) V_d voltage and f) V_q voltage.

The complex frequency spectrum of the phase currents and the electromagnetic torque with an open circuit fault are presented in Figs. 4.31 and 4.32 for simulated and experimental results respectively. A negative sequence component can be seen in these currents. As a result, an additional oscillatory components appears in the *d-q* voltage references at twice the fundamental excitation as shown in Figs. 4.29(e) and (f). It can also be observed that 4^{th} and 6^{th} harmonic components have appeared in the V_{sd} and V_{sq} voltages, which are the results of the presence of the 3^{rd} and 5^{th} harmonic components of the winding currents (due to saturation and non-linearity of the power converter) when they are transferred to the *d-q* reference frame.

In addition, this negative sequence component interacts with the fundamental stator flux and the third harmonic flux, thus giving rise to the appearance of an oscillatory component in the electromagnetic torque at double of the supply frequency. This is the main indicator of the presence of the fault when analysing the torque signal (Fig. 4.31(b)) [94]. Moreover, the third harmonic component of the flux does not cancel out as it does during balanced operation. This produces additional oscillatory components in the electromagnetic torque, mainly the second and fourth harmonic components as shown in Fig. 4.31(b). The saturation induced 3^{rd} and 5^{th} harmonic components of current interact with the fields of the space harmonics of the MMF respectively to create together a 4^{th} harmonic in the electromagnetic torque. The same concept is valid for the higher order harmonic components (6^{th}, 8^{th}, and 10^{th}) that appear in the electromagnetic torque.

By comparing Figs. 4.31(a) and 4.32(a), it can be seen that the simulation results for the stator winding current match the experimental results but with a slight mismatch in the amplitude of the 3^{rd} and 5^{th} components. This is due to the simplifications made in the modelling of the saturation effect, where the model parameters K_2, K_4, K_6 and ρ_2, ρ_4, ρ_6 have not been tuned for fault conditions. The agreement between the results obtained by simulation and experiment is suitable for the objectives of this project.

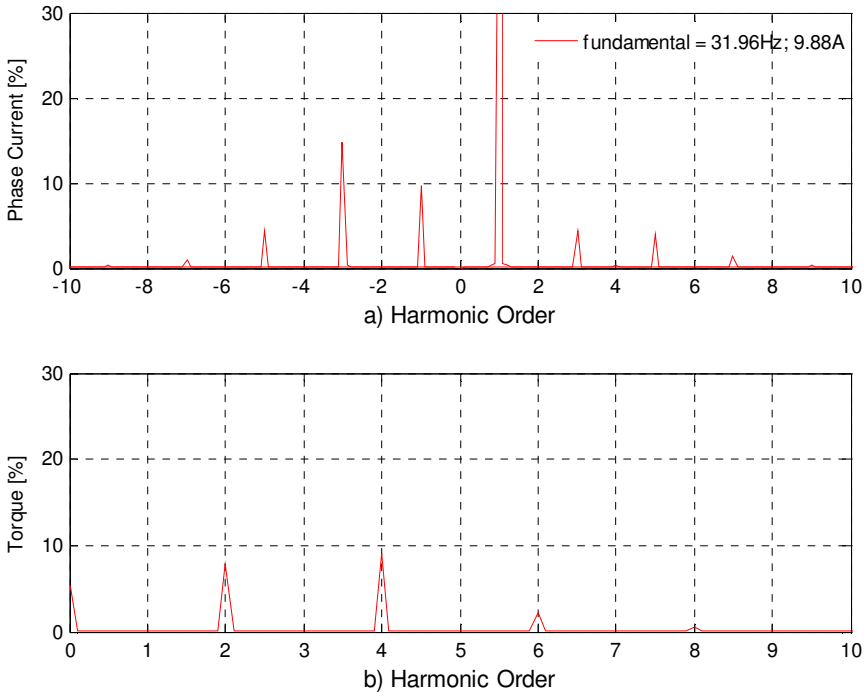

Fig. 4.31 Simulation results – Complex frequency spectrum of the a) phase current b) electromagnetic torque with open circuit in phase (*a*) at 200 rad/sec full rated flux, and no load.

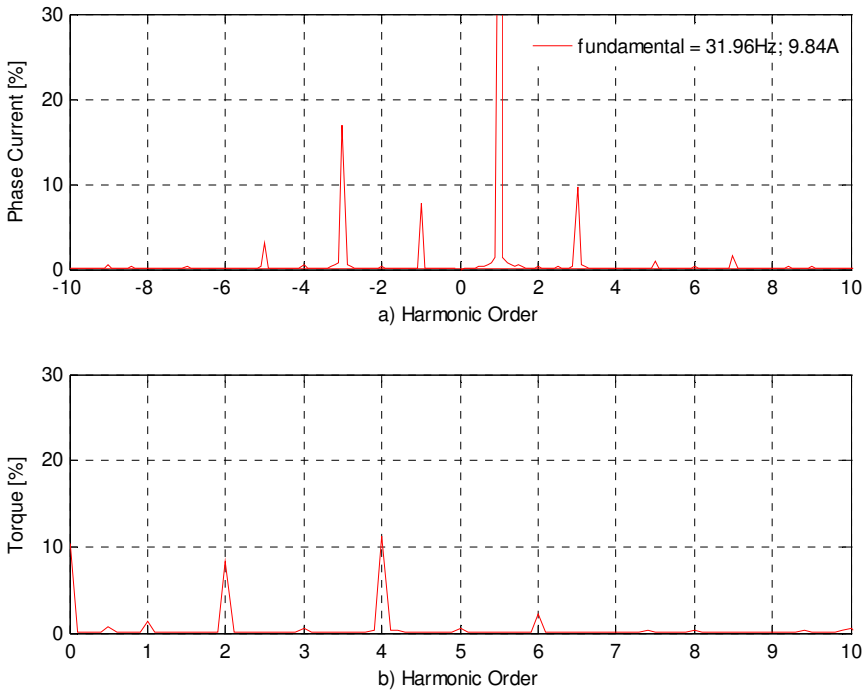

Fig. 4.32 Experimental results – Complex frequency spectrum of the a) phase current b) electromagnetic torque with open circuit in phase (*a*) at 200 rad/sec full rated flux, and no load.

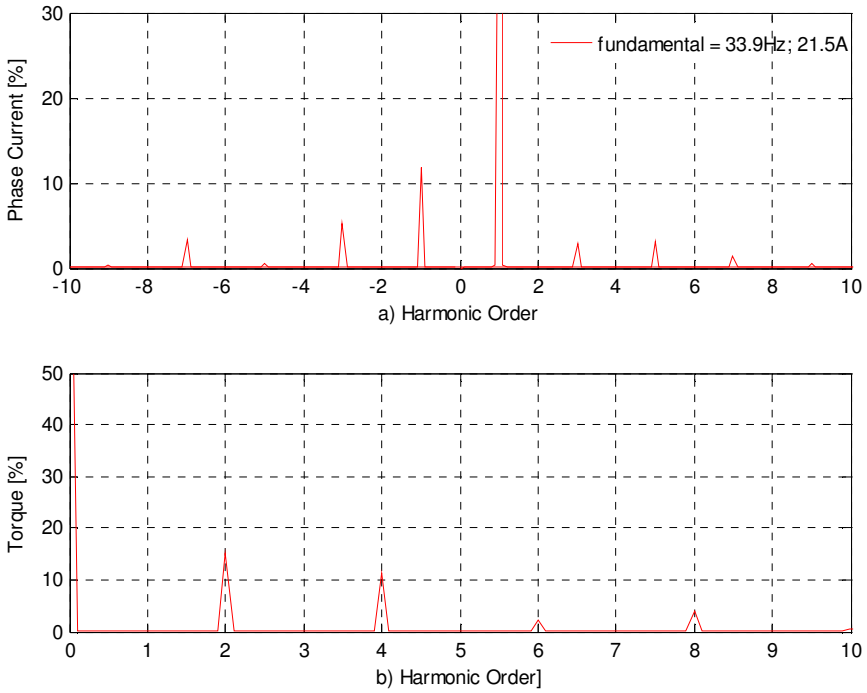

Fig. 4.33 Simulation results – Complex frequency spectrum of the a) phase current b) electromagnetic torque with open circuit in phase (*a*) at 200 rad/sec full rated flux, and full load.

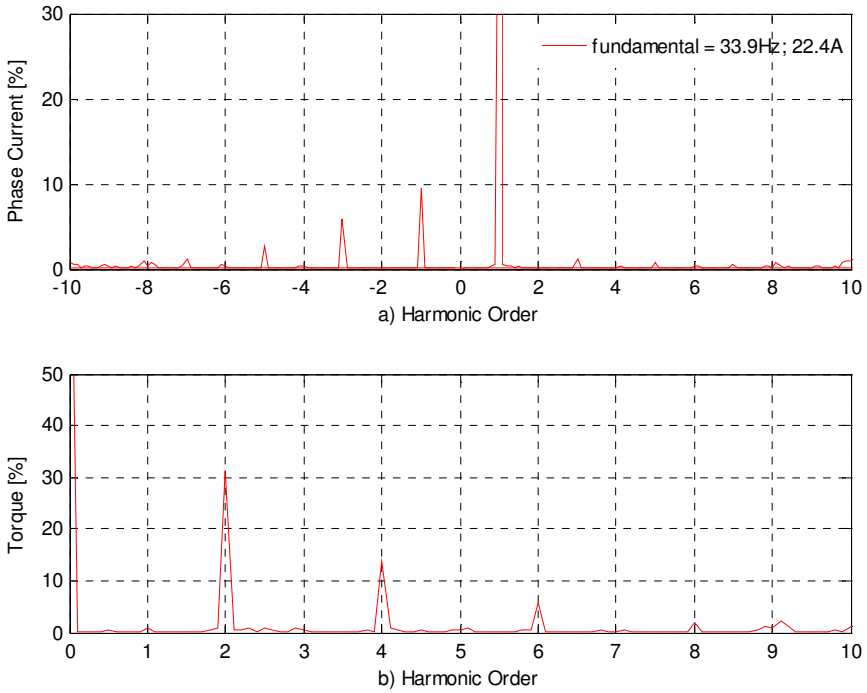

Fig. 4.34 Experimental results – Complex frequency spectrum of the a) phase current b) electromagnetic torque with open circuit in phase (*a*) at 200 rad/sec full rated flux, and full load.

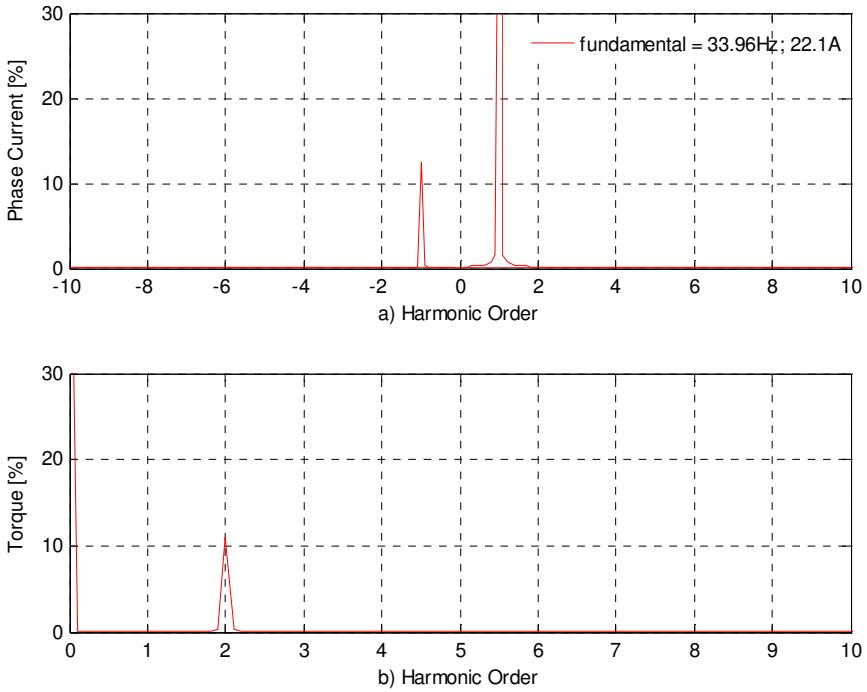

Fig. 4.35 Simulation results – Complex frequency spectrum of the a) phase current b) electromagnetic torque with open circuit in phase (*a*) at 200 rad/sec full rated flux, and full load and using linear iron.

Using the same conditions but imposing 100% of the nominal load, Figs. 4.33 and 4.34 show the phase currents and electromagnetic torque and it show harmonic components at 2fe, 4fe, 6fe, 8fe and 10fe. In addition, comparing Figs. 4.33(b) and 4.34(b), the magnitude of the 2nd component in the simulation result of the electromagnetic torque is smaller than the experimental value. This is due to the simplifications made in the modelling of the saturation effect where the saturation model has not been tuned for fault conditions. The experimental and simulation results are however in very good agreement and are suitable for the objectives of this project

Fig. 4.35 shows the simulation result for the same condition as in Fig. 4.33, but the saturation effects were eliminated to leave only the fundamental component. It can be seen that the 2nd harmonic component appears in the electromagnetic torque due to the interaction of the positive and negative sequence fundamental components of flux and current. This is the main indicator of the presence of the fault as mentioned earlier. Moreover, all other components have been eliminated by default. As can be seen from

these results, the operation without a fault tolerant control strategy is undesirable as it imposes severe torque pulsations on the drive.

4.4 CONCLUSION

The proposed simulation model of an induction machine which is able to model saturation and air gap space harmonic effects in the stationary *abc* reference frame has been validated by a comparison of simulation and experimental results. In addition, the behaviour of an induction machine drive with an open circuit fault has been investigated through simulation and experiment under various operating conditions.

The saturation model has been tuned to match the measured phase currents of the experimental system under healthy conditions. It is proved that by including the space harmonic and saturation effects, the model helped to predict some of the current harmonic components appearing in the presence of an open circuit fault. Thus, one of the main objectives of the proposed model has been met i.e. to be able to provide reasonable harmonic content in both current and torque under faulted operation.

It has been clarified that voltages, currents and torque distortions are due to a combination of three sources, the presence of the space harmonics (a consequence of the non-sinusoidal distribution of the winding), the presence of magnetizing flux harmonics (a consequence of the machine saturation), and the presence of the time harmonics (a consequence of the non-linear power converter effects). The effects of the inverter supply harmonics were included by tuning the saturation model. All the time harmonic components in the winding current (which are due to the saturation effects and non-linearity of the power converter) can be matched to the experimental measurements. However, supply harmonics will affect the winding current harmonic content, the air gap field and consequently the torque produced.

The control performance of the drive is still satisfactory even after an open circuit fault occurred while there is a path for the zero sequence component. Consequently, there is an unbalance in the amplitudes of the two remaining motor currents – they have two

different magnitudes. This is due to the existence of a negative sequence component in these currents. This is well predicted by the proposed model.

The negative sequence current component in the phase currents generates a torque component that opposes the developed torque of the machine. Therefore, for a given rotating speed and applied load, the presence of an open circuit fault results in an increased torque reference when compared to that of a healthy machine. In addition, this negative sequence component interacts with the fundamental stator flux and the third harmonic flux, thus giving rise to the appearance of an oscillatory component in the electromagnetic torque at double and fourth times the supply frequency. This is one of the indicators of the presence of the fault when analysing the torque signal.

As verified in this chapter, the developed simulation model describes accurately the behaviour of the induction machine drive with an open circuit fault. The simulation model presented in this work is fast, which produce a good compromise between the simulation time and modelling accuracy. It allows the evaluation of the operation of induction motors in the presence of space harmonics and saturation effects, as well as being able to test the robustness of different field oriented controlled drives under unbalanced conditions. Furthermore, the proposed model can give a better evaluation of torque pulsations since it can include both time and space harmonics. Moreover, it can save time and money by pointing out even a minor deficiency in any tested method for stator open circuit fault diagnosis or fault-tolerant operating strategy since the model provides a reliable test bench for evaluating the method before its application to a real drive system.

AN ON-LINE SCHEME FOR PHASE OPEN CIRCUIT FAULT DETECTION IN A DRIVE SYSTEM

5.1 INTRODUCTION

A novel scheme for phase open circuit fault detection designed specifically for a delta connected machine is presented in this chapter. During normal operating conditions, the motor phase currents contain triplen harmonics that circulate in the closed path formed by the delta winding connection. These components are not observed in the line current for the case of the healthy machine. For the case of a delta connected machine, when an open circuit occurs, the machine is transformed into a two phase star connected machine with access to the neutral point. As a result of the winding configuration, the triplen harmonics (third harmonic component) appear in the line currents since the system is not symmetrical. The presence of these components in the line currents contain information that can be used to detect which phase is open circuit. The presence of the open circuit will influence the distribution of the harmonics over the three line currents, especially for the case of the third harmonic component. This condition presents an opportunity to identify the location of the fault as a function of the estimated magnitude of the third harmonic component on the line current. The location of the open circuit is based on detecting a magnitude reduction for the third harmonic component of the current flowing to the motor's mid point connection. Based on this observation, an online algorithm is proposed to estimate the

third harmonic magnitude in the line current to identify the winding affected by the open circuit fault. This method could be embedded into the processing platform of the drive as a subroutine without extra cost (i.e. no extra hardware is required). Simulation and experimental tests were carried out to validate the proposed methods.

This chapter is structured as follows: Section 5.2 describes the theoretical foundation of the fault detection technique applied to a delta connected winding machine. The observation of third harmonic components in the stationary reference frame is presented in Section 5.3. The implementation of the online scheme for phase open circuit fault detection is discussed in section 5.4 which includes the online estimation of a DC value corresponding to the third harmonic component, the fault decision, and the fault identification. Section 5.5 describes the practical issues in the implementation of the proposed method. Finally, the chapter conclusions are presented in Section 5.6.

5.2 THEORETICAL FOUNDATION

A correct detection and identification of the winding affected by the open circuit is important since this determines the correct control action during post fault operation to keep the system working in an acceptable way during the fault. The effect of losing one phase in a star connected machine could be detected easily by observing the winding currents since the current will be zero for the faulty winding [19]. However, for the case of a delta connected machine the phase currents cannot be directly measured, due to the inaccessibility of the motor windings, or due to the connection in the terminal box that only allows the measurement of the line currents.

A delta connected induction machine has the triplen harmonic currents flowing in its windings during healthy operation. Under these conditions, the motor's primary flux path (through iron) is partially saturated causing the magnetising inductance to be nonlinear. The distortion harmonics of the magnetising current (the third is the major contributor) are caused by the nonlinear magnetising inductance and are essentially unaffected by all other inverter produced harmonics [121]. However, the motor phase currents contain a third harmonic component which is the predominant distortion component that circulates in the closed path formed by delta connection (see Fig.

5.1(a)). The characteristic of third harmonic current is a zero sequence component; this means that the third harmonic current does not appear in the line current in the healthy condition (Fig. 5.1(a)).

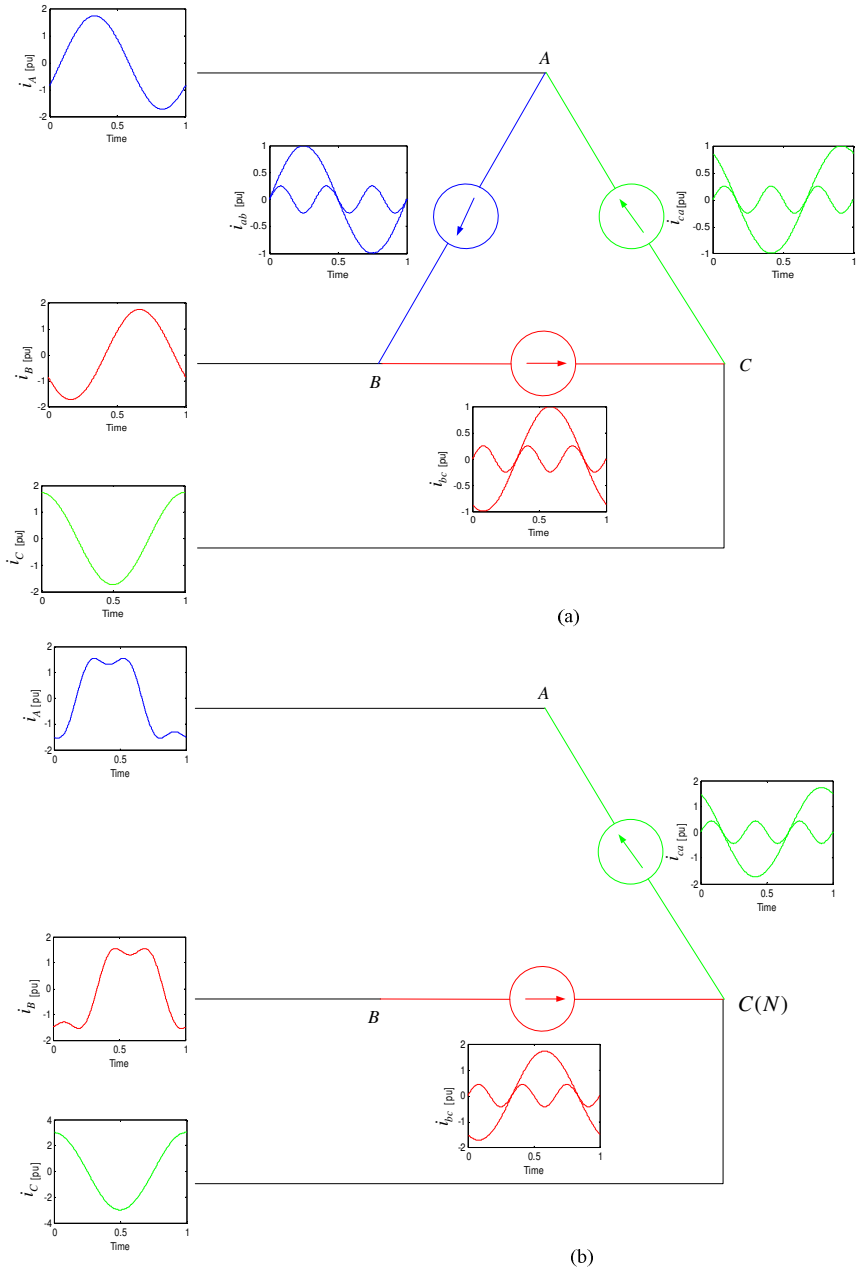

Fig. 5.1 The schematic diagram of delta connected machine considering the fundamental and third harmonic components in the phase and line connection. a) healthy condition, b) faulty condition when an open circuit fault occurs in phase *a*.

When an open circuit fault occurs in a delta-connected machine as shown in Fig. 5.1(b), the machine turns into a two-phase star connected system that has a connection to the windings mid point. Due to the unbalanced operating condition, the third harmonic current will not be a zero sequence component anymore, and therefore will not be canceled out in the line currents (see Fig. 5.1(b)). Another important observation in the remaining windings is the presence of a negative-sequence component in the supply currents [38]. The fundamental frequency reverse-rotating field (caused by the fundamental frequency voltage unbalance and the constructional asymmetry of the machine) interacts with the fundamental of the saturation that induced a specific permeance function to produce the large third harmonic current due to the presence of a matching pole pair associated with the third harmonic flux density component [82, 122]. As a result of the open circuit fault a strong third harmonic component is introduced in the supply currents of the motor which can be used as a clear indicator of the presence of winding fault. The presence of triplen harmonics in the machine currents could be used as primary feature to detect which is the winding affected by the open circuit fault.

5.3 DETECTION OF THE FAULT IN THE STATIONARY REFERENCE FRAME

The presence of an open circuit fault in one of the phases in a delta-connected machine results into a two-phase star connected machine where we have access to the neutral point. If the line currents measured during faulty operation are monitored and the frequency spectrum is obtained, the triplen harmonic frequencies will be clearly observed and will dominate the current distortion. The author proposes a scheme to detect and identify faults by using the triplen harmonic components observed in the line currents. This approach is described below.

When an open circuit fault appears, identification of the phase affected is important so that a fault tolerant control algorithm can be applied. Due to the imbalance introduced during the fault, the level of the triplen harmonics is increased. The location of the phase affected by the fault will determine the distribution of the harmonics observed over the three line currents of the machine. This is especially important for the third

order harmonic components. Note that under this condition, the magnitude of the triplen harmonics present in each of the three motor supply currents is different. Furthermore, it has been observed that the magnitude of the third harmonic component current which flows to the motor's mid point connection is always lower than the same harmonic of the other line currents. To verify this behaviour, a specially prepared machine with the ability to insert an open circuit fault in the winding between terminals A and B was used for the test (the machine was controlled using IRFO-VSI). Fig. 5.2 shows the experimentally measured line currents for the case of the machine operating first under healthy conditions and later, with an open circuit. Fig 5.3 shows the spectrum for the line currents during open winding fault operation. Note that under these conditions (after time = 5 sec), the harmonic distortion at triplen frequencies (third harmonic) change significantly those as shown in Fig. 5.2 (b). Note that in this case the lowest magnitude of the third harmonic component (Fig. 5.3) appears in the current flowing to the motor's mid point connection (terminal C). Therefore, once the lowest magnitude of the third harmonic component has been located, it will be easy to identify that phase affected by the open circuit, since the location of the faulted phase will be the winding that is placed in front of the neutral point as it is illustrated in Fig. 5.1(b).

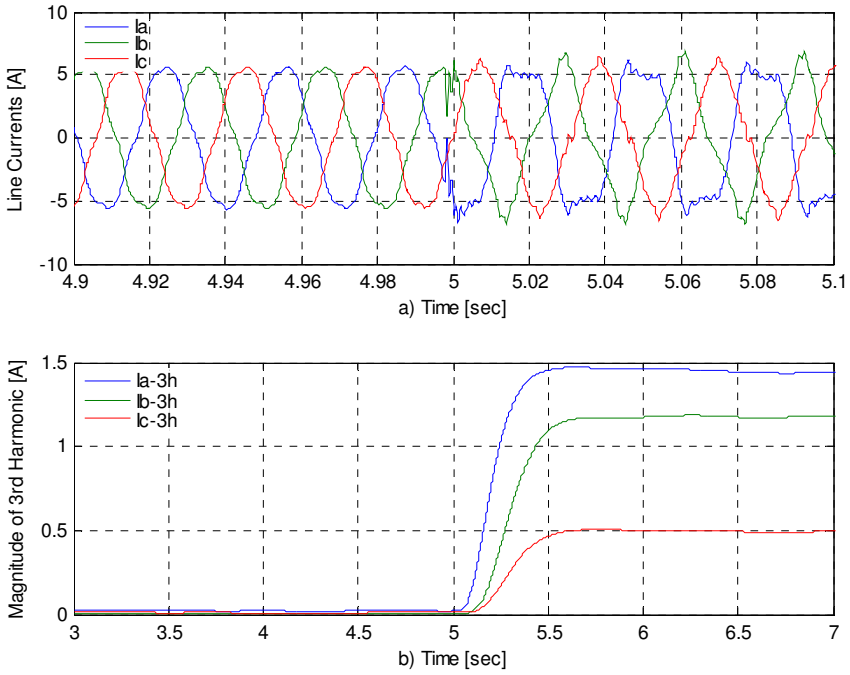

Fig. 5.2 Measured machine currents for the experimental system before and after an open circuit fault between terminals A to B. the machine is running at wr = 200 rad/sec, rated flux, at no load. a) terminal currents (line), b) magnitude for the 3rd order harmonic component.

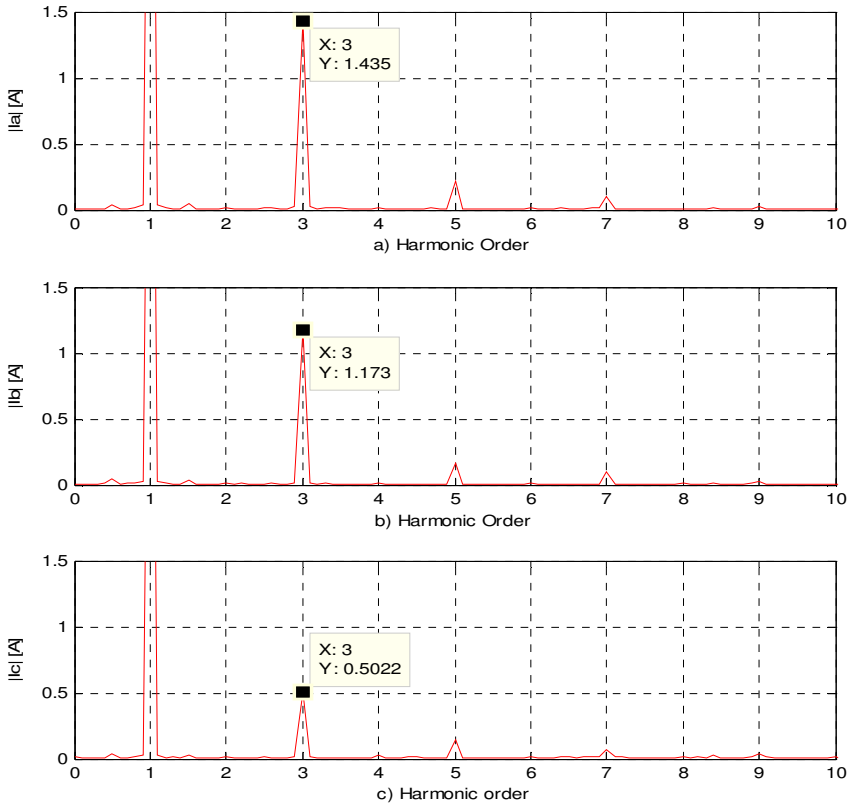

Fig. 5.3 Frequency spectrum of the terminal currents (line) for the case of an open circuit fault between terminals A and B, for no load (wr = 200 rad/sec) rated flux condition. a) Ia current, b) Ib current, c) Ic current.

5.4 IMPLEMENTATION OF THE PROPOSED APPROACH FOR THE PHASE DETECTION OF AN OPEN CIRCUIT FAULT

The fault diagnosis technique employed in this work is based on detecting the appearance of the third harmonic component in the line current. When this happens, the system should be able to identify the winding affected by the open circuit. The method proposed is explained in the next sections.

5.4.1 Estimation of the Magnitude of the Third Harmonic Component

The fault detection technique uses current measurements to calculate the magnitude of 3^{rd} order harmonic components in the line current. As 3^{rd} harmonic currents are the main variables, and they are usually zero sequence, their magnitude therefore cannot be estimated instantaneously [121]. The digital filtering necessary for the separation of

the magnitude of the third harmonic current from the overall stator current can be performed in several ways. Off-line fast Fourier transform (FFT) algorithms were used to obtain the experimental frequency spectrums shown in Fig. 5.3. It should be noted that FFT algorithms are not the best solution for real-time implementation. This is mainly due to their computational and memory requirements when processing large sequences of data. Note that for this application, only the frequency component at $3w_e$ is required. This section will present more appropriate alternatives for real-time implementations.

One approach is to observe the signals in a reference frame rotating at the speed of the particular harmonic component. Once the reference frame rotates at a certain frequency in either direction (clockwise or anti-clockwise), the space vector is decomposed into a stationary component and other components rotating in either direction. The proposed approach to on-line open circuit fault detection detects the third harmonic component in a reference frame rotating at the speed of the third harmonic component. This component will be observed as a DC component in the time domain, whereas other components rotating at a different speed appear as AC components. To extract the magnitude of the third harmonic component, it is assumed that the line stator current can be expressed as a summation of the fundamental component and its odd harmonics as in (5.1):

$$I(t) = |I_h|.\sin(w_e t) + |I_{3h}|.\sin(3w_e t + \phi_3) + |I_{5h}|.\sin(5w_e t + \phi_5) + |I_{7h}|.\sin(7w_e t + \phi_7) + .. \quad (5.1)$$

where $|I_h|, |I_{3h}|, |I_{5h}|$ and $|I_{7h}|$ are the magnitude of the 1st , 3rd , 5th , and 7th harmonic components respectively. While ϕ_3, ϕ_5 and ϕ_7 are the phase shift between the fundamental and 3rd, 5th, and 7th harmonic components respectively. The basic idea is to estimate the value of $|I_{3h}|$. The third harmonic component in the line current can be expressed as:

$$I_{3h}(t) = |I_{3h}|\sin(A) \quad (5.2)$$

where A is equal to $3w_e t + \phi_3$. The technique used in this work proposes a multiplication of the line current (5.1) by two terms: $\sin(B)$ and $\cos(B)$; where B is

equal to $3w_e t$ corresponding to the 3rd order component. For simplicity, in the following derivation only the 3rd order components are considered, other harmonics are ignored since they appear as an AC component (as described later). As a result of this technique, two equations are generated:

$$I_{3h}(t).\sin(B) = |I_{3h}|\sin(A).\sin(B) \tag{5.3}$$

$$I_{3h}(t).\cos(B) = |I_{3h}|\sin(A).\cos(B) \tag{5.4}$$

Multiplying (5.3) and (5.4) by two, and using the two common trigonometric operations we get:

$$2\sin(A)\cos(B) = \sin(A+B)+\sin(A-B) \tag{5.5}$$

$$2\sin(A)\sin(B) = \cos(A-B)-\cos(A+B) \tag{5.6}$$

Then (5.3) and (5.4) can be rearranged and written as:

$$2.I_{3h}(t).\sin(B) = |I_{3h}|(\sin(A+B)+\sin(A-B)) \tag{5.7}$$

$$2.I_{3h}(t).\cos(B) = |I_{3h}|(\cos(A-B)-\cos(A+B)) \tag{5.8}$$

Once (5.7) and (5.8) are implemented, a second order low pass filter (LPF) is used to extract the DC component and to filter out all the remaining AC components (i.e. $\sin(A+B)$ and $\cos(A+B)$). After the AC components have been eliminated, (5.7) and (5.8) can be rewritten as:

$$2.I_{3h}(t).\sin(B) = |I_{3h}|.\sin(A-B) \tag{5.9}$$

$$2.I_{3h}(t).\cos(B) = |I_{3h}|.\cos(A-B) \tag{5.10}$$

Ideally A - B is supposed to be zero, but this is true only if the phase shift between the 3rd order component and the two-terms that are multiplied by the line current in (5.3) and (5.4) are equal to zero ($\phi_3 = 0$). A different trigonometric operation is used as follows:

$$|I_{3h}| = \sqrt{\left(|I_{3h}|.\sin(A-B)\right)^2 + \left(|I_{3h}|.\cos(A-B)\right)^2} \tag{5.11}$$

$$= |I_{3h}|.\sqrt{\left(\sin(A-B)\right)^2 + \left(\cos(A-B)\right)^2} = |I_{3h}|$$

In this case, the DC component can easily be extracted. Fig. 5.4 shows the schematic diagram of the approach used to calculate the instantaneous value of the DC value of the 3rd harmonic component in each line current.

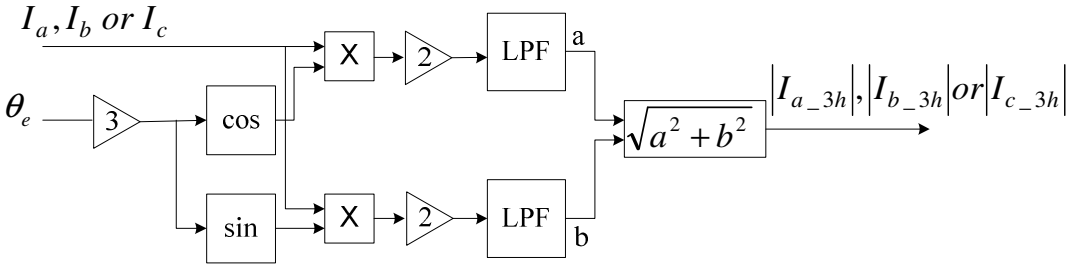

Fig. 5.4 Schematic diagram of the proposed approach to estimate the DC value of the third harmonic component of the line current.

When the third harmonic component has been estimated, a low pass filter (LPF) is used to extract the DC component, and to filter-out the AC components. In order to increase the accuracy of extraction, the cut-off frequency of the LPF should be adjusted as a function of the synchronous frequency, particularly during extremely low speeds. In this work the cut of frequency of the LPF is been fixed to 10Hz.

5.4.2 Fault Decision

Once the three DC values of the third harmonic component of the line currents have been estimated, the location of the open circuit fault can be detected. This is performed by analysing each DC value carefully in order to observe which current excess the preset fault threshold value (*Fault_thr*). The sensitivity of the proposed detection approach is strongly depended on the setting of parameter *Fault_thr*. If *Fault_thr* is selected tightly, then the detection will be very sensitive. When parameter *Fault_thr* is selected with a very wide range, then the accuracy of detection will be undermined. It can also be inferred that the appearance of the third harmonic component in the line

currents for a delta-connected machine is not dependent on the open circuit fault alone. It can also appear when there is inherent asymmetry in the machine, which is related to other types of stator fault e.g. the case of having unbalance in the voltage supply. For these reasons parameter *Fault_thr* should be selected and tuned carefully to prevent generating a false alarm. The limitations of proposed fault detection method are discussed in Section 5.5.

5.4.3 Fault Identification

After the presence of a fault has been detected, its location in the stator winding is performed by comparing the levels of the DC values of the third harmonic component for the three line currents. Once the lowest component has been located, it will be easy to identify the fault location. For example, when an open circuit fault occurs in the winding between terminals A and B as illustrated in Figs. 5.2 and 5.3, the lowest magnitude of the third harmonic component is observed in the current flowing to terminal C. This property is utilised to identify the location of the faulty winding in the machine and is valid for the other windings, for example, if an open circuit happed between terminals B and C the lowest magnitude of the third harmonic component will be observed in the current flowing to terminal A, and if the fault happens between terminal C and A the lowest component will be in the current flowing to terminal B. Therefore, the location of the faulted phase will be the winding that is placed in front of the neutral point.

The DC values of the third harmonic current components are compared with each other to assign the lowest value. The output of the threshold detection along with the location of the lowest DC value of the third harmonic were treated as a signature of the open winding fault in the delta connected machine. This signature is coded by 2 digits as illustrated in Table 5.1. For each phase, two digits are used; one is to represent the result of comparing the level of the DC value of the third harmonic component with the preset detection threshold, the other represents the location of the lowest third harmonic component. The localisation of a faulty winding is performed by comparing the actual signature with the reference signatures as listed in Table 5.1. After the fault

has been located and identified, the reconfiguration scheme of the fault tolerant controller can be achieved as will be discussed in Section 6.4.

Table 5.1 The diagnostic signatures for open circuit-winding-faults and their relationship to the DC values of the third harmonic components, which depend on the location of the fault

Relationship between the third harmonic current component	**Sine of DC values**	**Fault signature**	**Fault location**
I_{a_3h} or I_{b_3h} or I_{c_3h} > Fault_thr	$I_{c\_3h} < (I_{a\_3h}$ and $I_{b\_3h})$	1 1	Phase *a*
	$I_{a\_3h} < (I_{b\_3h}$ and $I_{c\_3h})$	1 2	Phase *b*
	$I_{b\_3h} < (I_{a\_3h}$ and $I_{c\_3h})$	1 3	Phase *c*
I_{a_3h} or I_{b_3h} or I_{c_3h} < Fault_thr	-	0 0	No fault

Threshold exceeded? (0 – No, 1 – yes)
Sign (0 – No fault, 1 – *a,* 2 – *b*, 3 – *c*)

5.5 LIMITATIONS AND PRACTICAL ISSUES

The main advantages of the proposed fault detection scheme were explained in the previous section; however there are several issues that need to be considered to enhance the performance of the approach for practical implementation. These issues are discussed in the next sections.

5.5.1 Imbalance in the Machine Winding

Imbalances in the windings of AC machines always exist, even for the case of healthy machines [37]. Such imbalances are usually caused by the discrete nature of the stator windings and the manufacturing process. One of the consequences of those inherent asymmetries is the unbalance of the three motor supply currents, which means that even for the case of a healthy motor the supply currents contain a negative-sequence component [38]. The fundamental frequency reverse-rotating field interacts with the fundamental of the saturation-induced specific permeance function to produce a third harmonic current due to the presence of a matching pole pair associated with the third harmonic flux density component [82, 122]. In this case the inherent asymmetries of

the motor may lead to the appearance of the third harmonic component in the supply currents, even when no faults are present in the motor. Furthermore, once the machine is assembled, the imbalance is expected to remain unchanged [37] and it usually does not give a large third harmonic component in the line currents. The third harmonic can be measured during a commissioning process when the machine is first operated. The fault detection algorithm could then be modified to measure not the absolute value of the third harmonic component of the line current but the relative changes. While such a modification would require only minimal changes to the detection algorithm, the fact that a commissioning process is required for each new machine adds processing requirements.

5.5.2 Limitation of the Transient Performance

Non-stationary operation results in fluctuations in the torque reference and speed which consequently generate fluctuations in the voltage references and the line currents. When non-stationary operation occurs with a rapid change in the torque or speed reference, the voltage references change rapidly, as do the line currents. Under fast transients, the machine accelerates from stand still operation condition to the demanded speed. This means that the proposed fault detection method that depended on the estimated magnitude of the third harmonic component of the line current may be influenced by the current fluctuation. The effect of the current limit of the speed controller and the regulation performance of the current controllers, such as overshoot in the current references and actual currents affect the way the machine currents are observed, especially during transients. Therefore, the proposed scheme may be unreliable under varying operating conditions, notably under fast transients. The main problem is the tendency to issue false alarms, which results from misinterpreting the transient current evolutions as a large magnitude of the third harmonic components. However, for the case when a small amount of fluctuation occurs during a non-stationary operation such as applying a load while the machine rotating at constant speed, the resultant fluctuation of the line currents and the changing frequency will be small; therefore the estimation technique will not be greatly affected and will effectively estimate the actual magnitude of the third harmonic component. This is due to the fact that the proposed estimation technique mainly depends on the estimated

electrical position θ_e using IRFO control (A.18). To overcome this problem, a control signal is adapted to activate the fault detection after the machine has reached a steady state condition. When a speed demand is applied, the machine is accelerated from a stand still to the desired speed reference. In this case, the control system will work without activating the fault detection technique. Once the measured speed reaches the speed reference, the line current will be settled down to their steady state value. In this case, the estimation technique of the third harmonic will produce reliable results.

The numerical value for the *activation_control* signal depends on the measured rotor speed. Initially, this variable is set to zero by a default; and the change of speed will be compared with the preset threshold value. If the change of measured speed is smaller than the threshed value, the *activation_control* will set to one, and the fault detection technique will be activated. This operation will be applied only once the machine has accelerated from the stand still condition; otherwise the fault detection algorithm is working online and observing the third harmonic component in the line current to detect the fault.

5.6 CONCLUSION

A new online detection method to detect and locate a stator open circuit fault by measuring the third harmonic component of the line currents of VSI conventional drive has been presented. In essence, the approach lies in the use of the magnitude of the third harmonic component current as a main diagnostic variable. The presence of a strong third harmonic component in the machine line currents is used as an indicator of an open circuit stator winding fault. With the measurement of this harmonic magnitude component, an approach was implemented which can effectively detect the presence of an open circuit fault once it is developed. The fault location is identified based on the lowest third harmonic component of the line current which appears always at the current flowing to the motor's neutral winding connection.

Note that inherent asymmetry may cause an unbalance in the three motor supply currents. As a consequence of this, the third harmonic component will be observed in the spectrum of the machine currents even during the absence of any stator fault. As a

result of this, the use of third harmonic component in the line current for the diagnosis of open circuit fault in IRFO induction motor drives is recommended only when it is not expectable on high degree of inherent asymmetry of the machine. Practical issues in the implementation of the proposed method have been discussed.

The technique can be easily implemented in standard IRFO vector control AC drives, with no additional hardware requirements. Only a small additional processing capability is requiring to implement the identification approach. Validation of the proposed method through simulations and experiments is provided in Section 7.2.

FAULT TOLERANT OPERATION OF AN INDUCTION MACHINE DRIVE

6.1 INTRODUCTION

In the previous chapter, a simple on-line open circuit fault detection method for an Induction machine drive was proposed. It is recognized in this work that an induction machine drive in a safety critical application does not only require a reliable open circuit fault detection method, but it also requires a proper remedial action that can maintain the drive in operation for certain amount of time until a corrective action can be provided.

A novel control algorithm for a fault tolerant induction machine drive is proposed in this chapter. It describes the development of an alternative fault control strategy specifically designed for a delta connected machine suddenly affected with an open circuit winding fault. The fault ride through is achieved without modification to either the power converter or the motor circuit. In fact, the proposed approach is also applicable to a fault tolerant drive containing an extra inverter leg connected to the neutral point of a star-connected machine. A novel feedforward compensation algorithm is introduced for the zero sequence component of the *dqo* reference voltages which considerably reduces the current and the torque ripple in the faulted drive. Two methods for controlling the neutral-point voltage are presented so that the available voltage capacity of the inverter is maximized in both, the normal and the fault mode. If the machine's "neutral point" voltage can be modulated, then a

reasonably high speed demand can be achieved before field-weakening control is required. Note that during high-speed operation the demand voltages of the current controller will normally exceed the available inverter voltage and a field-weakening controller must be adopted by controlling the flux current reference (i_{sd}^{*}) to prevent the inverter saturation [109]. The main idea of the proposed strategy is to try to reduce the stator voltage applied to the machine by reducing the magnetic flux while trying to maintain the required torque and speed by maintaining the required power. Since the machine is fed from an asymmetrical supply during a fault, the control algorithms need to be modified accordingly. Two different methods for field weakening control are presented in this chapter. The first method is an open loop field weakening controller using a conventional method. The second method is a new closed loop field weakening controller that relies on the inverter voltage references and the maximum output voltage of the inverter so that the available voltage capacity is maximized in both the normal and the fault mode. This chapter describes how a field-weakening controller needs to be modified in order to operate properly at high speed. The theoretical foundations of the strategy will be provided, and the validation of the strategy is carried out in Chapter 7.

This chapter is structured as follows: Section 6.2 describes and analyses the fault tolerant drive configurations. The fault tolerant control algorithm is presented in Section 6.3, which includes the derivation of the required motor currents and the feedforward strategy for operation with an open circuit fault. The implementation of the feedforward strategy for operation with an open circuit fault in a voltage-fed vector controlled drive is discussed in Section 6.4. Two methods for controlling the neutral point voltage and the two field weakening controllers are presented to extend the speed range operation in presence of the fault. Finally, chapter conclusions are contained in Section 6.5.

6.2 FAULT TOLERANT DRIVE CONFIGURATION

The main aim of fault tolerant drive system is to continue the operation of the drive in a satisfactory way in the presence of a fault. This means that control and a minimum

level of performance should be kept after a fault occurs. It should be noted that when operating with a fault, the system efficiency is typically reduced. Since operation with a fault represents an abnormal condition, the system efficiency is a secondary concern as long as the system is thermally able to accommodate the increased losses safely. Those additional losses during post-fault operation are typically modest and dependent on the selected topology [14].

A star connected 3-phase machine without a neutral connection effectively becomes a single phase machine when a phase open circuit occurs. It is clear that under this condition the machine cannot produce a smooth rotating MMF [16], and large torque pulsations will be produced at a twice the electrical frequency due to the presence of a large negative sequence component in the stator current [50]. If the neutral point of the machine is connected directly to the midpoint of the DC link [16], or to a fourth leg of an inverter [17-19] as shown in Figs. 6.1 and 6.2, then the stator currents can be controlled to produce a dominant rotating magnetic field that can emulate the normal operation of a healthy machine.

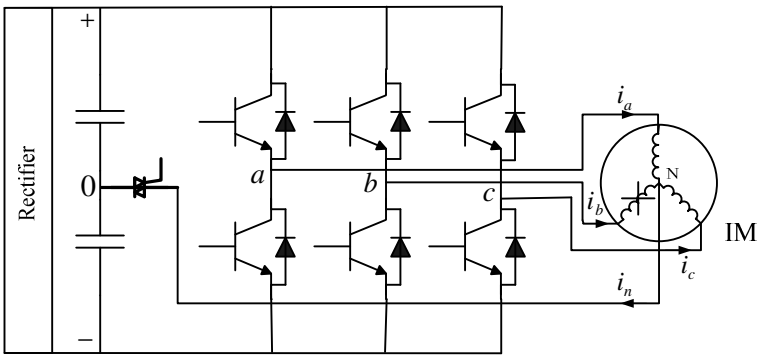

Fig. 6.1 Fault tolerant scheme based on the stator neutral point connected to the midpoint of the DC link.

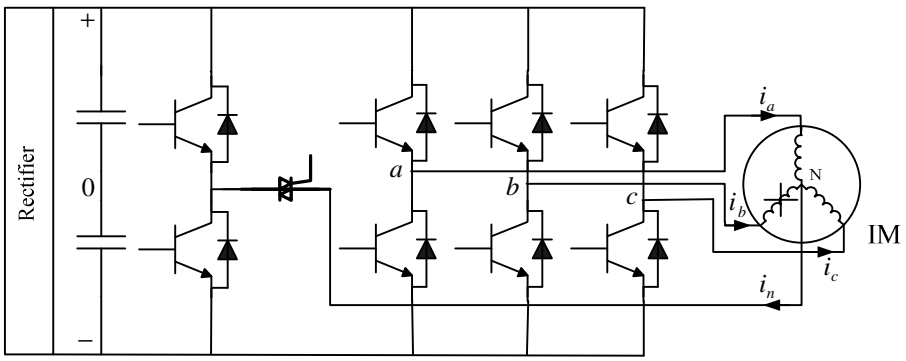

Fig. 6.2 Fault tolerant scheme based on the stator neutral point connected to a fourth inverter leg.

When the system detects an opened phase fault as in Fig. 6.1, the neutral point of the windings will be connected to the midpoint of the DC link capacitors by firing the TRIAC element so a path for zero sequence current can be provided. Since the faulted phase is disconnected, the two remaining healthy phase currents need to be shifted 30^o away from the axis of the faulted phase, and the amplitude of these current should be increased by $\sqrt{3}$ compared to the pre-faulted value in order to maintain the same torque level observed during healthy conditions [16]. This means that the same MMF (observed during healthy operation) will be kept when operating with a fault. Note that the increased value in the currents will be observed as a non-torque producing zero sequence current which achieves a constant flux trajectory and ensures a disturbance free operation of the system [14, 16]. A limited amount of control can be achieved here; however there is a significant limitation on the maximum available DC link voltage that can be applied to the machine which restricts motor line voltage and the operating range of the motor considerably. Note that the maximum phase voltage can be applied is limited to ±1/2 of the DC link voltage. As a result of the increase in the line currents ($\sqrt{3}$ times higher than the ones obtained during pre-fault operation) the semiconductor rated current needs to be increased by $\sqrt{3}$ times of the value used for the normal condition. Unfortunately, this approach also provides a path for 3^{rd} harmonic current which can lead to additional torque pulsations. In order to overcome this problem, [17-19] used a different topology based on the connection of the winding neutral point to an additional inverter leg as shown in Fig. 6.2. By implementing a

suitable control strategy for the additional leg, the available DC link voltage of the inverter during faulty operation is similar to that produced by a healthy system. In this way, the drive can supply the same speed and torque ranges as those observed before the fault. However, the drive voltage limits under operation with a fault may differ from those of healthy operation since the behaviour of the drive is also effected by the capability of the inverter in delivering zero-sequence voltage (as extra voltage). As a consequence of this a reduction in the speed and torque ranges produced during faulty operation can be observed respect to those produced in healthy condition. This will be discussed in the following sections. The topology of Fig. 6.2 has significant advantages with respect to that of Fig. 6.1 [16]. Since this scheme can improve the reliability of a standard three phase induction motor drive [19], by increasing the voltage capability of the inverter. One main advantage is that a connection to the midpoint of the DC bus is not required which avoids problems related to voltage unbalance in the DC link capacitors [14]. Further, the scheme avoids voltage fluctuations across the DC link capacitors when the machine operates at low speed [17, 18]. In summary, in order to maintain a constant flux trajectory and the same torque level observed during healthy conditions, the magnitude of the two remaining healthy phases need to be increased by a factor of $\sqrt{3}$ with a phase shift of 60^{o} between them should be applied in the presence of the open circuit fault. Note that the neutral leg in this fault tolerant scheme will carry 3 times the phase current [17].

For the particular case of a delta-connected machine, an open circuit fault in one of the phases turns the machine into a two-phase system that has a connection to the motor mid point as shown in Fig. 6.3. This has a similar configuration to that in Fig. 6.2. The inverter drive configuration does not need to be modified and the path for the zero sequence component is provided to develop an undisturbed rotating MMF even with one phase open circuit. In this case, the inverter is capable of applying ±1/2 of the DC link voltage across each of its terminals continuously for pre-fault and post-fault operation. Regarding the machine side for the case of the faulty condition, the winding current needs to be increased by $\sqrt{3}$ compared to the value under healthy conditions in order to maintain the same torque. In this case when an open circuit fault occurs, the phase currents passing through the remaining healthy windings are the line currents, while the inverter is still delivering the same current through its terminals. To keep the

system working efficiently at rated torque with one phase open circuit, the system needs to be thermally able to accommodate the increased losses due to the increment in the current magnitude. In this case, a compromise has to be made as to whether to limit the operation at a lower torque with nominal currents, or operation at full torque with a higher current. However, in this case there could be a reduction in the speed and torque ranges produced when operating with a fault compared to that produced during the healthy condition.

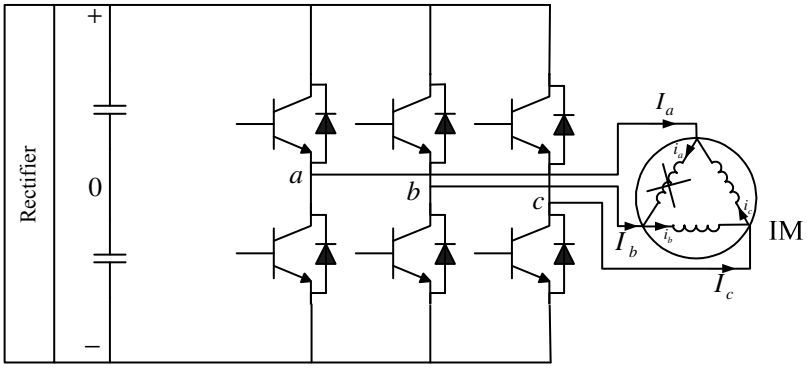

Fig. 6.3 Fault tolerant scheme for a delta connected machine with open circuit fault in Phase *a.*

6.3 FAULT TOLERANT CONTROL ALGORITHM

The fault tolerant schemes described in this work are applied specifically to a delta-connected machine fed from a standard three-leg inverter. However, the presented scheme is equally applicable to a drive with an extra inverter leg connected to the winding neutral point of a star connected machine.

The connection of the winding neutral point to the midpoint of the DC link provides a reduction in the size of the negative sequence current without any additional control [50]. For example, if a conventional vector control scheme is employed, the flux and speed controllers provide reference values for the flux and torque which produce currents i_{sd} and i_{sq} in a rotating dq frame of reference aligned with the rotor flux vector [123]. The usual assumption here is the use of a stationary to rotating reference frame transformation that neglects the zero sequence components (which are zero

under healthy and balanced conditions). When an open circuit fault occurs, the drive controllers react as they are still controlling a healthy system. As a consequence of this an adequate control of the negative and zero sequence components in the current is not possible, and the remaining currents in the two healthy phases have different amplitudes. Although the machine will produce a torque which has significantly less ripple and is able to start, the produced torque will contain considerable components at $2f_e$ and $4f_e$. The latter is due to the presence of saturation induced 3rd harmonic order in the phase currents which do not now cancel due to the unbalance of the system.

An alternate approach proposed for a machine fed from a **current controlled inverter** (i.e. a drive fed using a hysteresis controller rather than PWM) [16] suggests that the two remaining phase currents should be phase shifted by 30^o away from the faulty phase, and their magnitude should be increased by a factor of $\sqrt{3}$. This enlarged amplitude is necessary for delivering the same torque as in the healthy condition, while torque ripple is reduced by modifying the phase displacement. This has the effect of removing the negative sequence components in the current. Reference [16] demonstrated successful the drive operation in the presence of an open circuit fault. The speed range was significantly reduced compared to the healthy condition, and there can be significant ripple introduced onto the DC link midpoint voltage due to this neutral current. By connecting the star point to a fourth inverter leg a higher voltage capability for each faulted phase, as is provided demonstrated for a PM machine in [17, 18, 109].

6.3.1 Derivation of the Required Motor Currents for Operation with an Open Circuit Fault

This section introduces a fault tolerant strategy for a voltage fed vector controlled induction motor based on the approach suggested for permanent magnet machines [18]. A useful starting point for the derivation is to determine the desired machine currents for improved operation when an open circuit fault occurs, and then determine the required voltages for correct steady state operation. The following analysis considers an open circuit failure in phase *a*. A similar analysis can be performed for open circuit faults in phases *b* or *c*. The same basic control structure is assumed for

operation with and without a fault. When a fault occurs, it must be detected and located as it was discussed in the previous chapter. For a star connected machine, the star point of the motor is connected directly to a modulated fourth leg of the inverter, as that shown in Fig. 6.2. While for delta connected machine, the fault turns it into a two phase machine that has a connection to the neutral point as that shown in Fig. 6.3. The currents in the two remaining healthy phases must then be controlled to produce the same flux and torque levels in the machine as before the fault occurred. This means that the references for the current controllers (expressed in a synchronous *d-q* rotating frame) and the positive sequence currents in the stationary *α-β* reference frame should not be changed for steady state operation with or without an open circuit fault, and the negative sequence currents should be suppressed to eliminate torque pulsation. For a vector controlled drive, the flux and torque producing currents (i_{sd} and i_{sq}) are related to the *α-β-o* components by [65]:

$$\begin{bmatrix} i_{sd} \\ i_{sq} \\ i_o \end{bmatrix} = \begin{bmatrix} \cos(\theta_e) & \sin(\theta_e) & 0 \\ -\sin(\theta_e) & \cos(\theta_e) & 0 \\ 0 & 0 & 1 \end{bmatrix} \begin{bmatrix} i_\alpha \\ i_\beta \\ i_o \end{bmatrix} \tag{6.1}$$

where θ_e is the instantaneous angle of the reference frame, and i_o is the zero sequence component. The stationary frame *abc* variables are determined from the stationary frame *α-β* variables by using the following transforming equation [65]:

$$\begin{bmatrix} i_a \\ i_b \\ i_c \end{bmatrix} = \frac{2}{3} \begin{bmatrix} 1 & 0 & 1 \\ -\frac{1}{2} & \frac{\sqrt{3}}{2} & 1 \\ -\frac{1}{2} & -\frac{\sqrt{3}}{2} & 1 \end{bmatrix} \begin{bmatrix} i_\alpha \\ i_\beta \\ i_o \end{bmatrix} \tag{6.2}$$

By adopting the inverse of transformation (6.1) and using (6.2) [65], and assuming that a fast current control matches the machine currents to their references, the phase currents in the *abc* frame can be written as a function of the *d-q* current references for the healthy condition:

$$i_a = \frac{2}{3} i_{sd}^* \cos(\theta_e) - \frac{2}{3} i_{sq}^* \sin(\theta_e) \tag{6.3}$$

$$i_b = \frac{2}{3} i_{sd}^* \cos\left(\theta_e - \frac{2\pi}{3}\right) - \frac{2}{3} i_{sq}^* \sin\left(\theta_e - \frac{2\pi}{3}\right) \tag{6.4}$$

$$i_c = \frac{2}{3} i_{sd}^* \cos\left(\theta_e - \frac{4\pi}{3}\right) - \frac{2}{3} i_{sq}^* \sin\left(\theta_e - \frac{4\pi}{3}\right) \tag{6.5}$$

$$i_o = 0 \tag{6.6}$$

By adopting the inverse of transformation of (6.2), the zero sequence component of the stator current can be calculated as:

$$i_o = \frac{1}{2}(i_a + i_b + i_c) = \frac{1}{2} i_n \tag{6.7}$$

The neutral or star point current is defined in (6.8) under healthy operating conditions and is also equal zero:

$$i_n = i_a + i_b + i_c \tag{6.8}$$

When an open circuit fault occurs in phase *a*, then clearly (6.3 - 6.6) will change. As $i_a=0$, a zero sequence component will appear. If the *d-q* current components are to remain the same (i.e. the required torque and flux levels should remain the same) after the fault occurs, then, according to (6.1), the *α-β* current components before and after the fault must be the same. If $i_a=0$, then from (6.2):

$$i_o = -i_\alpha \tag{6.9}$$

and the remaining phase currents can be calculated from (6.2) as:

$$i_b = -i_\alpha + \frac{1}{\sqrt{3}} i_\beta \tag{6.10}$$

$$i_c = -i_\alpha - \frac{1}{\sqrt{3}} i_\beta \tag{6.11}$$

However, if the control method for improved operation during an open circuit fault has imposed (6.9) on the machine, so that the same *dq* and *αβ* current components continue to flow after the fault, the zero sequence current, calculated from (6.9) and the inverse of (6.1) becomes:

$$i_o = -i_\alpha = [i_{sq}^* \sin(\theta_e) - i_{sd}^* \cos(\theta_e)] \tag{6.12}$$

As a result, the reference neutral current for operation with a fault can be calculated by substituting (6.12) in (6.7) to give:

$$i_n = 2.[i_{sq}^* \sin(\theta_e) - i_{sd}^* \cos(\theta_e)] \tag{6.13}$$

By including (6.12) in (6.1) and (6.2), the desired phase current references for the faulted machine can be derived in terms of the i_{sdq}^{*} references:

$$i_a = 0 \tag{6.14}$$

$$i_b = \frac{2}{\sqrt{3}} i_{sd}^{*} \cos\left(\theta_e - \frac{5\pi}{6}\right) - \frac{2}{\sqrt{3}} i_{sq}^{*} \sin\left(\theta_e - \frac{5\pi}{6}\right) \tag{6.15}$$

$$i_c = \frac{2}{\sqrt{3}} i_{sd}^{*} \cos\left(\theta_e - \frac{7\pi}{6}\right) - \frac{2}{\sqrt{3}} i_{sq}^{*} \sin\left(\theta_e - \frac{7\pi}{6}\right) \tag{6.16}$$

By comparing the phase currents for a healthy machine (6.3 - 6.6) with (6.14 - 6.16), it can be seen that for operation with an open circuit in phase *a*, the two remaining phase currents are phase shifted 30^{o} away from the faulted phase and their magnitude increased by a factor of $\sqrt{3}$. It is important to emphasize that there are now no negative sequence components in the stator current as illustrated below.

The negative sequence component can be calculated by using the symmetrical component method [124];

$$\begin{bmatrix} i_{pos} \\ i_{neg} \\ i_{zer} \end{bmatrix} = \frac{1}{3} \begin{bmatrix} 1 & a & a^2 \\ 1 & a^2 & a \\ 1 & 1 & 1 \end{bmatrix} \begin{bmatrix} i_a \\ i_b \\ i_c \end{bmatrix} \tag{6.17}$$

where $a = 1e^{j\frac{2\pi}{3}} = -\frac{1}{2} + j\frac{\sqrt{3}}{2}$ and $a^2 = 1e^{j\frac{4\pi}{3}} = -\frac{1}{2} - j\frac{\sqrt{3}}{2}$. By substituting (6.14 – 6.16) in (6.17) and simplifying the equation by using the trigonometric operation, the negative sequence component can be calculated as:

$$i_{neg} = \frac{1}{3}\left(-i_{sq}^{*}\sin(\theta_e) + i_{sd}^{*}\cos(\theta_e) - ji_{sq}^{*}\cos(\theta_e) - ji_{sd}^{*}\sin(\theta_e)\right) = 0 \tag{6.18}$$

Therefore the pulsating torque is eliminated and the drive can produce a smooth torque with one phase open circuit, the same conclusion as [16] but obtained in a different way. The trade off is that the phase rms current for the remaining healthy phases is increased, and a more complicated controller is required. If a current source converter were used (using current hysteresis control [16]), then the elimination of negative sequence current components and reduction of torque ripple could be achieved in the presence of an open circuit fault by using (6.14 – 6.16) as the reference currents for the

healthy phases. However, most motor drives use PWM voltage source inverters employing voltage references, and therefore the following section shows how the same performance can be achieved from such systems.

6.3.2 Derivation of the Feedforward Strategy for Operation with an Open Circuit Fault

For a delta connected machine, the same basic control structure is assumed for operation with and without a fault. Under normal operating conditions, there is no neutral point and the zero sequence voltage equals zero. However, under fault conditions, the zero sequence voltage V_o is not equal zero and it needs to be controlled. This will be achieved through controlling the star point or neutral voltage V_n as shown in Fig. 6.4. This configuration is similar to the fault tolerant drive uses a forth inverter leg. When the fault occurs, the star point of the machine will be connected to a fourth leg by firing triac to allow a two independent stator currents controlled to produce a dominant rotating magnetic flux. Therefore, the fault tolerant schemes described in this section are equally applicable to both configurations. For steady state operation, the stator voltage motor equations can de derived in the *dqo* reference frame as [125]:

$$V_{sd} = r_s.i_{sd} - w_e \sigma L_s i_{sq} \tag{6.19}$$

$$V_{sq} = r_s.i_{sq} + w_e \sigma L_s i_{sd} + w_e \frac{L_m^2}{L_r} i_{sd} \tag{6.20}$$

$$V_n = r_s.i_n + L_{ls} \frac{di_n}{dt} \tag{6.21}$$

where r_s is the phase resistance; L_s, L_r, and L_m are the stator inductance, rotor inductance and magnetising inductance ($3L_{ms}/2$) respectively. L_{ls} is the stator leakage inductance; σ is the motor leakage factor, w_e is the angular velocity of the reference frame. V_{sd}, and V_{sq} are the direct and quadrature voltages. If the *d* and *q* axis currents are controlled accurately to match their references then (6.19) and (6.20) define the required *d* and *q* axis steady state voltages to achieve the flux and torque in both healthy and open circuit fault conditions. In (6.21), the derivative term must be

included during faulty steady state operation. This is because the neutral current i_n does not remain constant in the faulty operation condition.

The zero sequence voltage V_o is calculated using a similar method to (6.7):

$$V_n = 2.V_o \tag{6.22}$$

By substituting (6.22) and (6.12) into (6.21), V_o can be expressed by:

$$V_o = \frac{V_n}{2} = r_s\left(2i_{sq}^* \sin(\theta_e) - 2i_{sd}^* \cos(\theta_e)\right) + L_{ls}\frac{d}{dt}\left(2i_{sq}^* \sin(\theta_e) - 2i_{sd}^* \cos(\theta_e)\right) \tag{6.23}$$

The derivatives terms di_{sd}^* / dt and di_{sq}^* / dt are equal zero because i_{sd}^* and i_{sq}^* currents are constant values. As a result, V_o is equal to:

$$\mathrm{V_o} = \left(r_s i_{sq}^* + w_e L_{ls} i_{sd}^*\right)\sin(\theta_e) + \left(w_e L_{ls} i_{sq}^* - r_s i_{sd}^*\right)\cos(\theta_e) \tag{6.24}$$

Equation (6.24) defines the desired zero sequence voltage required in conjunction with V_{sd}, and V_{sq} of (6.19) and (6.20) to control the faulted machine to achieve the currents defined by (6.14 – 6.16); i.e. operation at a desired flux and torque with no torque pulsations.

In a similar way, if phase *b* is an open circuit, the desired zero sequence voltage V_o can be expressed by:

$$\begin{aligned} V_o = &\left(i_{sd}^*\left(-\frac{\sqrt{3}}{2}r_s - \frac{1}{2}L_{ls}w_e\right) - i_{sq}^*\left(\frac{1}{2}r_s - \frac{\sqrt{3}}{2}L_{ls}w_e\right)\right)\sin(\theta_e) \\ &+\left(i_{sd}^*\left(\frac{1}{2}r_s - \frac{\sqrt{3}}{2}L_{ls}w_e\right) - i_{sq}^*\left(\frac{\sqrt{3}}{2}r_s + \frac{1}{2}L_{ls}w_e\right)\right)\cos(\theta_e) \end{aligned} \tag{6.25}$$

While for the case of a fault in phase *c,* the desired zero sequence voltage V_o is expressed by:

$$\begin{aligned} V_o = &\left(i_{sd}^*\left(\frac{\sqrt{3}}{2}r_s - \frac{1}{2}L_{ls}w_e\right) - i_{sq}^*\left(\frac{1}{2}r_s + \frac{\sqrt{3}}{2}L_{ls}w_e\right)\right)\sin(\theta_e) \\ &+\left(i_{sd}^*\left(\frac{1}{2}r_s + \frac{\sqrt{3}}{2}L_{ls}w_e\right) + i_{sq}^*\left(\frac{\sqrt{3}}{2}r_s - \frac{1}{2}L_{ls}w_e\right)\right)\cos(\theta_e) \end{aligned} \tag{6.26}$$

Derivation of the zero sequence components of (6.25) and (6.26) are presented in Appendix G.

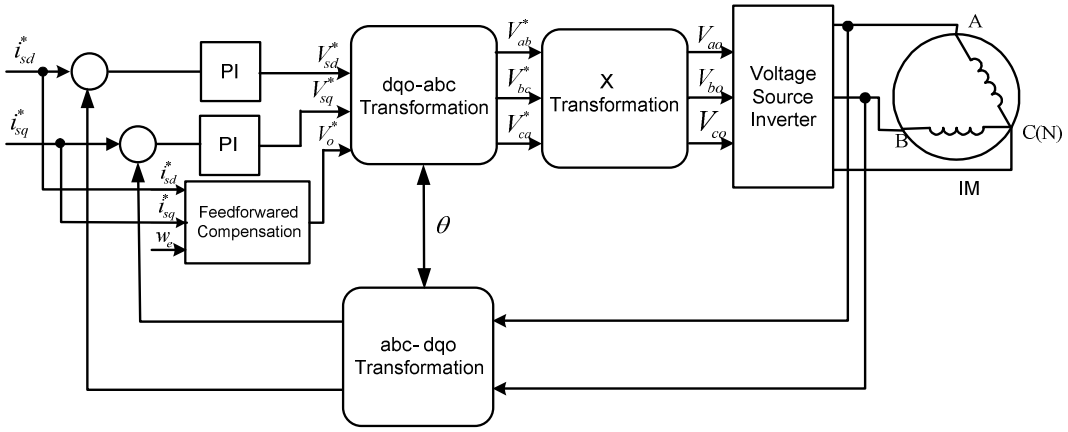

Fig. 6.4 Feedforward compensation with the PI control structure after a fault in phase *a*.

6.4 IMPLEMENTATION OF THE FEEDFORWARD STRATEGY FOR OPERATION WITH AN OPEN CIRCUIT FAULT

The fault tolerant voltage fed scheme is implemented as an extension of a standard vector control strategy for an induction motor. The general control scheme is shown in Fig. 6.4 which illustrates the specific case of a fault in phase *a*. Under both normal and faulty operation, the proportional plus integral controllers for *d* and *q* axis currents perform an accurate regulation with a bandwidth of 100Hz.

In the pre-fault condition for a delta connected machine, the output of the vector control system provides the line voltages demands. The transformation block X in Fig. 6.4 determines the PWM voltages demands with respect to the DC link midpoint, i.e. V_{ao}, V_{bo}, and V_{co}. These are $\sqrt{3}$ smaller than the line voltages and lag them by 30^o. The transformation X is therefore incorporates:

$$V_{ao} = \frac{(V_{ab}^* - V_{ca}^*)}{3} \tag{6.27}$$

$$V_{bo} = \frac{(V_{bc}^* - V_{ab}^*)}{3} \tag{6.28}$$

$$V_{co} = \frac{(V_{ca}^* - V_{bc}^*)}{3} \tag{6.29}$$

and the line to line voltage are calculated by:

$$V_{ab}^* = V_{ao} - V_{bo} \tag{6.30}$$

$$V_{bc}^* = V_{bo} - V_{co} \tag{6.31}$$

$$V_{ca}^* = V_{co} - V_{ao} \tag{6.32}$$

The phase currents can be calculated from the measured line currents as shown in Fig. 6.5(a):

$$i_{ab} = \frac{(I_a - I_b)}{3} \tag{6.33}$$

$$i_{bc} = \frac{(I_b - I_c)}{3} \tag{6.34}$$

$$i_{ca} = \frac{(I_c - I_a)}{3} \tag{6.35}$$

When an open circuit fault is detected and localized i.e. in phase *a*, the phase current will be constructed from the line currents as shown in Fig. 6.5(b) by:

$$i_{ab} = 0 \tag{6.36}$$

$$i_{bc} = I_b \tag{6.37}$$

$$i_{ca} = -I_a \tag{6.38}$$

In a similar way, if phase *b* is an open circuited, the phase current will be constructed from the line currents as shown in Fig. 6.5(c) by:

$$i_{ab} = -I_b \tag{6.39}$$

$$i_{bc} = 0 \tag{6.40}$$

$$i_{ca} = I_c \tag{6.41}$$

A similar situation is observed if phase *c* is an open circuit:

$$i_{ab} = I_a \tag{6.42}$$

$$i_{bc} = -I_c \tag{6.43}$$

$$i_{ca} = 0 \tag{6.44}$$

When the fault is detected in phase *a*, in this case the feedforward zero sequence voltage defined by (6.24) is introduced in the *dqo* reference frame. In a similar way if the fault is detected in phase *b*, the zero sequence voltage (6.25) is introduced in the reference frame. Finally, if a fault in phase *c* is detected, the zero sequence voltage defined by (6.26) is applied. A signal flow diagram of the zero sequence voltage calculation is shown in Fig. 6.6.

The following section discusses the two control schemes for the neutral point voltage using the transformation X in Fig. 6.4.

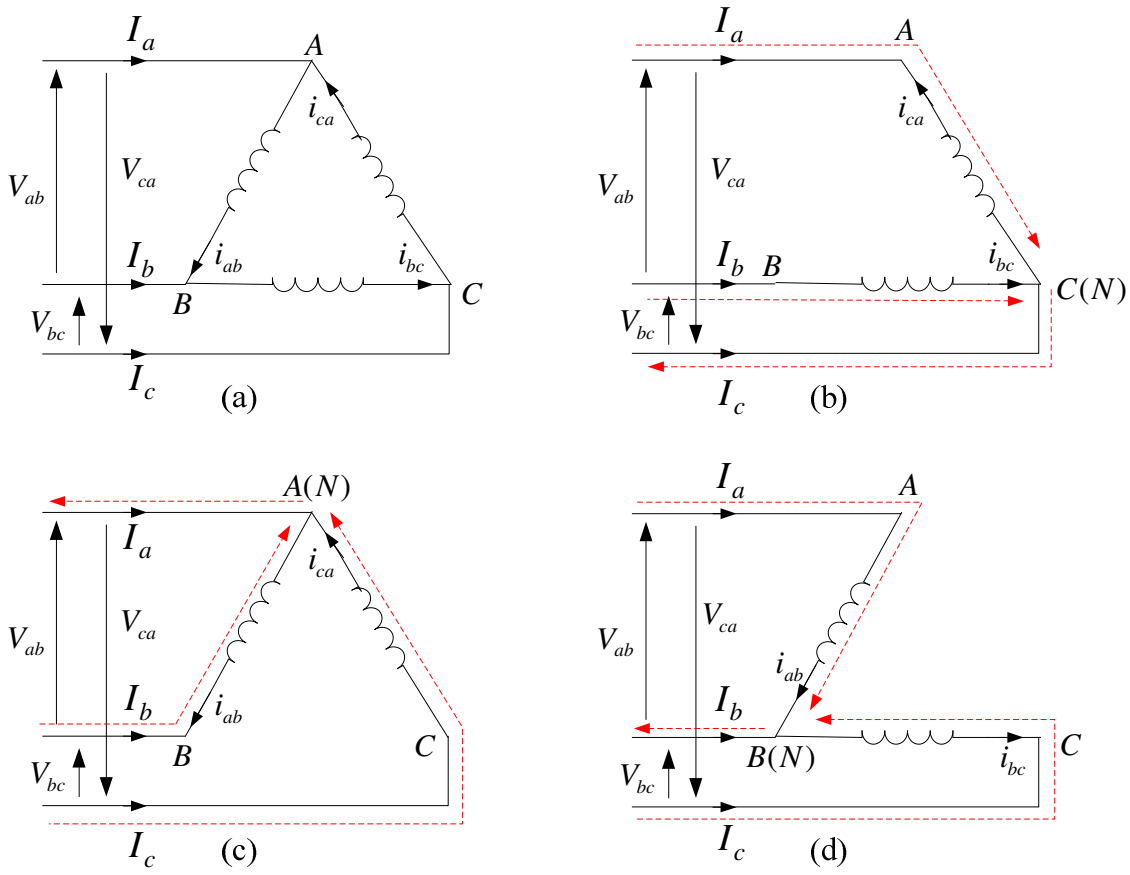

Fig. 6.5 Schematic diagram of delta connected machine: a) Pre-fault operation, b) open circuit fault in phase *a*, c) open circuit fault in phase *b*, d) open circuit fault in phase *c*. The red colour dashed line indicates the current direction during the faulty condition.

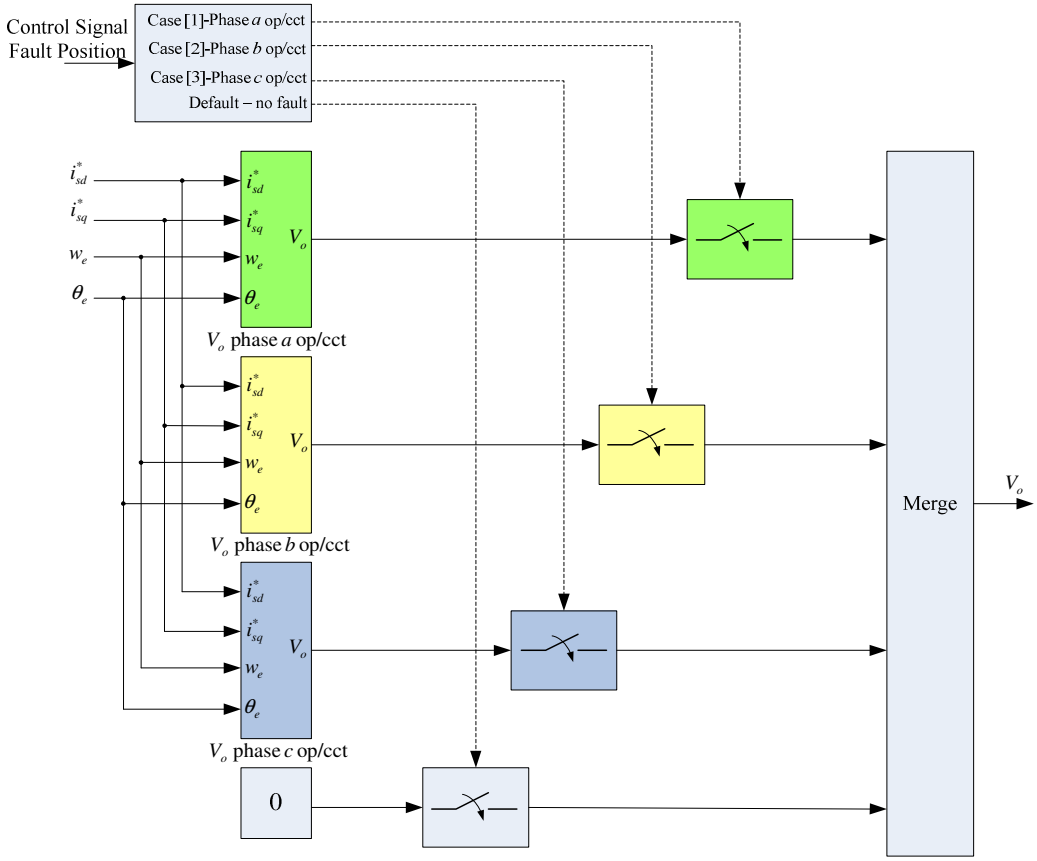

Fig. 6.6 Signal flow diagram of the zero sequence voltage calculation to overcome open circuit fault.

6.4.1 The Neutral Point Voltage Control Scheme

During faulty operation, the voltage of the neutral point V_n can be controlled in different ways. Since the open circuit fault occurs in one phase of a delta connected machine, the phase voltages in the remaining phases are asymmetric even during steady state. During this period the PWM voltage demands (with respect to the DC link midpoint from the current controllers) need to be modified from equation (6.27 – 6.29) in order to operate properly during the fault mode. This is achieved via the transformation block X in Fig. 6.4. For the inverter configuration shown in Fig. 6.3, two methods have been proposed to control the leg that connects to the neutral point which are described in the following sections.

6.4.1.1 Method I - Modulating the Neutral Point to Zero Voltage

The feature of this control is that the voltage of the leg that is connected to the neutral point (V_n) is controlled to be 0V. This is possible only if the configuration has the neutral point connected directly to the midpoint of the DC link, i.e. via thyristors or a triac [16]. When an open circuit fault occurs in phase *a* as shown in Fig. 6.5(b), *Method I* employs the following equations for the transformation X:

$$V_{ao} = -V_{ca}^{*} \tag{6.45}$$

$$V_{bo} = V_{bc}^{*} \tag{6.46}$$

$$V_{co} = 0 \tag{6.47}$$

For the case of an open circuit in phase *b* (Fig. 6.5(c)), the PWM voltages demands are calculated as:

$$V_{ao} = 0 \tag{6.48}$$

$$V_{bo} = -V_{ab}^{*} \tag{6.49}$$

$$V_{co} = V_{ca}^{*} \tag{6.50}$$

While for the case of a fault in phase *c*, the PWM voltage demands become:

$$V_{ao} = V_{ab}^{*} \tag{6.51}$$

$$V_{bo} = 0 \tag{6.52}$$

$$V_{co} = -V_{bc}^{*} \tag{6.53}$$

During fault operation while using *Method I*, the inverter is only able to provide a maximum voltage of the ±½ DC link voltage ($V_{\max}$) as the peak voltage between the output phases. The rated phase voltage of the delta connected machine that is used in this work is 415V (rms). When an open circuit fault occurs, the machine is transformed to a two phase star connected machine and the voltage of the neutral point (V_n) is controlled to be 0V. The control scheme has been designed so the machine operates under a field weakening mode at approximately half of the rated speed compared to the operation condition when it has a full voltage capacity (i.e. 415V rms). It should be noted that the rated power of the system will be reduced to half compared to the standard unfaulted inverter.

6.4.1.2 Method II - Modulating the Neutral Point Voltage

Another strategy is to control the voltage of the leg that connected to the neutral point (V_n) so that the amplitude of the voltage vector produced by the two remaining phases is minimised. This is obtained by ensuring that (V_n) remains smaller than those voltages in the remaining phases. If this condition is met, the approach is suitable for a high speed operation (although additional field-weakening may be needed). To fulfill this condition the selection of V_n is described in this section.

During healthy operating condition equations (6.27 – 6.29) are used to determine the PWM voltages demands with respect to the DC link midpoint. During a fault, the zero sequence voltage is not equal to zero and the summation of the output voltage references can be expressed as :

$$V_{ab}^{*} + V_{bc}^{*} + V_{ca}^{*} = 2.V_o \tag{6.54}$$

To get the benefit of using the transformation in (6.27 – 6.29) and to minimise the amplitude of the PWM voltages demand (i.e. V_{ao}, V_{bo}, and V_{co}), equation (6.54) needs to be modified in such a way to allow the transformation (6.27 – 6.29). This is achieved by:

$$V_{ab}^{*} + V_{bc}^{*} + V_{ca}^{*} - 2.V_o = 0 \tag{6.55}$$

If an open circuit fault occurs e.g. in phase *a*, the stator line voltage across the faulty winding V_{ab}^{*} is replaced by $V_{ab}^{*} - 2.V_o$ or $-(V_{bc}^{*} + V_{ca}^{*})$. This voltage together with the other two line voltages are passed to the transformation in (6.27 – 6.29). In this case, (6.55) will be valid in both faulty and healthy operation conditions.

In post fault operation condition when an open circuit fault occurs in phase *a* as shown in Fig. 6.5(b), *Method II* is used which considers the following equations for the transformation X:

$$V_{ao} = \frac{(U_n^{*} - V_{ca}^{*})}{3} \tag{6.56}$$

$$V_{bo} = \frac{(V_{bc}^{*} - U_n^{*})}{3} \tag{6.57}$$

$$V_{co} = \frac{(V_{ca}^* - V_{bc}^*)}{3} \tag{6.58}$$

where $U_n^* = -\left(V_{bc}^* + V_{ca}^*\right)$. In a similar way, if phase *b* is open circuited (Fig. 6.5(c)), the PWM voltages demands with respect to the DC link midpoint are:

$$V_{ao} = \frac{(V_{ab}^* - V_{ca}^*)}{3} \tag{6.59}$$

$$V_{bo} = \frac{(U_n^* - V_{ab}^*)}{3} \tag{6.60}$$

$$V_{co} = \frac{(V_{ca}^* - U_n^*)}{3} \tag{6.61}$$

where $U_n^* = -\left(V_{ab}^* + V_{ca}^*\right)$. Finally, a similar situation is observed if the open circuit fault happens in phase *c* with the following equations:

$$V_{ao} = \frac{(V_{ab}^* - U_n^*)}{3} \tag{6.62}$$

$$V_{bo} = \frac{(V_{bc}^* - V_{ab}^*)}{3} \tag{6.63}$$

$$V_{co} = \frac{(U_n^* - V_{bc}^*)}{3} \tag{6.64}$$

where $U_n^* = -\left(V_{ab}^* + V_{bc}^*\right)$.

During post fault operation by using *Method II*, the inverter is able to provide a maximum value of the DC link voltage equivalent to the peak value of the voltage across two of its output legs. Furthermore, *Method II* allows the inverter to supply a higher limit for the line-to-line voltage across the faulted machine than in the case of *Method I*, which is beneficial at higher speeds. Despite the advantages of using *Method I*, still there is a problem in the approach since there could be a reduction in the speed and torque ranges during post fault operation compared to that produced in the healthy condition. This is a result of the existence of a zero-sequence voltage which requires an extra voltage to be produced by the inverter. An adaptive field weakening approach has been implemented which allows the operation up to rated speeds. The scheme is described in the following section.

6.4.2 Field Weakening Control for Post Fault Operation Condition

In general, it is possible to operate the machine above the base speed by using field weakening [126]. The field weakening region is entered into when the maximum voltage output of the inverter feeding the motor is reached. The region of operation below the base speed is called the constant torque region, where the inverter will provide whatever voltage necessary to fully flux the machine and to provide up to the rated current (rated torque). Operation above the base speed is in the constant power region. Operation in this region is bounded to the limit of rated voltage and rated current, but rated current no longer corresponds to rated torque, because the motor is operating with reduced flux.

Different field weakening approaches have been proposed in the past. The commonly used method is the conventional field weakening. This method consists in varying the rotor flux reference in proportion to the inverse of the rotor speed [116]. In this method, the machine cannot yield the maximum output torque in the field-weakening region, because the voltage margin required to regulate current is not maintained [116]. Some approaches have been proposed to overcome this problem in [127, 128]. However, these approaches also cannot fully ensure the maximum torque operation over the entire high-speed range, which is well described in [129]. A different method has been proposed in [130]. The proposed scheme could provide the maximum torque in the field-weakening region by controlling the machine voltage according to the optimal voltage pattern selected to produce the maximum torque. The maximum torque in the same study was defined as the maximum absolute value of the torque under the limit conditions of voltage and current at a particular speed in the field-weakening region.

In this work, two different field weakening methods have been proposed which are used in conjunction with the fault tolerant control algorithm. The first the conventional field weakening method has been used as an open loop field weakening control due to its simplicity. The aim of using this method is to extend the speed range operation during post fault operation. This method has fulfilled the needs of the fault tolerant control proposed in this study. However the scheme has some

limitations which mean it cannot reach maximum torque. In order to solve this problem a closed loop field weakening control has been proposed as an additional technique to the fault tolerant scheme. This scheme controls the inverter voltage in such a way that the maximum limit voltage is not exceeded and produces a maximum torque. The following two sections will discuss the two different approaches.

6.4.2.1 Open loop field weakening control

The open loop field-weakening controller is obtained by controlling the i_{sd}^{*} current demand. The inputs to the field-weakening controller are dependent on the rotor speed demand and the selection of V_n. In this case, closed loop flux control is necessary. In the constant torque region, the flux is kept constant, however in the field weakening region, the flux is controlled by using a PI controller as illustrated in Fig. 6.7 [131].

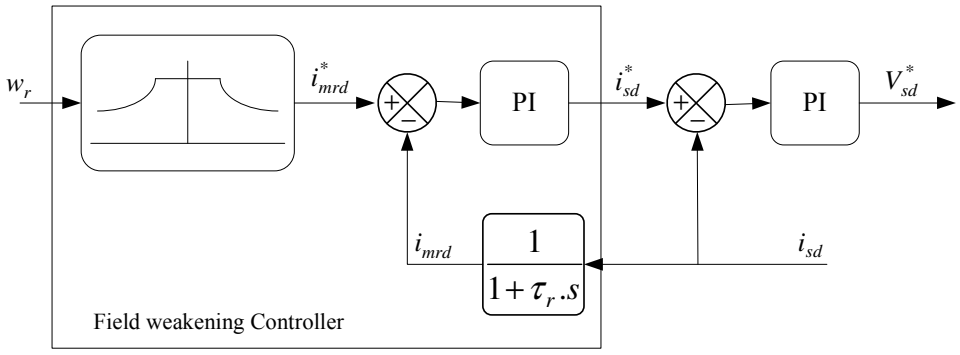

Fig. 6.7 Implementation of the open loop field weakening control.

Above base speed, conventional field-weakening states that the flux command currents i_{mrd}^{*} should be controlled by:

$$i_{mrd}^{*} = \frac{w_{base}}{w_r}.I_d \tag{6.65}$$

where I_d is the rated d-axis current, w_{base} is the base speed when the inverter reached the maximum voltage output. The maximum voltage $V_{\max}$ is determined by the available DC link voltage V_{dc} and the PWM strategy. In this work, a standard sinusoidal PWM strategy is used, and then $V_{\max}$ is limited to $V_{dc}/2$.

The value w_{base} for the two methods needs to be calculated when the maximum voltage output $V_{\max}$ is reached. In a post fault operation condition, the three demand voltage outputs of the current controllers are unbalanced, due to the existence of the zero sequence component. Therefore, w_{base} can be calculated graphically from the relationship of the speed versus the demand voltages in the fault operation condition by using the simulation model. When an open circuit fault does occur (e.g. in phase *a*) and *Method I* is used, different speed demand values are given to the simulation model for both no load and full load conditions. The system is been left operational until it reaches a steady state operation condition, then the three phases demand voltages are captured as shown in Fig. 6.8.

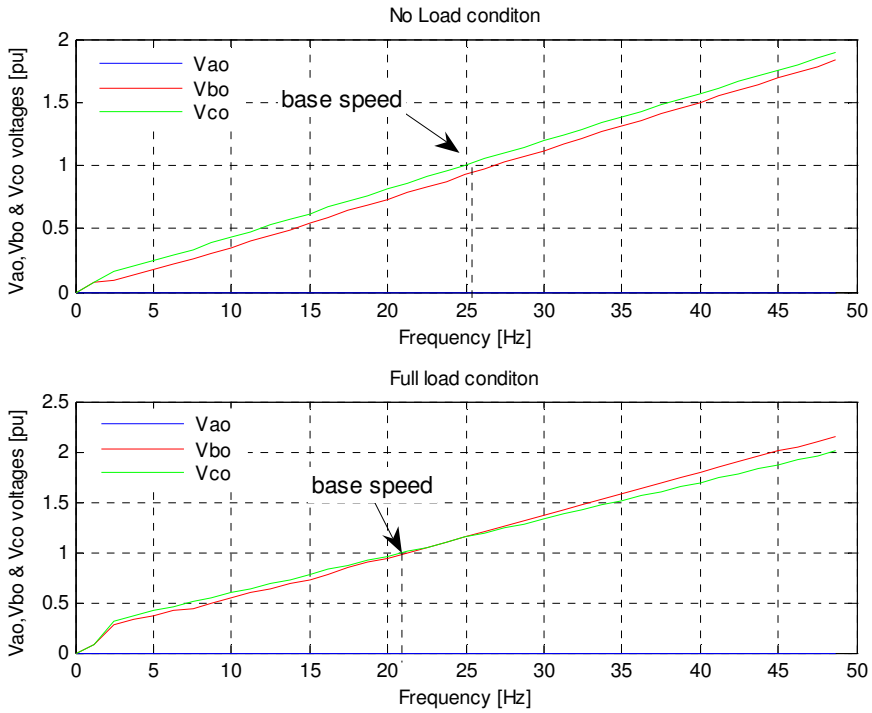

Fig. 6.8 The relationship of the speed frequency and the PWM voltages demands with respect to the DC link midpoint for an open circuit fault in phase *a* when *Method I* (neutral point control) is used.

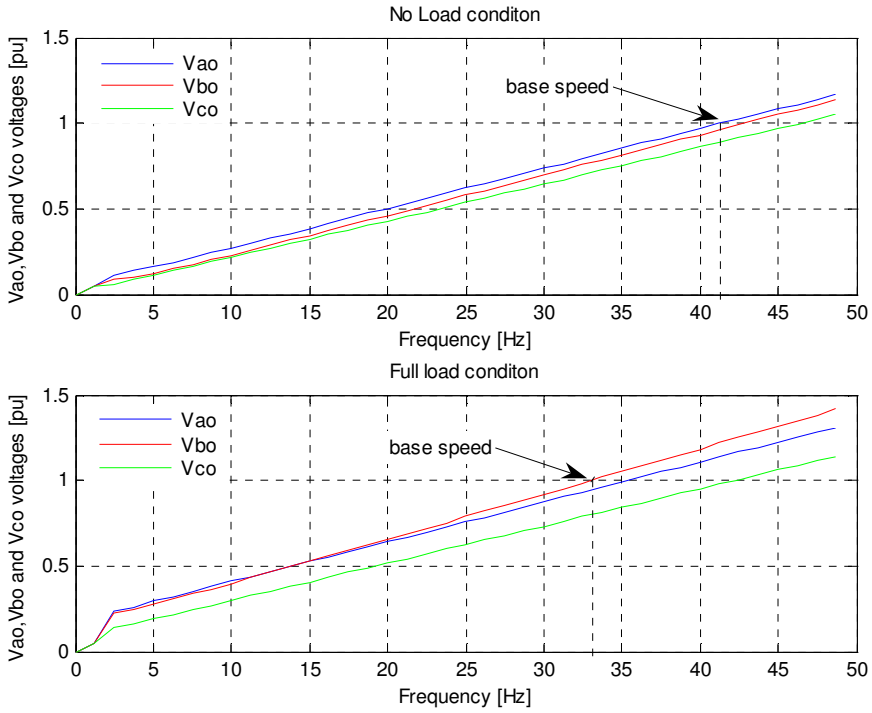

Fig. 6.9 The relationship of the speed, frequency and the PWM voltages demands with respect to the DC link midpoint for open circuit fault in phase *a* when *Method II* (neutral point control) is used.

In Fig. 6.8 the PWM voltages demands are presented in terms of a base quantity, which is equal to $V_{dc}/2$. This voltage is the maximum value that can be given to the inverter terminals without over-modulation problems. From Fig. 6.8, the highest voltage reaches 1 pu ($V_{dc}/2$ maximum voltage) at approximately 25.2Hz for a no load test, while for the case of full load, the highest voltage reaches the 1 pu at approximate 21.1Hz. Therefore, the base speed (w_{base}) for *Method I* is fixed to 21.1Hz.

A similar test was conducted to find the base speed value w_{base} when *Method II* was used. Fig. 6.9 shows the relationship between the three voltage demands versus frequency. It is evident that the highest voltage reaches the 1 pu at approximately 41.4Hz at no load and for the case of full load the highest voltage hits the 1 pu limit at approximate 33Hz. From these measurements the base speed (w_{base}) for *Method II* was fixed to 33Hz. It should be noted that the price paid for the extended constant power region is a sacrifice in the torque producing capability. For example, from Fig. 6.8, note that one per unit voltage is reached at 21.1 Hz by using *Method I*, while

that from Fig. 6.9 the one per unit voltage is reached at 33Hz by using *Method II*. Therefore, according to this discussion it is clear that the torque capability of the drive is more affected by using *Method I* than *Method II* in order to meet the constant power limit requirements.

6.4.2.2 Closed Loop Field Weakening Control

The maximum output torque and mechanical power developed by the machine is ultimately dependent of the inverter capability to supply the rated currents without voltage restrictions. Therefore, considering the limited voltage and current capacities, it is desirable to consider a control scheme which yields the best possible torque-per-ampere characteristic over the entire speed range. In the high speed range, the output torque capability depends on the field weakening strategy. Therefore, a closed loop field weakening controller is obtained by controlling the i_{sd}^* current demand as:

$$\frac{di_{sd}^*}{dt} = \gamma\left(V_{\max}^2 - V_{sd}^2 - V_{sq}^2\right) \tag{6.66}$$

where γ is a positive gain. This technique has been suggested by [130], and it has been modified by [132]. The basic idea is to select the reference (set-point) i_{sd}^* such that the modulus of the stator voltage vector $V_s = V_{sd} + jV_{sq}$, and $|V_s| = \sqrt{V_{sd}^2 + V_{sq}^2}$ are always equals to $V_{\max}$. Thus, if $|V_s| > V_{\max}$ then i_{sd}^* is decreased, while for the case when if $|V_s| < V_{\max}$ then i_{sd}^* is increased. This process continues until the value which yields nominal flux is reached. This strategy is suitable in pre-fault mode since V_{sd} and V_{sq} are constant in steady state and the three voltage demands (V_{ao}, V_{bo} and V_{co}) are symmetric with respect to their maximum and minimum values. However, because of the existence of the zero sequence component V_o which is not equal to zero during fault operation, $|V_s| = \sqrt{V_{sd}^2 + V_{sq}^2}$ does not reflect the maximum voltage, and the three voltage demands (V_{ao}, V_{bo} and V_{co}) are asymmetric with respect to their maximum and minimum values. The controller in (6.66) is not directly applicable in the case of the fault mode (i_{sd}^* will not be updated correctly), instead, i_{sd}^* can be ideally updated as:

$$i_{sd}^{*} = \int \gamma (V_{\max} - V_m).dt + I_d \qquad i_{sd}^{\min} < i_{sd}^{*} < I_d \tag{6.67}$$

where V_m is the maximum value of the three voltage demands (V_{ao}, V_{bo} and V_{co}), $i_{sd}^{\min}$ is the minimum allowed value (to prevent complete demagnetization and i_{sd} from becoming negative at transients) and I_d is the rated d-axis current. Expression V_m is not known but can be obtained by using an adaptive filter which has been used to estimate the magnitude of the three voltages demands. The magnitude of V_m will be determined from the highest magnitude value of the three estimated voltages ($|\hat{V}_{ao}|$, $|\hat{V}_{bo}|$ and $|\hat{V}_{co}|$). A schematic diagram showing the calculation of the inverter demand voltages is presented in Fig. 6.10.

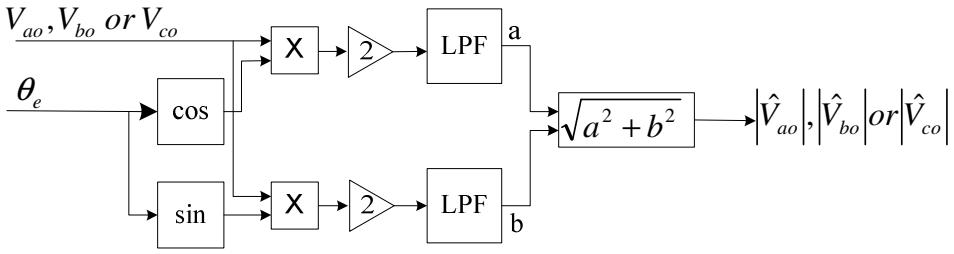

Fig. 6.10 Schematic diagram of the proposed adaptive filter illustrating how the voltage references $|\hat{V}_{ao}|$, $|\hat{V}_{bo}|$ and $|\hat{V}_{co}|$ are obtained.

In Fig. 6.10 the LPF denotes a low pass filter, hats (^) are used to indicate a filtered signal i.e. $|\hat{V}_{ao}|$ is an estimate of $|V_{ao}|$ obtained using a filter. A schematic diagram of the closed loop field weakening controller that adjust the machine input voltage according the inverter maximum voltage to produce the maximum torque is illustrated in Fig. 6.11. It can be inferred that this method can be utilised in both operation modes, the pre fault and the post fault modes. The main advantage of this scheme is that it does not need to fix the base speed such as in the case of conventional field weakening, and it automatically optimizes operation to load level. When the required machine voltage begins to exceed the maximum voltage due to the increase of the operating frequency, the system will enter the field weakening region and the integral controller adjusts i_{sd}^{*} so that the highest inverter voltage cannot exceed $V_{\max}$.

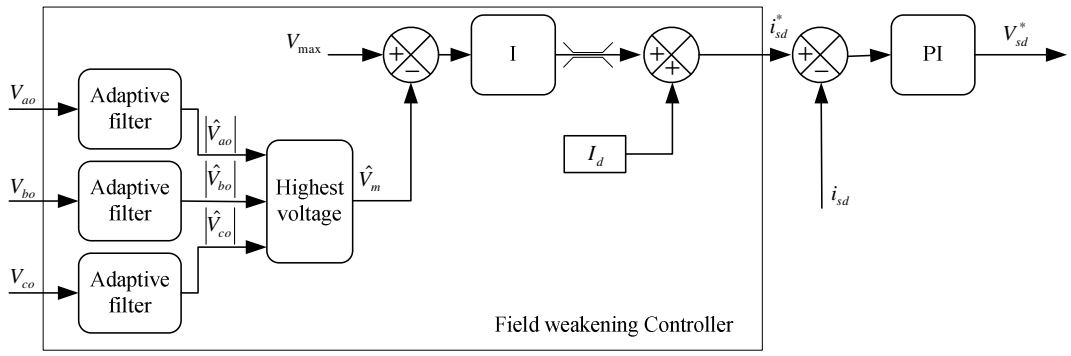

Fig. 6.11 Schematic diagram of the proposed closed loop field weakening control.

The basic idea of using the field weakening control is to reduce the stator voltage by reducing the rotating magnetic flux during fault operation. However this should be made while maintaining the required torque and speed, and consequently, the required power. This means that the stator current under the field weakening operation is larger than that prior to the control activation. As a result of this process, a larger stator copper loss will be generated when compared to pre fault operation. If the increased copper loss results in the stator winding temperature exceeding the critical temperature, the operation under the proposed strategy should be terminated. However, temperature rise in the stator winding under the proposed strategy is not instantaneous. The temperature will rise to some critical level with a certain time constant. This implies that the operating area and duration under the proposed strategy must be restricted, which is related to the physical parameters of the machine. It can also be inferred that the allowable area and duration under the proposed strategy is strongly related to the amplitude of the required stator current. It should be noted that the remedial operational strategy is not to operate the drive under a defective condition for a long time, but just to keep the machine temporarily in operation (although with an unbalanced supply) until there is an opportunity to solve the problem.

6.5 CONCLUSION

A new strategy and its implementation for post open-circuit fault operation of a drive in safety-critical applications have been proposed and discussed in this chapter. This technique considers the post fault operation of an induction machine where a connection is available to the neutral point of the machine windings during post fault operation. The fault tolerant schemes described in this chapter are equally applicable to either a fault tolerant drive with an extra inverter leg connected to the neutral point of a star connected machine or for a delta connected machine fed from a standard three leg inverter, with an open circuit winding.

A novel feed-forward compensation algorithm is introduced for the zero sequence component of the *dqo* reference voltages which has a considerable influence on the performance of the motor during an open circuit fault. The scheme eliminates the negative sequence current components and reduces the torque pulsations and the harmonic content of the machine currents. Two methods for controlling the neutral-point voltage were presented so that the available voltage capacity of the inverter is maximized in both during normal and fault mode. For operation at higher speeds, an additional field-weakening control algorithm was incorporated with feedforward compensation in order to minimize the phase voltages of the remaining phases during the post fault mode.

The proposed fault tolerant control scheme can be embedded into an existing commercial inverter system as a subroutine. No additional hardware is required. Validation of the proposed strategy is provided in Chapter 7.

CHAPTER 7

VERIFICATION OF THE FAULT DETECTION AND FAULT TOLERANT OPERATING STRATEGIES

7.1 INTRODUCTION

The on-line detection method to detect and diagnose stator open circuit faults by using the third harmonic component in the motor line currents that was proposed in Chapter 5, is verified through simulation and experiment. In addition, the proposed fault tolerant control operating strategy that was proposed in Chapter 6 is also validated through simulations and experiments. The proposed strategy has a considerable influence on the performance of the motor during an open circuit fault when a feedforward compensation algorithm is introduced for the zero sequence component of the *dqo* reference voltages. In practice, the open circuit fault detection and fault-tolerant operating strategy are both verified by simulation and experiment.

This chapter is structured as follows: Section 7.2 presents the simulation and experimental results to validate the on-line detection method for detection and diagnosis of a stator open circuit fault. The verification of the fault tolerant operating strategy through simulation and experiment is presented in Section 7.3. The online fault detection with the fault tolerant strategy were combined together to drive the fault ride through system. In addition, for comparison, the results of using the two methods for controlling the neutral-point voltage with the two different field weakening control schemes are presented in Section 7.4. Section 7.5 presents the experimental results of low speed operating condition, and the conclusions is presented in Section 7.6.

7.2 SIMULATION AND EXPERIMENTAL RESULTS FOR FAULT DETECTION TECHNIQUE

To validate the use of the proposed on-line detection method, a four-pole 4kW delta connected machine model as modified in Chapter 3 is utilised. All the experimental tests and simulation results were obtained with the machine operating with an IRFO control structure.

7.2.1 Simulation Results

The simulations to show the behaviour of the delta connected motor drive with a stator open circuit fault are performed under the conditions defined in Table 7.1. These conditions illustrate that the proposed open circuit fault detection method are effective regardless of the operation mode. The simulation of the faulty machine has been carried out with an open circuit fault in phase *a.*

The simulation result for the transition between healthy, and fault mode condition (open circuit in phase *a*) at a speed of 200 rad/sec, rated flux and 50% of the nominal load is presented in Fig. 7.1. The fault condition was made by imposing an open circuit fault in phase *a* at t = 2.5sec. The transit response of the line current produced before and after the presence of an open phase fault is presented in Fig. 7.1(a). The magnitude of the third harmonic component of the line currents which was estimated as discussed in section 5.4.1 are presented in Fig. 7.1(b). The fault detection signal and the fault location that depends on the levels of the magnitude of the third harmonic components are presented in Figs. 7.1(c & d) respectively. Figs. 7.2 and 7.3 show the spectrum of the line currents of the motor during healthy and fault mode respectively using the same operating conditions as shown Fig. 7.1.

Table 7.1 Simulation Conditions showing the behaviour of the induction motor drive system for verifying the proposed fault detection technique

Item	Unit	Conditions
Control Mode	-	IRFO
Reference Speed	[Rad/sec]	200
Torque Reference	[N.m]	0/13/26
Rated Field Current i_{sd}	[A]	4.9
Rated Torque Current i_{sq}	[A]	9
Limit of Torque Current i_{sq}	[A]	10.5
Fault Location	-	On the *a*-phase winding

For the healthy operation condition, the behaviour of the induction motor drive is perfectly normal and the spectrum of the motor supply currents does not contain any third harmonic as shown in Fig. 7.2. When an open circuit fault is imposed, the appearance of the third harmonic is obvious in the spectrum of the line currents of the motor (Fig. 7.3). In addition, the third harmonic component appears in the line currents after the fault occurs as illustrated in Fig. 7.1(b). The amplitude of this harmonic is large that its presence may be inferred from the shape of the current waveforms of the motor line currents (Fig. 7.1(a)). In the spectrum of the motor line currents, the third harmonic is clear, as predict during the analysis that was carried out in Section 5.2. The fault has been detected at time = 2.59 sec after the output of third harmonic estimator exceeds the fault threshold value (Fig. 7.1(c)); this occurs within 0.09 sec. This is mainly dependent on the threshold value and on the response of the LPF used. The fault identification algorithm locates the fault in phase *a* as shown in Fig. 7.1(d). This was made using the lowest third harmonic component which is the line current I_c for the a phase fault considered, and is now effectively the neutral current, as shown in Figs. 7.1(b) and 7.3(c). In addition, it has been observed that a very good agreement between the on-line estimated magnitude of the third harmonic in Fig. 7.1(b), and the spectrum analysis of the line currents shown in Fig. 7.3. These figures show the accuracy of the online estimated component of the third harmonic current are very good for the three line currents compared with that of the offline technique (FFT).

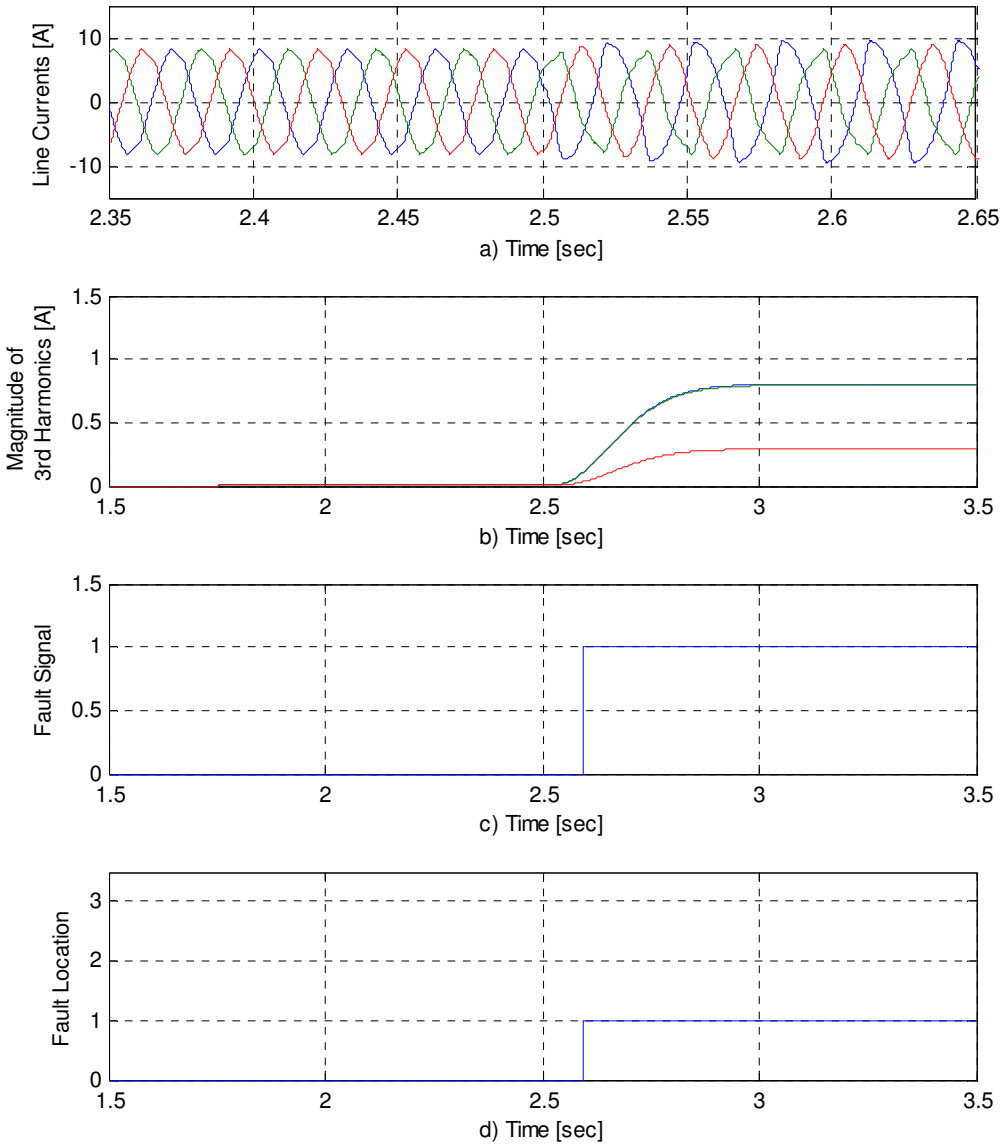

Fig. 7.1 Simulation results, transition between pre fault and fault mode at 200rad/sec, full flux and 50% of nominal load with open circuit in phase *a*. a) three line currents, b) on-line estimation of the magnitude of the third harmonic component in the line currents, c) fault detection signal, d) fault location.

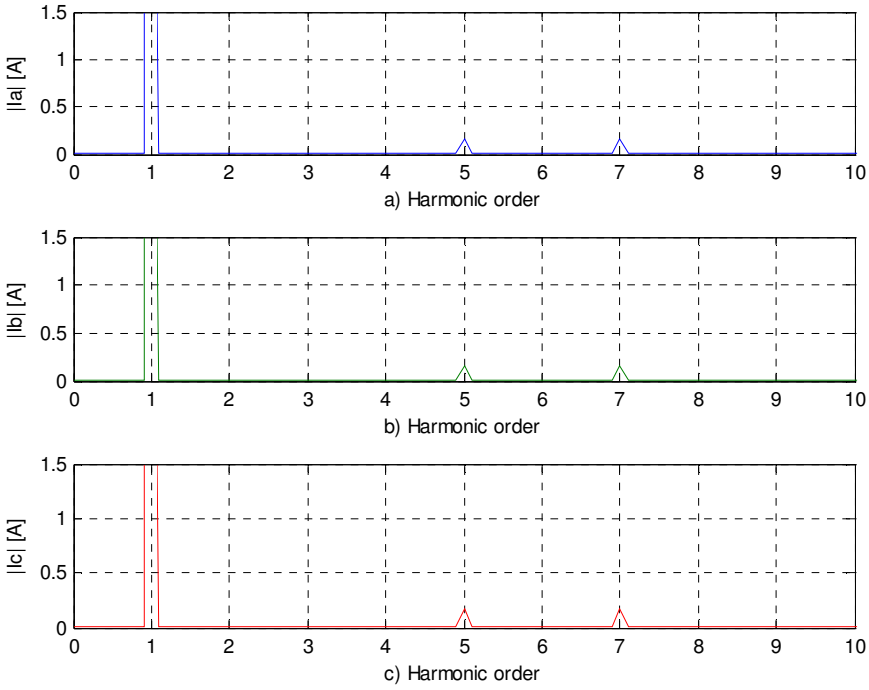

DFig. 7.2 Simulation result, frequency spectrum for healthy condition of the line currents for induction machine drive at 200rad/sec, full flux, and 50% of the nominal load a) I_a, b) I_b, c) I_c

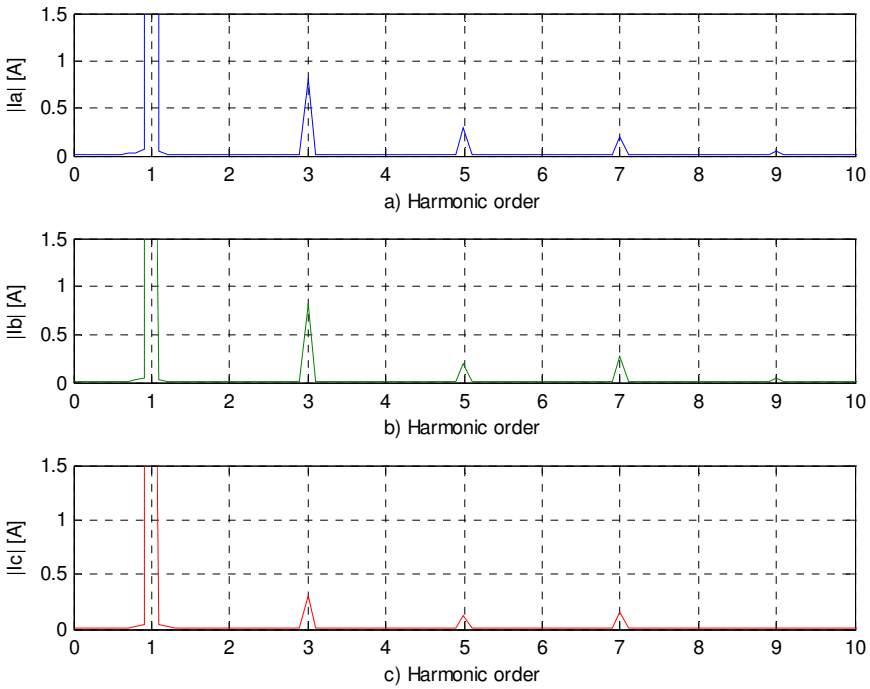

Fig. 7.3 Simulation result, frequency spectrum of the line currents for induction machine drive at 200rad/sec, full flux, and 50% of the nominal load with open circuit in phase *a*. a) I_a, b) I_b, c) I_c

To verify the proposed detection method works well even at different load conditions, two different tests have been carried out using the same conditions used in Fig. 7.1, but with different load level. Figs. 7.4 and 7.5 show the simulation results for the transition between healthy, and fault mode condition (open circuit in phase *a*) at a speed of 200 rad/sec, rated flux with no load and 100% of the nominal load respectively. The fault condition was made by imposing an open circuit fault in phase *a* at time = 2 sec for Fig. 7.4, and at time = 2.5 sec for Fig. 7.5. The transient response of the line current produced before and after the presence of an open phase fault is presented in Figs. 7.4(a) and 7.5(a). The magnitudes of the third harmonic components are presented in Figs. 7.4(b) and 7.5(b). The fault detection signal and the fault location are presented in Figs. 7.4(c & d) and 7.5(c & d) respectively. It is evident that the third harmonic component appears in the line currents after the fault occurs as shown in Figs. 7.4(b) and 7.5(b). The fault has been detected after the output of third harmonic estimator exceeds the fault threshold value as illustrated in Figs. 7.4(c) and 7.5(c); this took place within 0.09 sec. The fault identification algorithm locates the fault in phase *a* as shown in Figs. 7.4(d) and 7.5(d). It can be inferred that the proposed fault detection method works regardless of the load level, and it can be used to detect the fault independently of the applied load level by observing the third harmonic component in the line currents.

Other test was carried out to show that the proposed detection methods work well when the open circuit fault occurred in different windings. Fig. 7.6 shows the simulation results for the transition between healthy and fault mode condition when the open circuit fault occurred in different winding at a speed of 200 rad/sec, rated flux and 100% of the nominal load. The fault conditions were made by imposing an open circuit fault for a duration of one second in phase *a* at time = 3 sec, in phase *b* at time = 5 sec, and in phase *c* at time = 7 sec respectively. The transit response of the line current produced before and after the presence of an open phase fault is presented in Figs. 7.6(a). It can be observed that the third harmonic component appears in the line currents after the fault occurs in phase *a* when the time is between 3 to 4 sec as shown in Figs. 7.6(b).

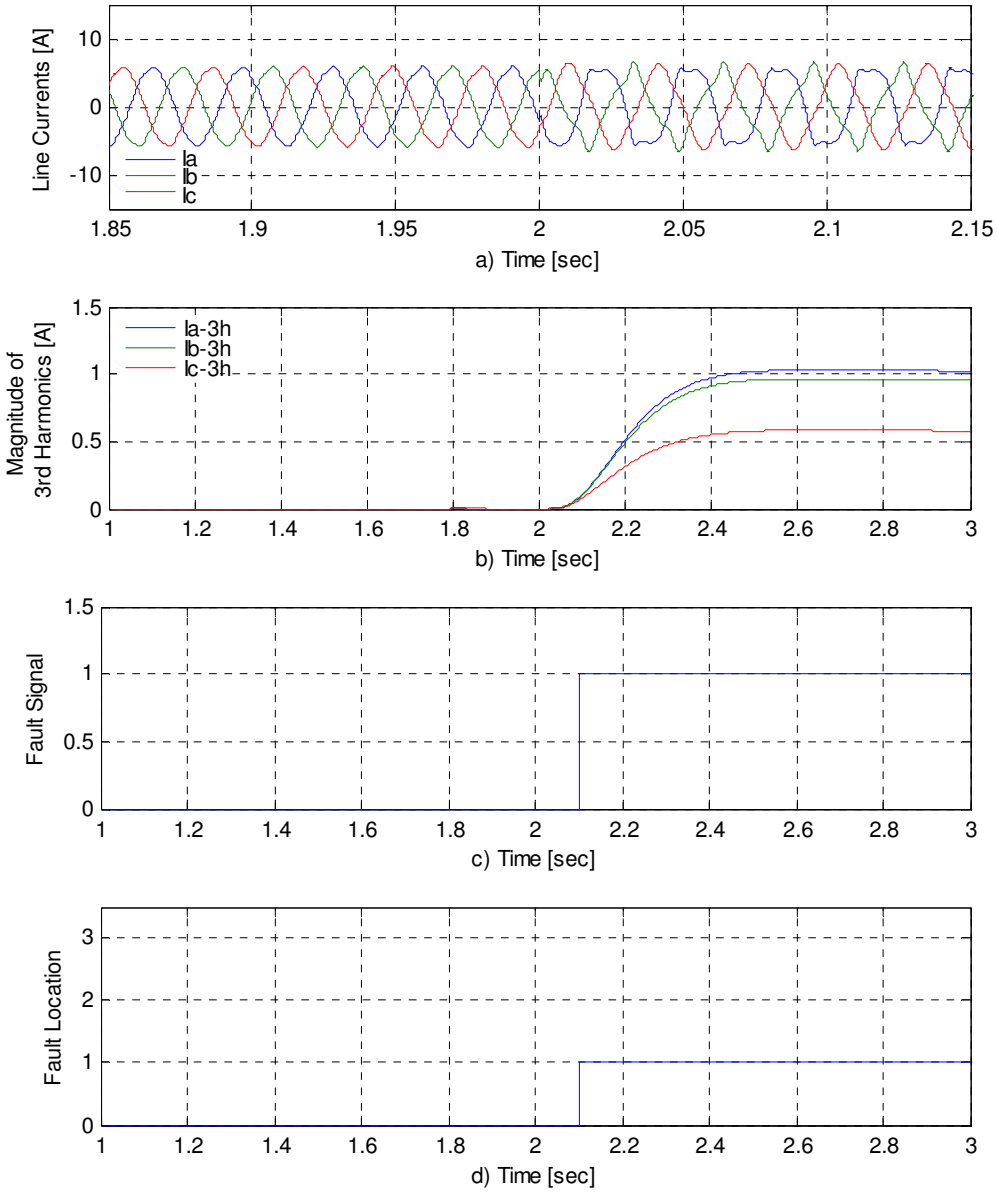

Fig. 7.4 Simulation result, Transition between pre fault and fault mode at 200rad/sec, full flux and no load with open circuit in phase *a*. a) three line currents, b) on-line estimation of the magnitude of the third harmonic component in the line currents, c) fault detection signal, d) fault location.

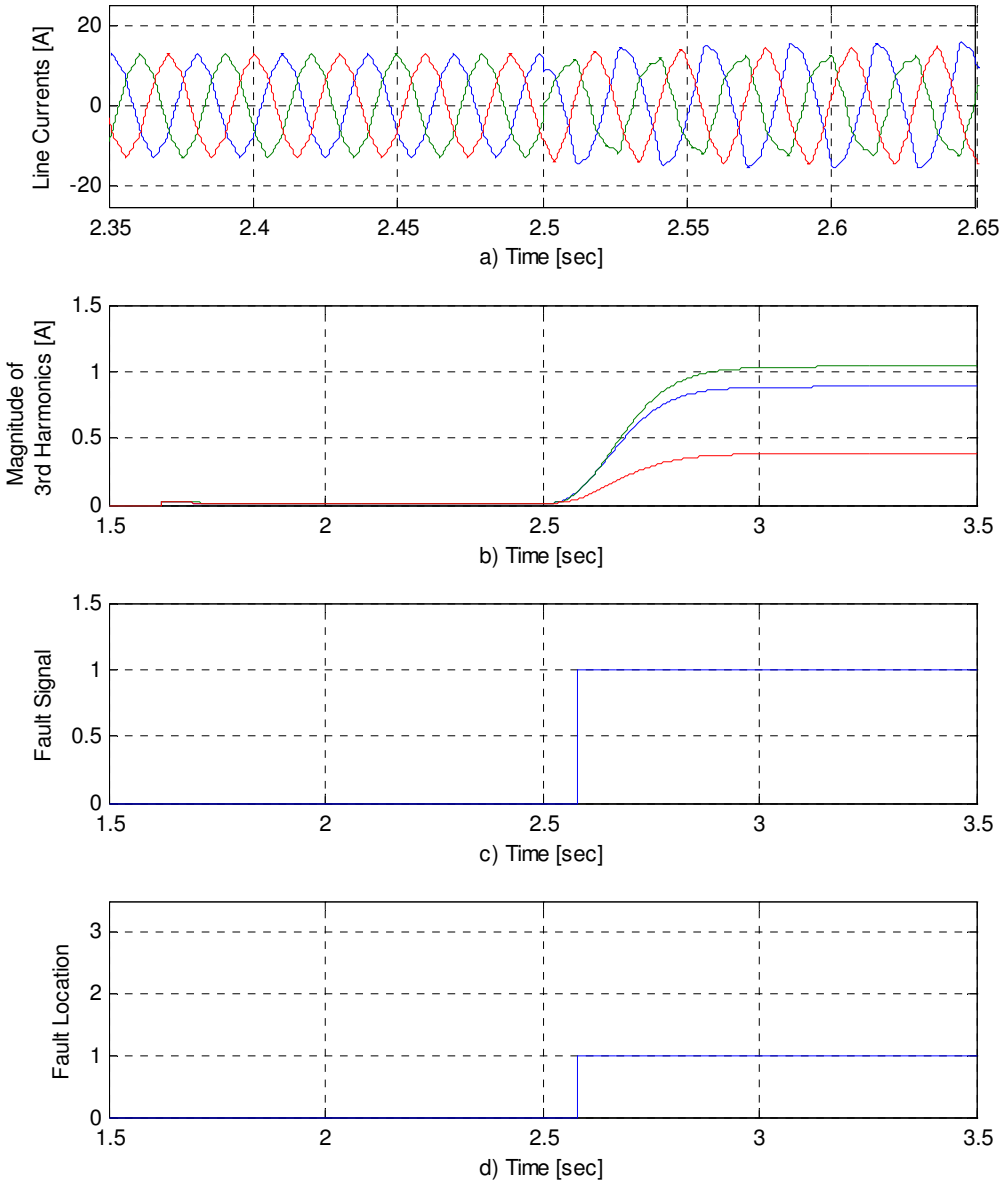

Fig. 7.5 Simulation results, transition between pre fault and fault mode at 200rad/sec, full flux and 100% of the nominal load with open circuit fault in phase *a*. a) three line currents, b) on-line estimation of the magnitude of the third harmonic component in the line currents, c) fault detection signal, d) fault location.

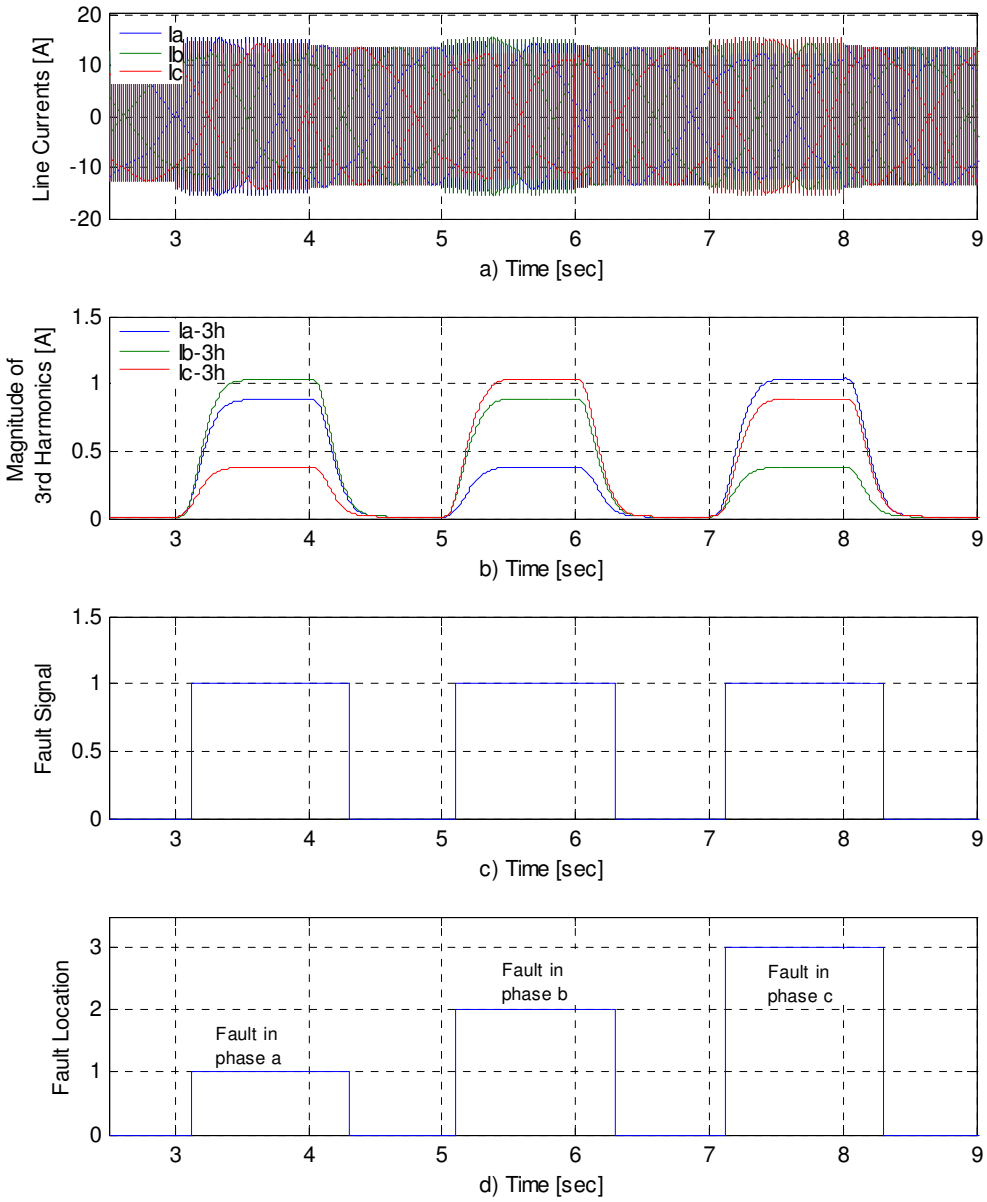

Fig. 7.6 Simulation result, Transition between pre fault and fault mode at 200rad/sec, full flux and 100% of the nominal load with open circuit fault in phase *a, b,* and *c*. a) three line currents b) on-line estimation of the magnitude of the third harmonic component in the line currents c) fault detection signal d) fault location.

The fault has been detected after the output of third harmonic estimator exceeds the fault threshold value as shown in Figs. 7.6(c); this occurs within 0.09 sec. The fault identification algorithm locates the fault in phase *a* as shown in Figs. 7.6(d) where the lowest third harmonic component appear in the line current I_c (neutral point). At time =

4sec, the open circuit fault that has been imposed is reconnected and the machine returns back to work in the healthy condition. The fault detection signal goes off when the output of the on-line estimator third harmonic component does not exceed the fault threshold value. The third harmonic component appears again in the line currents after the fault occurs in phase *b* between the period of 5 to 6 sec as shown in Figs. 7.6(b). The fault has been detected as shown in Figs. 7.6(c) and the fault is located in phase *b* as shown in Figs. 7.6(d), where the lowest third harmonic component is appeared in the line current Ia. Once again, when the open circuit fault was occurred in phase *c* during time = 7 to 8 sec, the fault has been detected and located in phase *c* as shown in Figs. 7.6(d), where the lowest third harmonic component appears in the line current I_b Fig. 7.6(b). The simulation results show that the proposed fault detection method is effectively works regardless of the fault location, and it can locate the fault by observing the lowest level of the third harmonic component in the line currents.

7.2.2 Experimental Results

This section validates the proposed fault detection method experimentally. For comparison, the same operating conditions were used as illustrated in Table 7.1. Fig. 7.7 shows the experimental results for the transition between healthy and fault mode (open circuit in phase *a*) at a speed of 200 rad/sec, rated flux and 50% of the nominal load (c.t. Fig. 7.1). Fig. 7.7 starts with the healthy machine. At time = 5.474 sec the open circuit fault occurs in phase *a*. The transient response of the line current produced before and after the fault occurs was presented in Fig. 7.7 (a). The magnitudes of the third harmonic components of the line currents are presented in Fig. 7.7(b). The fault detection signal and the fault location are presented in Figs. 7.7(c & d) respectively. Figs. 7.8 and 7.9 show the spectrum analysis of the line currents during healthy and faulty mode, respectively. By comparing Figs. 7.1 – 7.3 with the Figs. 7.7 – 7.9 during the healthy operation conditions, the transient of current is well predicted by the model, and the behaviour of the induction motor drive is perfectly normal and the spectrum of the motor supply currents does not contain any third harmonic.

The diagnosis of the fault condition is made at time = 5.56 sec (this occurs within 0.09 sec) after the output of third harmonic estimator exceeds the fault threshold value. The

fault identification algorithm locates the fault in phase *a* as shown in Fig. 7.7(d). The waveform shapes of the current are similar in both results. It was observed that higher order oscillations existed in line currents of the experimental results (Fig. 7.7(a)), indicating the existence of higher order harmonics in the flux (e.g. slot harmonics). These are not present in the simulation result, as the model only accounts for the 3rd, 5th and 7th harmonics of the flux distribution. Figs. 7.1(b) and 7.7(b) show the estimated magnitudes of the third harmonic components in the line currents, and show a slight mismatch in the amplitude of the simulation results compared to that of the experimental results. This is due to the simplifications made in the modelling of the saturation effect, where the model parameters K_2, K_4, K_6 and ρ_2, ρ_4, ρ_6 have not been tuned for fault conditions. Once again, the simulation and experimental results are in a good match and are suitable for the objectives of this project.

To show that the proposed detection methods work well even at different load conditions in the experimental environment, two different tests have been carried out using the same conditions as in Fig. 7.7 but with different load levels. Fig. 7.10 presents the experimental results for the transition between healthy, and faulty mode condition (open circuit in phase *a*) at a speed of 200 rad/sec, rated flux and no load (the same operating conditions applied in Fig. 7.4). The transient response of the line current produced before and after the fault is presented in Figs. 7.10(a). The estimated third harmonic components are presented in Figs. 7.10(b). The fault detection signal and the fault location are presented in Figs. 7.10(c & d) respectively. The fault occurs at time = 5 sec and its detection is verified at time = 5.09 sec. The fault identification algorithm locates the fault in phase *a* as shown in Figs. 7.10(d). By comparing the simulation results (Fig.7.4) with the experimental results (Fig. 7.10) for the healthy operation condition, the transient of current is well predicted by the model. It can be seen that the simulation results for the line current match the experimental results but with a slight mismatch in the magnitude of the third harmonic components (Figs. 7.4(b) and 7.10(b)). This is due to the simplifications made in the modelling of the saturation effect, where the saturation model has not been tuned for fault conditions. However, the experimental and simulation results are in very good agreement and are suitable for the objectives of this project.

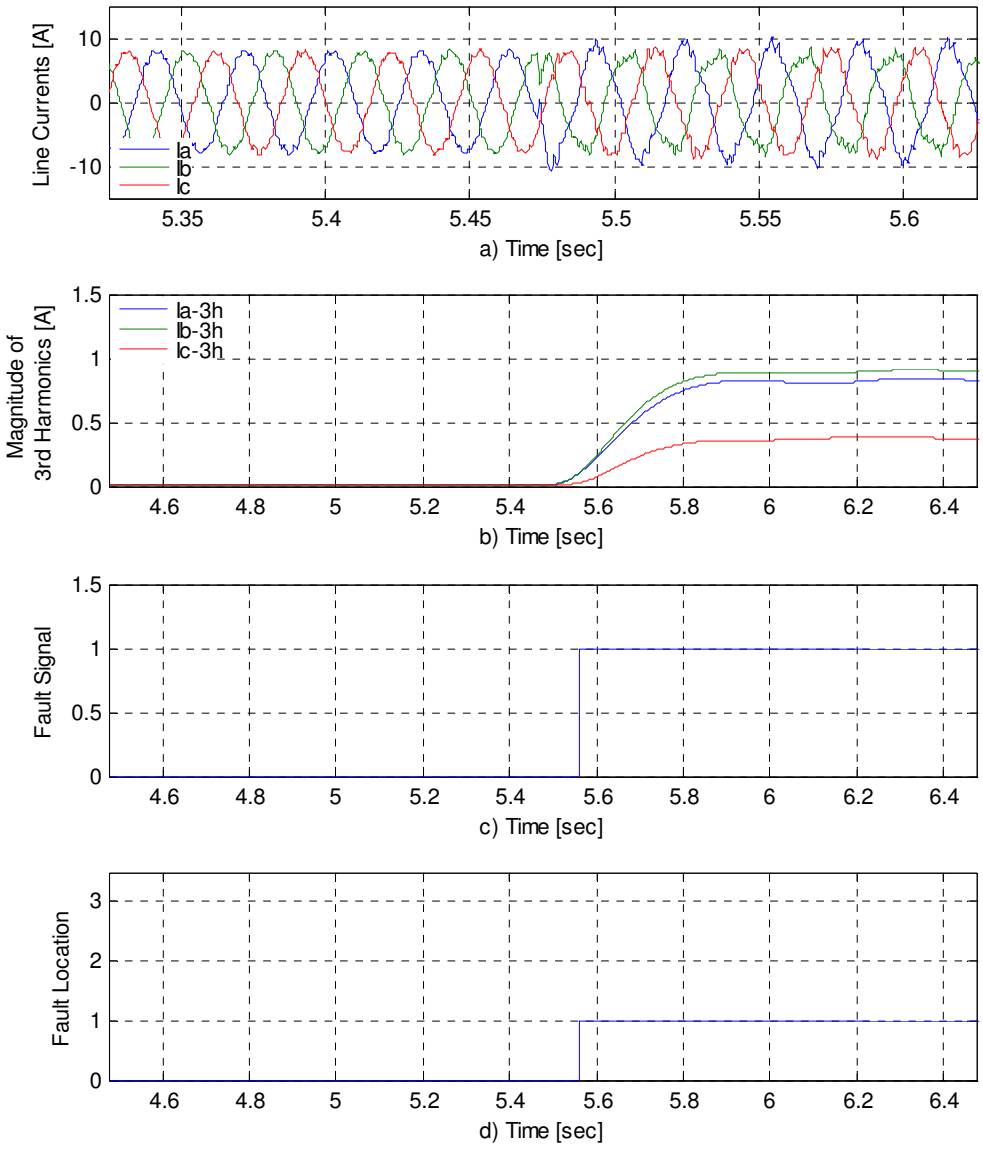

Fig. 7.7 Experimental result, Transition between pre fault and fault mode at 200rad/sec, full flux and 50% of nominal load with open circuit in phase *a*. a) three line currents, b) on-line estimation of the magnitude of the third harmonic component in the line currents, c) fault detection signal, c) fault location.

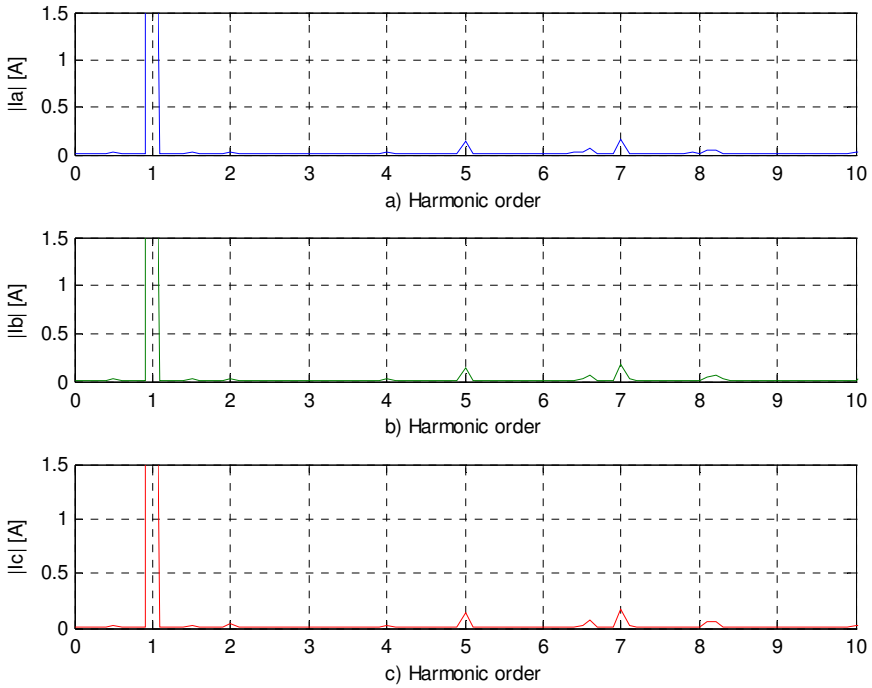

Fig. 7.8 Experimental result, frequency spectrum for healthy condition of the line currents for induction machine drive at 200rad/sec, full flux, and 50% of the nominal load a) I_a, b) I_b, c) I_c

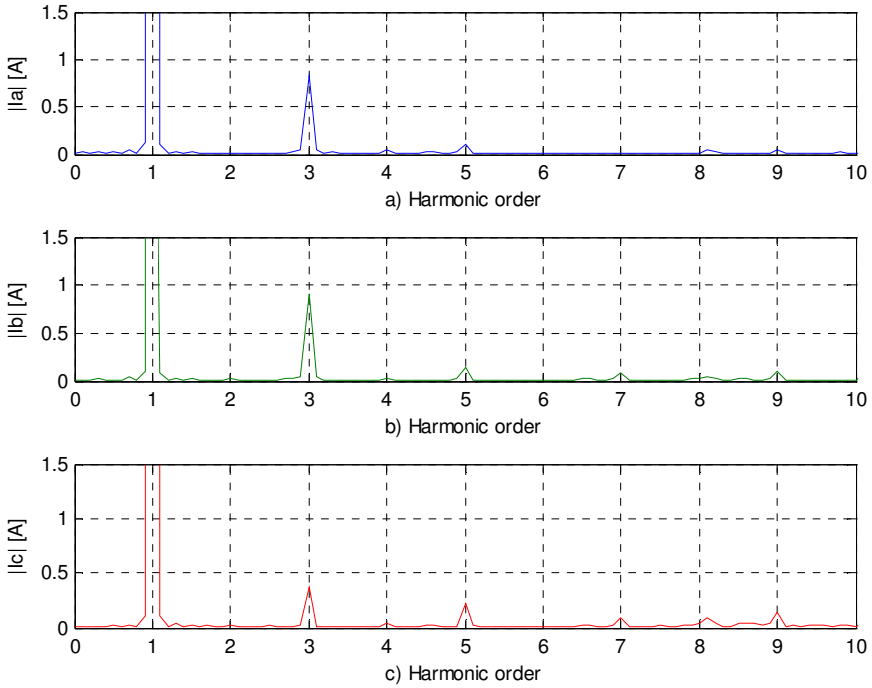

Fig. 7.9 Experimental result, frequency spectrum of the line currents for induction machine drive at 200rad/sec, full flux, and 50% of the nominal load with open circuit in phase *a*. a) I_a, b) I_b, c) I_c

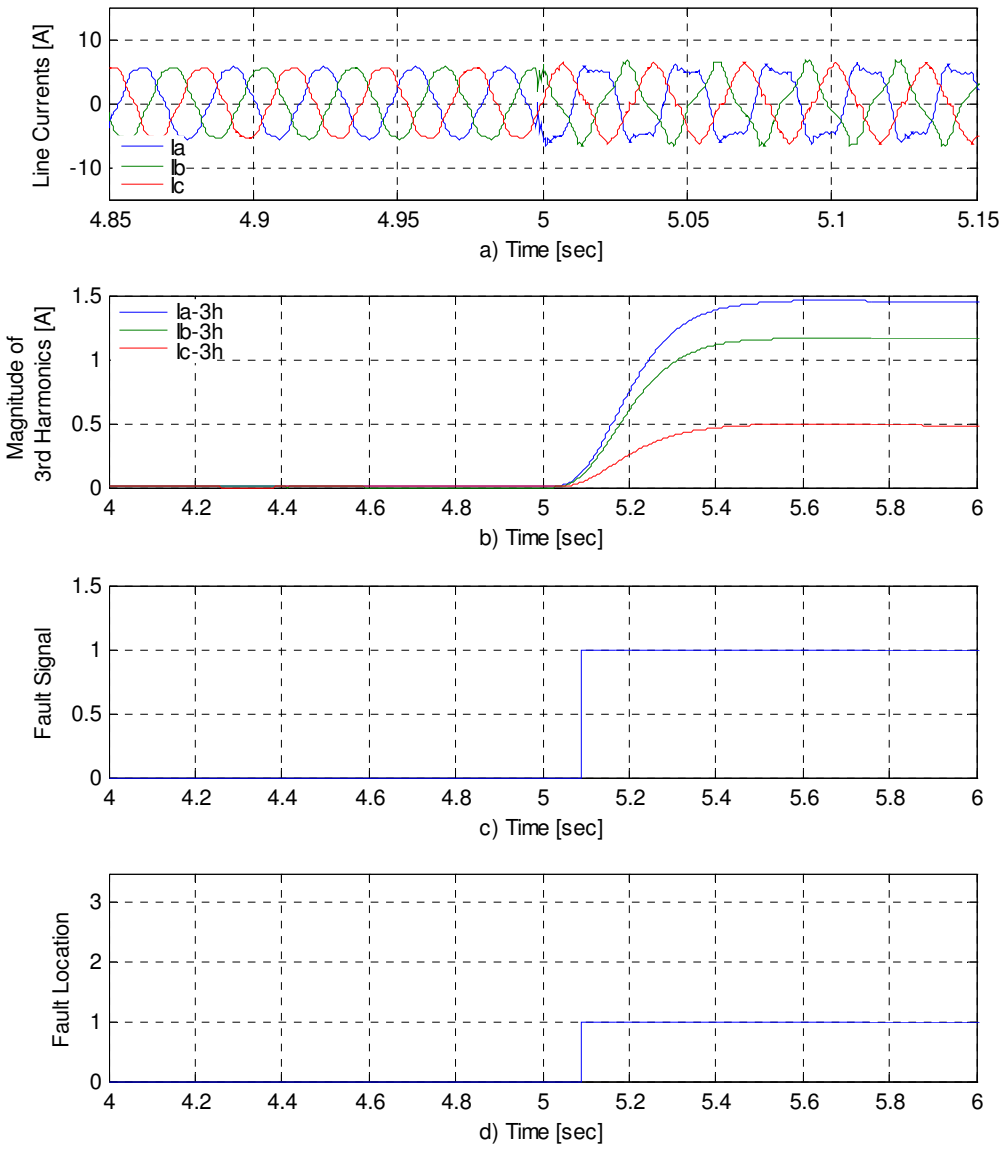

Fig. 7.10 Experimental results, transition between pre fault and faulty mode at 200rad/sec, full flux and no load with an open circuit fault in phase *a*. a) three line currents, b) on-line estimation of the magnitude of the third harmonic component in the line currents, c) fault detection signal, d) fault location.

The experimental results for the transition between healthy and fault condition (open circuit in phase *a*) at a speed of 200 rad/sec, rated flux and 100% of nominal load (the same operating conditions as Fig. 7.5) is presented in Fig. 7.11. The transit response of the line current produced before and after the fault is presented in Figs. 7.11(a). The estimated third harmonic components are presented in Figs. 7.11(b). The fault detection signal and the fault location are presented in Figs. 7.11(c) – (d) respectively. The fault condition is simulated at time = 5.62 sec, and its detection is realized at time = 5.71 sec (this occurs within 0.09 sec). The fault was located in phase *a* (Fig. 7.11(d)) by using the lowest third harmonic component as shown in the line current I_c (neutral point) Fig. 7.11(b).

By comparing the simulation results (Fig. 7.5) with the experimental results (Fig. 7.11), it can be observed that the simulation results for the line current match the experimental results but with a slight mismatch in the magnitude of the third harmonic components (Figs. 7.5(b) and 7.11(b)). This is due to the simplifications made in the modelling of the saturation effect, where the model parameters K_2, K_4, K_6 and ρ_2, ρ_4, ρ_6 have not been tuned for fault conditions. In addition, the experimental results also show some higher order oscillations (Fig. 7.11(a)), indicating the existence of higher order harmonics in the flux (e.g. slot harmonics). Once again, the simulation and experimental results are in very good correlation and are suitable for the objectives of this project.

It can be inferred that the proposed fault detection method works effectively regardless of the load level, and it can detect the fault quite independently of the applied load level by observing the third harmonic component in the line currents.

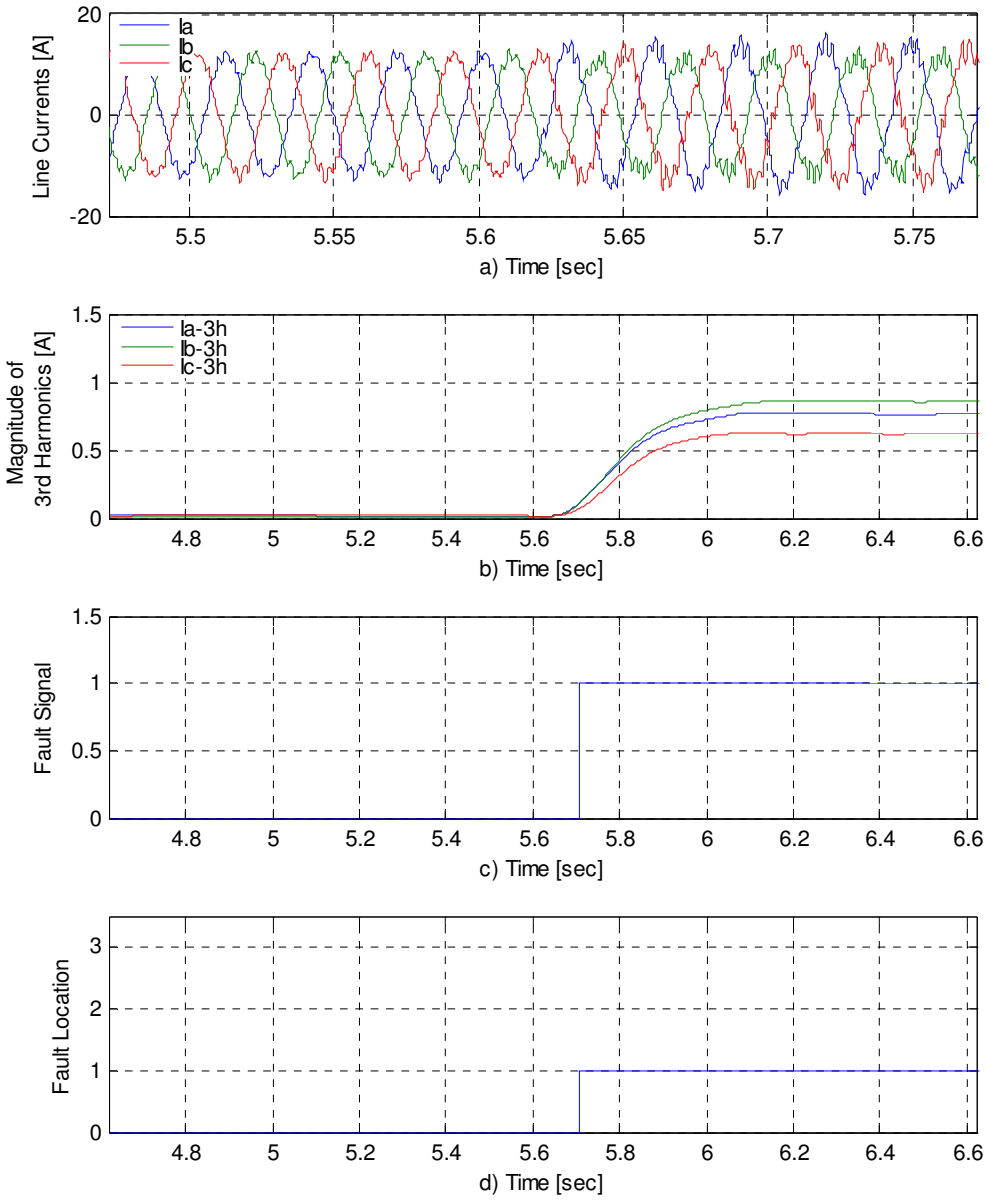

Fig. 7.11 Experimental result, transition between pre fault and faulty mode at 200rad/sec, full flux and 100% of nominal load with open circuit in phase *a*. a) three line currents, b) on-line estimation of the magnitude of the third harmonic component in the line currents, c) fault detection signal, d) fault location.

An alternative test has been carried out to show the performance of the proposed detection technique when the machine are rotating at a low speed and light load condition. Fig. 7.12 presents the experimental results for the transition between healthy, and fault mode (open circuit in phase *a*) at a speed of 31.4 rad/sec, rated flux and no load. The transient response of the line current produced before and after the fault is presented in Figs. 7.12(a). The estimated third harmonic components are presented in Figs. 7.12(b). The fault detection signal and the fault location are presented in Figs. 7.12(c & d) respectively. The fault condition was made by imposing an open circuit fault in phase *a* at instant time = 4.62 sec. The fault has not been detected as shown in Fig. 7.12(c). This is because the third harmonic component does not exceeded the fault threshold value. A problem arises specifically while running at a low speed and light load level in the IRFO induction machine drive. The amplitude of the third harmonic present in each one of the three motor line currents is very small (Fig. 7.12(c)). There are different reasons behind that: at low speed, the third harmonic currents in the stator phase windings during healthy condition are affected by the resistive nature of both the rotor and stator, causing the observed magnitude of the third harmonic component to be comparatively much lower than expected [121]. In addition, during fault conditions, the magnitude of the third harmonic will be reduced due to the effect of the current controllers of the IRFO, where the frequency of the third harmonic will be exist within the range of the current controller bandwidth (100Hz). Furthermore, the current (time) harmonics created by non-linear power converter effects are eliminated as well by the current controller. Therefore, based on these experimental results, it is possible to conclude that the diagnostic technique based on the detection of the third harmonic in the motor line current in IRFO induction motor drives has limitations at low speeds. The magnitude of the third harmonic component is reduced and becomes lower than the fault threshold value; consequently the fault will not be detected while the machine is running. Through different experimental tests, it has been observed that the proposed fault detection algorithm fails when the machine is running at speeds less than 5Hz. This problem will be further discussed in the fault tolerant control, when it will be proved that at low speed the machine can work well without the feedforward compensation algorithm Section 7.5.

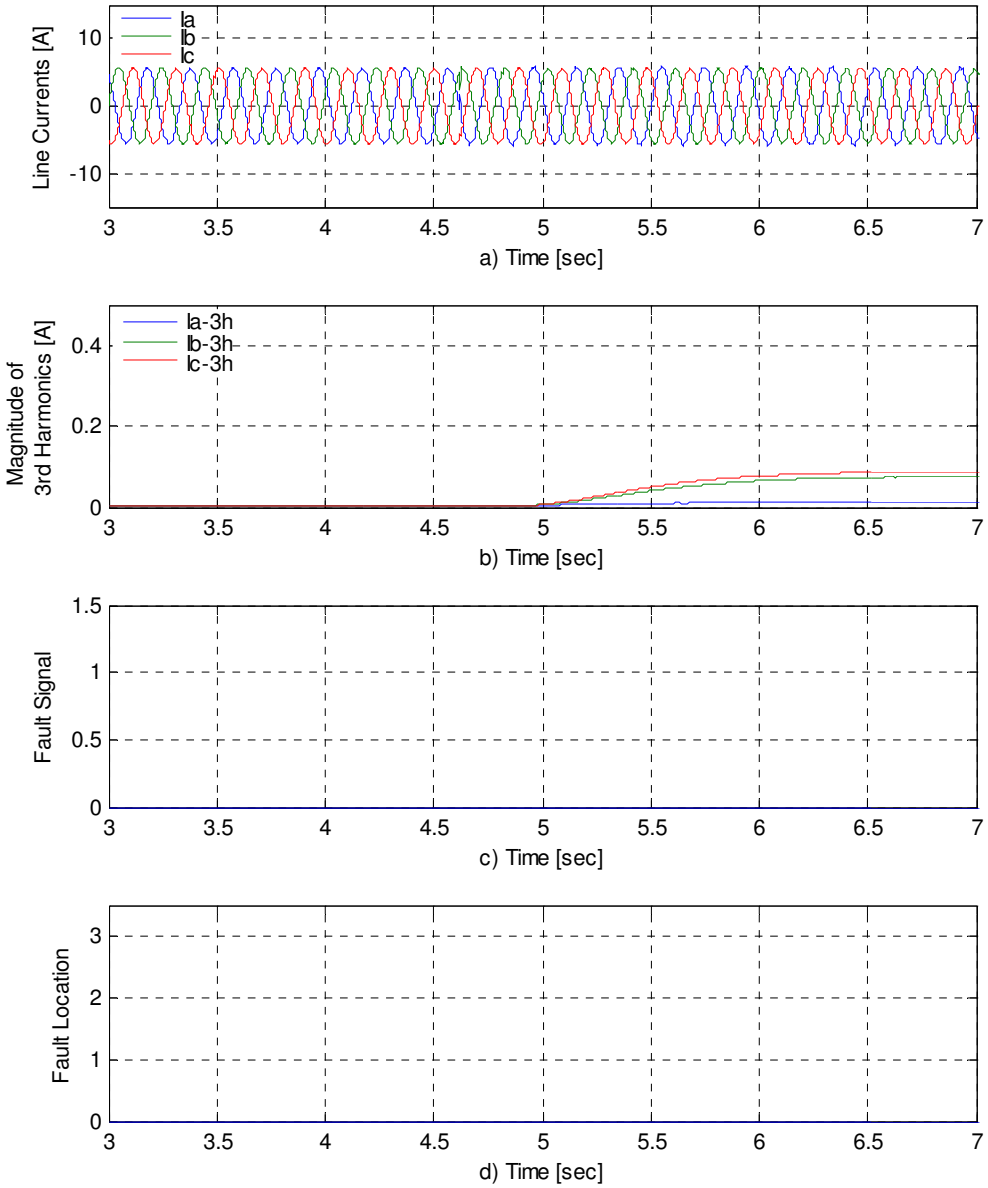

Fig. 7.12 Experiential result, transition between pre fault and faulty mode at 31.4rad/sec, full flux and no load with open circuit fault in phase *a*. a) three line currents, b) on-line estimation of the magnitude of the third harmonic component in the line currents, c) fault detection signal, d) fault location.

7.3 SIMULATION AND EXPERIMENTAL RESULTS OF FAULT TOLERANT CONTROL

This section presents the usefulness of using the proposed fault tolerant control technique for delta connected induction machine when an open circuit winding fault occurs. The basic approach employs a feedforward term to control the zero sequence voltage in the *dqo* frame of reference as discussed in Section 6.3. All the experimental tests and simulation results were obtained with the machine operating with IRFO control structure as presented in Fig. 6.4.

The simulations and experimental tests to show the behaviour of the delta connected motor drive with a stator open circuit fault performed under the conditions defined in Table 7.2. The machine was driven at 150 rad/sec to prevent the occurrence of a voltage saturation problem of the drive. This problem is discussed in section 7.4. The simulation of the faulty machine has been carried out with an open circuit fault in phase *a.*

Table 7.2 Simulation and experimental conditions showing the behaviour of the induction motor drive system for verifying the proposed fault tolerant control technique

Item	**Unit**	**Conditions**
Control Mode	-	IRFO with feedforward compensation terms
Reference Speed	[Rad/sec]	150
Torque Reference	[N.m]	27
Rated Field Current i_{sd}	[A]	4.9
Rated Torque Current i_{sq}	[A]	9
Limit of Torque Current i_{sq}	[A]	10.5
Fault Location	-	On the a-phase winding

The simulations to show the behaviour of an induction machine drive with a stator open circuit fault are performed under the conditions 150 rad/sec, full rated flux, and 100% of the nominal load. Fig. 7.13 starts with the healthy machine. At time = 2.5 sec the open circuit fault occurs in phase *a*. The transient responses of the speed and developed torque produced before and after the presence of an open phase fault are presented in Figs. 7.13(a) and (b), respectively. The phase currents, *d* and *q* current components, the current controller output V_{sd} and V_{sq} voltages are presented in Figs. 7.13(c-f), respectively. Fig. 7.14 shows the simulation results for the same operating conditions as in Fig. 7.13 but after the feedforward compensation term has been applied. At time = 3.5 sec, the feedforward terms (6.24) is introduced into the zero sequence component of the *d-q* reference voltages. Fig. 7.15 shows the frequency spectrum for the same operating conditions as in Fig. 7.13 after the fault occurs. For comparison, Fig. 7.16 shows the frequency spectrum for the same operating conditions as in Fig. 7.14 after the feedforward term is applied. The complex frequency spectrum of the phase currents and the electromagnetic torque with an open circuit fault are presented in Figs. 7.15 (a & b) and 7.16 (a & b) respectively. The spectrum analysis of the current controller output V_{sd} and V_{sq} voltages are presented in Figs. 7.15 (c & d) and 7.16 (c & d).

For the condition where there is *NO* feedforward term is introduced in the *dqo* reference frame during fault mode, there is an unbalance in the amplitudes of the three motor supply currents as shown in Figs. 7.13(c) and 7.14(c). This is due to the existence of a negative sequence fundamental component in these currents [94]. The two remaining motor currents have two different magnitudes (i_b = 12.54A and i_c = 14.84A) and the presence of a negative sequence fundamental component in these currents is shown in Fig. 17.5(a). As a result, an additional oscillatory component appears in the *d-q* voltage references at twice the fundamental excitation as shown in Figs. 7.15(c & d). It can also be observed that the 4^{th} and 6^{th} harmonic components have appeared in the V_{sd} and V_{sq} voltages, which are due to the presence of the 3^{rd} and 5^{th} harmonic components of the winding currents (due to saturation and non-linear power converter effects) when they are transferred to the *d-q* reference frame.

In addition, this negative sequence component interacts with the fundamental stator flux, thus giving rise to the appearance of an oscillatory component in the electromagnetic torque at double the supply frequency. This would be the main indicator of the presence of the fault when analysing the torque signal (Fig. 7.15(b)) [94]. Moreover, the third harmonic component of the flux does not cancel out as it does during balanced operation. This produces additional oscillatory components in the electromagnetic torque, mainly the 2^{nd} and 4^{th} harmonic components as shown in Fig. 7.15(b). The saturation induced 3^{rd} and 5^{th} harmonic components of the current interact with the fields of the space harmonics of the MMF respectively to create together a 4^{th} harmonic in the electromagnetic torque. The same concept is valid for the higher order harmonic components (6^{th}, 8^{th}, and 10^{th}) that appear in the electromagnetic torque. It is clear from these results, operation without a fault tolerant control strategy is undesirable as it imposes severe torque pulsations on the drive.

Furthermore, for the results presented in Figs. 7.14 (b) and (d – e), the torque reference with feedforward compensator decreases slightly when compared to that before feedforward compensation is utilised. This is explained by the fact that the torque component generated from the negative sequence current component that acts against the developed torque is eliminated by eliminating the negative sequence current component. The decreased torque reference and eliminated negative sequence current component lead to decreased amplitude of the *q*-axis current reference. While the flux controller maintains the same amplitude of the *d*-axis current reference as shown in the green and red traces of Fig. 7.14(d). Consequently, the simulated results in Figs. 7.14(e & f) show that an open circuit fault results in a decrease in the amplitudes of the *d*-and *q*-axis voltage references when compared to those for the fault condition without compensation.

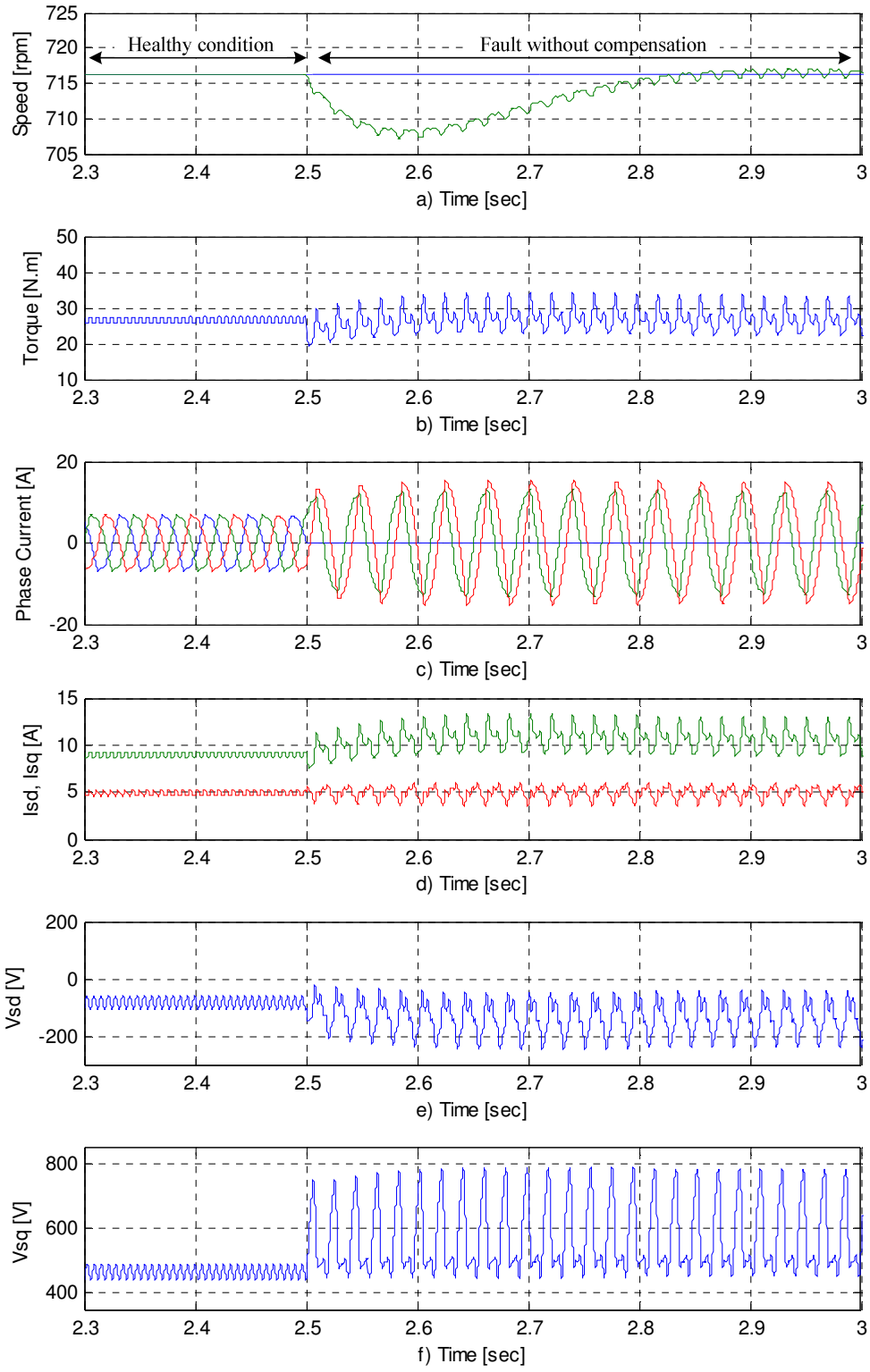

Fig. 7.13 Simulation results of induction motor using IRFO vector control at 150 rad/sec rotating speed, full rated flux and 100% of the nominal load before and after an open circuit fault in phase *a*. a) speed, b) torque, c) phase currents, d) *d-q* current components, e) V_d voltage, f) V_q voltage.

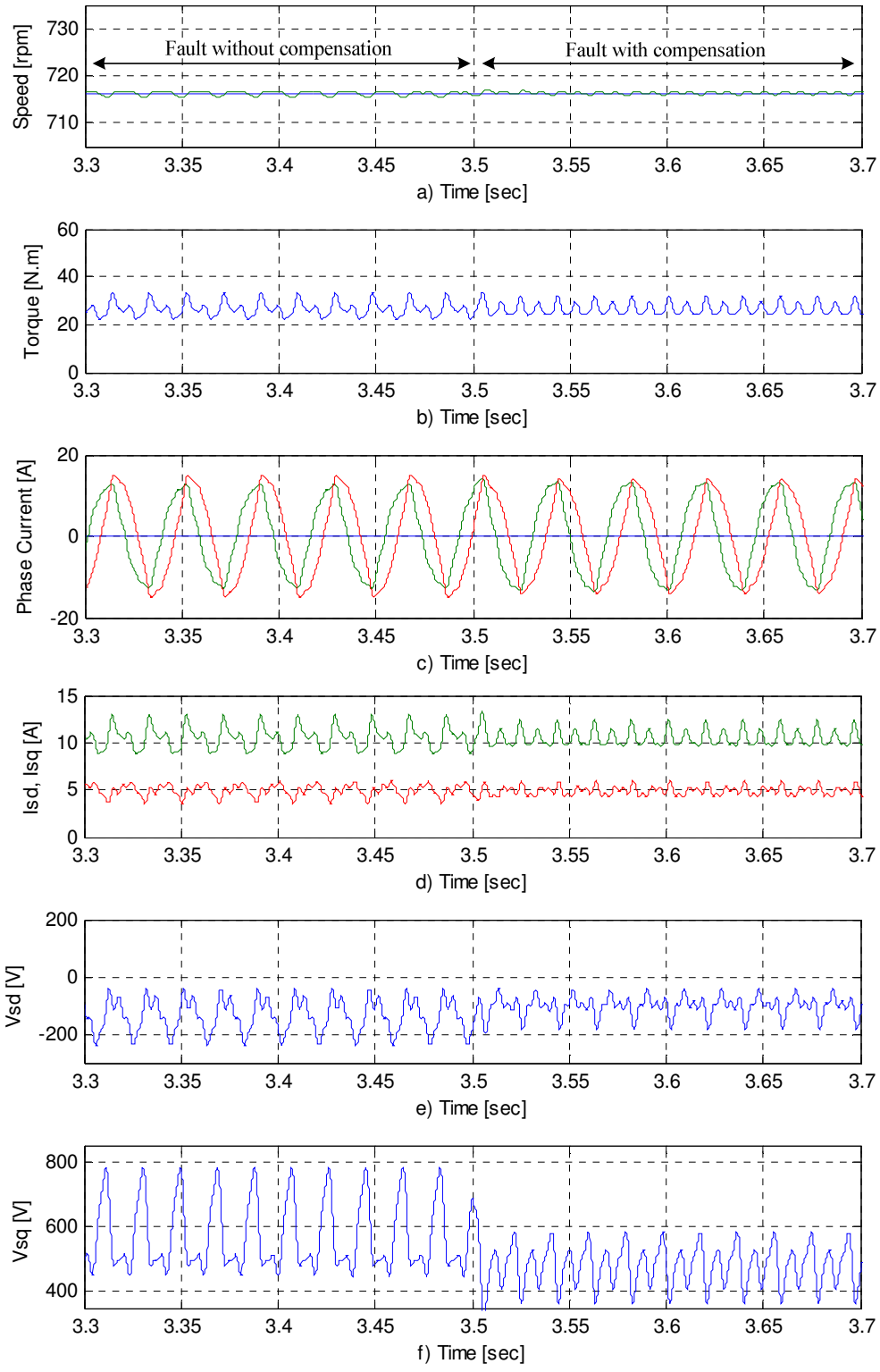

Fig. 7.14 Simulation results of induction motor using IRFO vector control at 150rad/sec rotating speed, full rated flux and 100% of the nominal load with an open circuit fault in phase *a* before and after the feedforward compensation term applied. a) speed, b) torque, c) phase currents, d) *d-q* current components, e) V_d voltage, f) V_q voltage.

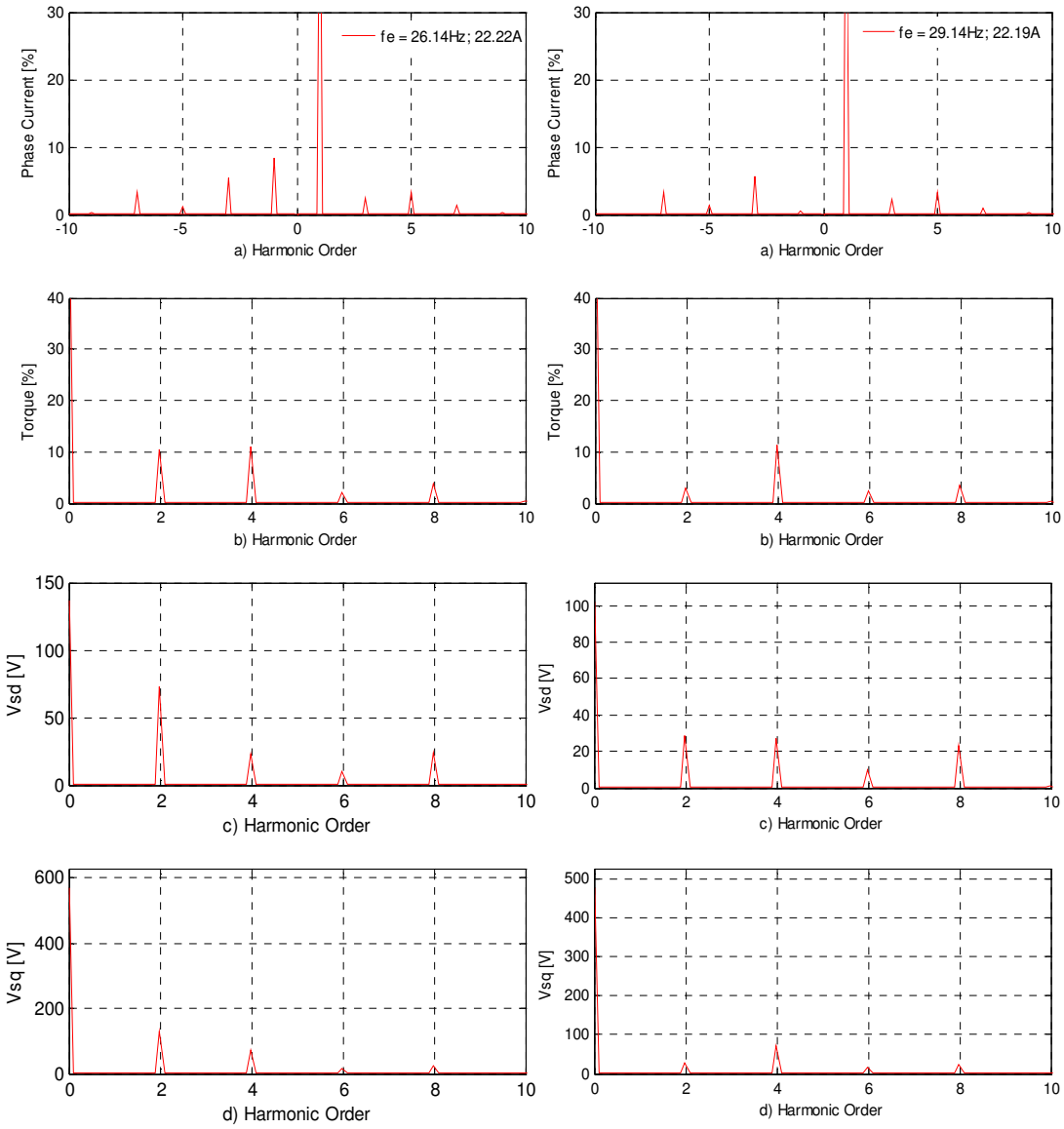

Fig. 7.15 Simulation results, two dimension complex frequency spectrum at 150 rad/sec, full rated flux and 100% of the nominal load with an open circuit in phase *a* a) phase currents, b) torque, c) V_d voltage, d) V_q voltage.

Fig. 7.16 Simulation results, two dimension complex frequency spectrum with the feedforward compensation at 150rad/sec, full rated flux and 100% of the nominal load with an open circuit in phase *a* a) phase currents, b) torque, c) V_d voltage, d) V_q voltage.

For comparison and validating the simulation and experimental results, Figs. 7.17 – 7.20 show the experimental results for the same operating conditions as Figs. 7.13 – 7.16. By comparing Figs. 7.17 and 7.18 with Figs. 7.13 and 7.14, the transient of the current is well predicted by the model. The experimental results also show some higher order oscillations, indicating the existence of higher order harmonics in the flux (e.g. slot harmonics). These are not present in the simulation result, as the model only accounts for the 3^{rd}, 5^{th} and 7^{th} harmonic of flux distribution. Figs. 7.18(e & f) and 7.14(e & f) show the behaviour of the *d-q* voltages, with a slight reduction in amplitude of the simulation results compared to the experimental results. This is due to the simplifications made in the modelling of the saturation effect, where the saturation model has not been tuned for fault conditions. Once again, the simulation and experimental results are in very good correlation.

By comparing Figs. 7.15(a) and 7.19(a), the simulation results for the stator winding current match the experimental results but with a slight mismatch in the amplitude of the 5^{rd} and 7^{th} components. This is probably due to the simplifications made in the modelling of the saturation effect. The saturation model has been tuned when the machine was running under faulty condition - a different operating condition to the one used in this test. Similarly comparing Figs. 7.19(b) and 7.15(b), the magnitude of the 2^{nd} component in the simulation result of the electromagnetic torque is smaller than the experimental value. This is probably due to the estimation method used to calculate the electromagnetic torque experimentally is not very accurate (Section 4.2). The experimental and simulation results are however in very good agreement and are suitable for the objectives of this project.

The simulation and experimental results demonstrate that the proposed feedforward compensation scheme has a considerable influence on the performance of an induction motor with an open circuit fault, reducing torque pulsations and the harmonic content of the motor current.

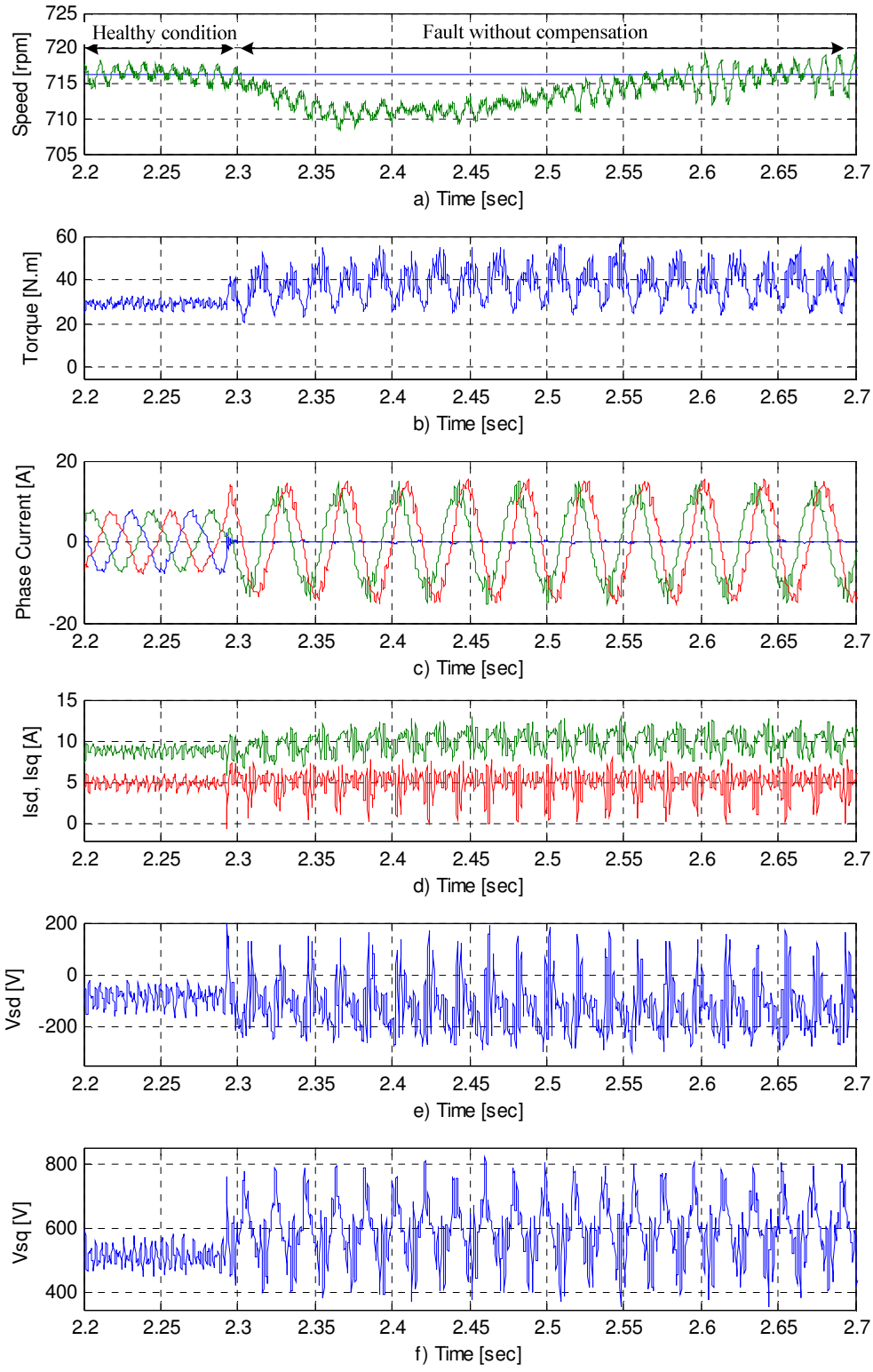

Fig. 7.17 Experimental results of induction motor using IRFO vector control at 150rad/sec rotating speed, full rated flux and 100% of the nominal load before and after an open circuit fault in phase *a*. a) speed, b) torque, c) phase currents, d) *d-q* current components, e) V_d voltage, f) V_q voltage.

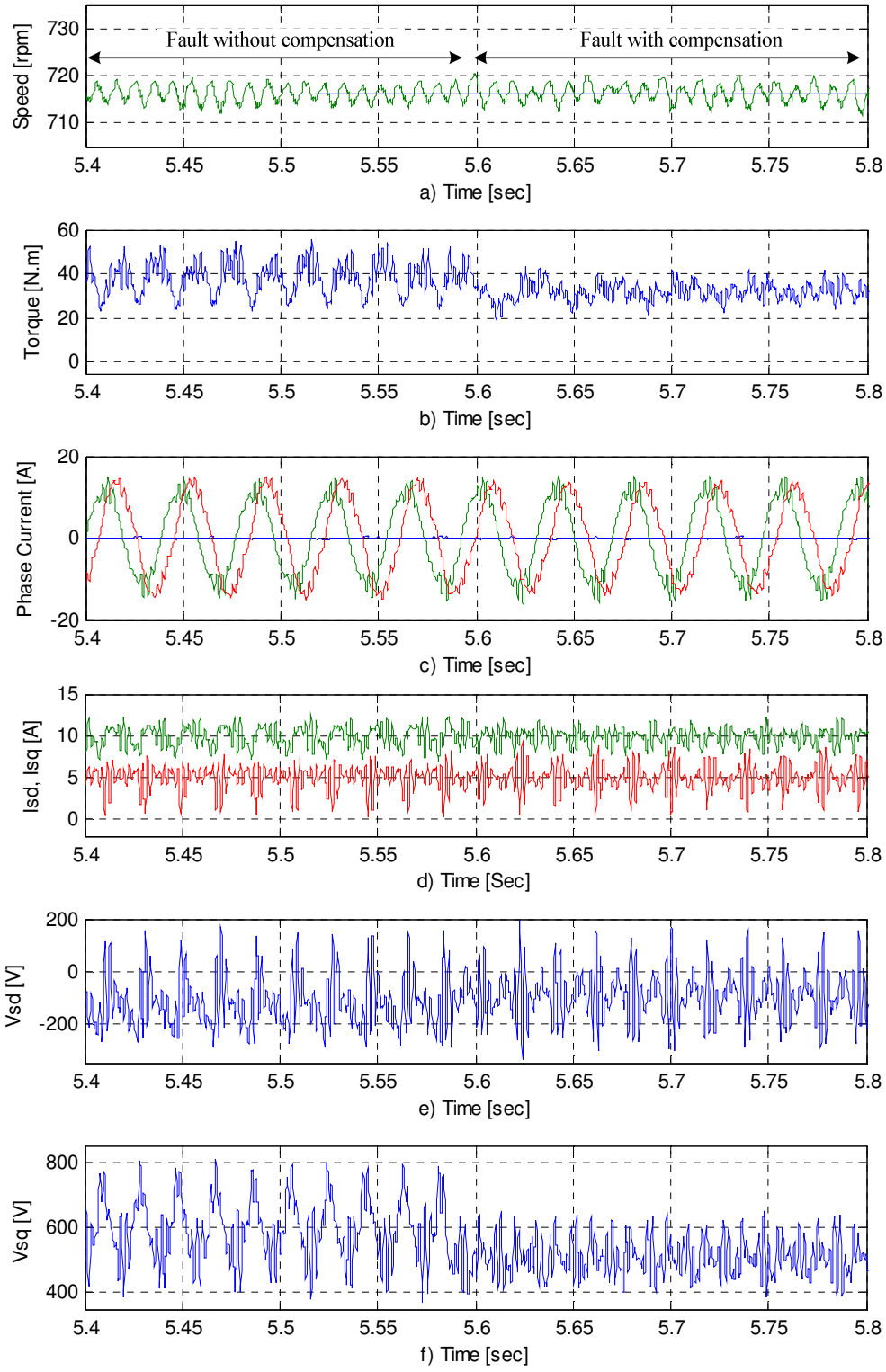

Fig. 7.18 Experimental results of induction motor using IRFO vector control at 150rad/sec rotating speed, full rated flux and 100% of the nominal load with an open circuit fault in phase *a* before and after the feedforward compensation term applied. a) speed, b) torque, c) phase currents, d) *d-q* current components, e) V_d voltage, f) V_q voltage.

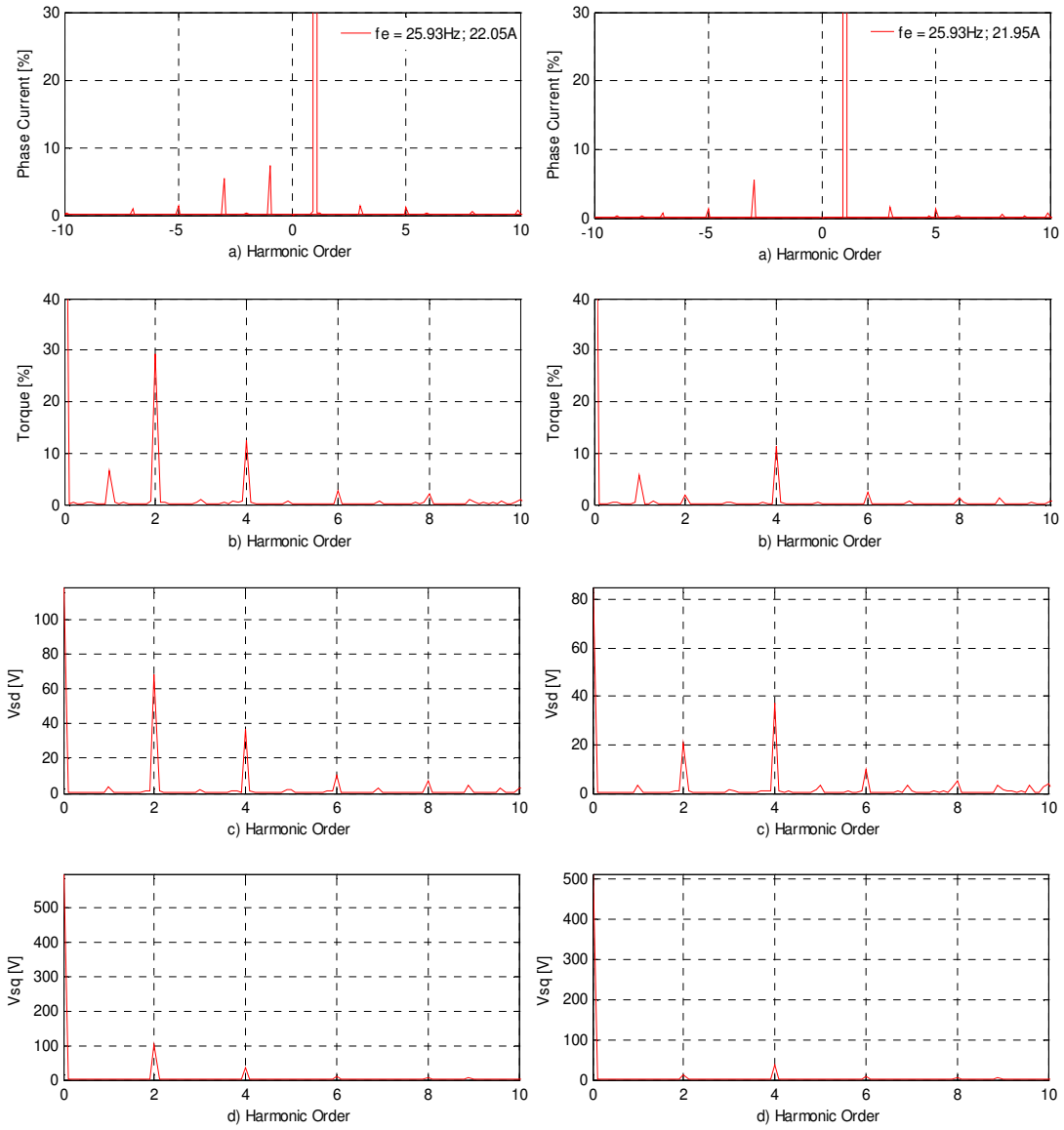

Fig. 7.19 Experimental results, two dimension complex frequency spectrum at 150 rad/sec, full rated flux and 100% of the nominal load with an open circuit in phase *a* a) phase currents, b) torque, c) V_d voltage, d) V_q voltage

Fig. 7.20 Experimental results, two dimension complex frequency spectrum with the feedforward compensation at 150rad/sec, full rated flux and 100% of the nominal load with an open circuit in phase *a* a) phase currents, b) torque, c) V_d voltage, d) V_q voltage

A further test was carried out using the simulation model and using linear (i.e. non-saturating) iron. Fig. 7.21 shows the simulation result for the same condition as in Figs. 7.13 and 7.14, but the saturation effects were eliminated to leave only the fundamental component. When the fault occurred at time = 2.5 sec, the 2^{nd} harmonic component appears in the electromagnetic torque due to the interaction of the positive and negative sequence fundamental components of flux and current. This is the main indicator of the presence of the fault as mentioned earlier. Moreover, all other components have been eliminated by default. At time = 2.8 sec the feedforward compensation term is utilised to eliminate the negative sequence current component. By comparing Figs.7.22 and 7.23, one can realize that under the control strategy described, the negative-sequence fundamental component in the winding currents has been eliminated. In addition, the oscillatory component in the electromagnetic torque at double the supply frequency is reduced as shown in Figs.7.22 (b) and 7.23 (b). The two remaining motor currents are now equal in magnitude as shown in Fig. 7.21(c). The result in Figs. 7.21(e & f) and 7.23 (c & d) show the *d-q* voltages at the inverter terminals. They do not have the unwanted second harmonics after the feedforward terms was applied. As indicated from these results, the operation of an induction motor with an open circuit fault without the proposed feedforward compensation scheme is undesirable as it imposes severe torque pulsations on the drive.

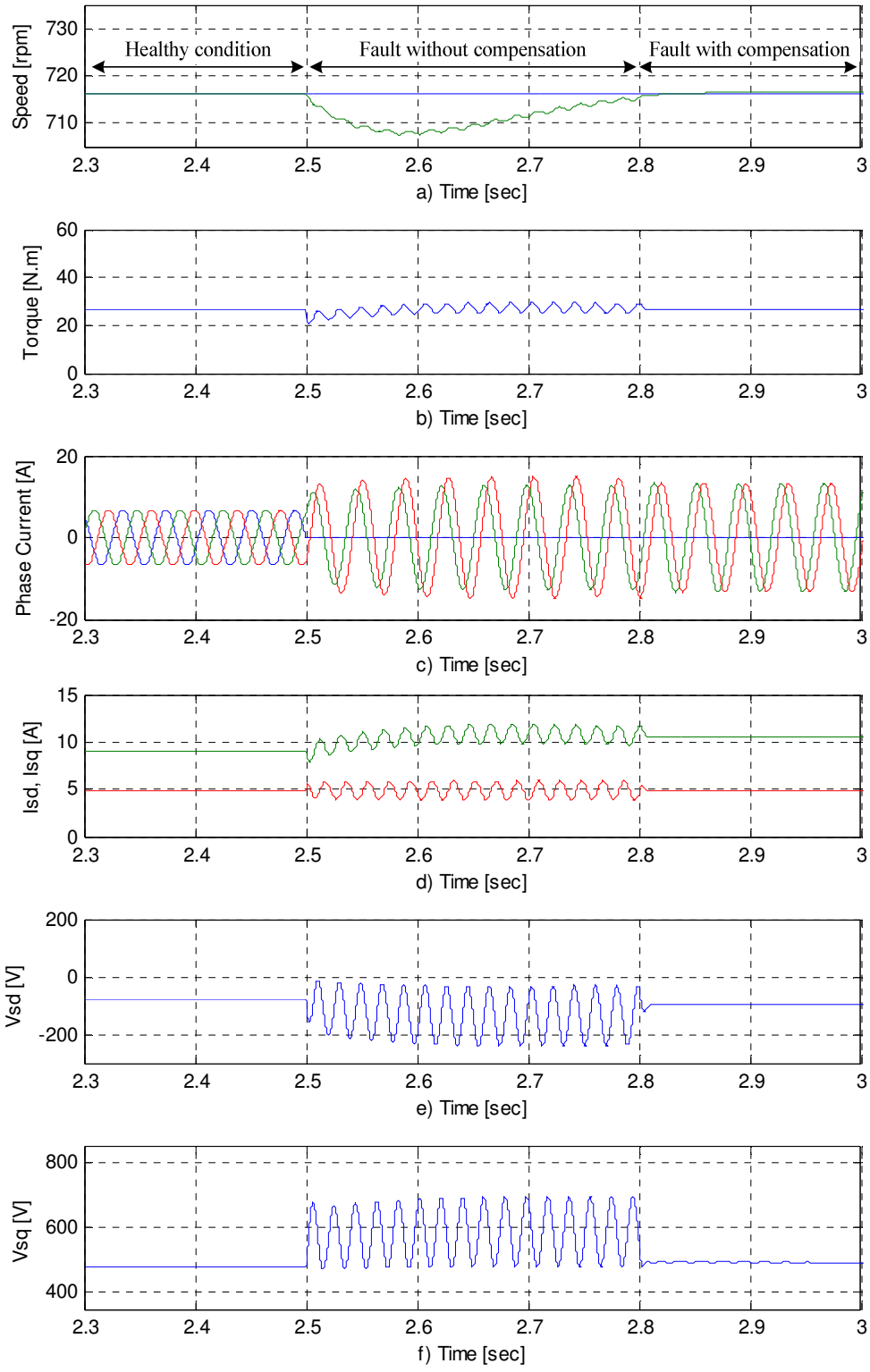

Fig. 7.21 Simulation results of induction motor using IRFO vector control at 150rad/sec rotating speed, full rated flux and 100% of the nominal load using linear iron with an open circuit fault in phase *a* before and after the feedforward compensation term applied. a) speed, b) torque, c) phase currents, d) *d-q* current components, e) V_d voltage, f) V_q voltage.

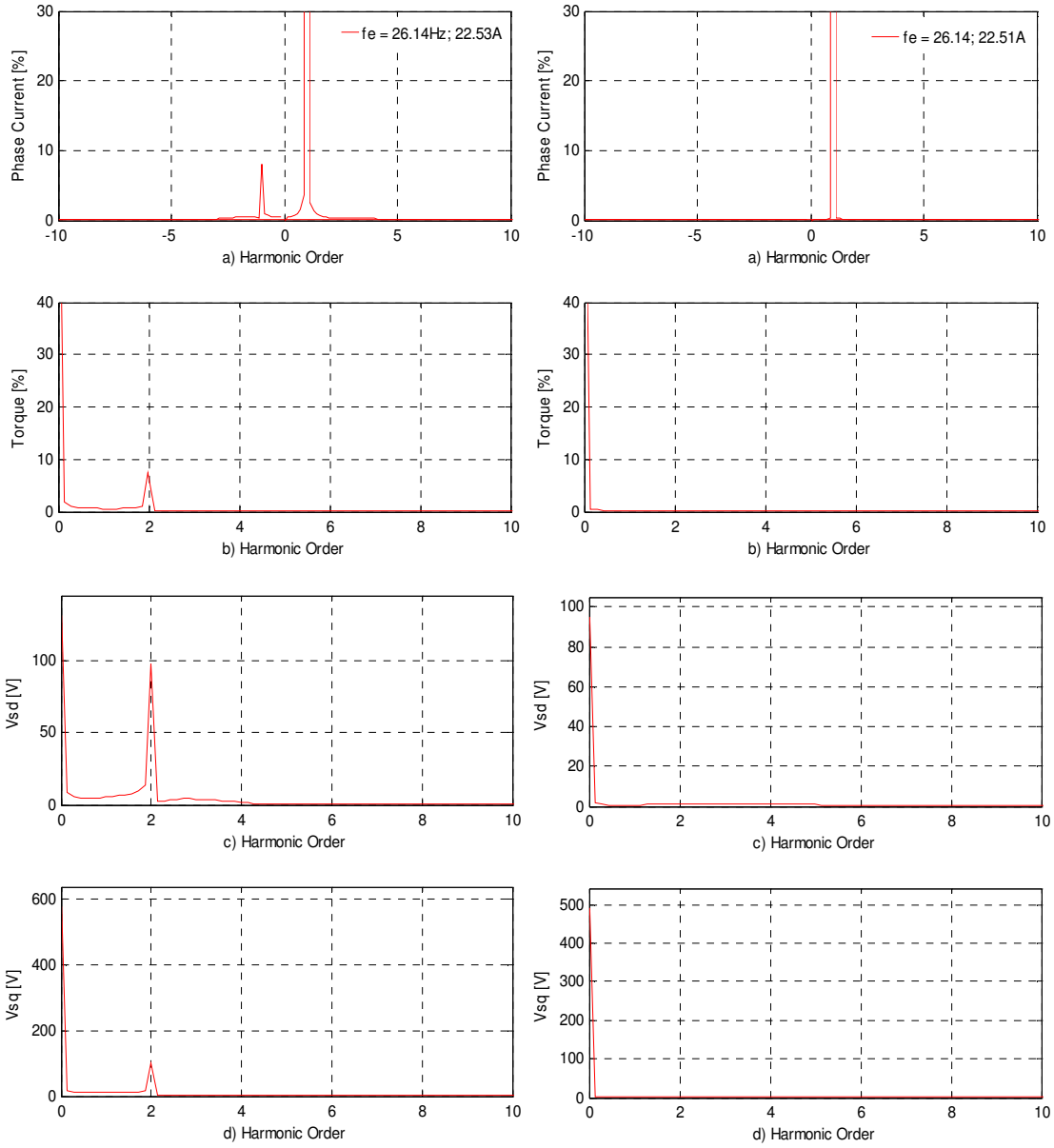

Fig. 7.22 Simulation results, two dimension complex frequency spectrum at 150 rad/sec, full rated flux and 100% of the nominal load using linear iron with an open circuit in phase *a* a) phase currents, b) torque, c) V_d voltage, d) V_q voltage

Fig. 7.23 Simulation results, two dimension complex frequency spectrum with the feedforward compensation at 150rad/sec, full rated flux and 100% of the nominal load using linear iron with an open circuit in phase *a* a) phase currents, b) torque, c) V_d voltage, d) V_q voltage

7.4 SIMULATION AND EXPERIMENTAL EVALUATION OF THE FAULT RIDE THROUGH SYSTEM

The section aims to verify the key prosperities of the fault tolerant control algorithm described in Section 6.4 (i.e. fault tolerant control with the proposed online fault detection technique and operation of the field weakening region). The simulation and experimental results of the fault control strategy specifically for delta connected induction motors, which suffer an open winding fault are presented in this section. Fault ride through is achieved without any modification to the power converter or motor circuit. The basic approach employs a feedforward term to control the zero sequence voltage in the *dqo* frame of reference as discussed in Section 7.3. For operation at higher speeds, two different field weakening algorithms are incorporated with the feedforward compensation scheme.

This section is divided into two subsections; the first presents the fault operation of the induction machine by modulating the neutral point to zero volts (*Method I*) as discussed in Section 6.4.1.1. The second subsection presents and discusses the operation of the fault operation condition of the induction machine by modulating the neutral point voltage (*Method II*) as discussed in Section 6.4.1.2. For each one of these modulating methods of the neutral point, two different field weakening control techniques were used to validate the fault tolerant control technique with different operating conditions.

7.4.1 Results of Using Method I – Modulating the Neutral Point Voltage to 0V

During fault operation, the voltage of the neutral point is maintained to be 0V in this method. This is achieved via the transformation block X in Fig. 6.4. When an open fault occurs in phase *a, Method I* employs the equations (6.45 – 6.47) for the transformation X. Two different field weakening methods have been proposed which are used in conjunction with the fault tolerant control algorithm. The following two sections will discuss and present the results of the two different schemes.

7.4.1.1 Results of Using Method I and Open Loop Field Weakening Control

The experimental results for the transition between healthy, faulted and fault corrected mode (open circuit in phase *a*) using Method *I* at a speed of 200 rad/sec rotating speed, rated flux and no load is presented in Fig. 7.24. At this speed, an open loop field weakening control scheme is required while in the fault mode. Without field weakening, machine control would be lost and the motor would stall. Fig. 7.24 starts with a healthy machine. The fault was made by imposing an open circuit fault in phase *a* at time = 3.475 sec. The transient responses of the speed and developed torque produced before and after the presence of an open phase fault are presented in Figs. 7.24(a & b), respectively. The three phase currents, *d* and *q* current components with its references, the current controller output V_{sd} and V_{sq} voltages are presented in Figs. 7.24(c – g), respectively. The complex frequency spectrum of the phase currents and developed torque with an open circuit fault produced before and after applying the feedforward compensation term are presented in Figs. 7.25 (a – d) respectively.

During the period time = 3.475 – 3.565 sec, no feedforward term is introduced in the *dqo* reference frame. The two remaining motor currents have two different magnitudes (i_b = 5.3A and i_c = 6.12A), and the presence of a negative sequence component in these currents is shown in frequency spectra of Fig. 7.25(a). In addition, the third harmonic component of the flux does not cancel out as it does during balanced operation. This produces additional oscillatory components in the electromagnetic torque, mainly the second harmonic component as shown in Fig. 7.25(b).

The operation of the on-line fault detection and identification algorithm detects the fault when the third harmonic component appears in the line currents after the fault occurs. The fault has been detected at time = 3.565 sec after the output of third harmonic estimator exceeds the fault threshold value; this occurs within 0.09 sec.

The feedforward term is introduced in the *dqo* reference frame with the open loop field weakening controller that was illustrated in Fig. 6.7. The proper current control was maintained by reducing the stator phase-neutral voltage by field weakening (i.e.

reducing i_{sd}^{*}). It can be seen that the reduction of i_{sd}^{*} is limited to 1.7A as shown in Fig. 7.24(d). This limit is chosen to prevent a complete demagnetization and i_{sd} from becoming negative at transients. Once the flux has settled, the steady state value of the i_{sd}^{*} will be the same value of i_{mrd}^{*} which is calculated using equation (6.65). Consequently, the speed controller maintains a constant speed. After the system has settled, it can be observed that the ripple in the speed, torque, and current are significantly decreased. For comparison, the frequency spectra of Figs. 7.25(a & b) (no compensation) and 7.25(c & d) show that the negative-sequence component in the current and the 2nd harmonic component in the electromagnetic torque are reduced when the feedforward compensation term is used. Furthermore, it can be seen that the positive and negative third harmonic components in the current are also reduced. This is mainly due to the reduction in the flux, which is a result of using field weakening control. In addition, all inductance parameters are known to be nonlinear functions of the motor flux level, and hence may change either intentionally, under field weakening, or unintentionally, under detuning of the controller [133]. Consequently, the variation of the machine inductance with flux level can affect the performance of the induction motor drive under IRFO control. This problem can be over come by using a lookup table that contains the inductance values as a function of the i_{sd} to change the controller values for rotor time constant ($T_r = L_r / R_r$), stator and rotor self inductance (L_s, L_r), stator and rotor leakage inductance (L_{ls}, L_{lr}) that have been used for vector control algorithm and the calculation of the zero sequence voltage. The variation of the inductance values with the flux level is not included in this work and set to be for a future work.

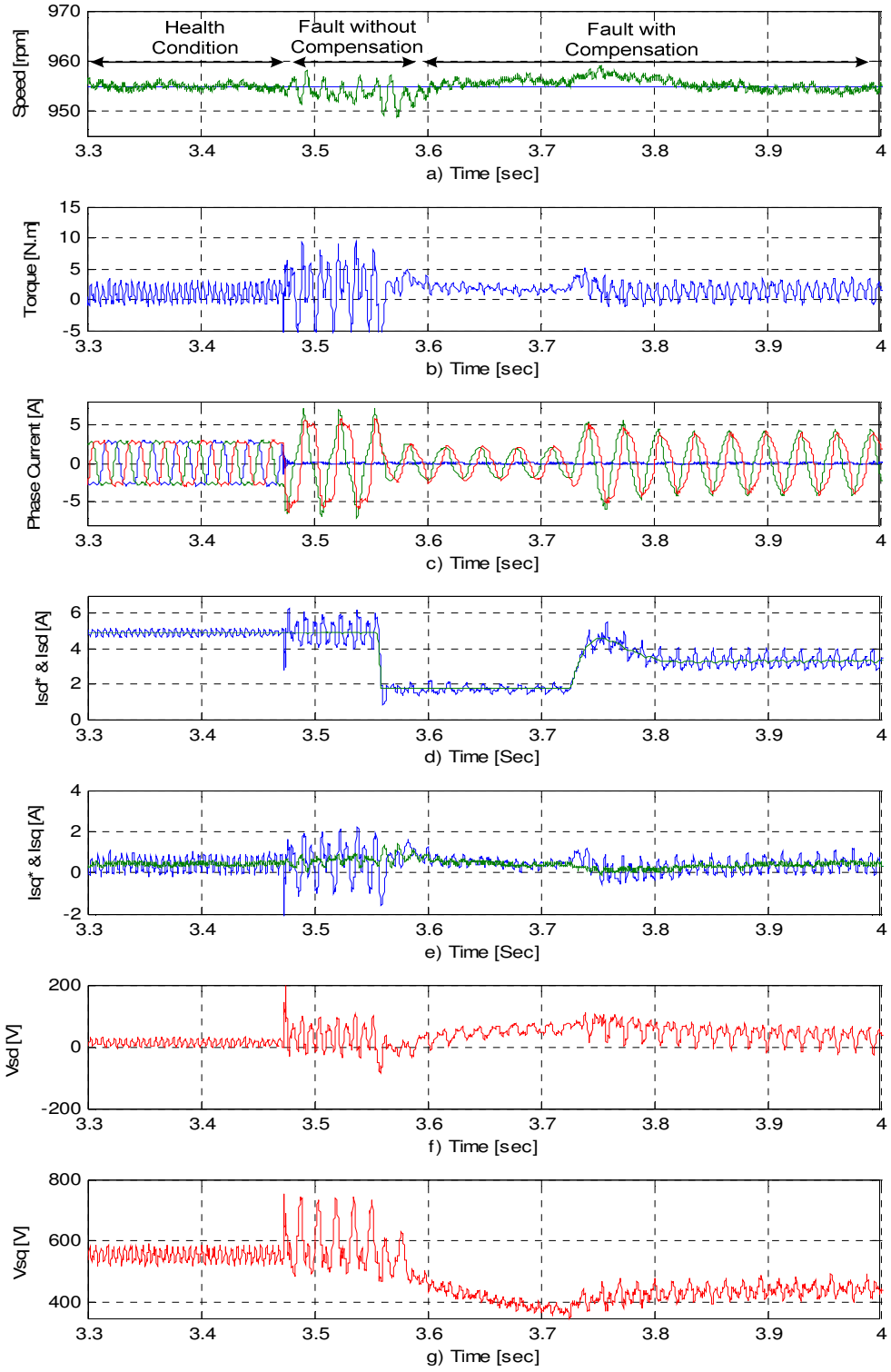

Fig. 7.24 Experimental results, transition between pre fault and fault mode with the compensation algorithm (Method I) and open loop field weakening at 200 rad/sec rotating speed and no load with an open circuit in phase *a*. a) speed, b) torque, c) phase currents, d) I_{sd} & I_{sd} ref., e) I_{sq} & I_{sq} ref., f) V_d voltage, g) V_q voltage.

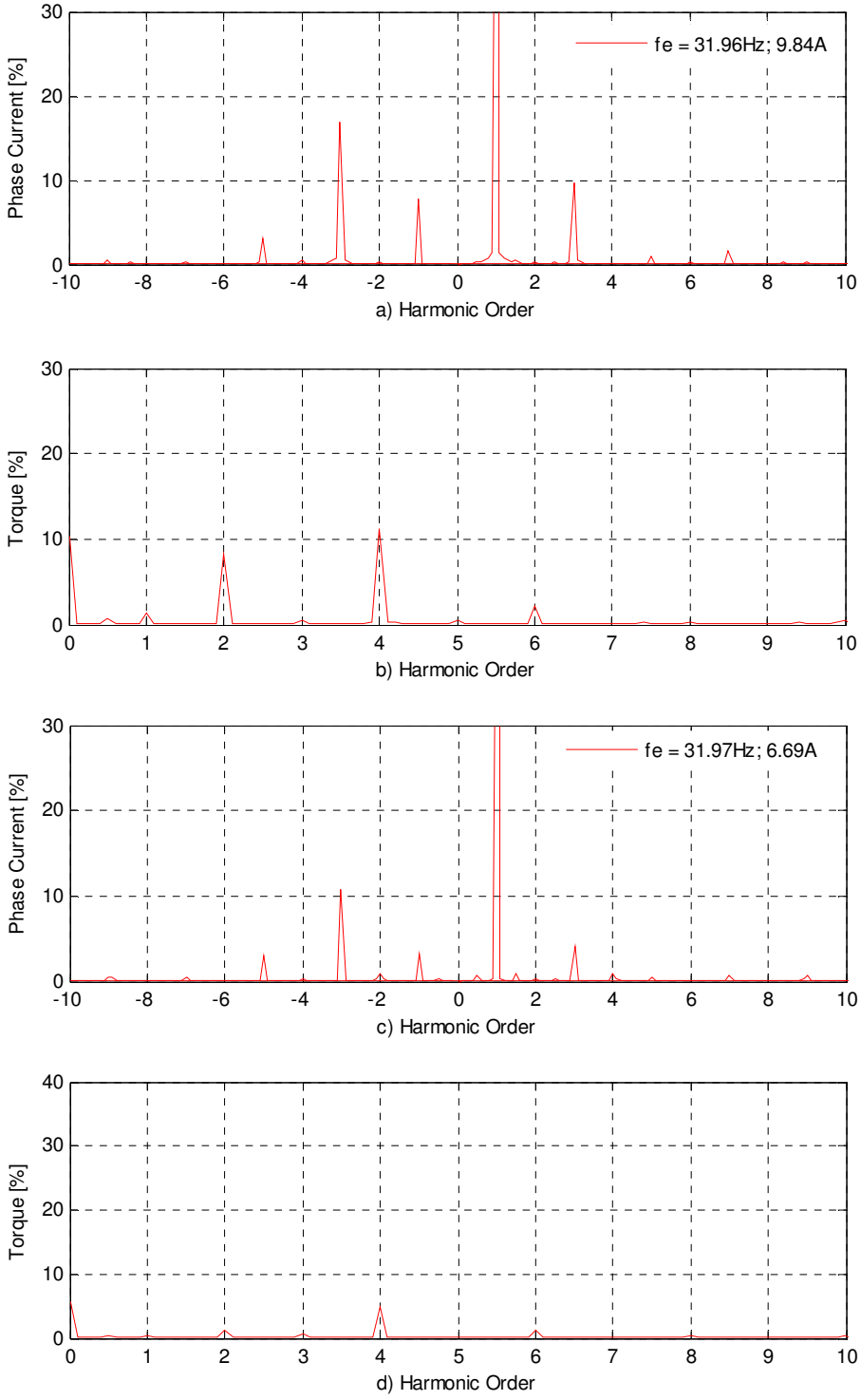

Fig. 7.25 Experimental results, two dimension complex frequency spectrum at 200 rad/sec and no load before and after the feedforward terms applied with an open circuit in phase. a) phase currents, b) torque, c) phase currents with compensation, d) torque with compensation.

For comparison, Figs. 7.26 and 7.27 show the simulation results for the same operating conditions as Figs. 7.24 and 7.25. Fig. 7.26 starts with the healthy machine, at time = 2.7 sec, and the open circuit fault occurs in phase *a.* The transient of current is well predicted by the model. The control performance of the drive is still satisfactory even after an open circuit fault has occurred. The experimental results also show some higher order oscillations, indicating the existence of higher order harmonics in the flux (e.g. slot harmonics). These are not present in the simulation result as mentioned earlier. During the period time = 2.7 – 2.79 sec, no feedforward term is introduced in the *dqo* reference frame. The two remaining motor currents have two different magnitudes (i_b = 5.19A and i_c = 6.14A), and the presence of a negative sequence component in these currents is shown in frequency spectra of Fig. 7.27(a). By comparing Figs. 7.25(a & b) with 7.27(a & b), it can be seen that the current and electromagnetic torque is well predicted by the model. The fault has been detected at time = 2.79 sec after the output of third harmonic estimator exceeds the fault threshold value and the fault is located in phase *a*. The feedforward term is introduced in the *dqo* reference frame with the field weakening controller and a proper current control was maintained by reducing the stator phase-neutral voltage by field weakening (i.e. reducing i_{sd}^{*}). As a result, the speed controller maintains a constant rotating speed. After the system has settled, it can be seen that the ripple in the speed, torque, and current are reduced. The frequency spectra of Figs. 7.27(a & b) (no compensation) and 7.24(c & d) show that the negative-sequence component in the current and the 2nd harmonic component in the electromagnetic torque are reduced when the feedforward compensation term is used. It can be seen that the positive and negative 3rd harmonic components in the current are left the same as before applying the field weakening control. This is due to the saturation profiles of the proposed induction model being tuned when the machine was working under full rated flux and different load levels as discussed in Section 3.5. Therefore, the magnitude of the third harmonic component of the current did not change as it was expected after the flux level reduced. With the exception of this 3rd harmonic component, the agreement between the results obtained by simulation and experiment is suitable for the objectives of this project.

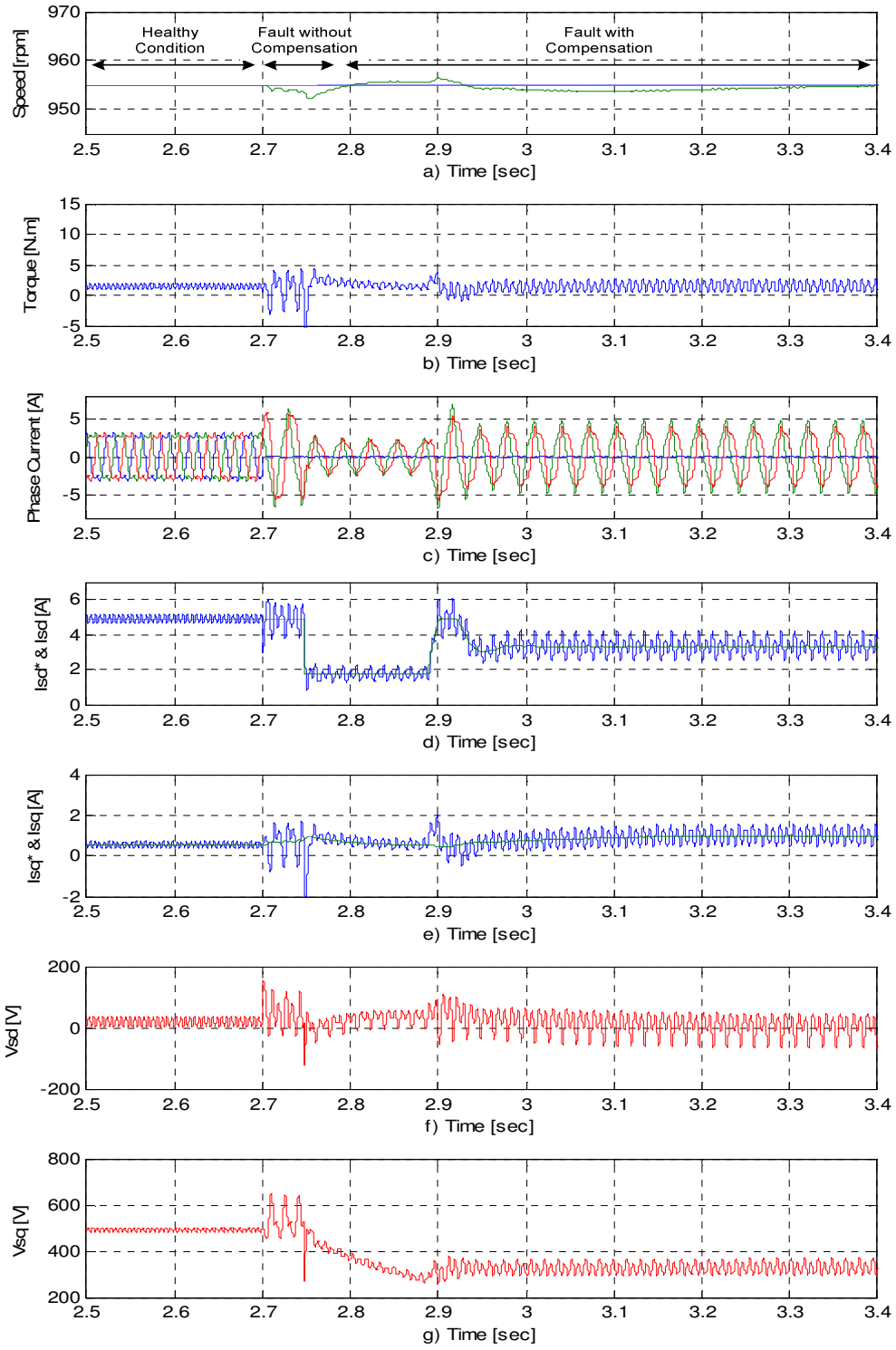

Fig. 7.26 Simulation results, transition between pre fault and fault mode with the compensation algorithm (Method I) and open loop field weakening at 200 rad/sec rotating speed and no load with an open circuit in phase *a*. a) speed, b) torque, c) phase currents, d) I_{sd} & I_{sd} ref., e) I_{sq} & I_{sq} ref., f) V_d voltage, g) V_q voltage.

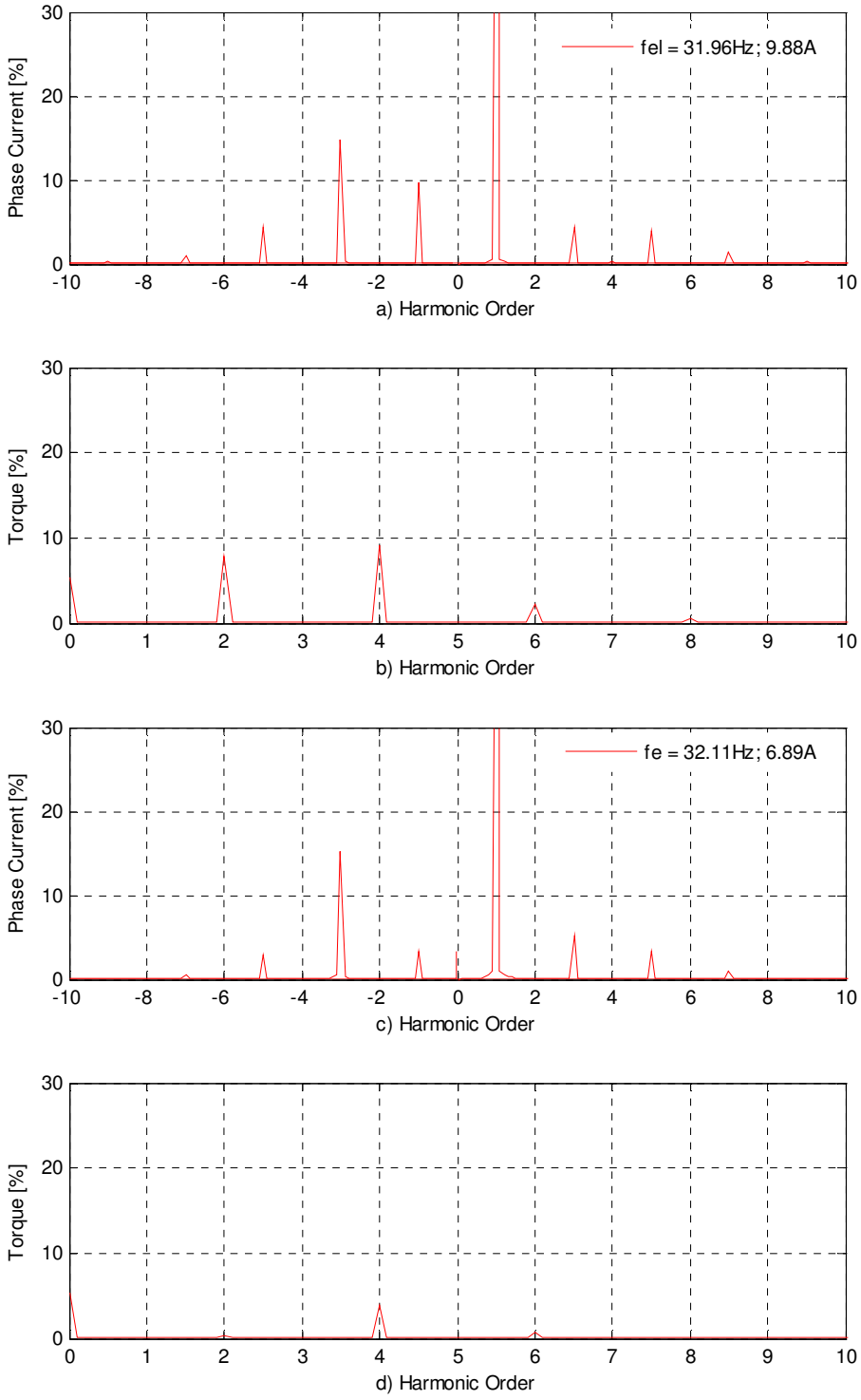

Fig. 7.27 Simulation results, two dimension complex frequency spectrum at 200 rad/sec rotating speed and no load before and after the feedforward terms applied with an open circuit in phase *a*. a) phase currents, b) torque, c) phase currents with compensation, d) torque with compensation.

7.4.1.2 Results of Using Method I and Closed Loop Field Weakening Control

The experimental results for the transition between healthy, faulted and fault corrected mode (open circuit in phase *a*) using Method *I* at a speed of 200 rad/sec rotating speed, rated flux and no load are presented in Fig. 7.28. At this speed, closed loop field weakening control scheme is required and utilised in fault mode. This operating condition is similar to the results that presented in Section 7.4.1.1, in order to compare the performance of the two field weakening schemes. Fig. 7.28 starts with the healthy machine. The fault condition was made by imposing an open circuit fault in phase *a* at time = 2.83 sec. The transient responses of the speed and developed torque produced before and after the presence of an open phase fault are presented in Figs. 7.28(a) and (b), respectively. The three phase currents, *d* and *q* current components with its references, the current controller output V_{sd} and V_{sq} voltages are presented in Figs. 7.28(c to g), respectively. The complex frequency spectrum of the phase currents and developed torque with an open circuit fault produced before and after applying the feedforward compensation term are presented in Figs. 7.29 (a – d) respectively.

During the period time = 2.83 – 2.91 sec, no feedforward term is introduced in the *dqo* reference frame. The two remaining motor currents have two different magnitudes (i_b = 5.3A and i_c = 6.12A), and the presence of a negative sequence component in these currents and the second harmonic component in the electromagnetic torque are shown in frequency spectra of Figs. 7.29(a & b).

The fault has been detected at time = 2.91 sec after the output of third harmonic estimator exceeds the fault threshold value; this occurs within 0.08 sec. During the period time = 2.91 – 3.3 sec, The feedforward term is introduced in the *dqo* reference frame and the PWM voltage demands are calculated through the equations (6.45 – 6.47). It can be seen that the performance of the system was very poor and there are large ripples in the speed, torque and current during this period. This is due to the voltage saturation (over modulation) of the inverter. A limited amount of control can be achieved here; however there is a significant limitation on the maximum available DC link voltage that can be applied to the machine which restricts the motor line voltage and the operating range of the motor considerably. Note that the maximum

phase voltage can be applied is limited to ±1/2 of the DC link voltage ($V_{\max}$ is equal to 320V for the available DC link voltage). When the fault occurs and the new configuration of the PWM voltage demands is utilised without reducing the flux level, the voltage demand passed to the inverter is bigger than $V_{\max}$. Therefore, the inverter was unable to provide enough voltage to the machine. Consequently, i_{sd} and i_{sq} were unable to follow their demands currents as illustrated in Figs. 7.28(d & e). The error is increased and both PI current controllers give large control signals which eventually are limited as shown in Fig. 7.28(f & g). As a result, the PWM voltage demands were increased as shown in Fig. 7.30. When the required machine voltage begins to exceed the maximum voltage due to the increase of the operating frequency, the system enters the field weakening region and the integral controller adjusts i_{sd}^{*} so that the highest inverter voltage cannot exceed $V_{\max}$ as shown in Fig. 7.30. The delay of adjusting i_{sd}^{*} was due to slow response of the adaptive filter that been used to estimate the highest magnitude value of the three PWM voltage demands as demonstrated in Fig. 6.10. Without field weakening, machine control would be lost and the motor would stall.

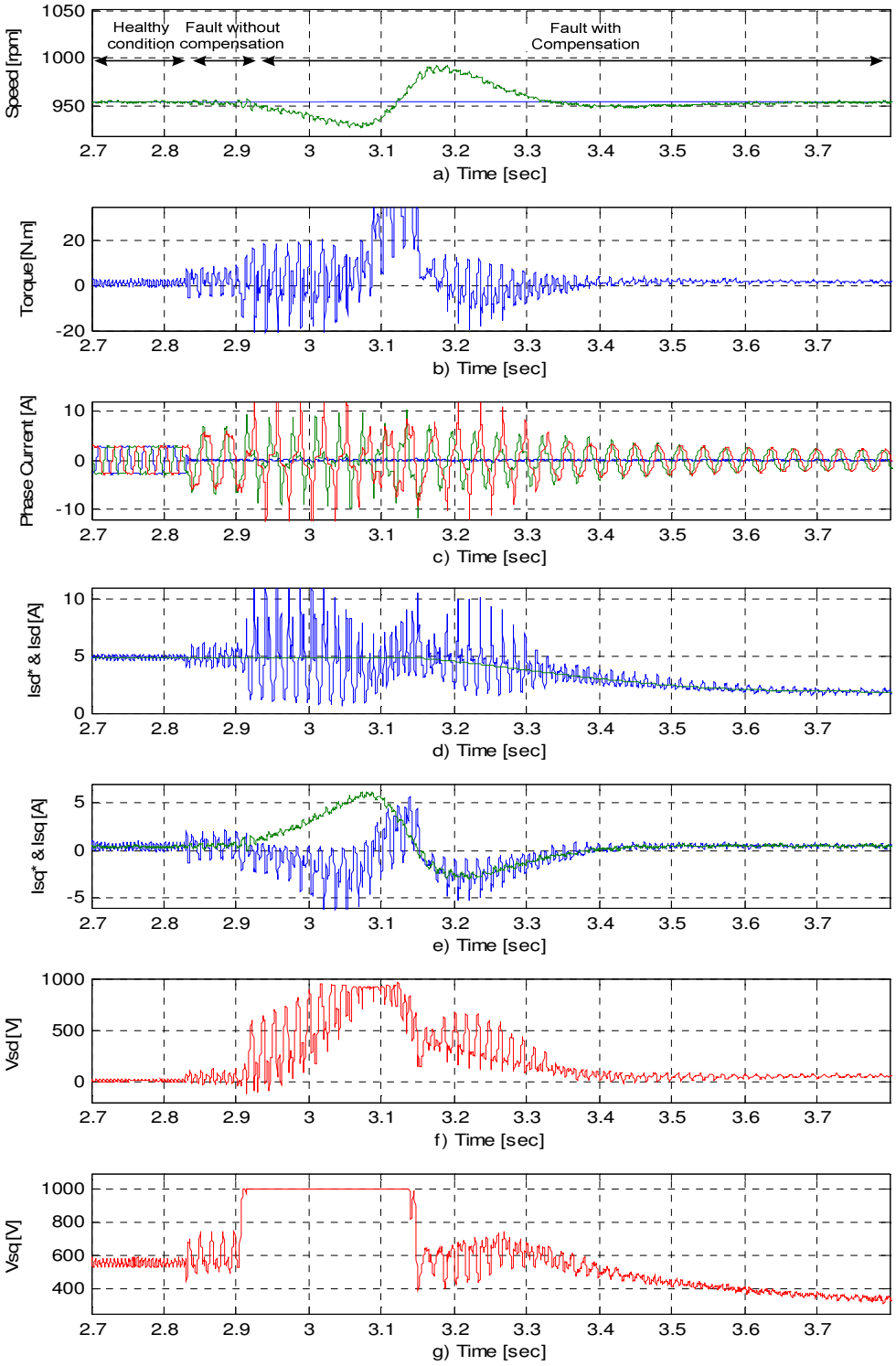

Fig. 7.28 Experimental results, transition between pre fault and fault mode with the compensation algorithm (Method I) and close loop field weakening at 200 rad/sec rotating speed and no load with an open circuit in phase *a*. a) speed, b) torque, c) phase currents, d) I_{sd} & I_{sd} ref., e) I_{sq} & I_{sq} ref., f) V_d voltage, g) V_q voltage.

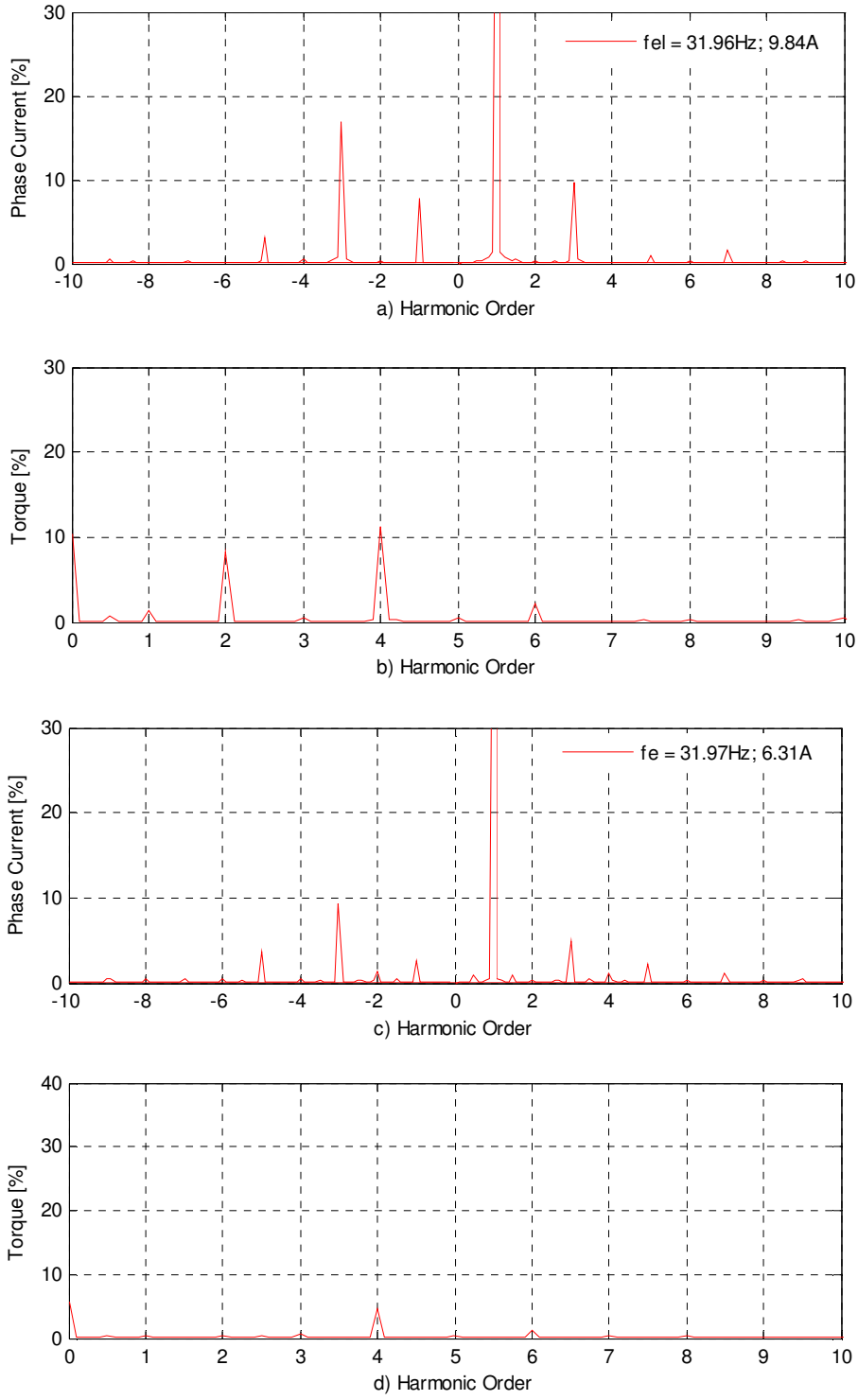

Fig. 7.29 Experimental results, two dimension complex frequency spectrum at 200 rad/sec rotating speed and no load before and after the feedforward terms applied with an open circuit in phase *a*. a) phase currents, b) torque, c) phase currents with compensation, d) torque with compensation.

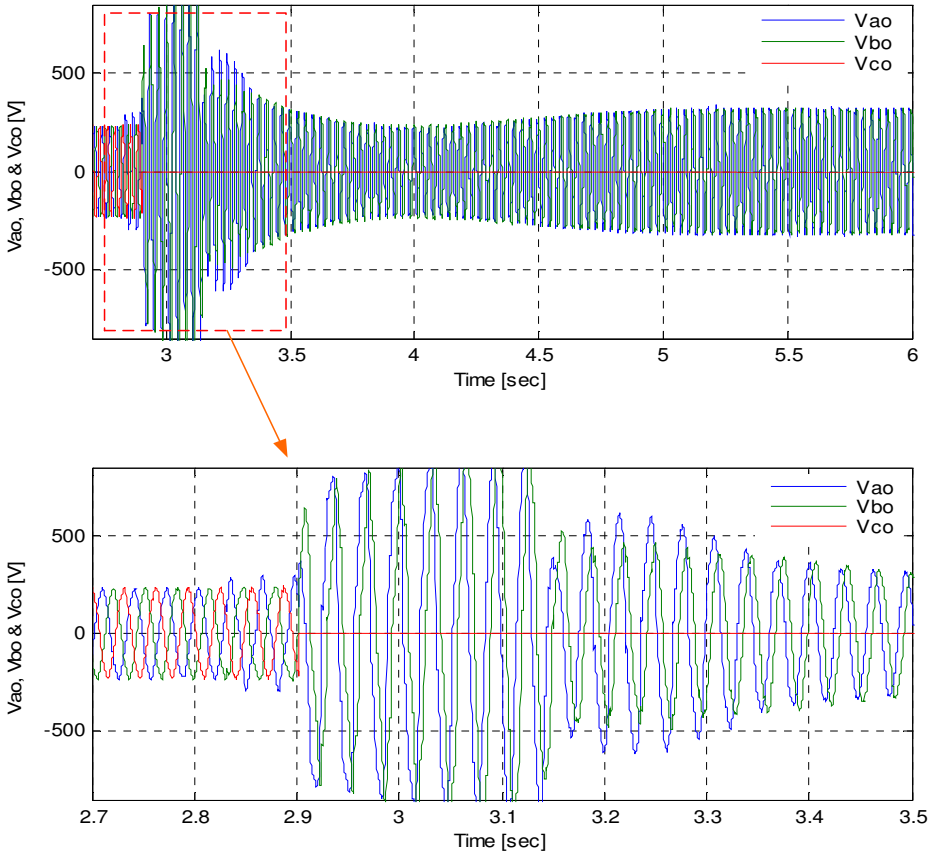

Fig. 7.30 Experimental results, transition of the PWM voltage demands between pre fault and fault mode with the compensation algorithm (Method I) and close loop field weakening at 200 rad/sec rotating speed and no load with an open circuit in phase *a*.

After time = 3.3 sec, the closed loop field weakening controller adjusts the machine input voltage according the inverter maximum voltage, rotating frequency and the load level. The main advantage of this scheme is that it does not need to fix the base speed such as in the case of conventional field weakening and it automatically optimises operation to the load level. After the system has settled, it can be seen that the ripple in the speed, torque, and current are reduced. The frequency spectra of Figs. 7.29(a & b) (no compensation) and 7.29(c & d) show that the negative-sequence component in the current and the 2^{nd} harmonic component in the electromagnetic torque are reduced when the feedforward compensation term is used.

7.4.2 Results of Using Method II – Modulating the Neutral Point Voltage

During fault operation, the voltage of the neutral point is controlled so that the amplitude of the voltage vector produced by the two remaining phases is minimised. This is obtained by ensuring that (V_n) remains smaller than those voltages in the remaining phases. If this condition is met, this approach is suitable for a high speed operation (although additional field-weakening may be needed). This is achieved via the transformation block X in Fig. 6.4. When an open fault occurs i.e. in phase *a, Method II* employs the equations (6.56 – 6.58) for the transformation X. The two different field weakening methods have been utilised which are used in conjunction with the fault tolerant control algorithm. The usefulness of using *Method II* (neutral point control) is demonstrated by choosing a higher speed and load level operating condition compared to the operating condition that was used in *Method I*. The following two sections will discuss and present the results of the two different approaches.

7.4.2.1 Results of Using Method II and Open Loop Field Weakening Control

The experimental results for the transition between healthy, faulted and fault corrected mode (open circuit in phase *a*) using Method *II* at a speed of 250 rad/sec rotating speed, rated flux and 50% of the nominal load is presented in Fig. 7.31. During this speed, open loop field weakening control scheme is required in fault mode. Without field weakening, machine control would be lost and the motor would stall. Fig. 7.31 starts with the healthy machine. The fault condition was made by imposing an open circuit fault in phase *a* at time = 3.1 sec. The transient responses of the speed and developed torque produced before and after the presence of an open phase fault are presented in Figs. 7.31(a) and (b), respectively. The three phase currents, *d* and *q* current components with its references, the current controller output V_{sd} and V_{sq} voltages are presented in Figs. 7.31(c to g), respectively. The complex frequency spectrum of the phase currents and developed torque with an open circuit fault produced before and after applying the feedforward compensation term are presented in Figs. 7.32 (a – d) respectively.

During the period time = 3.1 – 3.16 sec, no feedforward term is introduced in the *dqo* reference frame. The two remaining motor currents have two different magnitudes (i_b = 7.39A and i_c = 9.36A), and the presence of a negative sequence component in these currents and second harmonic component in the developed torque are shown in frequency spectra of Fig. 7.32(a) and (b). The saturation induced 3rd and 5th harmonic components of current interact with the fields of the space harmonics of the MMF that having the same number of poles respectively to create together a 4th harmonic in the electromagnetic torque. The fault has been detected and located in phase *a* at time = 3.16 sec after the output of third harmonic estimator exceeds the fault threshold value; this occurs within 0.06 sec.

The feedforward term is introduced in the *dqo* reference frame with the field weakening controller. The proper current control was maintained by reducing the stator phase-neutral voltage by field weakening (i.e. reducing i_{sd}^*). It can be seen that the reduction of i_{sd}^* is limited to 1.7A as shown in Fig. 7.31(d). Once the flux has settled, the steady state value of the i_{sd}^* will be the same value of i_{mrd}^* that been calculated using equation (6.65). As a result, the speed controller maintains a constant speed. After the system has settled, it can be seen that the ripple in the speed, torque, and current are reduced. For comparison, the frequency spectra of Figs. 7.32(a & b) (no compensation) and 7.32(c & d) show that the negative-sequence component in the current and the second harmonic component in the electromagnetic torque are reduced when the feedforward compensation term is used. Furthermore, it can be seen that the positive and negative third harmonic components in the current are also reduced. As a result the fourth harmonic component of the electromagnetic torque is reduced. This is mainly due to the reduction in the flux, which is a result of using field weakening control.

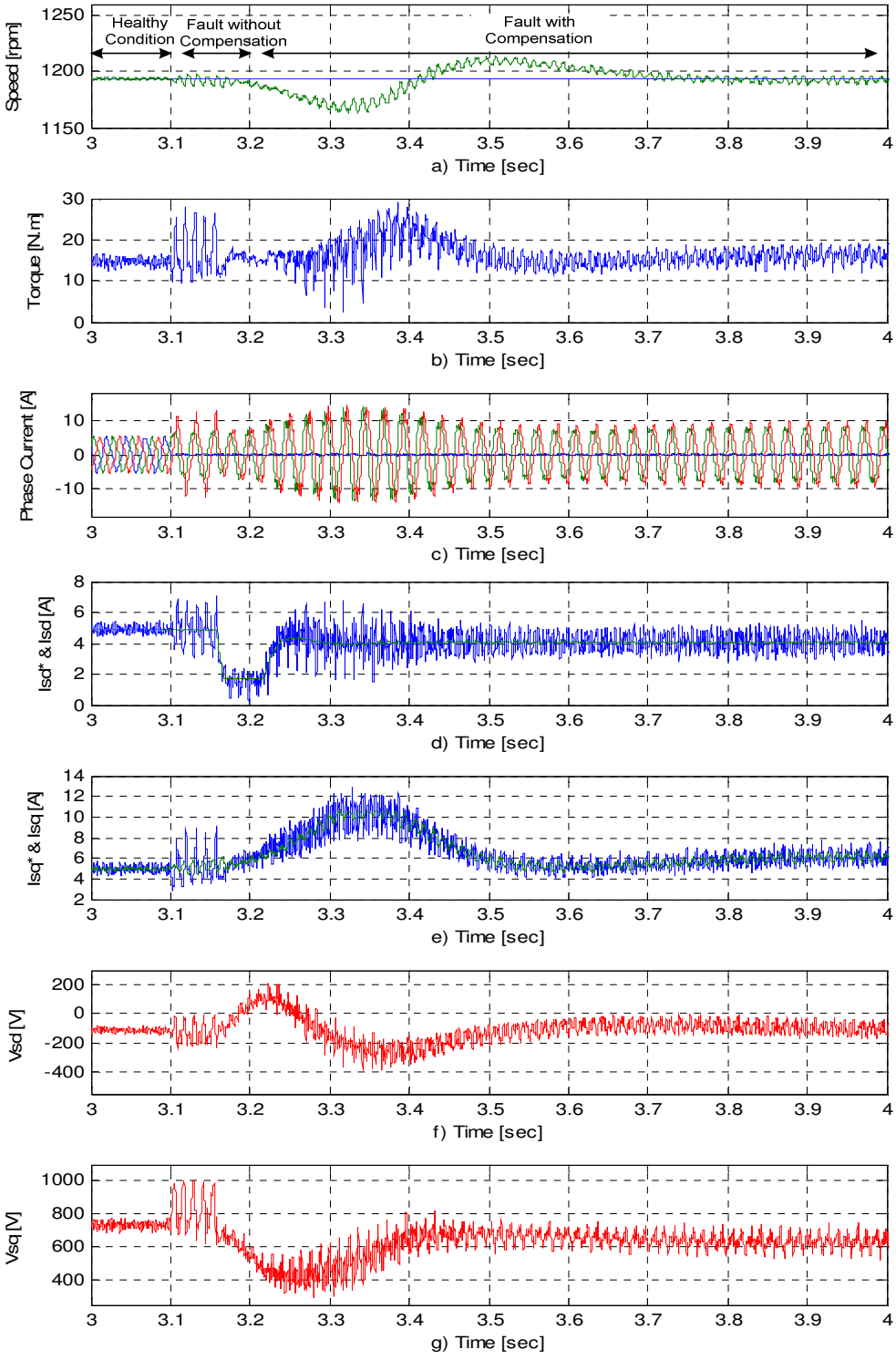

Fig. 7.31 Experimental results, transition between pre fault and fault mode with the compensation algorithm (Method II) and open loop field weakening at 250 rad/sec rotating speed and 50% of the nominal load with an open circuit in phase *a*. a) speed, b) torque, c) phase currents, d) I_{sd} & I_{sd} ref., e) I_{sq} & I_{sq} ref., f) V_d voltage, g) V_q voltage.

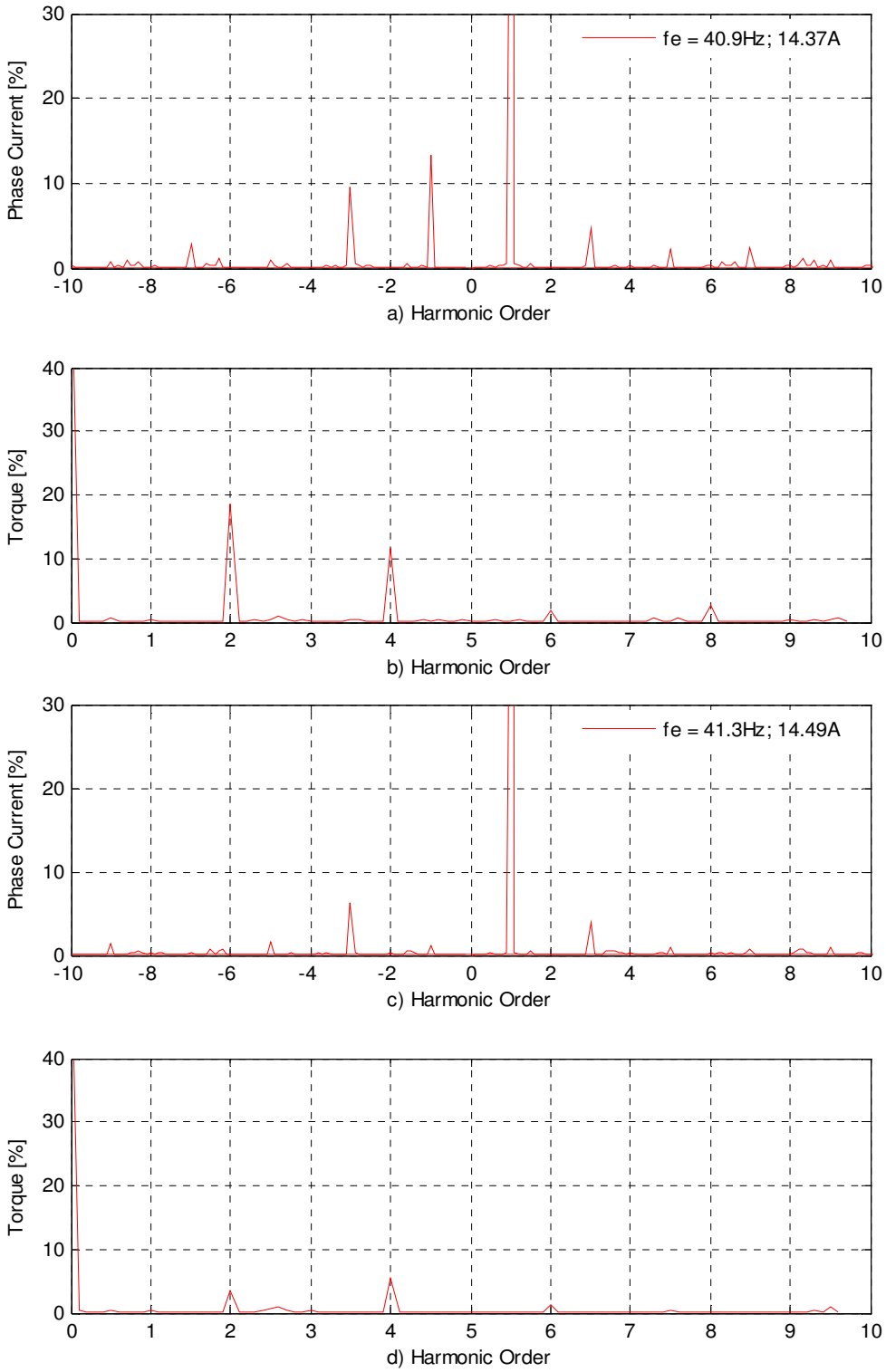

Fig. 7.32 Experimental results, two dimension complex frequency spectrums at 250 rad/sec rotating speed and 50% of the nominal load before and after the feedforward terms applied with an open circuit in phase *a*. a) phase currents, b) torque, c) phase currents, with compensation, d) torque with compensation.

7.4.2.2 Results of Using Method II and Closed Loop Field Weakening Control

Fig. 7.33 shows the experimental results for the transition between healthy, faulted and fault corrected mode (open circuit in phase *a*) using the same condition as in Fig. 7.31. During this speed, closed loop field weakening control scheme is required and utilised in fault mode. This operating condition is similar to the results that presented in Section 7.4.2.1, in order to compare the performance of the two field weakening schemes under the same operating condition. Fig. 7.33 starts with the healthy machine. The fault condition was made by imposing an open circuit fault in phase *a* at time = 2.53 sec. The transient responses of the speed and developed torque produced before and after the presence of an open phase fault are presented in Figs. 7.33(a) and (b), respectively. The three phase currents, *d* and *q* current components with its references, the current controller output V_{sd} and V_{sq} voltages are presented in Figs. 7.33(c – g), respectively. The complex frequency spectrum of the phase currents and developed torque with an open circuit fault produced before and after applying the feedforward compensation term are presented in Figs. 7.34(a – d) respectively. For comparison, Figs. 7.35 and 7.36 show the simulation results for the same operating conditions as Figs. 7.33 and 7.34.

For the result presented in Fig. 7.33, during the period time = 2.53 – 2.6 sec, no feedforward term is introduced in the *dqo* reference frame. The two remaining motor currents have two different magnitudes and the presence of a negative sequence component in these currents and the second harmonic component in the electromagnetic torque are evidenced in the frequency spectra of Figs. 7.34(a) and (b). Once again, the fault has been detected and located in phase *a* at time = 2.6 sec after the output of third harmonic estimator exceeds the fault threshold value; this occurs within 0.07 sec. The feedforward term is introduced in the *dqo* reference frame with the field weakening controller and the proper current control was maintained by reducing the stator phase-neutral voltage by field weakening (i.e. reducing i_{sd}^{*}). The closed loop field weakening controller is adjusted machine input voltage according the inverter maximum voltage to produce the maximum torque. As a result, the speed controller

maintains a constant speed. After the system has settled, it can be seen that the ripple in the speed, torque, and current are reduced.

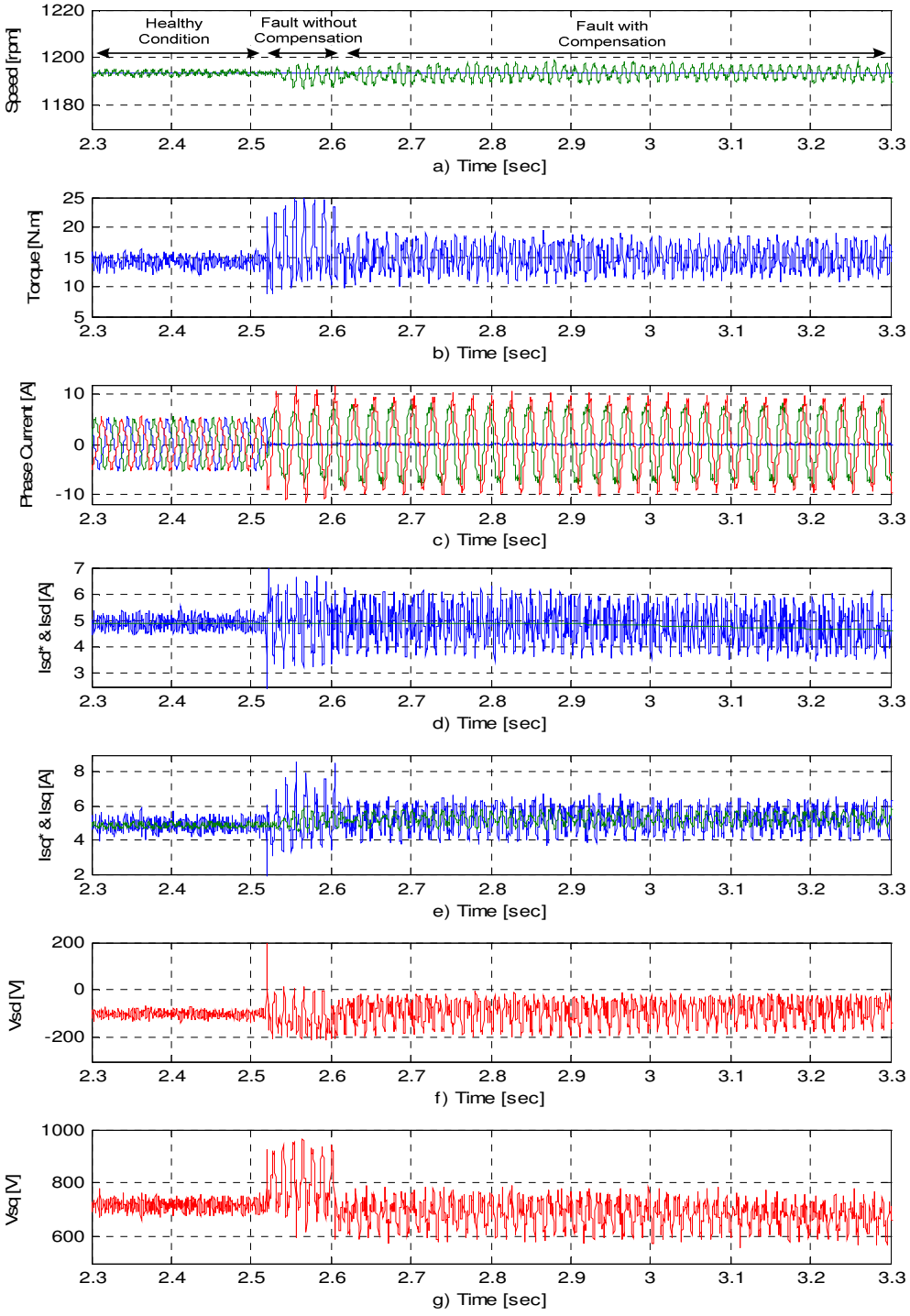

Fig. 7.33 Experimental results, transition between pre fault and fault mode with the compensation algorithm (Method II) and close loop field weakening at 250 rad/sec rotating speed and 50% of the nominal load with an open circuit in phase *a*. a) speed, b) torque, c) phase currents, d) I_{sd} & I_{sd} ref., e) I_{sq} & I_{sq} ref., f) V_d voltage, g) V_q voltage.

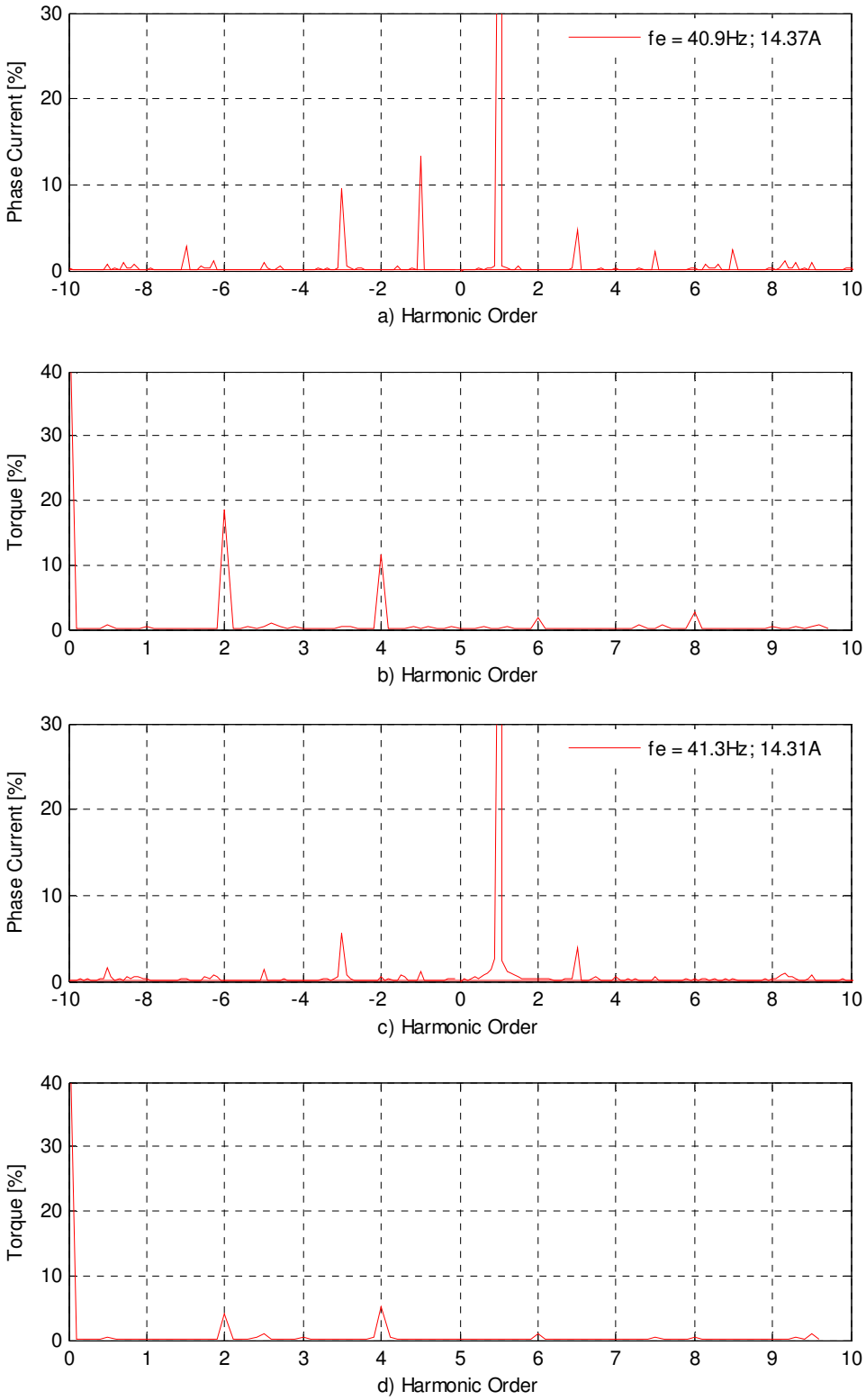

Fig. 7.34 Experimental results, two dimension complex frequency spectrum at 250 rad/sec rotating speed and 50% of the nominal load before and after the feedforward terms applied with an open circuit in phase *a*. a) phase currents, b) torque, c) phase currents with compensation, d) torque with compensation.

The frequency spectra of Figs. 7.34(a & b) (no compensation) and 7.34(c & d) show that the negative-sequence component in the current and the second harmonic component in the electromagnetic torque are reduced when the feedforward compensation term is used. Furthermore, it can be seen that the positive and negative third harmonic components in the current are also reduced. This is mainly due to the reduction in the flux, which is a result of using field weakening control. Furthermore, by comparing Figs. 7.33(d) and 7.31(d), the reference value of i_{sd}^{*} is kept to 4.2A by using the closed loop field weakening scheme while i_{sd}^{*} is stalled to 4A using the other scheme. Therefore, according to this discussion, it is clear that the torque capability of the drive is reduced by using open loop field weakening than closed loop scheme.

For the simulation results presented in Figs. 7.35 and 7.36, the machine starts with the healthy machine, at time = 2.6 sec the open circuit fault occurs in phase *a*. The transient of current is well predicted by the model. During the period time = 2.6 – 2.67 sec, no feedforward term is introduced in the *dqo* reference frame. The two remaining motor currents have two different magnitudes and the presence of a negative sequence component in these currents is shown in frequency spectra of Fig. 7.36(a). By comparing Figs. 7.34(a & b) with 7.36(a & b), it can be seen that the current and electromagnetic torque is well predicted by the model. The fault has been detected at time = 2.67 sec after the output of third harmonic estimator exceeds the fault threshold value and the fault is located in phase *a*, this was made by using the lowest third harmonic component that appeared in the line current I_C (neutral point). The feedforward term is introduced in the *dqo* reference frame with the field weakening controller and a proper current control was maintained by reducing the stator phase-neutral voltage by field weakening (i.e. reducing i_{sd}^{*}). As a result, the speed controller maintains a constant speed. After the system has settled, it can be seen that the ripple in the speed, torque, and current are reduced. The frequency spectra of Figs. 7.36(a & b) (no compensation) and 7.36(c & d) show that the negative-sequence component in the current and the second harmonic component in the electromagnetic torque are reduced when the feedforward compensation term is used. It can be seen that the positive and negative third harmonic components in the current are left the same as before applying the field weakening control.

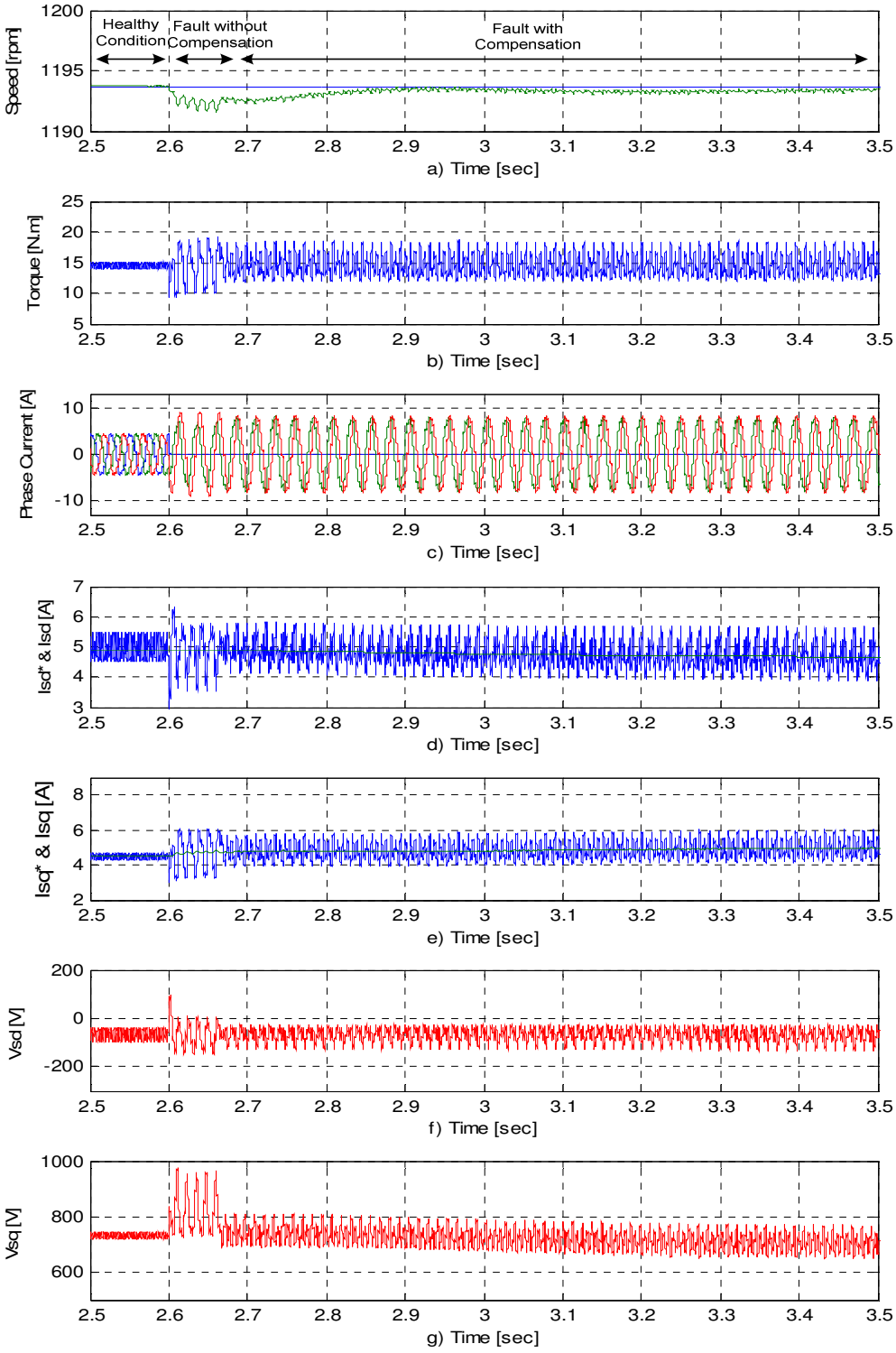

Fig. 7.35 Simulation results, transition between pre fault and fault mode with the compensation algorithm (Method II) and close loop field weakening at 250 rad/sec rotating speed and 50% of the nominal load with an open circuit in phase *a*. a) speed, b) torque, c) phase currents, d) I_{sd} & I_{sd} ref., e) I_{sq} & I_{sq} ref., f) V_d voltage, g) V_q voltage.

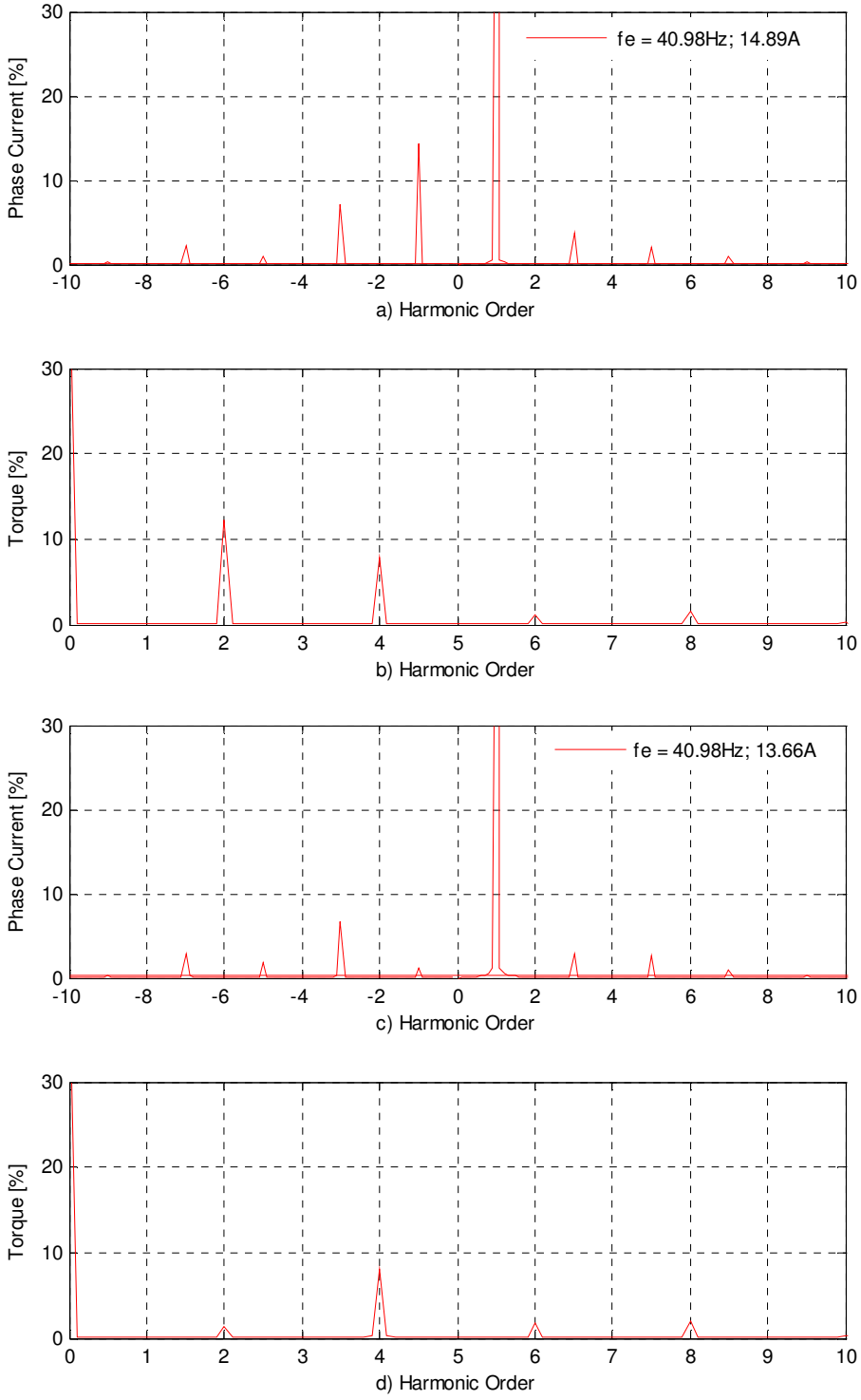

Fig. 7.36 Simulation results, two dimension complex frequency spectrums at 250 rad/sec rotating speed and 50% of the nominal load before and after the feedforward terms applied with an open circuit in phase *a*. a) phase currents, b) torque, c) phase currents with compensation, d) torque with compensation.

This is because of the saturation profiles of the proposed induction model is been tuned when the machine was working under full rated flux and different load levels as mentioned earlier. Therefore, the magnitude of the third harmonic component of the current did not change as it would in the experimental system after the flux level reduced. The agreement between the results obtained by simulation and experiment is suitable for the objectives of this project.

7.5 EXPERIMENTAL RESULTS FOR LOW SPEED OPERATION

The low speed limitation of the proposed fault detection technique has been discussed in Section 7.2 (the results presented in Fig. 7.12). An alternative test has been carried out to show the performance of the proposed fault tolerant technique when the machine are rotating at a low speed and light load condition. Fig. 7.37 presents the experimental results for the transition between healthy, fault condition (open circuit in phase *a*) and fault corrected mode by using the compensation terms at a speed of 31.4 rad/sec, rated flux and 55% of the nominal load. The transient responses of the speed and developed torque produced before and after the presence of an open phase fault are presented in Figs. 7.37(a) and (b), respectively. The three phase currents, *d* and *q* current components with its references, the current controller output V_{sd} and V_{sq} voltages are presented in Figs. 7.37(c to g), respectively. For comparison, Fig. 7.38 shows the experimental results for the same operating conditions as Fig. 7.37 but after the feedforward compensation term was applied. In addition, the complex frequency spectrum of the phase currents and developed torque with an open circuit fault produced before and after applying the feedforward compensation term are presented in Figs. 7.25 (a – f) respectively.

Fig. 7.37 starts with the healthy machine. The fault condition was made by imposing an open circuit fault in phase *a* at time = 2.63 sec. The fault has not been detected as was presented in Fig. 7.12; this is because the level of the third harmonic component of the line currents did not exceed the fault threshold value. For the condition where no feedforward compensation term is introduced in the *dqo* reference frame when a fault occurs, the two remaining motor currents have slightly two different magnitudes (i.e. i_b = 8.75A and i_c = 9.05A) as shown in Fig. 7.37(c) and the presence of a small

negative sequence component in these currents is shown in Fig. 7.39(c). As a result, additional oscillatory components appear in the *d-q* voltage references at twice the fundamental excitation as shown in Figs. 7.37(f & g). This small negative sequence component interacts with the field of the fundamental stator flux, thus giving rise to the appearance of an oscillatory component in the electromagnetic torque at a double the supply frequency (Fig. 7.39(d)). It can be seen that the magnitude of 4^{th}, 6^{th}, 8^{th}, and 10^{th} harmonic components are very small. In addition, it can also be seen that the magnitude of the positive and negative 3^{rd}, 5^{th}, and 7^{th} harmonic components in the winding currents (due to saturation) are very small as shown in Fig. 7.39(c). Therefore, low magnitude 4^{th} and 6^{th} harmonic components appeared in the V_{sd} and V_{sq} voltages which are smaller than expected. The existence of 4^{th} and 6^{th} harmonic components were due to the presence of the 3^{rd}, 5^{th}, and 7^{th} harmonic components of the winding currents (due to saturation and non-linear power converter effects) when they are transferred to the *d-q* reference frame.

A conclusion can be drawn here; the magnitude of the 3^{rd} harmonic component was very small due to the affect of the PI current controllers of the IRFO, where the frequency of the 3^{rd} harmonic component was within the range of the current controller bandwidth (100Hz). Also, the current (time) harmonics created by non-linear power converter effects are reduced by the current controller. The current controllers filter out all the harmonics which exist in the range of its band width and impose only the fundament component. A small magnitude of negative sequence harmonic component (less than 2.4%) appears in the winding currents. Consequently, a small second harmonic component (less than 5% of the nominal value) appears in the developed torque.

At time = 6.9 sec the compensation term was added manually. It can be seen that the two remaining motor currents have approximately equal magnitudes (i.e. i_b = 8.8A and i_c = 8.9A) as shown in Fig. 7.38(c) and less than 1.8% of the fundamental negative sequence component is present in these currents as shown in Fig. 7.39(e). As a result, less than 3.3% of the nominal value of the rated torque has appeared as a second harmonic component in the developed torque (Fig. 7.39(f)). By comparing these results with results of the high speed operation that were presented in Section 7.4, in this operation condition the feedforward compensation term does not make a

significant improvement at particularly low speeds (less than 5Hz) compared to high speed because the current controllers will make the compensation themselves by forcing only the fundament current into the machine winding and reducing the influence of the negative sequence component. As a result, less harmonic ripple appears in the electromagnetic torque.

The experimental results presented confirm that the drive can operate without compensation in fault mode at low speed with only a small ripple in the developed torque and that the limitation of the proposed fault detection technique does not affect the over all performance of the machine drive in this operating condition.

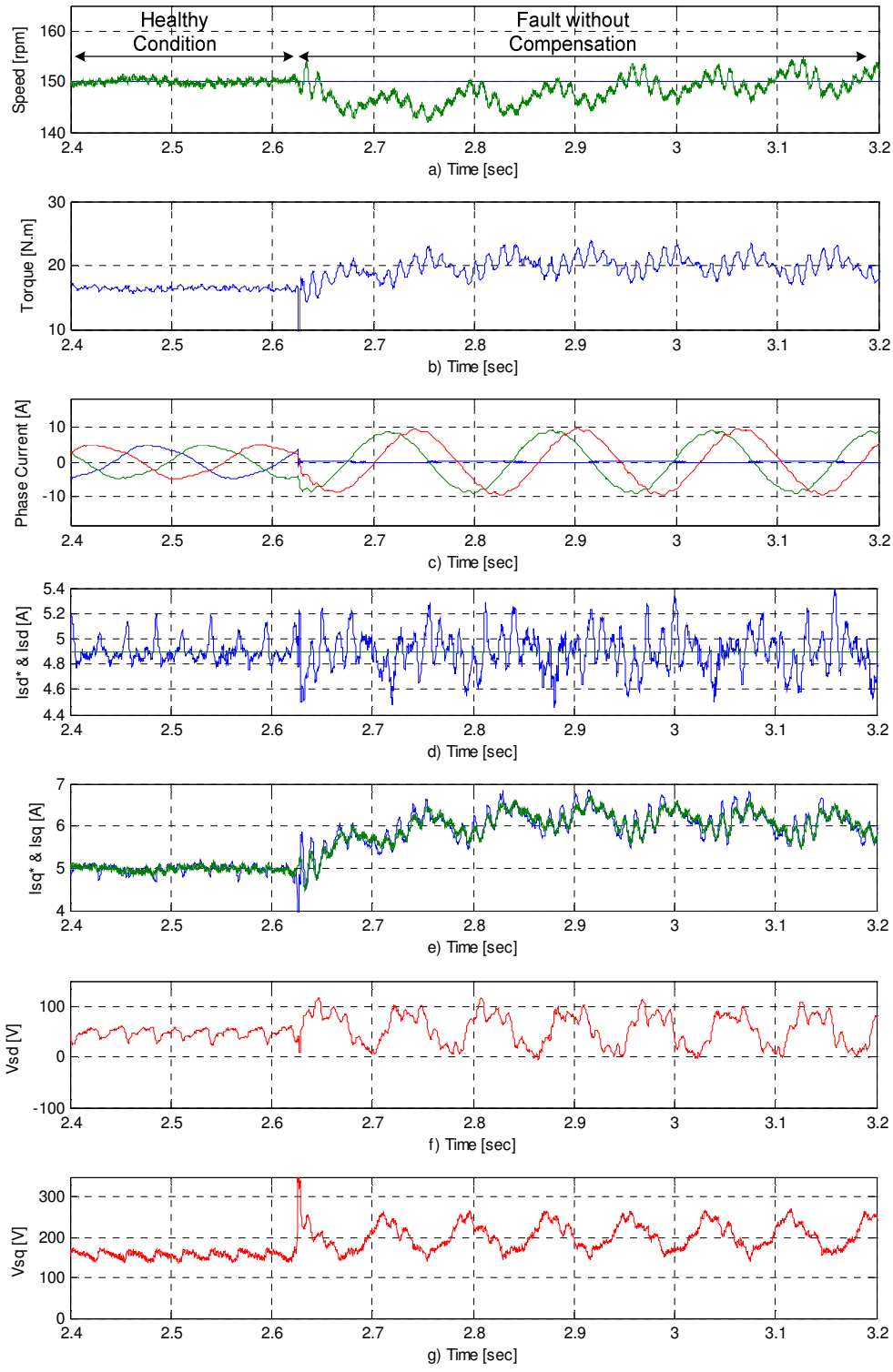

Fig. 7.37 Experimental results of induction motor using IRFO vector control at 31.4 rad/sec rotating speed, full rated flux and 55% of the nominal load before and after an open circuit fault in phase *a*. a) speed, b) torque, c) phase currents, d) *d-q* current components, e) V_d voltage, f) V_q voltage.

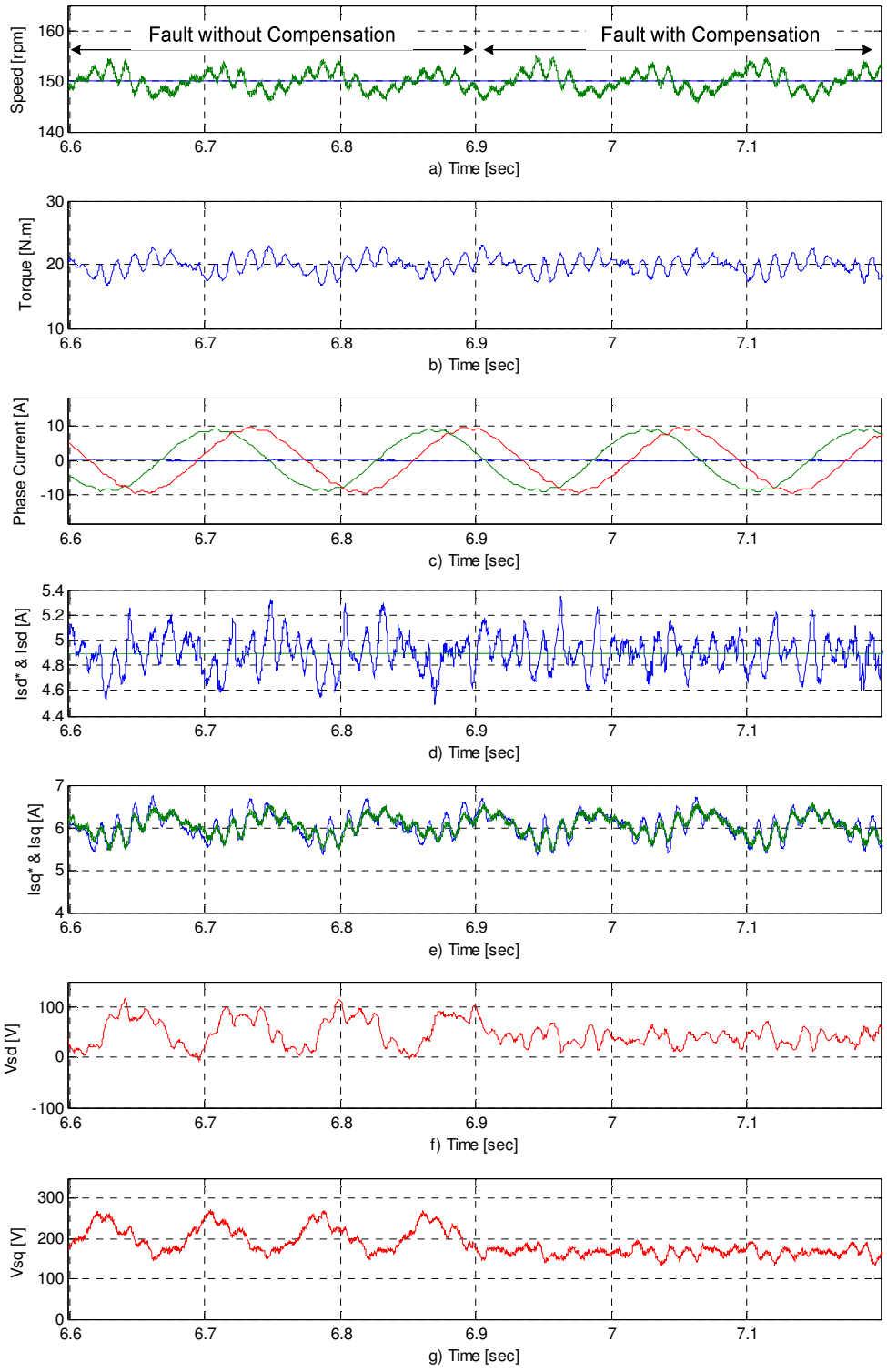

Fig. 7.38 Experimental results of induction motor using IRFO vector control at 31.4 rad/sec rotating speed, full rated flux and 55% of the nominal load with an open circuit fault in phase *a* before and after the feedforward compensation term applied. a) speed, b) torque, c) phase currents, d) *d-q* current components, e) V_d voltage f) V_q voltage.

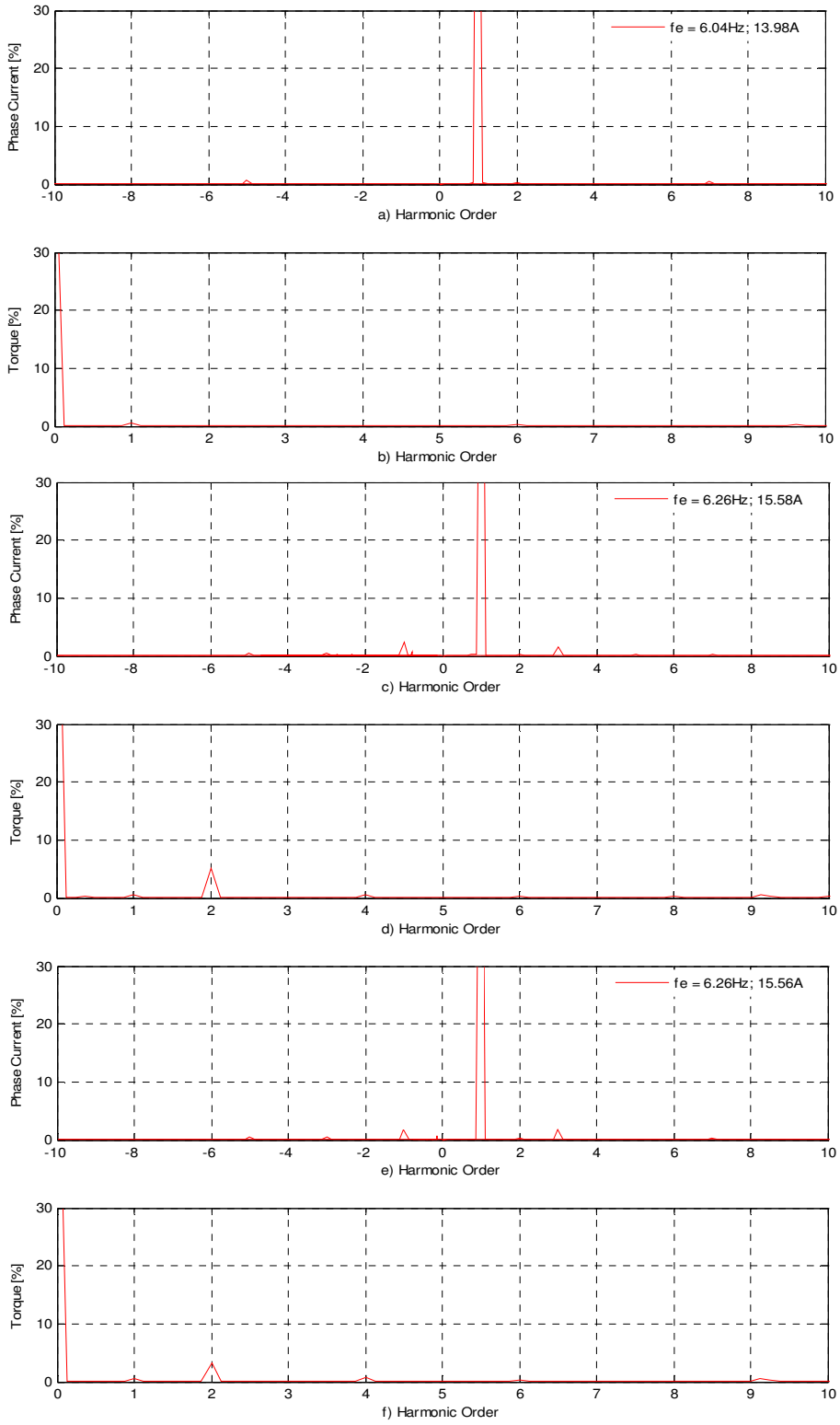

Fig. 7.39 Experimental results, two dimension complex frequency spectrums at 31.4 rad/sec rotating speed and 55% of the nominal load before and after the feedforward terms applied with an open circuit in phase. a) healthy phase currents, b) healthy torque, c) faulty phase currents, d) faulty torque, e) faulty phase currents with compensation, f) faulty torque with compensation.

7.6 CONCLUSION

In the first part of this chapter, the on-line detection method to detect and diagnose stator open circuit fault by using the third harmonic component in the motor line currents, which was proposed in Chapter 5, has been verified through simulation and experiment. The important facts, which have been confirmed during the verification of the proposed strategy, are summarized as follows:

- The presence of a strong third harmonic component in the machine line currents is used as an indicator of an open circuit stator winding fault.
- With the measurement of this component, an approach was implemented which can effectively detect the presence of an open circuit fault once it is developed.
- The fault location is identified based on the lowest third harmonic component of the line current which appears always at the current flowing to the motor's neutral winding connection.
- The proposed fault detection method works independently of applied load level.
- The results produced a positive and fast response to detect the fault and identify the fault location.
- The proposed fault detection method fails when the machine is running at speeds less than 5Hz.
- The results show that the limitation of the proposed fault detection method at low speed does not have a big influence on the performance of the induction machine drive when the fault occurred.

These features make the proposed fault detection method reliable and cost effective. Thus, the technique can be easily implemented in standard IRFO vector control AC drives, with no additional hardware requirements. Only a small additional processing capability is required to implement the identification approach.

Secondly, the proposed fault tolerant control operating strategy which was proposed in Chapter 6 has been also validated through simulation and experiment. As verified, the proposed strategy has a considerable influence on the performance of the motor

during an open circuit fault when a feedforward compensation algorithm is introduced for the zero sequence component of the *dqo* reference voltages. The important facts, which have been observed during the verification of the proposed strategy, are summarized as follows:

- The results show that the scheme eliminates the negative sequence current components and reduces the torque pulsations and the harmonic content of the machine currents.
- Two methods for controlling the neutral-point voltage were presented so that the available voltage capacity of the inverter is maximized in both during normal and fault mode. *Method II* allows the control to impose a higher maximum line-to-line voltage across the faulted machine than *Method I*, which is beneficial at higher speeds.
- For operation at higher speeds, an additional field-weakening control algorithm was incorporated with feedforward compensation in order to minimize the phase voltages of the remaining phases during the post fault mode. The reduction in the voltage can be effectively carried out by appropriately adjusting the rotating magnetic flux (i.e. by reducing i_{sd}^{*}).
- For operation at higher speeds with open loop field weakening control, the results show that the torque capability of the drive is more affected by using *Method I* than *Method II* in order to meet the constant power limit requirements. Where the maximum voltage is reached at 21.1 Hz by using *Method I*, the maximum voltage is reached at 33Hz by using *Method II*.
- The closed loop field weakening controller can be utilised in both operation modes, in pre fault and the post fault modes. The main advantage of this scheme is that it does not need to fix the base speed such as in the case of conventional field weakening, and it automatically optimizes operation to load level. When the required machine voltage begins to exceed the maximum voltage due to the increase of the operating frequency, the system will enter the field weakening region and the integral controller adjusts i_{sd}^{*} so that the highest inverter voltage cannot exceed the maximum voltage.
- Fault ride through is achieved without any modification to the power converter or motor circuit. This fault tolerant control system can quickly recover the

control performance because of its fast fault detection time and simple reconfiguration of system controller.

- These fault tolerant control methods can be easily embedded into existing commercial converter drive systems without any extra hardware and can improve the reliability of the conventional commercial drives.

The developed simulation model describes accurately the behaviour of the induction machine drive with an open circuit fault. The simulation model presented in this work is fast, which produces a good compromise between the simulation time and modelling accuracy, even when a high performance controller is included in the simulation. The usefulness of the model is demonstrated by the development of a the feedforward control algorithm for a vector controlled three-phase induction motor drive, which is required to operate with a phase open circuit fault. It allows the evaluation of the operation of induction motors in the presence of space harmonics and saturation effects, as well as being able to test the robustness of different field oriented controlled drives under unbalanced conditions. Moreover, it can save time and money by pointing out even a minor deficiency in any tested method for stator open circuit fault diagnosis or fault-tolerant operating strategy since the model provides a reliable test bench for evaluating the method before its application to a real drive system.

CONCLUSIONS AND RECOMMENDED FUTURE WORK

8.1 CONCLUSION

The scope of this work was to increase the stator open winding fault tolerance of induction motor drives, particularly for safety critical applications. This objective was achieved in three stages.

a) The development of a more realistic simulation models which reflects saturation and space harmonics effects, whilst at the same time having a relatively low computational requirement to allow it to be used in conjunction with the simulation of high performance control algorithms and power electronic equipment. This simulation model could then be used to fully assess the motor drive systems, and in particular to assess the performance and fault tolerant capabilities of existing and new drive designs.

b) The development of a new fault detection algorithm which does not require extra hardware.

c) The development of new control algorithms for fault ride through.

Although the three-phase induction machine is one of the most representative rotating electrical machines used in the present industrial driven equipment due to its robustness and versatility, it is crucial to develop an open circuit fault-tolerant operating strategy for induction machine drives that prevents the complete loss of availability of the drives in the presence of an open circuit fault. The drive should be

maintained in its normal operating condition to prevent a potential serious accident involving loss of human life or interrupting critical industrial processes.

The first step towards the objective of this work was to investigate the characteristics of a stator open circuit turn fault in an induction machine drive. To achieve this, a model of an induction machine with an open winding fault was derived and integrated with a PWM-VSI model as presented in Chapter 3. In the derivation of the machine model, an equivalent circuit based approach was adapted for a faster simulation speed. For more realistic simulations, this model was extended to include space harmonics and machine saturation effects and provides a useful tool for simulation of symmetrical and asymmetrical conditions that require short simulation time, even for the case where a high performance controller was included in the simulation. The improvement was obtained by including a variation of the machine inductance with rotor position and flux position. The space harmonic effect was incorporated on the machine's mutual inductance as a function of rotor position and the saturation effect was incorporated as a flux position-dependant component in the stator mutual inductance. Using the developed model, the characteristics of a stator open circuit fault in an induction machine drive was extensively investigated taking into account the effects of the drive's operation. The effectiveness of the developed model was verified by the simulation and experimental results as discussed in Chapter 4. The developed simulation model described accurately the behaviour of the induction machine drive with an open circuit fault. The simulation model presented in this work is fast, which produces a good compromise between the simulation time and modelling accuracy, even when a high performance controller is included in the simulation.

The usefulness of the model was demonstrated by the development of the on line open circuit fault detection and the feedforward control algorithm for a vector controlled three-phase induction motor drive, which is required to provide operation with a phase open circuit fault. This allows the evaluation of the operation of induction motors in the presence of space harmonics and saturation effects, as well as being able to test the robustness of different field oriented controlled drives under unbalanced conditions. Furthermore, the proposed model can give a better evaluation of torque pulsations since it can include both time and space harmonics. Moreover, it can save time and money by pointing out even a minor deficiency in any tested method for stator open

circuit fault diagnosis or fault-tolerant operating strategy since the model provides a reliable test bench for evaluating the method before its application to a real drive system, as discussed in detail in Chapters 5 to 7.

An on-line fault detection and diagnosis algorithm based on the measurement of the third harmonic component in the motor line currents was developed in this work as discussed in Chapter 5. The basis of the proposed method was that when an open circuit occurs for a delta connected machine, the machine is transformed into a two phase star connected machine with access to the neutral point. As a result of the affected winding configuration, the third harmonic component appeared in the line currents since the system was not symmetrical. This was reflected on the distribution of the harmonics over the three line currents, especially for the case of the third harmonic component. Therefore, the location of the open circuit winding fault was based on detecting the magnitude reduction for the third harmonic component of the current flowing to the motor's mid point connection. The simulation and experimental results in Chapter 7 verified that the developed open circuit fault detection method worked effectively; it showed that the proposed fault detection method works independently of applied load level. Also, it produced a positive and fast response to detect the fault and identify the fault location. The use of the presence of the third harmonic component in the line current for open winding fault detection gave distinct benefits over conventional current fault detection methods. It is quite simple and easy to implement online and embedded into the processing platform of the drive as a subroutine without extra cost (i.e. no extra hardware is required), where the current sensors are already available in any PWM-VSI drive.

A new open circuit fault tolerant operating strategy for induction machine drives which was specifically designed for a delta connected machine suddenly affected by an open circuit winding faults was developed in Chapter 6. The review in Chapter 2 clearly showed that all the previous strategies did not consider this case. Most of the previous research dealt with an open circuit fault for a star connection machine and most of the previous strategies have unsatisfactory performance characteristics with respect to cost, efficiency, or availability. The fault ride through was achieved without any modification to either the power converter or the motor circuit and more importantly, it prevented the complete loss of availability of a drive in the presence of

a stator open circuit fault. A novel feedforward compensation algorithm was introduced for the zero sequence component of the *dqo* reference voltages which considerably reduced the current and the torque ripple in the faulted drive motor. The simulation and experimental results as presented in Chapter 7 clearly showed that the developed strategy for induction motor drives eliminates the negative sequence current components and reduces the torque pulsations and the harmonic content of the machine currents. Two methods for controlling the neutral point voltage were also presented so that the available voltage capacity of the inverter is maximised in both normal and fault mode. For high speed operation, open and closed loop field-weakening controllers were adopted by controlling the flux level to prevent inverter saturation. For operation at higher speeds with open loop field weakening control, the results showed that the torque capability of the drive was more affected by using *Method I* than *Method II* in order to meet the constant power limit requirements. The maximum voltage was reached at 21.1Hz by using *Method I*, compared with 33Hz by using *Method II*. The closed loop field weakening controller could be utilised in both operation modes, in pre fault and post fault modes. The main advantage of this scheme was that it did not need to fix the base speed such as in the case of conventional field weakening, and it automatically optimised operation to load level. When the required machine voltage began to exceed the maximum voltage due to the increase of the operating frequency, the system entered the field weakening region and the integral controller adjusts i_{sd}^{*} so that the highest inverter voltage cannot exceed the maximum voltage. Fault ride through was achieved without any modification to the power converter or motor circuit. This fault tolerant control system can quickly recover control performance because of its fast fault detection time and simple reconfiguration of system controller. These fault tolerant control methods can be easily embedded into existing commercial converter drive systems without any extra hardware and can improve the reliability of conventional commercial drives.

Another important contribution of the proposed strategy is that the same principle can be applied to either induction machines or permanent magnet synchronous machines. To verify the generality of the principle of the developed feedforward compensation algorithm, a stator open circuit fault-tolerant operating strategy was applied to permanent magnet synchronous machine drive containing an extra inverter leg

connected to the neutral point of a star-connected machine [23]. Simulation and experiment results verified the usefulness of the compensation algorithm to reduce the current and torque ripples in the faulted drive motor.

The work described in this thesis has resulted in several publications. Five conference papers, four have been published and one journal and conference paper has been submitted for review.

8.2 RECOMMENDED FUTURE WORK

In this thesis, control algorithms for induction machine drives were presented under healthy and faulty operation conditions. Although this work has provided contributions to the areas of modelling induction machines, stator open circuit fault detection and fault-tolerant operating strategies, there are several directions in which further research could enhance the results presented in this work.

A phase-variable based model of an induction machine with the inclusion of space harmonic and saturation effects has proved to be an efficient and reasonably accurate design tool to model and improve vector control drive performance both under healthy and faulty situations. For the proposed model, the saturation effect is incorporated into the stator mutual inductances as a function of stator flux position. The saturation profiles (K_2, K_4, and K_6) of the proposed induction model were tuned when the machine was working under full rated flux and at different load levels. An improvement to this model would be the incorporation of saturation effects in the stator mutual inductances and the magnetizing inductance L_m as a function of stator flux level. This can be achieved by obtaining the saturation curve of the magnetizing inductance as a function of stator flux level via experimental test. Based on the relative deviation of magnetizing inductance value with the stator flux level, it can define a saturation factor which will be used to provide the average saturation level of the entire motor and changing the saturation profiles (K_2, K_4, and K_6) to reflect that flux level change. This will improve the performance of the machine model to describe the

behaviour of a stator open circuit fault more accurately when the system enters the field weakening region.

In addition, all inductance parameters are known to be nonlinear functions of the motor flux level, and hence may change either intentionally, under field weakening, or unintentionally, under detuning of the controller. Consequently, the variation of the machine inductance with flux level can affect the performance of the induction motor drive under indirect rotor field oriented control. This problem can be over come by using a lookup table that contains the inductance values as a function of the flux current i_{sd} to change the controller values for the rotor time constant, stator and rotor self inductance, stator and rotor leakage inductance that have been used for vector control algorithm and the calculation of the zero sequence voltage.

The effect of open circuit winding fault upon the operation of induction machine is considered in this work. It will be useful to modify this model to investigate the effects of different winding faults upon the operation of the induction machine drive, such as a stator short circuit fault. Phase variable based machine models can be easily modified if the stator turn fault is considered to exist in one coil of the same phase. Modelling such faults requires the modification of the faulted phase differential equation together with the introduction of an additional differential equation defining the shorted turns modelled as if they were an additional phase winding magnetically coupled to all the other circuits in the machine, but without any external source connected to it. Once this model is been modified then it will be useful to use this model to investigate the performance of the faulty machine and also to look at various stator short circuit fault detection and post fault control strategies.

Furthermore, phase variable based machine models can be easily modified to build a multi phase induction machine model. This model can be extended to include space harmonics and machine saturation effects and provides a useful tool for simulation of symmetrical and asymmetrical conditions that require short simulation time, even in the case where a high performance controller is included in the simulation. Further research on how to implement and use this model to identify some of the current harmonic components appearing under faulty conditions is recommended.

Although tolerance to open circuit faults is added, the induction machine drive needs the input from a position sensor in order to operate and function appropriately. Normally an algorithm for sensorless control can be applied, but its performance will deteriorate or perhaps will not function at all, if an open circuit fault does occur. Accordingly, it is highly recommended for further research to consider an algorithm for achieving a sensorless control that operates properly, also in faulty mode in order to improve the reliability of the drive.

THE PRINCIPLE OF THE ROTOR FLUX ORIENTED CONTROL OF INDUCTION MACHINE

Field orientated vector control allows an AC machine to be controlled like a separately excited DC machine, where the field and the torque control are decoupled. Hence, a high dynamic torque response can be achieved. Different field orientation schemes were proposed such as the stator field orientation, air-gap field orientation and rotor field orientation [125], and the most popular one in the industry application is the rotor field orientation.

The basis of field-orientated control [116, 123, 125] involves the control of the stator current of an induction machine in such a way that one component of current is always aligned with the field and a second component is always orthogonal. For a rotor field orientation, the flux component of the stator current is aligned with the *d*-axis of a synchronously rotating *d-q* frame, thus produce the rotor flux. While the orthogonal component is aligned with the *q*-axis, it will be the torque producing current. The stator current vector diagram for rotor field orientation is shown in Fig. A.1.

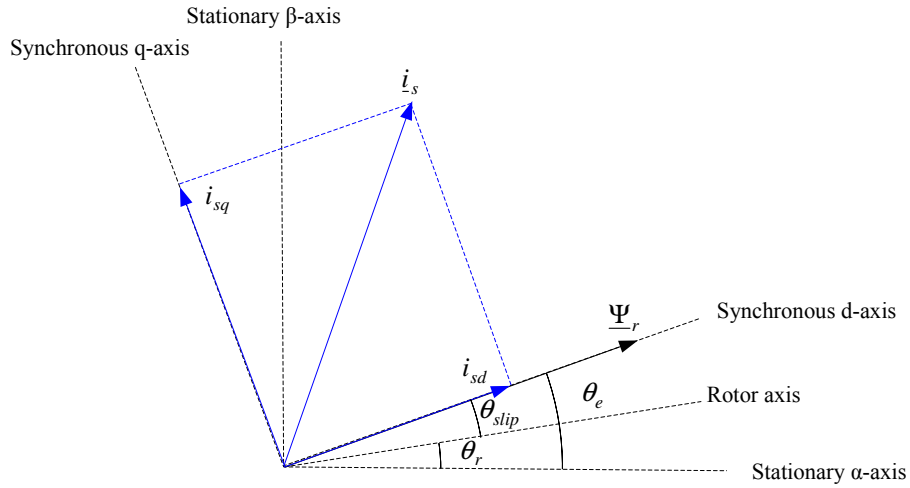

Fig. A.1 Current vector diagram for a vector controlled induction machine using rotor field orientation

Angles θ_r and θ_e are defined as:

$$\theta_r = \int w_r .dt \tag{A.1}$$

$$\theta_e = \int w_e .dt \tag{A.2}$$

In a *d-q* axis frame rotating at synchronous speed w_e, the stator and rotor voltage equations are [125]:

$$V_{sd} = i_{sd} r_s + \sigma L_s \frac{d}{dt} i_{sd} - w_e \sigma L_s i_{sq} + \frac{L_m}{L_r} \frac{d}{dt} \Psi_{rd} - w_e \frac{L_m}{L_r} \Psi_{rq} \tag{A.3}$$

$$V_{sq} = i_{sq} r_s + \sigma L_s \frac{d}{dt} i_{sq} + w_e \sigma L_s i_{sd} + \frac{L_m}{L_r} \frac{d}{dt} \Psi_{rq} + w_e \frac{L_m}{L_r} \Psi_{rd} \tag{A.4}$$

$$V_{rd} = 0 = \Psi_{rd} - L_m i_{sd} + \frac{L_r}{R_r} \frac{d}{dt} \Psi_{rd} - w_{slip} \frac{L_r}{r_r} \Psi_{rq} \tag{A.5}$$

$$V_{rq} = 0 = \Psi_{rq} - L_m i_{sq} + \frac{L_r}{R_r} \frac{d}{dt} \Psi_{rq} + w_{slip} \frac{L_r}{r_r} \Psi_{rd} \tag{A.6}$$

where the total leakage coefficient σ is defined as

$$\sigma = 1 - L_m^2 / L_s L_r \tag{A.7}$$

and the slip frequency w_{slip}

$$w_{slip} = w_e - w_r = P(\theta_e - \theta_r) \tag{A.8}$$

The torque produced assuming a transformation convention as in Appendix B is:

$$T_e = \frac{2}{3}\frac{P}{2}\frac{L_m}{L_r}\left(\Psi_{rd} i_{sq} - \Psi_{rq} i_{sd}\right) \tag{A.9}$$

The field orientation concept implies that the motor current should be controlled using two components; one orientated in phase (flux component) and the other is a quadrature (torque component) to the rotor flux vector Ψr. This is accomplished by choosing *we* to be the instantaneous speed of Ψr and locking the phase of the reference system such that the rotor flux is aligned to the d-axis resulting in the constraint:

$$\Psi_{rq} = 0 \tag{A.10}$$

the *d-q* rotor voltage equations (A.5) and (A.6) become:

$$0 = \Psi_{rd} - L_m i_{sd} + \frac{L_r}{r_r}\frac{d}{dt}\Psi_{rd} \tag{A.11}$$

$$0 = -L_m i_{sq} + w_{slip}\frac{L_r}{r_r}\Psi_{rd} \tag{A.12}$$

and the torque produced can be written as:

$$T_e = \frac{2}{3}\frac{P}{2}\frac{L_m}{L_r}.\Psi_{rd}.i_{sq} \tag{A.13}$$

The torque relation (A.13) shows that the torque can be controlled directly by controlling i_{sq}, assuming the flux is kept constant. Also, by using (A.12), the slip relation or vector constraint can be given as in equation (A.14).

$$w_{slip} = \frac{r_r.L_m}{L_r.\Psi_{rd}} i_{sq} = \frac{r_r}{L_r}\frac{i_{sq}}{i_{mrd}} \tag{A.14}$$

where

$$\Psi_{rd} = L_m.i_{mrd} \tag{A.15}$$

i_{mrd} is the equivalent magnetising current. By combining (A.15) and (A.11) to eliminate Ψ_{rd} yields the equation relating i_{sd} and i_{mrd} i.e.:

$$\frac{L_r}{r_r}.\frac{di_{mrd}}{dt} + i_{mrd} = i_{sd} \tag{A.16}$$

This relation between the flux command current and i_{mrd} is a first-order linear transfer function with a time constant τ_r where:

$$\tau_r = \frac{L_r}{r_r} \tag{A.17}$$

The equations (A.13), (A.14) and (A.16) are particularly interesting for indirect rotor field orientation (IRFO) control. (A.13) provides a means of controlling the electromagnetic torque by using i_{sq}, (A.16) provides a means of controlling the rotor flux linkage by using i_{sd}, and the machine slip can be obtained from (A.14). The flux angle determining the position of the synchronous reference frame which is requierd for the calculation of i_{sd} and i_{sq} using:

$$\theta_e = \int (w_r + w_{slip}).dt \tag{A.18}$$

Fig. A.2 illustrates the concept of how the rotor flux position can be imposed in the IRFO control.

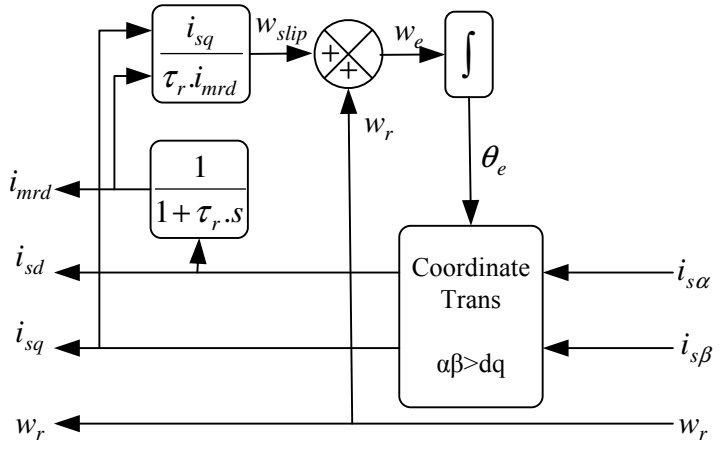

Fig. A.2 IRFO Vector Control Scheme

A typical current control scheme is illustrated in Fig.A.3. It is designed by assuming the plant $G(s) = 1/(r_s + \sigma L_s s)$, and the machine operates with constant rotor flux. The w_e associated terms are called voltage compensation terms, which can be calculated from equations (A.3) and (A.4) after substituted $\psi_{rq} = 0$. These terms are called

feedforward voltage compensation terms and used to improve the performance of the *d-q* control loops.

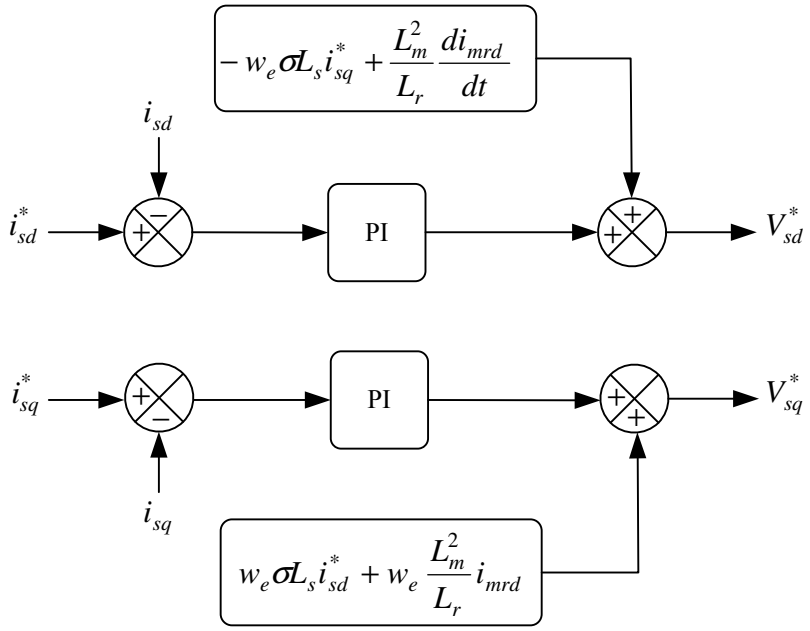

Fig. A.3 Stator current control loop

REFERENCE FRAMES AND TRANSFORMATION CONVENTION

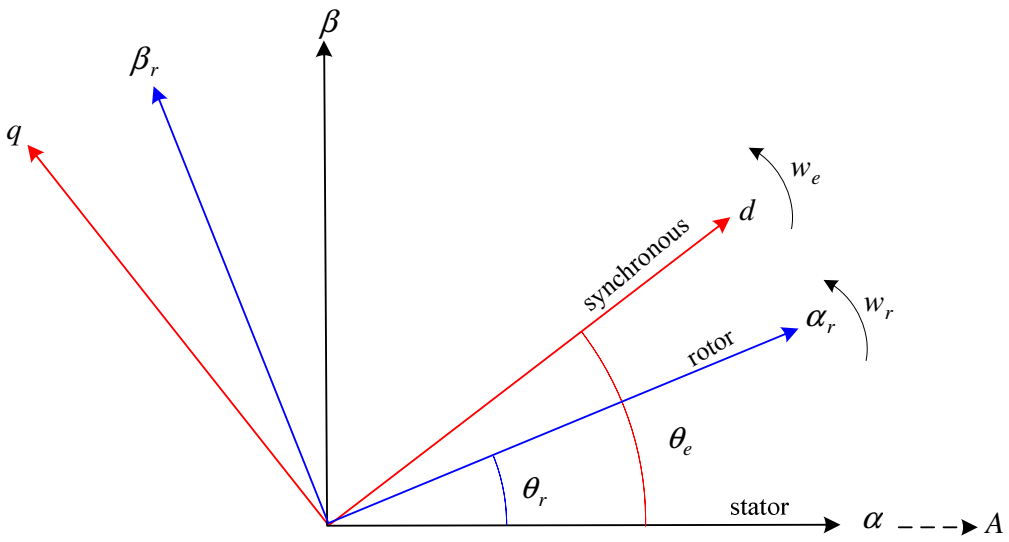

Fig. B.1 Stator, rotor, synchronous reference frame

Fig. B.1 shows the reference frames used to develop the vector control theory. The 2-axis stator frame is fixed as in the physical stator. By applying the Clark transform [125], the α-axis of the stator frame is aligned with the a-phase of the 3-phase system. The one and a half-times peak transformation convention is used throughout this thesis. Consider for a 3-phase system:

$$u_{sa}(t) = \sqrt{2}.U_s.\cos(w.t + \phi) \tag{B.1}$$

$$u_{sb}(t) = \sqrt{2}.U_s.\cos(w.t + \phi - \frac{2\pi}{3}) \tag{B.2}$$

$$u_{sc}(t) = \sqrt{2}.U_s.\cos(w.t + \phi + \frac{2\pi}{3}) \tag{B.3}$$

where U_s is the rms magnitude of the phase quantity (voltage, current, or flux). The *α-β-o* transformation is defined as:

$$u_s(t) = \left(u_{sa}(t) + u_{sb}(t).e^{j\frac{2\pi}{3}} + u_{sc}(t).e^{j\frac{4\pi}{3}} \right) = \frac{3}{2}\sqrt{2}U_s.e^{j(wt+\phi)} \tag{B.4}$$

or

$$\begin{bmatrix} \alpha \\ \beta \\ o \end{bmatrix} = \begin{bmatrix} 1 & \cos\left(\frac{2\pi}{3}\right) & \cos\left(\frac{4\pi}{3}\right) \\ 0 & \sin\left(\frac{2\pi}{3}\right) & \sin\left(\frac{4\pi}{3}\right) \\ \frac{1}{2} & \frac{1}{2} & \frac{1}{2} \end{bmatrix} . \begin{bmatrix} a \\ b \\ c \end{bmatrix} = \begin{bmatrix} 1 & -\frac{1}{2} & -\frac{1}{2} \\ 0 & \frac{\sqrt{3}}{2} & -\frac{\sqrt{3}}{2} \\ \frac{1}{2} & \frac{1}{2} & \frac{1}{2} \end{bmatrix} . \begin{bmatrix} a \\ b \\ c \end{bmatrix} \tag{B.5}$$

Using this transformation, the magnitude of *α-β-o* phasor is equal to 3/2 times the peak value of the stator phasor.

Transformation from the fixed stator frame to any rotating frame makes use of the rotating vector angle within the fixed frame, through application of the Park transform [125]. The equations shown below are for transformation of *α-β-o* to the synchronous *d-q-o* frame.

$$\begin{bmatrix} d \\ q \\ o \end{bmatrix} = \begin{bmatrix} \cos(\theta_e) & \sin(\theta_e) & 0 \\ -\sin(\theta_e) & \cos(\theta_e) & 0 \\ 0 & 0 & 1 \end{bmatrix} . \begin{bmatrix} \alpha \\ \beta \\ o \end{bmatrix} \tag{B.6}$$

MOTOR PARAMETERS

The parameters of the machine considered in this work are detailed below:

Nameplate Data

	Manufacturer	Asea
	Phases	3
	Connection	Delta
	Rated Power	4kW
	Poles	4
	Frequency	50Hz
	Rated Volts	415V
	Rated Current	8.4A
	Rated Speed	1420rpm
	Rated Torque	26.9Nm

Construction Details

	Core Length	0.03kgm^2
	Air Gap Length	104.5mm
	Stator Slots	36
	Rotor Slots	28

Motor Parameters

r_s	5.25Ω
r_r	3.76 Ω
L_s	0.574H
L_r	0.567H
L_m	0.534H
J for AC and DC Machines	$0.152 kgm^2$
B_m for AC and DC Machines	$0.0147 kgm^2/s$
T_r	0.151s
σ	0.123
i_{sd} rated value	4.9A
i_{sq} rated value	9A

SPEED, CURRENT, FIELD CONTROL LOOPS DESIGN

D.1 Speed Controller Design

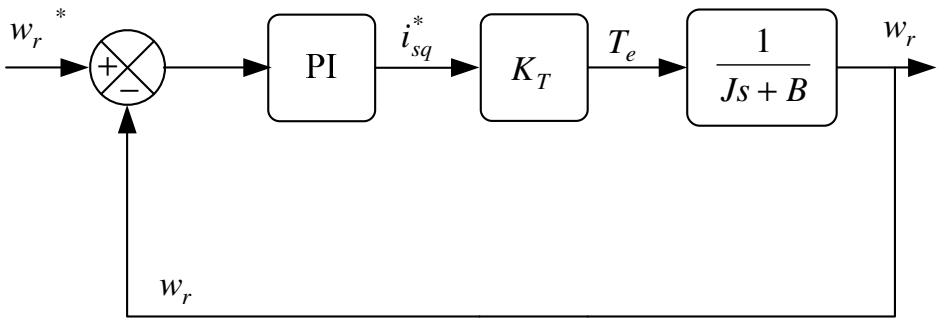

Fig. D.1 Structure of the speed control loop

The structure of the speed control loop is shown in Fig. D.1. The s-domain transfer function for the PI controller is:

$$PI(s) = \frac{k_c(s + a_c)}{s} \tag{D.1}$$

The characteristic equation for the above speed control loop is solved for $1 + G(s)H(s) = 0$. This is where J = 0.152, B_m = 0.0143, P = 4, $K_T = \frac{2}{3}\frac{p}{2}\frac{L_m^2}{L_r} i_{sd}^* = 3.288$ (ignoring units).

$$0 = s^2 + \left(\frac{B + 2k_c K_T}{J}\right)s + \frac{2k_c K_T a_c}{J} \tag{D.2}$$

$$0 = s^2 + \left(\frac{0.0143 + 3.288k_c}{0.152} \right) s + \frac{3.288k_c a}{0.152}$$

The coefficients in the above equation are equated with those in the following equation, which defines the desired closed loop dynamics, thus solving for k_c and a_c. This is with $\zeta = 0.707,\ w_n$ =10 rad/sec.

$$0 = s^2 + 2\zeta w_n s + w_n^2 \tag{D.3}$$

$$= s^2 + 14.14s + 100$$

Thus

$$k_c = \frac{(0.152 * 14.14) - 0.0143}{3.288} = 0.649 \tag{D.4}$$

$$a_c = \frac{(0.152 * 100)}{(3.288 * 0.649)} = 7.119 \tag{D.5}$$

The PI transfer function is therefore

$$PI(s) = \frac{0.649(s + 7.119)}{s} \tag{D.6}$$

D.2 Current Controller Design

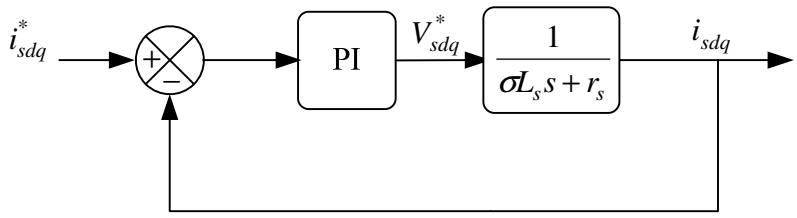

Fig. D.2 Structure of the current control loop

The reduced structure of the current control loop is shown in Fig. D.2. The s-domain transfer function for the PI controller is:

$$PI(s) = \frac{k_c(s + a_c)}{s} \tag{D.7}$$

The characteristic equation for the above current control loop is solved for $1+G(s)H(s)=0$. This is where $\sigma = 0.123,\ L_s = 0.574,\ r_s = 5.25$ (ignoring units).

$$0 = s^2 + \left(\frac{r_s + k_c}{\sigma L_s}\right)s + \frac{k_c a_c}{\sigma L_s} \tag{D.8}$$

$$0 = s^2 + \left(\frac{5.25 + k_c}{0.07065}\right)s + \frac{k_c a_c}{0.07065}$$

The coefficients in the above equation are equated with those in the following equation, which defines the desired closed loop dynamics, thus solving for k_c and a_c. This is with $\zeta = 0.707,\ w_n$ =100 Hz = 628.32 rad/sec.

$$0 = s^2 + 2\zeta w_n s + w_n^2 \tag{D.9}$$

$$= s^2 + 888.44s + 394784$$

Thus

$$k_c = (0.07065 * 888.44) - 5.25 = 57.52 \tag{D.10}$$

$$a_c = \frac{(0.07065 * 394784)}{(57.52)} = 484.92 \tag{D.11}$$

The PI transfer function is therefore

$$PI(s) = \frac{57.52(s + 484.92)}{s} \tag{D.12}$$

D.2 Field Controller Design

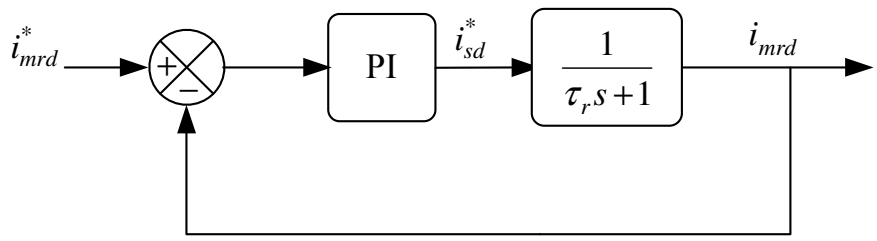

Fig. D.3 Structure of the field control loop

The reduced structure of the field control loop is shown in Fig. D.3. The s-domain transfer function for the PI controller is:

$$PI(s) = \frac{k_c(s + a_c)}{s} \tag{D.13}$$

The characteristic equation for the above field control loop is solved for $1 + G(s)H(s) = 0$. This is where $\tau_r = 0.151$ sec.

$$0 = s^2 + \left(\frac{1 + k_c}{\tau_r}\right)s + \frac{k_c a_c}{\tau_r} \tag{D.14}$$

$$0 = s^2 + \left(\frac{1 + k_c}{0.151}\right)s + \frac{k_c a_c}{0.151}$$

The coefficients in the above equation are equated with those in the following equation, which defines the desired closed loop dynamics, thus solving for k_c and a_c. This is with $\zeta = 0.707$, w_n=20 Hz = 125.66 rad/sec.

$$0 = s^2 + 2\zeta w_n s + w_n^2 \tag{D.15}$$

$$= s^2 + 177.69s + 15790$$

Thus

$$k_c = (0.151 * 177.69) - 1 = 25.83 \tag{D.16}$$

$$a_c = \frac{(0.151 * 15790)}{(25.83)} = 92.3 \tag{D.17}$$

The PI transfer function is therefore

$$PI(s) = \frac{25.83(s + 92.3)}{s} \tag{D.18}$$

EXPERIMENTAL SETUP AND IMPLEMENTATION OF A STATOR OPEN CIRCUIT FAULT

E.1 SYSTEM SCHEMATIC OF THE RIG

This appendix describes the hardware and software solutions that were used to develop and test the vector control algorithms. The rig used and developed in this work, was originally used in projects by Sumner, Blasco and Turl [134] [135] [136].

The test rig utilise standard squirrel-cage 4kW induction machines and 7.5kW IGBT inverter. The overall structure of the drive rig is shown in Fig E.1. Motor drive rig consists of a delta connected winding, 4-poles, 4kW, closed and skewed slot, squirrel cage induction motor which was manufactured by Asea. This machine is fed by a 7.5kW FKI Industrial Drives IGBT inverter and fitted with 2,500-line encoder. The inverter has an integral dynamic braking resistor fitted suitable to dissipate energy due to deceleration.

The induction machine is coupled to a DC machine that associate with a converter of higher power rating that acts as a loading devices. The load DC machine is rated at l0kW and fed by a Eurotherm 4-quadrant converter. The DC drive is configured to operate under its own control and are set-up to provide variable torque demands. An external control box varies the torque demand to the drive by varying a feed back reference voltage.

Data measurements, signal-acquisition, signal-conditioning and digital input/output circuits connect the processing hardware to the motor drive. Processing capability is provided by using the DS1104 controller card, which is placed into the PCI slot of a personal computer (P4). The DS1104 card contains all necessary peripherals (ADC, DAC, counters, timers, and PWM etc.) and computing power (offered by the MPC8240 PowerPC 603e master-processor and TMS320F240 slave-DSP) for implementation of complex drives structures. This card is working with MatLab/Simulink simulation environment. It can connect the variable of simulation structure to the all necessary peripherals by generating code (executed on the target processor) based on the simulation structure. The software associated with the card provides the control for the implementation process from simulation up to real time experiment.

The IGBT inverter of the rig is modified to allow access to the gate drive circuit of the power devices. The modification is achieved whilst still retaining manufacturer safety and protection functionality. The gate drive circuit is interfaced to current mirror card and this circuit is itself interfaced to a PC via a DS1104 card using the PWM signals and running motor control code.

The external circuits include an inverter interface board, and a transducer board were built by Turl [136]. For further details, refer to [136]. The filter/amplification board and a current mirror board were used in other development work within the PEMC group at Nottingham University.

The developed system is capable of running what would be considered high performance AC motor control, while the DSP and host PC set-up is set to provide a highly flexible experimental research platform. The motor test bed is shown in Fig. E.2. the information about the motor, such as the number of rotor slots is gathered from the works of Blasco and Sumner [134] [135]. The motor electrical parameters were determined through no load and locked rotor tests, these values were listed in Appendix C.

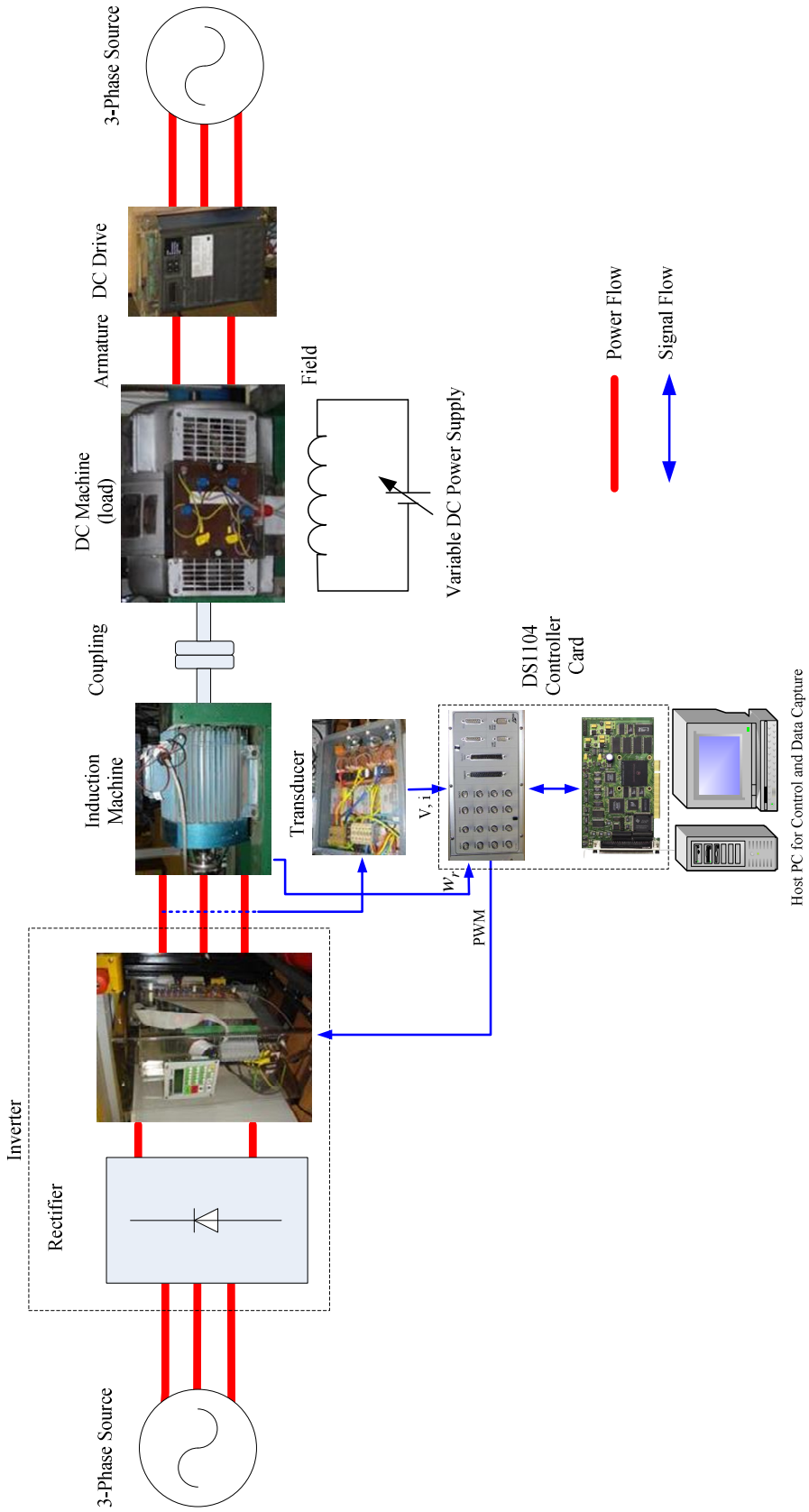

Fig. E.1 Overall structure of the experimental system

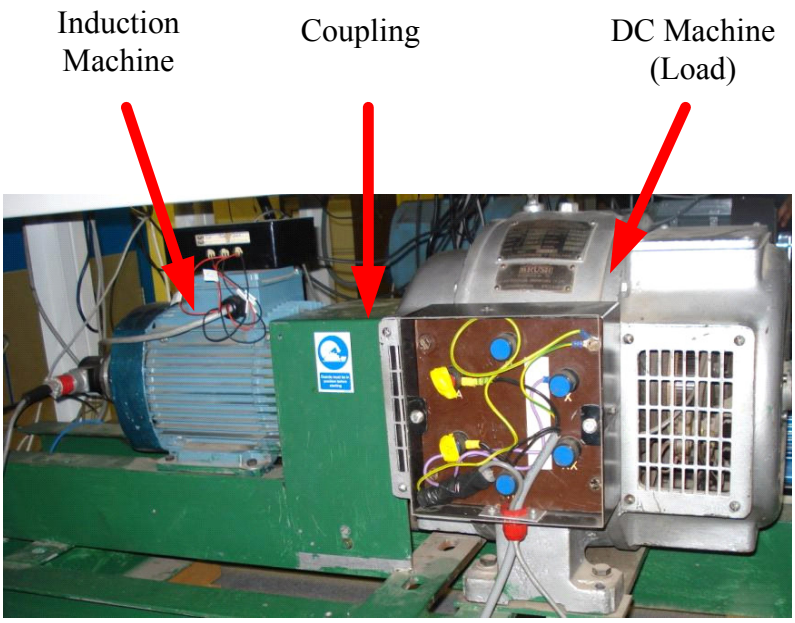

Fig. E.2 Drive rig

E.2 THE DSPACE DS1104 CONTROLLER BOARD

All subsystems of the experimental equipments are controlled from the PC via the DS1104 controller card. The computing power necessary for real time control tasks is provided by the MPC8240 PowerPC 603e processor and TMS320F240 DSP on the card. The communication between the processors and peripherals has place on the internal 24 bit wide bus. An efficient interrupt system is provided for this card to improve its performance. The dSPACE system consists of three components: the DS1104 controller board itself, a breakout panel for connecting signal lines to the DS1104 controller board, and software tools for operating the DS1104 board through the SIMULINK block diagram environment. A block diagram of DS1104 controller board is illustrated in Fig. E.3.

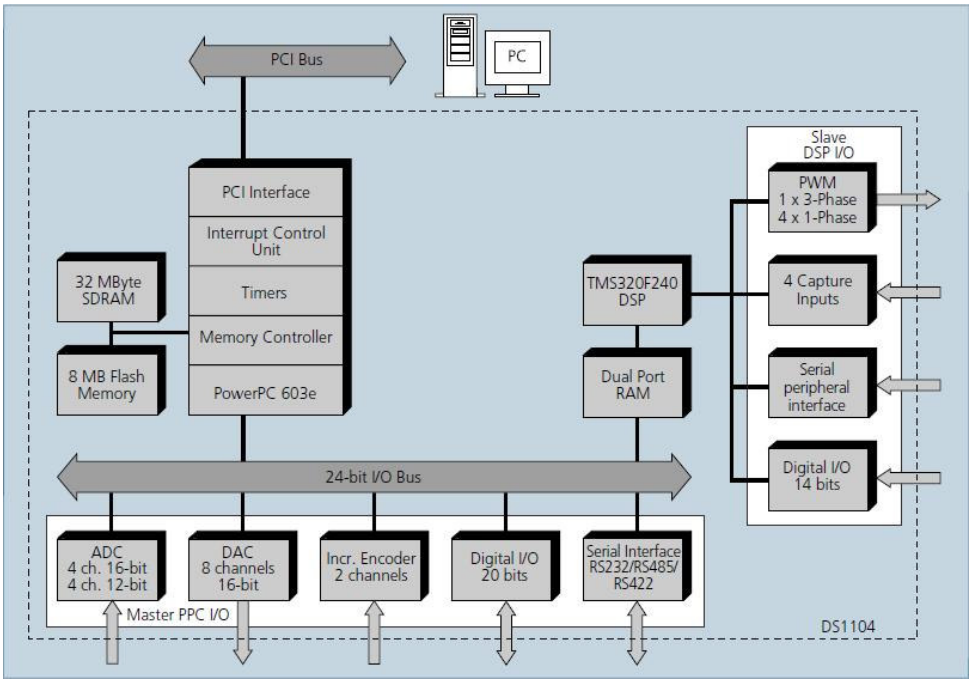

Fig. E.3 Block diagram of the DS1004 controller board

The DS1104 has eight D/A converters 16-bit, each with an output range of ±10 V, also it contains eight A/D channels. The first four channels share a single 16-bit A/D converter through an analogue multiplexer. The remaining four channels each has a dedicated 12-bit A/D converter, allowing for a simultaneous sampling of four analogue input signals. The input range for all eight channels is ±10 V. It also consist of a 20-bit parallel digital I/O Single bit selectable for input or output, two PWM ports, and two incremental encoder channels to picks up the encoder signal of the motor to measure the rotor speed. The external devices include all necessary interfaces and measurement hardware required to control the motor drives are connected to the DS1104 R&D Controller Board via the breakout panel. Fig. E.4 shows the breakout panel for the dSPACE DS1104 R&D Controller Board. For further details about the DS1104 controller card, refer to [137].

Fig. E.4 The breakout panel of the dSPACE DS1104 R&D Controller Board.

A powerful software environment is provided by DSPACE to support all stages of the development of an application from the simulation to physical measurements. By using the RTI blocks which are provided with this card and compatible with MatLab/Simulink, the simulation files can be build to complete the connections to the hardware. The resulted Simulink structures are compiled automatically yielding the real time program code executable on the controller card's processors.

E.3 DSP TO MOTOR DRIVE INTERFACE SYSTEM

This section details the connection of the motor drives to the DS1104 controller card through the external devices. The specifications for the development of equipment interfaced to the DS1104 R&D controller card are contained in the dSPACE Control Desk Experiment Guide [137]. The component of different parts of this hardware interface are outlined in the following sections.

E.3.1 Inverter Interface - Incorporating Dead-time Protection

The output from the PWM port on the controller board is fed to the inverter interface as 3-channel corresponding to the three motor phases (current level gate drive signals by using current mirror board). This arrangement is suitable for higher noise immunity, through out an electrically noisy environment, than sending voltage level signals. These signals are eminently suited to drive an opto-coupler inputs (necessary isolation for safety). The signals are not suitable to directly drive the power devices, and must first be separated into six channels for the inclusion of dead-time delays. In this work the dead-time delay was set at 5μsec. The minimum and maximum pulse time were set to be 10 μsec and 115 μsec [136]. The power supply for this circuit is derived from the inverter's itself. Then, the outputs from the circuit are interfaced directly to the manufacturer gate drivers. The interface circuit also includes necessary protection functionality. The board fitted to the FKI inverter is shown in Fig. E.5. A manual trip button is used and added to inhibit the operation of the inverter. It is logically ORed with hardware over-current and over-voltage protection trip signals from the inverter. Any of these trip conditions disables the PWM signals applied to the inverter switching devices. The manual trip button is useful when the control of the

system is lost.

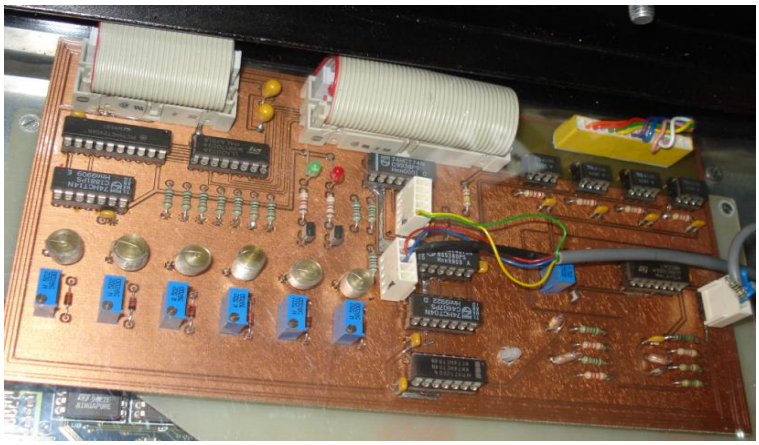

Fig. E.5 Interface card of the FKI industrial drive inverter

E.3.2 Voltage and Current Measurement

Line-to-line voltages and line currents are measured in the motor rig by suitable transducers placed between the inverter output and the motor input terminals. Current measurements are required for the current controllers in vector control and for drive protection in commercial products. Generally, two currents are measured but in the case of this project, provision is made to measure all three currents on the rig. The transducers used are LEM hall-effect devices. Voltage measurements are not used in this project. As the inverter can be considered, a voltage source sometimes reference value of the voltages will be used when it is needed. The outputs of the transducers are passed through necessary signal conditioning circuit (amplifiers with gain and offset adjustment). Connection is made to the breakout panel of the DS1104 controller card using screened cable and BNC type connection.

E.3.3 Analogue Filtering

The outputs of the current transducers are passed via the screened cable, through filters and into the connection of the A/D converters in the breakout panel of the DS1104 control board. The filters are 2^{nd} order low-pass butterworth type, with a cut-off frequency of around 1300Hz, and are used to prevent anti-alias effects associated with a digitally sampled system [138].

E.4 IMPLEMENTING THE DRIVE STRUCTURES

In order to perform the implementation of a drive structure on DS1104 based experimental equipment, there are four steps to follow:

- Through MatLab/Simulink, the simulation model of the desired drive structure can be build by using RTI blocks.
- Defining of the sampling unit.
- Implementation of the software measuring, protection and command subsystem.
- Implementation of the virtual control panel.

Fig. E.6 reveals the general structure for the implemented drive system. For a different drive system, the implementation of the measurement, protection, command block, and the control structure block will be adjusted according to the requested task. As observed from Fig. E.6 the block *DS1104SLAVE_PWMINT* represents the RTI block which connects the simulation structure to the real PWM interrupt of the DS1104 card.

E.4.1 Defining the Sampling Unit

In case of the PWM inverter fed motor drives, it is desirable to synchronise the control algorithm computation and data acquisition with PWM clock-frequency. In this work the switching frequency was set to 4 kHz. Acquisition is aligned with the PWM, hence, the measurement is not obtained immediately following the PWM switching edge. Aligned acquisition alleviates the possibility of error, and noise pick up associated with the switching edges. This can be achieved on DS1104 controller card based systems, where the slave processor accomplishes the PWM. The TMS320F240 DSP will create an interrupt request on the middle of each PWM period according to the settings in the *DS1104SLAVE_PWMINT* interrupt management RTI block. The interrupt will trigger the data acquisition and the computing of the control strategy as illustrated in Fig. E.6, this is known as “single timer tasking mode”.

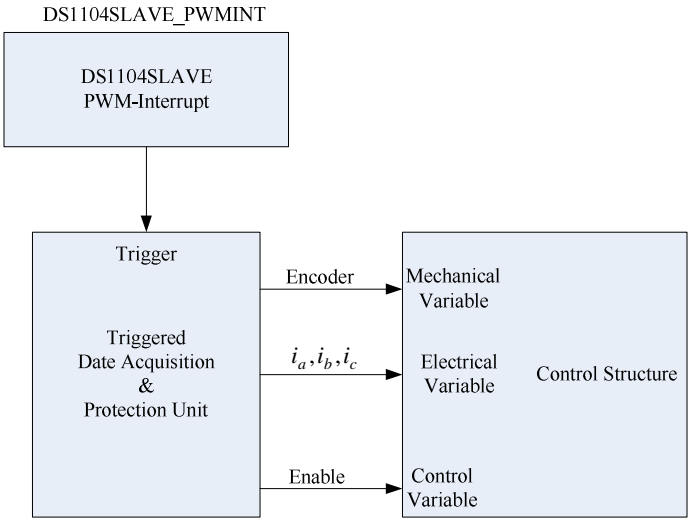

Fig. E.6 Structure of an implemented drive system

E.4.2 Implementation of the Measuring, Protection and Command subsystem

The measuring, protection and command subsystem is illustrated in Fig. E.7. This consists of three main points:

- *Measuring Unit:* takes over the acquisitioned and processing data (stator currents and rotor speed).
- *Protection Unit:* inhibits the drive system in case of an over-current and over-speed. These functions are performed by a software;
- *Command Unit:* It enables or disables the PWM signals applied to the inverter switching devices according to the output of the protection unit and the state of a push button in the virtual control panel, which was used to start or stop the control system.

The "enable" signal controls the whole system. The drive is enabled if the protection unit has not detected an out of range condition and the user has started the control system. The enable signal acts on software level enabling the running of the control strategy program. Also it works on a hardware level, whereas this signal is passed to the controller card via a digital output port. This signal is ORed with inverter hardware protection signals and manual trip signal to enable or disable the PWM signals applied to the inverters IGBTs.

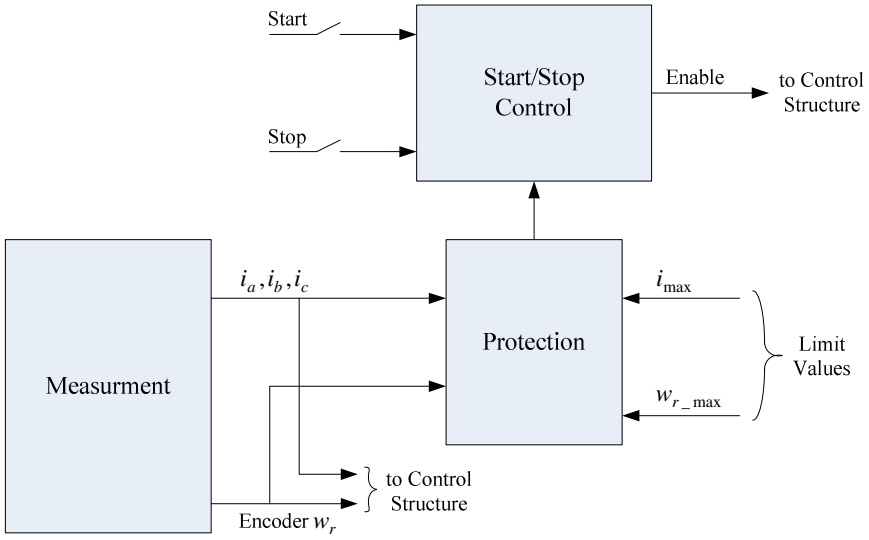

Fig. E.7 Block schematic of the measuring, protection and command subsystem

E.4.3 The Control Strategy Implementation Subsystem

The implementation of the control system for the electrical drive is based on the Simulink structures of the IRFO control which was discussed in chapter three and Appendix A. In the Matlab/Simulink environment the voltage computation is made using IRFO control by generating a three-phase voltages, which will be transformed in duty factors. These voltages will be the control signals of the RTI DS1104SL_DSP_PWM block, which generates the PWM signals. For safety reasons, the duty factor is limited between 1% minimum and 99% maximum values.

E.4.4 The Implementation of the Virtual Control Environment

The virtual control environment associates to the development of the virtual control panel were executed according to the followings:

- Setting the data acquisition unit on the workspace;
- Setting of the virtual control units on the workspace;
- Setting the virtual monitoring units on the workspace;
- Parameterisation of the units on the workspace;
- Assignment of the variables to the units on the workspace.

The *control settings* unit is a feature of the development system that controls the data acquisition. The purpose of this unit is to give access to the user to set:

- The duration of the data acquisition.
- Choosing between single or continuous acquisition.
- Starting and stopping point of the acquisition.
- Trigger event of the acquisition.
- Trigger variable and its value.

This acquisition control unit must to be used in every virtual control panel application.

The *control units* can be push-buttons, radio-buttons, switches and potentiometers etc. Therefore, the user gives commands through these control units, delivering data to the environment. The data monitoring units (LED-s, digital and analogue visualization units, Y– t and Y–X plots etc.) offers information on the variations of the variables of the application. Fig. E.8 presents a sample of virtual panel for the IRFO control drive application.

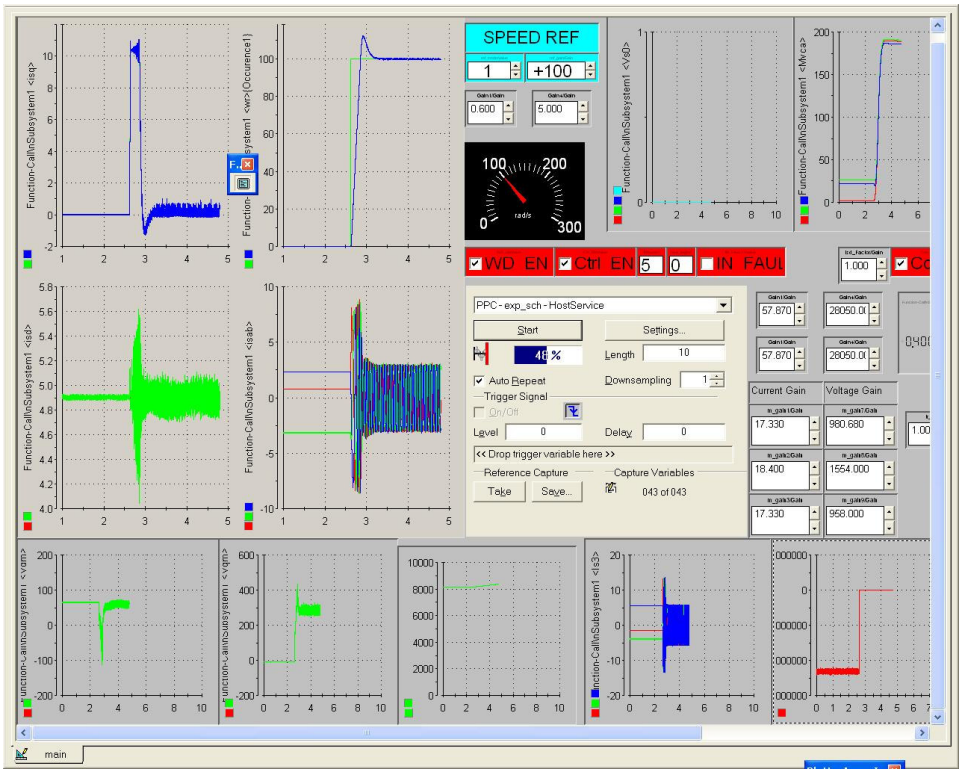

Fig. E.8 The layout of the virtual control panel

E.5 IMPLEMENTATION OF A STATOR OPEN CIRCUIT FAULT

To create an open circuit fault in one of the phase winding, a high resistor is connected in series with the faulty phase winding as being described in chapter three. In this case, no current will start passing through the faulty winding. The implementation of the fault is achieved when one end of the high resistance is connected to the coil in the *a*-phase winding and the other end is connected to a terminal A. The access to the coil connection was made by opening the terminal connection box of the motor. The implementation of the open circuit fault is shown in Fig. E.9. For a healthy operation condition, the ends of the high resistor are short circuited together by using a contactor. For faulty operation condition, the contactor is realised to be open circuit to let the current start passing throughout the high resistance.

The contactor is controlled by a drive circuit that was designed for this purpose. A digital control signal is used from the DS1104 controller board to control the drive circuit of the contactor. This signal is controlled via a push button in the virtual control panel, which was used to start or stop faulty operation period.

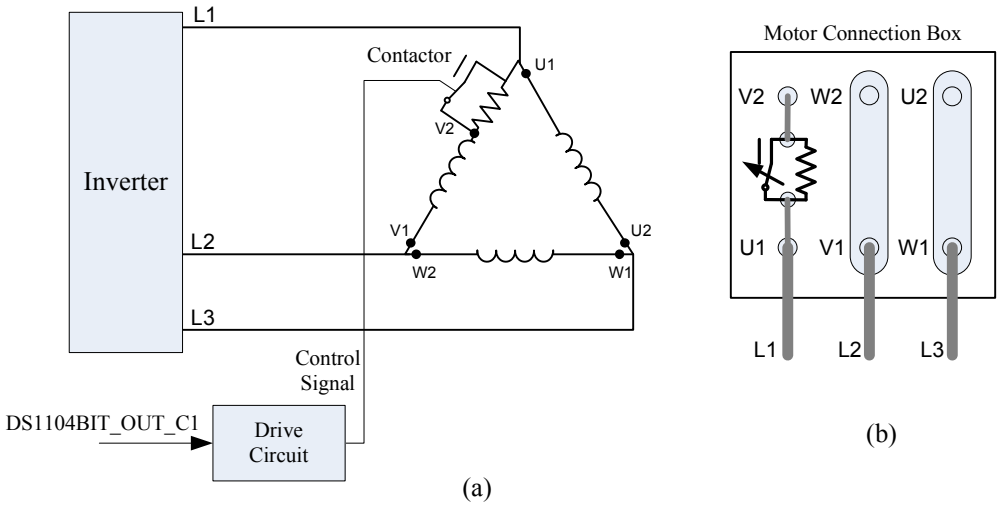

Fig. E.9 Schematic diagram of the open circuit fault implementation

THE DERIVATION OF THE PHASE CURRENTS OF THREE PHASE INDUCTION MACHINE WITH A MISSING PHASE

In a sinusoidally distributed winding of a symmetric three phase machine, the fundamental current for each phase can be written as:

$$i_{as} = I\cos(\omega t + \phi)$$

$$i_{bs} = I\cos(\omega t + \phi - 2\pi/3) \quad \text{(F.1)}$$

$$i_{cs} = I\cos(\omega t + \phi + 2\pi/3)$$

In this case, the rotating MMF generated by the armature currents is the sum of the individuals MMF components caused by each of the three phases; i.e.:

$$MMF_t = MMF_a + MMF_b + MMF_c \quad \text{(F.2)}$$

$$MMF_t = N.i_{as} + aN.i_{bs} + a^2N.i_{cs} \quad \text{(F.3)}$$

Where MMF_t is the total MMF, MMF_a, MMF_b, and MMF_c are the rotating MMF generated by the *abc* phase currents respectively. $a = 1\angle 120^o$ while N is the effective number of stator turns per phase. For balanced three phase operation, the total MMF can be written as:

$$MMF_t = \frac{3}{2}Fe^{j\theta} = \frac{3}{2}F(\cos(\theta) + j\sin(\theta)) \quad \text{(F.4)}$$

Where $F = NI$ and $\theta = (\omega t + \phi)$

Assuming that an open circuit fault suddenly occurs in phase *b*. the total MMF during the fault (MMF_{tf}) will be the sum of MMF_a and MMF_c which can be represented as:

$$MMF_{tf} = N.i_{asf} + a^2 N.i_{csf} = N.i_{asf} + N.i_{csf}\left(\cos\left(240^o\right) + j\sin\left(240^o\right)\right) \quad \text{(F.5)}$$

Where i_{asf} and i_{csf} are the phase current during the fault. A forward rotating MMF is maintained after phase *b* is open circuited by equating the real and imaginary parts of (F.4) and (F.5) as follows:

$$\frac{3}{2}F\cos(\theta) = N.i_{asf} + N.i_{csf}\cos\left(240^o\right) \quad \text{(F.6)}$$

$$\frac{3}{2}F\sin(\theta) = N.i_{csf}\sin(\left(240^o\right) \quad \text{(F.7)}$$

From these two equations, it can be determined that

$$i_{csf} = -\sqrt{3}I\sin(\theta) \quad \text{(F.8)}$$

$$i_{asf} = \frac{3}{2}I\left(\cos(\theta) - \frac{1}{\sqrt{3}}\sin(\theta)\right) \quad \text{(F.9)}$$

which is equivalent to:

$$i_{asf} = \sqrt{3}I\cos(\omega.t + \phi + \pi/6) \quad \text{(F.10)}$$

$$i_{csf} = \sqrt{3}I\cos(\omega.t + \phi + \pi/2) \quad \text{(F.11)}$$

In a similar way, if phase *a* is an open circuited, a forward rotating field is achievable if:

$$i_{bsf} = \sqrt{3}I\cos(\omega.t + \phi - 5\pi/6) \quad \text{(F.12)}$$

$$i_{csf} = \sqrt{3}I\cos(\omega.t + \phi + 5\pi/2) \quad \text{(F.13)}$$

The same happens if phase *c* is open circuited which gives:

$$i_{asf} = \sqrt{3}I\cos(\omega.t + \phi - \pi/6) \quad \text{(F.14)}$$

$$i_{bsf} = \sqrt{3}I\cos(\omega.t + \phi - \pi/2) \quad \text{(F.15)}$$

DERIVATION OF THE FEEDFORWARD COMPENSATION TERMS

In this appendix, the derivation of the zero sequence components of equations (6.25) and (6.26) are presented. For a vector controlled drive, the flux and torque producing currents (i_{sd} and i_{sq}) are related to the *α-β-o* components by:

$$\begin{bmatrix} i_{sd} \\ i_{sq} \\ i_o \end{bmatrix} = \begin{bmatrix} \cos(\theta_e) & \sin(\theta_e) & 0 \\ -\sin(\theta_e) & \cos(\theta_e) & 0 \\ 0 & 0 & 1 \end{bmatrix} \begin{bmatrix} i_\alpha \\ i_\beta \\ i_o \end{bmatrix} \tag{G.1}$$

where θ_e is the instantaneous angle of the reference frame, and i_o is the zero sequence component. The stationary frame *abc* variables are determined from the stationary frame *α-β* variables by using the following transforming equation:

$$\begin{bmatrix} i_a \\ i_b \\ i_c \end{bmatrix} = \frac{2}{3} \begin{bmatrix} 1 & 0 & 1 \\ -\frac{1}{2} & \frac{\sqrt{3}}{2} & 1 \\ -\frac{1}{2} & -\frac{\sqrt{3}}{2} & 1 \end{bmatrix} \begin{bmatrix} i_\alpha \\ i_\beta \\ i_o \end{bmatrix} \tag{G.2}$$

By adopting the inverse of transformation of (G.2), the zero sequence component of the stator current can be calculated as:

$$i_o = \frac{1}{2}(i_a + i_b + i_c) = \frac{1}{2} i_n \tag{G.3}$$

The neutral or star point current is defined in (G.4) under healthy operating conditions and is also equal zero:

$$i_n = i_a + i_b + i_c \tag{G.4}$$

If an open circuit fault occurs in phase *b* ($i_b=0$), a zero sequence component will appear. Then from (G.2):

$$i_o = \frac{1}{2} i_\alpha - \frac{\sqrt{3}}{2} i_\beta \tag{G.5}$$

The zero sequence current, calculated from (G.5) and the inverse of (G.1) becomes:

$$i_o = \frac{1}{2} i_\alpha - \frac{\sqrt{3}}{2} i_\beta = \frac{1}{2}\left(i_{sd}^* \cos(\theta_e) - i_{sq}^* \sin(\theta_e)\right) - \frac{\sqrt{3}}{2}\left(i_{sd}^* \sin(\theta_e) + i_{sq}^* \cos(\theta_e)\right) \tag{G.6}$$

As a result, the reference neutral current in the faulty operation condition can be calculated by substitute (G.6) in (G.3) to give:

$$i_n = \left(i_{sd}^* \cos(\theta_e) - i_{sq}^* \sin(\theta_e)\right) - \sqrt{3}\left(i_{sd}^* \sin(\theta_e) + i_{sq}^* \cos(\theta_e)\right) \tag{G.7}$$

For a steady state operation, the stator voltage motor equations can be derived in the *dqo* reference frame as:

$$V_{sd} = r_s i_{sd} - w_e \sigma L_s i_{sq} \tag{G.8}$$

$$V_{sq} = r_s i_{sq} + w_e \sigma L_s i_{sd} + w_e \frac{L_m^2}{L_r} i_{sd} \tag{G.9}$$

$$V_n = r_s i_n + L_{ls} \frac{di_n}{dt} \tag{G.10}$$

The zero sequence voltage V_o is calculated using a similar method to (G.3):

$$V_n = 2.V_o \tag{G.11}$$

By substituting (G.11) and (G.6) into (G.10), V_o can be expressed by:

$$\begin{aligned} V_o = \frac{V_n}{2} = r_s &\left(\left(i_{sd}^* \cos(\theta_e) - i_{sq}^* \sin(\theta_e)\right) - \sqrt{3}\left(i_{sd}^* \sin(\theta_e) + i_{sq}^* \cos(\theta_e)\right)\right) \\ &+ L_{ls} \frac{d}{dt}\left(\left(i_{sd}^* \cos(\theta_e) - i_{sq}^* \sin(\theta_e)\right) - \sqrt{3}\left(i_{sd}^* \sin(\theta_e) + i_{sq}^* \cos(\theta_e)\right)\right) \end{aligned} \tag{G.12}$$

The derivatives terms di_{sd}^* / dt and di_{sq}^* / dt are equal zero because i_{sd}^* and i_{sq}^* currents are a constant values. As a result, V_o is equal to:

$$V_o = \left(i_{sd}^* \left(-\frac{\sqrt{3}}{2} r_s - \frac{1}{2} L_{ls} w_e \right) - i_{sq}^* \left(\frac{1}{2} r_s - \frac{\sqrt{3}}{2} L_{ls} w_e \right) \right) \sin(\theta_e) + \left(i_{sd}^* \left(\frac{1}{2} r_s - \frac{\sqrt{3}}{2} L_{ls} w_e \right) - i_{sq}^* \left(\frac{\sqrt{3}}{2} r_s + \frac{1}{2} L_{ls} w_e \right) \right) \cos(\theta_e) \quad \text{(G.13)}$$

If an open circuit fault occurs in phase *c* ($i_c=0$), a zero sequence component will appear. Then from (G.2):

$$i_o = \frac{1}{2} i_\alpha + \frac{\sqrt{3}}{2} i_\beta \quad \text{(G.14)}$$

The zero sequence current, calculated from (G.14) and the inverse of (G.1) becomes:

$$i_o = \frac{1}{2} i_\alpha + \frac{\sqrt{3}}{2} i_\beta = \frac{1}{2} \left(i_{sd}^* \cos(\theta_e) - i_{sq}^* \sin(\theta_e) \right) + \frac{\sqrt{3}}{2} \left(i_{sd}^* \sin(\theta_e) + i_{sq}^* \cos(\theta_e) \right) \quad \text{(G.15)}$$

As a result, the reference neutral current in the faulty operation condition can be calculated by substitute (G.15) in (G.3) to give:

$$i_n = \left(i_{sd}^* \cos(\theta_e) - i_{sq}^* \sin(\theta_e) \right) + \sqrt{3} \left(i_{sd}^* \sin(\theta_e) + i_{sq}^* \cos(\theta_e) \right) \quad \text{(G.16)}$$

By substituting (G.11) and (G.15) into (G.10), V_o can be expressed by:

$$V_o = \frac{V_n}{2} = r_s \left(\left(i_{sd}^* \cos(\theta_e) - i_{sq}^* \sin(\theta_e) \right) + \sqrt{3} \left(i_{sd}^* \sin(\theta_e) + i_{sq}^* \cos(\theta_e) \right) \right) + L_{ls} \frac{d}{dt} \left(\left(i_{sd}^* \cos(\theta_e) - i_{sq}^* \sin(\theta_e) \right) + \sqrt{3} \left(i_{sd}^* \sin(\theta_e) + i_{sq}^* \cos(\theta_e) \right) \right) \quad \text{(G.17)}$$

As a result, V_o is equal to:

$$V_o = \left(i_{sd}^* \left(\frac{\sqrt{3}}{2} r_s - \frac{1}{2} L_{ls} w_e \right) - i_{sq}^* \left(\frac{1}{2} r_s + \frac{\sqrt{3}}{2} L_{ls} w_e \right) \right) \sin(\theta_e) + \left(i_{sd}^* \left(\frac{1}{2} r_s + \frac{\sqrt{3}}{2} L_{ls} w_e \right) + i_{sq}^* \left(\frac{\sqrt{3}}{2} r_s - \frac{1}{2} L_{ls} w_e \right) \right) \cos(\theta_e) \quad \text{(G.18)}$$

REFERENCES

[1] S. Nandi, H. A. Toliyat, and L. Xiaodong, "Condition monitoring and fault diagnosis of electrical motors-a review," Energy Conversion, IEEE Transactions on, vol. 20, pp. 719-729, 2005.

[2] A. Siddique, G. S. Yadava, and B. Singh, "A review of stator fault monitoring techniques of induction motors," Energy Conversion, IEEE Transactions on, vol. 20, pp. 106-114, 2005.

[3] A. H. Bonnett, A. H. Bonnett, and G. C. Soukup, "Cause and analysis of stator and rotor failures in three-phase squirrel-cage induction motors," Industry Applications, IEEE Transactions on, vol. 28, pp. 921-937, 1992.

[4] T. G. Hebetler, "Current-based condition monitoring of electrical machines in safety critical application," presented at The 13th Power Electronics and Motion Control Conference EPE-PEMC 2008, 2008.

[5] B. A. Welchko, T. M. Jahns, and S. Hiti, "IPM synchronous machine drive response to a single-phase open circuit fault," Power Electronics, IEEE Transactions on, vol. 17, pp. 764-771, 2002.

[6] S. Dwari and L. Parsa, "An optimal control technique for multiphase PM machines under open-circuit faults," Industrial Electronics, IEEE Transactions on, vol. 55, pp. 1988-1995, 2008.

[7] M. El Hachemi Benbouzid, "A review of induction motors signature analysis as a medium for faults detection," Industrial Electronics, IEEE Transactions on, vol. 47, pp. 984-993, 2000.

[8] R. V. White and F. M. Miles, "Principles of fault tolerance," presented at Applied Power Electronics Conference and Exposition APEC '96. Eleventh Annual Conference Proceedings, 1996.

[9] J.-R. Fu and T. A. Lipo, "Disturbance-free operation of a multiphase current-regulated motor drive with an opened phase," Industry Applications, IEEE Transactions on, vol. 30, pp. 1267-1274, 1994.

[10] N. Bianchi, S. Bolognani, and M. D. Pre, "Impact of stator winding of a five-phase permanent-magnet motor on postfault operations," Industrial Electronics, IEEE Transactions on, vol. 55, pp. 1978-1987, 2008.

[11] L. Parsa and H. A. Toliyat, "Fault-tolerant interior-permanent-magnet machines for hybrid electric vehicle applications," Industry Applications, IEEE Transactions on, vol. 56, pp. 1546-1552, 2007.

[12] C. Gerada, K. Bradley, H. Xiaoyan, A. Goodman, C. Whitley, and G. Towers, "A 5-phase fault-tolerant brushless permanent magnet motor drive for an

aircraft thin wing surface actuator," presented at IEEE International Electric Machines & Drives Conference IEMDC '07, 2007.

[13] J.-R. FU and T. A. LIPO, "A strategy to isolate a switching device fault in a current regulated motor drive," Electric machines and power systems, vol. 24, pp. 911-920, 1996.

[14] B. A. Welchko, T. A. Lipo, T. M. Jahns, and S. E. Schulz, "Fault tolerant three-phase AC motor drive topologies: a comparison of features, cost, and limitations," Power Electronics, IEEE Transactions on, vol. 19, pp. 1108-1116, 2004.

[15] R. L. de Araujo Ribeiro, C. B. Jacobina, E. R. C. da Silva, and A. M. N. Lima, "Fault-tolerant voltage-fed PWM inverter AC motor drive systems," Industrial Electronics, IEEE Transactions on, vol. 51, pp. 439-446, 2004.

[16] L. Tian-Hua, F. Jen-Ren, and T. A. Lipo, "A strategy for improving reliability of field-oriented controlled induction motor drives," Industry Applications, IEEE Transactions on, vol. 29, pp. 910-918, 1993.

[17] S. Bolognani, M. Zordan, and M. Zigliotto, "Experimental fault-tolerant control of a PMSM drive," Industrial Electronics, IEEE Transactions on, vol. 47, pp. 1134-1141, 2000.

[18] N. Bianchi, S. Bolognani, M. Zigliotto, and M. A. Z. M. Zordan, "Innovative remedial strategies for inverter faults in IPM synchronous motor drives," Energy Conversion, IEEE Transaction on, vol. 18, pp. 306-314, 2003.

[19] M. Beltrao de Rossiter Correa, C. Brandao Jacobina, E. R. Cabral da Silva, and A. M. Nogueira Lima, "An induction motor drive system with improved fault tolerance," Industry Applications, IEEE Transactions on, vol. 37, pp. 873-879, 2001.

[20] K. Sangshin, K. Taehyung, and O. Vodyakho, "Four-leg based matrix converter with fault resilient structures and controls for electric vehicle and propulsion systems," presented at Vehicle Power and Propulsion Conference VPPC 2007, 2007.

[21] K. Sangshin and H. A. Toliyat, "Fault-tolerant topologies and switching function algorithms for three-phase matrix converter based AC motor drives against open and short phase failures," presented at Electric Machines & Drives Conference IEMDC '07. IEEE International, 2007.

[22] W. Lina, X. Fuyuan, S. Kai, and H. Lipei, "A novel safe shutdown strategy for matrix converter even under fault condition," presented at Twentieth Annual IEEE Applied Power Electronics Conference and Exposition APEC, 2005.

[23] S. Khwan-on, L. d. Lillo, L. Empringham, P. Wheeler, C. Gerada, N. M. Othman, O. Jasim, and J. Clare, "Fault tolerant power converter topologies for

PMSM drives in aerospace applications," presented at 13th International European Power Electronics and Applications Conference EPE'09, 2009.

[24] D. Kastha and B. K. Bose, "Investigation of fault modes of voltage fed inverter system for induction motor drive," Industry Applications, IEEE Transactions on, vol. 30, pp. 1028-1038, 1994.

[25] D. Kastha and B. K. Bose, "Fault mode single-phase operation of variable frequency induction motor drive and improvement of pulsating torque characteristics," Industry Applications, IEEE Transactions on, vol. 41, pp. 426–433, 1994.

[26] N. Mehala and R. Dahiya, "Motor current signature analysis and its applications in induction motor fault diagnosis," International Journal of Systems Applications, Engineering & Development, vol. 2, pp. 29-35, 2007.

[27] G. B. Kliman and J. Stein, "Methods of motor current signature analysis," Electric Power Components and Systems, pp. 463-474, 1992.

[28] G. M. Joksimovic and J. Penman, "The detection of inter-turn short circuits in the stator windings of operating motors," Industrial Electronics, IEEE Transactions on, vol. 47, pp. 1078-1084, 2000.

[29] S. M. A. Cruz and A. J. Marques Cardoso, "Stator winding fault diagnosis in three-phase synchronous and asynchronous motors, by the extended Park's vector approach," presented at Industry Applications Conference, Conference Record of the IEEE, 2000.

[30] J. Aguayo, A. Claudio, L. G. Vela, and S. Gentile, "A survey of fault diagnosis methods for induction motors drives under inverter fault conditions," presented at Electrical and Electronics Engineering (ICEEE' 04). 1st International Conference on, 2004.

[31] S. M. A. Cruz and A. J. M. Cardoso, "The method of multiple reference frames applied to the diagnosis of stator faults in three-phase induction motors," presented at Power Electronics and Motion Control Conference (IPEMC '04), The 4th International, 2004.

[32] S. M. A. Cruz and A. J. M. Cardoso, "Multiple reference frames theory: a new method for the diagnosis of stator faults in three-phase induction motors," Energy Conversion, IEEE Transactions on, vol. 20, pp. 611-619, 2005.

[33] G. B. Kliman, W. J. Premerlani, R. A. Koegl, and D. Hoeweler, "A new approach to on-line turn fault detection in AC motors," presented at Thirty-First Annual Meeting Industry Applications Conference (IAS '96), 1996.

[34] M. Arkan, D. K. Perovic, and P. Unsworth, "Online stator fault diagnosis in induction motors," Electric Power Applications, IEE Proceedings -, vol. 148, pp. 537-547, 2001.

[35] J. L. Kohler, J. Sottile, and F. C. Trutt, "Condition monitoring of stator windings in induction motors. I. Experimental investigation of the effective negative-sequence impedance detector," Industry Applications, IEEE Transactions on, vol. 38, pp. 1447-1453, 2002.

[36] F. Briz, M. W. Degner, P. Garcia, and A. B. Dicz, "Induction machine diagnostics using zero sequence component," presented at Industry Applications Conference, Conference Record of the Fourteenth IAS Annual Meeting, 2005.

[37] F. Briz, M. W. Degner, A. ZamarrónJuan, and M. Guerrero, "Online stator winding fault diagnosis in inverter-fed AC machines using high-frequency signal injection," Industry Applications, IEEE Transactions on, vol. 39, 2003.

[38] S. M. A. Cruz and A. J. M. Cardoso, "Diagnosis of stator inter-turn short circuits in DTC induction motor drives," Industry Applications, IEEE Transactions on, vol. 40, pp. 1349-1360, 2004.

[39] V. Devanneaux, H. Kabbaj, B. Dagues, and J. Faucher, "An accurate model of squirrel cage induction machines under rotor faults," presented at Electrical Machines and Systems (ICEMS 2001), Proceedings of the Fifth International Conference on, 2001.

[40] N. Bianchi, S. Bolognani, and G. Comelato, "Finite element analysis of three-phase induction motors: comparison of two different approaches," Energy Conversion, IEEE Transactions on, vol. 14, pp. 1523-1528, 1999.

[41] A. Tenhunen and A. Arkkio, "Modelling of induction machines with skewed rotor slots," Electric Power Applications, IEE Proceedings -, vol. 148, pp. 45-50, 2001.

[42] W. N. Fu, S. L. Ho, and H. C. Wong, "Design and analysis of practical induction motors," Magnetics, IEEE Transactions on, vol. 37, pp. 3663-3667, 2001.

[43] W. N. Fu, S. L. Ho, H. L. Li, and H. C. Wong, "An effective method to reduce the computing time of nonlinear time-stepping finite-element magnetic field computation," Magnetics, IEEE Transactions on, vol. 38, pp. 441-444, 2002.

[44] W. N. Fu, S. L. Ho, H. L. Li, and H. C. Wong, "A multislice coupled finite-element method with uneven slice length division for the simulation study of electric machines," Magnetics, IEEE Transactions on, vol. 39, pp. 1566-1569, 2003.

[45] P. Dziwniel, B. Boualem, F. Piriou, J. P. Ducreux, and P. Thomas, "Comparison between two approaches to model induction machines with skewed slots," Magnetics, IEEE Transactions on, vol. 36, pp. 1453-1457, 2000.

[46] S. Mezani, B. Laporte, and N. Takorabet, "Saturation and space harmonics in the complex finite element computation of induction motors," Magnetics, IEEE Transactions on, vol. 41, pp. 1460-1463, 2005.

[47] L. Alberti, N. Bianchi, and S. Bolognani, "Finite element modeling of induction motor for variable speed drives," presented at Electrical Machines (ICEM 2008), 18th International Conference on, 2008.

[48] K. J. Bradley and A. Tami, "Reluctance mesh modelling of induction motors with healthy and faulty rotors," presented at Industry Applications Conference, 1996. Thirty-First IAS Annual Meeting, (IAS '96), Conference Record of the 1996 IEEE, 1996.

[49] P. Sewell, K. J. Bradley, J. C. Clare, P. Wheeler, A. Ferrah, R. Magill, and S. Sunter, "Dynamic reluctance mesh modelling of induction motors," presented at ICEM'98, Istanbul, Turkey, 1998.

[50] C. Gerada, "Dynamic field models of electrical machines and their control systems applied to performance enhancement and fault tolerance," in Electrical and Electronic Engineering Department, PhD Thesis: The University of Nottingham, England, 2005.

[51] C. Gerada, K. Bradley, M. Sumner, and P. Sewell, "Evaluation of a vector controlled induction motor drive using the dynamic magnetic circuit model," in IEEE IAS. Salt Lake 2003.

[52] H.Meshgin-Kelk, J. Milimonfared, and H. A. Toliyat, "Interbar currents and axial fluxes in healthy and faulty induction motors," Industry Applications, IEEE Transactions on, vol. 40, pp. 128-134, 2004.

[53] G. Didier, H. Razik, A. Abed, and A. Rezzoug, "On space harmonics model of a three phase squirrel cage induction motor for diagnosis purpose," in EPE - PEMC 2002, 2002.

[54] G. Didier, H. Razik, and A. Rezzoug, "An induction motor model including the first space harmonics for broken rotor bar diagnosis," European Transaction on Electrical Power, vol. 15, pp. 229 - 243, 2005.

[55] X. Luo, Y. Liao, H. A. Toliyat, A. El-Antably, and T. A. Lipo, "Multiple coupled circuit modeling of induction machines," Industry Applications, IEEE Transactions on vol. 31, pp. 311 -318, 1995.

[56] G. Houdouin, G. Barakat, B. Dakyo, and E. Destobbeleer, "A method for the simulation of inter-turn short circuits in squirrel cage induction machines," in EPE-PEMC 2002, 2002.

[57] M. Boucherma, M. Y. Kaikaa, and A. Khezzar, "Park model of squirrel cage induction machine including space harmonics effects," Journal of Electrical Engineering, vol. 57, pp. 193 - 199, 2006.

[58] H. A. Toliyat, S. Bhattacharya, M. M. Rahimian, and T. A. Lipo, "Transient analysis of induction machines under internal faults using winding function," Research Report 92-1, Departmental of Electrical and Computer Engineering, University of Wisconsin-Madison, March 1992.

[59] N. A. Al-Nuaim and H. A. Toliyat, "A novel method for modeling dynamic air-gap eccentricity in synchronous machines based on modified winding function theory," Energy Conversion, IEEE Transactions on, vol. 13, pp. 156-162, 1998.

[60] H. A. Toliyat, M. S. Arefeen, and A. G. Parlos, "A method for dynamic simulation and detection of air-gap eccentricity in induction machines," Industry Applications, IEEE Transactions on, vol. 32, pp. 910-918, 1996.

[61] S. E. Zouzou, A. Ghoggal, A. Aboubou, M. Sahraoui, and H. Razik, "Modeling of induction machines with skewed rotor slots dedicated to rotor faults," presented at Diagnostics for Electric Machines, Power Electronics and Drives (SDEMPED 2005), 5th IEEE International Symposium on, 2005.

[62] S. Nandi and S. Nandi, "Modeling of induction machines including stator and rotor slot effects," Industry Applications, IEEE Transactions on, vol. 40, pp. 1058-1065, 2004.

[63] H. Guldemir, "Prediction of induction motor line current spectra from design data," in Electrical and Electronic Engineering Department, PhD Thesis: The University of Nottingham, England, 1999.

[64] H. Guldemir and K. J. Bradley, "An improved approach to the prediction of line current spectrum in induction machines," Electrical Engineering, vol. 86, pp. 17–24, 2003.

[65] S. E. Lyshevski, Electromechanical Systems, Electric Machines and Applied Mechatronics. Florida: CRC Press, Boca Raton, 1999.

[66] M. Belhaj, P. Gu´erin, and M. E. Za¨ım, "An harmonic model of the induction machine supplied by non sinusoidal voltages," The European Physical Journal Applied Physics, vol. 43, pp. 189-195, 2008.

[67] M. Belhaj, P. Guérin, M. E. Zaïm, and L. Abdeljalil, "Influence of the frequential identification tests on the induction machine modelling," Eur. Phys. J. Appl. Phys., vol. 47, pp. 31101, 2009.

[68] H. Kabbaj, X. Roboam, Y. Lefevre, and J. Faucher, "Skin effect characterization in a squirrel cage induction machine," presented at Industrial Electronics, 1997. ISIE '97., Proceedings of the IEEE International Symposium on, 1997.

[69] S. Canat and J. Faucher, "Fractionnal order : frequential parametric identification of the skin effect in the rotor bar of squirrel cage induction

machine," presented at ASME Design Engineering Technical Conferences, 2003.

[70] H. Henao, C. Martis, and G. A. Capolino, "An equivalent internal circuit of the induction machine for advanced spectral analysis," Industry Applications, IEEE Transactions on, vol. 40, pp. 726-734, 2004.

[71] C. Delmotte-Delforge, H. He´nao, G. Ekwe, P. Brochet, and G. A. Capolino, "Comparison of two modeling methods for induction machine study: application to diagnosis," The International Journal for Computation and Mathematics in Electrical and Electronic Engineering, vol. 22, pp. 891-908, 2003.

[72] G. Aroquiadassou, A. Cavagnino, H. Henao, A. Boglietti, and G.-A. Capolino, "A new circuit-oriented model for the analysis of six-phase induction machine performances," Electric Power Systems Research, vol. 78, pp. 1798–1805, 2008.

[73] P. L. Alger, Induction machines , Their Behavior and Uses. Australia: Gordon and Breach 1995.

[74] M. Poloujadoff, "The theory of three phase induction squirrel cage motors," Electric Power Components and Systems, vol. 13, pp. 245 - 264, 1987.

[75] A. Charette, J. Xu, A. Lakhsasi, Z. Yao, and V. Rajagopalan, "Modeling and simulation of saturated induction motors," presented at Computers in Power Electronics, 1996., IEEE Workshop on, 1996.

[76] L. Jingchuan and X. Longya, "Investigation of cross-saturation and deep bar effects of induction motors by augmented d-q modeling method," presented at Industry Applications Conference, Thirty-Sixth IAS Annual Meeting., 2001.

[77] J. O. Ojo, A. Consoli, and T. A. Lipo, "An improved model of saturated induction machines," Industry Applications, IEEE Transactions on, vol. 26, pp. 212-221, 1990.

[78] H. Hofmann, S. R. Sanders, and C. R. Sullivan, "Stator-flux-based vector control of induction machines in magnetic saturation," Industry Applications, IEEE Transactions on, vol. 33, pp. 935-942, 1997.

[79] C. R. Sullivan and S. R. Sanders, "Models for induction machines with magnetic saturation of the main flux path," Industry Applications, IEEE Transactions on, vol. 31, pp. 907-917, 1995.

[80] J. C. Moreira and T. A. Lipo, "Modeling of saturated AC machines including air gap flux harmonic components," Industry Applications, IEEE Transactions on, vol. 28, pp. 343-349, 1992.

[81] T. A. Lipo and Y. Liao, "Effect of saturation third harmonic on the performance of squirrel-cage induction machines," Electrical Machines and Power Systems vol. 22, pp. 155-173, 1994.

[82] S. Nandi, "A detailed model of induction machines with saturation extendable for fault analysis," Industry Applications, IEEE Transactions on, vol. 40, pp. 1302-1309, 2004.

[83] D. Bispo, L. Martins, Neto, J. T. de Resende, and D. A. de Andrade, "A new strategy for induction machine modeling taking into account the magnetic saturation," Industry Applications, IEEE Transactions on, vol. 37, pp. 1710-1719, 2001.

[84] V. Donescu, A. Charette, Z. Yao, and V. Rajagopalan, "Modeling and simulation of saturated induction motors in phase quantities," Energy Conversion, IEEE Transaction on, vol. 14, pp. 386-393, 1999.

[85] O. A. Mohammed, S. Liu, Z. Liu, and N. Abed, "Physical phase variable models of electrical equipments and their applications in integrated drive simulation for shipboard power system," presented at Electric Ship Technologies Symposium, 2005 IEEE, 2005.

[86] O. A. Mohammed, S. Liu, and Z. Liu, "Phase-variable model of PM synchronous machines for integrated motor drives," Science, Measurement and Technology, IEE Proceedings- vol. 151, pp. 423 - 429, 2004.

[87] N. A. O. Demerdash and P. Baldassari, "A combined finite element-state space modeling environment for induction motors in the ABC frame of reference: the no-load condition," Energy Conversion, IEEE Transactions on vol. 7, pp. 698 - 709, 1992.

[88] P. Baldassari and N. A. Demerdash, "A combined finite element-state space modeling environment for induction motors in the ABC frame of reference: the blocked-rotor and sinusoidally energized load conditions," Energy Conversion, IEEE Transactions on vol. 7, pp. 710 - 720, 1992.

[89] R. Peuget, S. Courtine, and J. P. Rognon, "Fault detection and isolation on a PWM inverter by knowledge-based model," Industry Applications, IEEE Transactions on, vol. 34, pp. 1318-1326, 1998.

[90] D. U. Campos-Delgado, D. R. Espinoza-Trejo, and E. Palacios, "Fault-tolerant control in variable speed drives: a survey," Electric Power Applications, IET, vol. 2, pp. 121-134, 2008.

[91] M. E. H. Benbouzid and G. B. Kliman, "What stator current processing-based technique to use for induction motor rotor faults diagnosis?," Energy Conversion, IEEE Transactions on, vol. 18, pp. 238-244, 2003.

[92] M. E. H. Benbouzid, M. Vieira, and C. Theys, "Induction motors' faults detection and localization using stator current advanced signal processing

techniques," Power Electronics, IEEE Transactions on, vol. 14, pp. 14-22, 1999.

[93] R. R. Obaid and T. G. Habetler, "Current-based algorithm for mechanical fault detection in induction motors with arbitrary load conditions," presented at Industry Applications Conference, 38th IAS Annual Meeting. Conference Record of the, 2003.

[94] S. M. A. Cruz and A. J. M. Cardoso, "Modelling and simulation of DTC induction motor drive for stator winding faults diagnosis," in EPE 2003. Toulouse, France, 2003.

[95] H. Rodriguez-Cortes, A. M. Stankovic, and C. Hadjicostis, "Model-Based Broken Rotor Bar Detection on an IFOC Driven Squirrel Cage Induction Motor," presented at Proceedings Of The American Control Conference, 2004.

[96] S. Bachir, S. Tnani, J. C. Trigeassou, and G. Champenois, "Diagnosis by parameter estimation of stator and rotor faults occurring in induction machines," Industrial Electronics, IEEE Transactions on, vol. 53, pp. 963-973, 2006.

[97] S. Bachir, G. Champenois, S. Tnani, and J. P. Gaubert, "Stator faults diagnosis in induction machines under fixed speed," presented at Power Electronics and Applications, 2005 European Conference on, 2005.

[98] C. S. Kallesøe, P. Vadstrup, H. Rasmussen, and R. Izadi-Zamanabadi, "Estimation of stator winding faults in induction motors using an adaptive observer scheme," presented at 39th IEEE industry applications conference IAS' 04 annual meeting Seattle, 2004.

[99] W. T. Thomson and R. J. Gilmore, "Motor current signature analysis to detect faults in induction motor drives - fundamentals, data interpretation and industrial case histories" presented at Proceedings of 32nd Turbomachinery Symposium, Texas, USA, 2003.

[100] M. A. Laughton, "Artificial intelligence techniques in power systems," presented at Artificial Intelligence Techniques in Power Systems (Digest No: 1997/354), IEE Colloquium on, 1997.

[101] S. Altug, C. Mo-Yuen, and H. J. Trussell, "Fuzzy inference systems implemented on neural architectures for motor fault detection and diagnosis," Industrial Electronics, IEEE Transactions on, vol. 46, pp. 1069-1079, 1999.

[102] R. M. Tallam, T. G. Habetler, and R. G. Harley, "Self-commissioning training algorithms for neural networks with applications to electric machine fault diagnostics," Power Electronics, IEEE Transactions on, vol. 17, pp. 1089-1095, 2002.

[103] K. Kyusung, A. G. Parlos, and R. Mohan Bharadwaj, "Sensorless fault diagnosis of induction motors," Industrial Electronics, IEEE Transactions on, vol. 50, pp. 1038-1051, 2003.

[104] V. T. Tran, B.-S. Yang, M.-S. Oh, and A. C. C. Tan, "Fault diagnosis of induction motor based on decision trees and adaptive neuro-fuzzy inference," Expert Systems with Applications, vol. 36, pp. 1840-1849, 2009.

[105] P. Milanfar and J. H. Lang, "Monitoring the thermal condition of permanent-magnet synchronous motors," Aerospace and Electronic Systems, IEEE Transactions on, vol. 32, pp. 1421-1429, 1996.

[106] K. S. Smith, R. Li, and J. Penman, "Real-time detection of intermittent misfiring in a voltage-fed PWM inverter induction-motor drive," Industrial Electronics, IEEE Transactions on, vol. 44, pp. 468-476, 1997.

[107] S. Abramik, W. Slezynski, J. Nieznanski, and H. Piquet, "A diagnostic method for online fault detection and localization in vsi-fed ac drives," presented at Power Electronics and Applications, EPE 2003, 10th European Conference on, 2003.

[108] R. L. de Araujo Ribeiro, C. B. Jacobina, E. R. C. da Silva, and A. M. N. Lima, "Fault detection of open-switch damage in voltage-fed PWM motor drive systems," Power Electronics, IEEE Transactions on, vol. 18, pp. 587-593, 2003.

[109] O. Wallmark, L. Harnefors, and O. Carlson, "Control algorithms for a fault-tolerant pmsm drive," Industrial Electronics, IEEE Transactions on, vol. 54, pp. 1973-1980, 2007.

[110] P. C. Sen, Priciples of electric machines and power electronics. USA: John Wiley & Son, 1997.

[111] B. Heller and V. Hamata, Harmonic field effects in induction machines. Amsterdam: Elsevier Scientific 1977.

[112] The MathWork manual, Simulink model-based and system-based design: The MathWorks, 2002.

[113] A. A. Jimoh and R. D. Findlay, "Parasitic torques in saturated induction motors," Energy conversion, ieee transactions on, vol. 3, pp. 157-163, 1988.

[114] C. Gerada, K. Bradley, M. Sumner, G. Asher, and J. Arellano-Padilla, "Permanent Magnet Synchronous machines for Saliency-based, Self-Sensored Motion Control," presented at Industrial Electronics Society (IECON 2007), 33rd Annual Conference of the IEEE, 2007.

[115] O. Jasim, C. Gerada, M. Sumner, and J. Arellano-Padilla, "A simplified model for induction machines with faults to aid the development of fault tolerant

drives," presented at The 13th Power Electronics and Motion Control Conference EPE-PEMC' 08, 2008.

[116] D. W. Novotinty and T. A. Lipo, Vector control and dynamics of AC drives: Clarendon Press Oxford, 1996.

[117] F. Briz, M. W. Degner, P. García, and A. B. Diez, "Induction machine diagnostics using zero sequence components," presented at IEEE IAS'05, Hong Kong, China, 2005.

[118] S. Williamson and S. Smith, "Pulsating torque and losses in multiphase induction machines," Industry Applications, IEEE Transactions on, vol. 39, pp. 986-993, 2003.

[119] Programmable AC Source 61705 User's Manual: Chroma ATE INC., 2007.

[120] N. R. Klaes, "Parameter identification of an induction machine with regard to dependencies on saturation," IEEE Transactions on Industry Applications, vol. 29, pp. 1135-1140, 1993.

[121] G. A. Covic and J. T. Boys, "Operating restrictions for third harmonic control of flux in induction machines," Electric Power Applications, IEE Proceedings B, vol. 139, pp. 485-496, 1992.

[122] S. Nandi, "Detection of stator faults in induction machines using residual saturation harmonics," Industry Applications, IEEE Transactions on, vol. 42, pp. 1201-1208, 2006.

[123] W. Leonhard, Control of electrical drives: Springer Germany, 1996.

[124] J. William D. Stevenson, Elements of power system analysis, Fourth Edition ed: McGRAW-HILL BOOK COMPANY, 1982.

[125] P. Vas, Vector Control of AC Machines: Clarendon Press Oxford, 1990.

[126] A. Hughes, Electric Motors and Drives: Newnes, 1990.

[127] X. Xu and D. W. Novotny, "Selection of the flux reference for induction machine drives in the field weakening region," Industry Applications, IEEE Transactions on, vol. 28, pp. 1353-1358, 1992.

[128] X. Xu, R. de Doncker, and D. W. Novotny, "Stator flux orientation control of induction machines in the field weakening region," presented at Industry Applications Society Annual Meeting, Conference Record of the IEEE, 1988.

[129] K. Sang-Hoon and S. Seung-Ki, "Maximum torque control of an induction machine in the field weakening region," Industry Applications, IEEE Transactions on, vol. 31, pp. 787-794, 1995.

[130] K. Sang-Hoon and S. Seung-Ki, "Voltage control strategy for maximum torque operation of an induction machine in the field-weakening region," Industrial Electronics, IEEE Transactions on, vol. 44, pp. 512-518, 1997.

[131] G. Asher, "Induction motor drives course notes," Induction motor drives module, University of Nottingham, 2006.

[132] L. Harnefors, K. Pietilainen, and L. Gertmar, "Torque-maximizing field-weakening control: design, analysis, and parameter selection," Industrial Electronics, IEEE Transactions on, vol. 48, pp. 161-168, 2001.

[133] M. Sumner and G. M. Asher, "Auto-commissioning for voltage-referenced voltage-fed vector-controlled induction motor drives," Electric Power Applications, IEE Proceedings B, vol. 140, pp. 187-200, 1993.

[134] M. Sumner, "Vector controlled induction motor drive using transputer parallel processors," in Electrical and Electronic Engineering Department, PhD Thesis: The University of Nottingham, England, 1990.

[135] R. Blasco-Gimenez, "High performance sensorless vector control of induction motor drives," in Electrical and Electronic Engineering Department, PhD Thesis: The University of Nottingham, England, 1996.

[136] G. Turl, "A synchronised multi-motor control system using hybrid sensorless induction motor drives," in Electrical and Electronic Engineering Department, PhD Thesis: The University of Nottingham, England, 2002.

[137] dSPACE Control Desk Experiment Guide. Padeborn, Germany, 2004.

[138] L. Balmer, Signal and Systems-an Introduction: Prentice Hall, 1991.

[139] I. Boldea, S. A. Nasar, The Induction Machine Handbook: CRC Press, 2002.